INTEGRATED COMPUTATIONAL ALLOY DESIGN, SINGLE CRYSTAL GROWTH, AND CHARACTERIZATION OF NICKEL BASE SUPERALLOYS

by

Mehdi Montakhabrazlighi

B.S., Materials science and Engineering, University of Tabriz, 2003

M.S., Materials science and Engineering, Sharif University of Technology, 2006

Submitted to the Institute for Graduate Studies in
Science and Engineering in partial fulfillment of
the requirements for the degree of
Doctor of Philosophy

Graduate Program in Mechanical Engineering
Boğaziçi University
2018

ACKNOWLEDGEMENTS

I would like to express my sincere appreciation and gratitude to Dr. Ercan Balıkçı, my thesis supervisor, for his unforgettable passion, guidance, insightful advice, and constructive suggestions through my PhD study. He generously spent his time and thought me how to organize my research finding, maintain high morals, and motivated me to explore in depth in the field of single crystal superalloys.

I also have to thank the members of my PhD committee, Dr. Turan Özturan, Dr. Can Aydıner, Dr. Cevat Sarıoğlu, and Dr. Nuri Solak for evaluation of my thesis and their guidance in the period of this study.

Many thanks also go to Dr. Nuri Ersoy and Dr. Jeremy Mason for their support in this dissertation.

My special thanks go to Mr. Ibrahim Mutlu, Mr. Yüksel Gezer, and Mr. Bünyamin Gezer who helped me in the experimental part of the thesis.

I would like to thank Dr. Baki Altuncevahir at Istanbul Technical University for providing arc vacuum melting equipment for preparing the master alloys.

I would also like to thank my friends, Mr. Aydin Sheikhi, Mr. Mert Bacak, and Mr. Arün Altınçekiç for their support and help to finish this study.

Finally, I would like to thank my wife for her continued support, enthusiasm, dedication, and passion that helped me accomplish this study. I will never forget her sympathy and encouragement who gave me the reason to go on, even during the difficult times.

This work is funded by the Scientific and Technological Research Council of Turkey (TUBITAK) under the grant number 112M783. I am grateful for their support.

ABSTRACT

INTEGRATED COMPUTATIONAL ALLOY DESIGN, SINGLE CRYSTAL GROWTH, AND CHARACTERIZATION OF NICKEL BASE SUPERALLOYS

This dissertation is formed by a part of work conducted in a TUBITAK project (112M783). In the dissertation, first alloy design of a third generation superalloy, and then its production as single crystals, heat treatments, and creep tests are investigated. A combined Neural Network (NN) – PHAse COMPutation (PHACOMP) – CALculation of PHAse Diagrams (CALPHAD) method is applied to alloy development of single crystal Ni base superalloys with low density and high creep resistance. PHACOMP method is used for estimation of the volume fraction of the γ' and a parameter named M_d which is an index showing the propensity of the alloys towards formation of the TCP phases. Neural network is used for modeling the density and rupture time by training and testing a network with a set of the known experimental alloy compositions. Modeling results is combined with data obtained from PHACOMP to render very useful scatter plots for the effect of alloying elements; stress, temperature and volume fraction of the γ' phase on density, rupture strength and formation of TCP phases in the Ni base single crystal superalloys. A third generation alloy (ERBALLOY) was designed and produced by two methods, vertical Bridgman (VB), and vertical Bridgman with a submerged baffle (VBSB). The effect of low melt height on solidification characteristics of the alloys is studied. Evolution of the phases is simulated by CALPHAD bases Thermo-Calc software. The solution and aging heat treatment of the alloys are modeled with Dictra and TC-Prisma software. Characterization of the microstructure is performed by optical, scanning transmission electron microscope (SEM), and electron probe microanalysis (EPMA). The creep behavior of the ERBALLOY is tested at an intermediate and a high temperature and showed reasonable agreement with NN results. The approach used in this study is in line with the Materials Genome Initiative (GMI) and Integrated Computational Materials Engineering (ICME), and it can be applied for designing low density-creep resistant single crystal superalloys for critical parts of the aircraft/gas turbine engines.

ÖZET

NIKEL ESASLI SÜPERALAŞIMLARIN ENTEGRE HESAPLAMALI ALAŞIM TASARIMI, TEK KRISTAL OLARAK ÜRETIMI VE KARAKTERIZASYONU

Bu tez çalışması 112M783 numaralı TÜBİTAK projesi kapsamında elde edilen araştırma sonuçlarının bir kısmından oluşturulmuştur. Tez çalışmasında, önce bir üçüncü nesil süperalasım tasarlanmış, daha sonra ise bu alaşımın tek kristal olarak üretimi, ısıl işlemleri ve sürünme davranışları incelenmiştir. Kombine olarak kullanılan sinir ağı (NN: Neural Network)–PHACOMP (PHAse COMPutations)–CALPHAD (CALculation of PHAse Diagrams) yöntemleri, düşük yoğunluklu ve yüksek sürünme direncine sahip tek kristal Ni bazlı süperalaşımların alaşım tasarlanmasına uygulanmıştır. PHACOMP metodu, γ' hacimsel miktarını ve M_d parametresini hesaplamak için kullanılmıştır. M_d parametresi alaşımların TCP fazlarının oluşmasına yönelik eğilimini tahmin etmek için kullanılır. NN modelleme sonuçları, PHACOMP yönteminden elde edilen verilerle birleştirilmiş ve çok değerli malzeme seçim dağılım grafikleri oluşturmak için kullanılmıştır. Bu grafikler Ni esaslı tek kristal süper alaşımlarda bulunan alaşım elementlerinin, stresin, sıcaklığın ve γ' hacimsel miktarının, Ni bazlı süper alaşımların yoğunluk ve sürünme kopma mukavemeti üzerindeki etkisini belirlemek için kullanılmıştır. Tasarlanan üçüncü nesil bir alaşım (ERBALLOY), düşey Bridgman (VB) ve düşük sıvı yükseklikli Bridgman (VBSB) yöntemleriyle üretilmiştir. Düşük sıvı yüksekliğinin katılaşma karakteri üzerindeki etkisi çalışılmıştır. Katılaşmış alaşımların çözelti ve yaşlanma ısıl işlemleri Dictra ve TC-Prisma yazılımları ile modellenmiştir. Mikroyapı karakterizasyonu optik, taramalı elektron mikroskobu (SEM) ve elektron prob mikroanaliz (EPMA) yöntemleriyle yapılmıştır. ERBALLOY'un sürünme davranışını belirlemek için orta ve yüksek sıcaklıkta testler yapılmıştır. Deneysel sonuçlar ile NN sonuçları arasında makul bir uyum görülmüştür. Tezde kullanılan bu yaklaşım Malzeme Gen Girişimi (MGI) ve Entegre Hesaplamalı Malzeme Mühendisliği (ICME) yaklaşımları ile uyumludur. Sonuçlar havacılık/gaz türbini motorları için düşük yoğunluklu ve yüksek sürünme dayanımlı tek kristal süperalaşımların tasarlanması için değerlendirilebilir.

TABLE OF CONTENTS

ACKNOWLEDGEMENTS iii

ABSTRACT iv

ÖZET v

LIST OF FIGURES ix

LIST OF TABLES xix

LIST OF SYMBOLS xxi

LIST OFACRONYMS/ABBREVIATIONS xxiv

1. INTRODUCTION 1

1.1. Introduction to Superalloys 4

1.1.1. Nickel Base Superalloys 5

1.1.1.1. Gamma (γ) 7

1.1.1.2. Gamma Prime (γ') 8

1.1.1.3. Carbides 9

1.1.1.4. TCP Phases 10

1.1.2. Alloying Elements 15

1.1.3. Mechanical Properties 17

1.1.4. Processing of Superalloys 19

1.2. Superalloys Design 24

1.2.1. Integrated Computational Materials Engineering (ICME) 27

1.2.2. Alloy Design by Electronic Approach (PHACOMP) 28

1.2.3. Alloy Design by CALPHAD 30

1.2.4. Alloy Design by Neural Network (NN) 41

1.3. Production of Single Crystal Superalloys 46

1.3.1. Vertical Bridgman (VB) Method 50

1.3.2. Vertical Bridgman with Submerged Baffle (VBSB) Method 52
1.4. Heat Treatments of Single Crystal Superalloys 54
1.4.1. Solution Treatment 54
1.4.2. Aging Heat Treatment 55
1.4.2.1. Nucleation 55
1.4.2.2. Growth 58
1.4.2.3. Coarsening 60
1.5. Creep Rupture Behavior of Single Crystal Ni Base Superalloys 63
1.6. Objectives 65
2. MATERIALS AND METHODS 67
2.1. Alloy Design of Ni Base Superalloys 67
2.1.1. Neural Network Modeling 67
2.1.2. CALPHAD Modeling 68
2.2. Single Crystal Growth of Designed Ni Base Suepralloys 70
2.2.1. Experimental Setup 70
2.2.2. Growth of the Alloys by the VB and VBSB Methods 70
2.3. Heat Treatment of the Grown Alloys 73
2.3.1. Solution Treatments 73
2.3.2. Aging Treatments 75
2.4. Creep Rupture Behavior of the Grown Alloys 75
2.5. Composition and Microstructure Characterization 77
3. RESULTS and DISCUSSION 78
3.1. Alloy Design of Ni Base Superalloys 78
3.1.1. Neural Network Modeling of the Density and Rupture Life 78
3.1.1.1. Re 80

3.1.1.2. Cr 86

3.1.1.3. Al 88

3.1.1.4. Ta/W 90

3.2. CALPHAD Modeling of the Phase Evolution and Critical Temperatures 95

3.2.1. Equilibrium Module. 95

3.2.2. Scheil Module. 98

3.3. Microstructure of the Grown Single Crystal Superalloys 106

3.3.1. Solidification versus Withdrawal Velocity 106

3.3.2. Orientation of Dendrites 108

3.3.3. Mushy Zone and Melt Back Transition Region 110

3.3.4. Primary Dendrite Arm Spacing and Core Size 114

3.3.5. Porosity 119

3.4. Heat Treatments of the Grown Single Crystal Superalloys 126

3.4.1. Solution Treatments 126

3.4.1.1. Moddeling Results 131

3.4.2. Aging Treatments 135

3.4.2.1. Precipitate Size and Morphology 136

3.4.2.2. TC-Prisma Prediction of Precipitate Size and Morphology 145

3.4.3. TCP Phases 147

3.5. Rupture Behavior of the Grown Single Crystal Superalloys 153

4. CONCLUSION 163

5. FUTURE WORKS 165

6. REFERENCES 167

LIST OF FIGURES

Figure 1.1. Variation of the alloying elements from the early conventional cast to the modern fourth generation superalloys [1]. 6

Figure 1.2. Crystal structure of the Gamma (γ) phase. 7

Figure 1.3. Crystal structure of the Gamma-prime (γ') phase. 8

Figure 1.4. The crystal structure of the major TCP phases in single crystal superalloys a) σ, b) μ, c) P, and d) R [63]. 11

Figure 1.5. The yield stress behavior of some single crystal superalloys with temperature. 17

Figure 1.6. Tensile strength of some superalloys as a function of temperature. 18

Figure 1.7. Directional solidification of a turbine blade in single crystal form [86]. 22

Figure 1.8. Typical plot of the solidification velocity versus thermal gradient for single crystal superalloys [71]. 23

Figure 1.9. B_o versus M_d plot showing the alloying angle. Commercial alloys are shown with their position in the M_d-B_o plot. 29

Figure 1.10. Dependence of the alloying angle and volume fraction of γ'. 30

Figure 1.11. Amount of phases vs. temperature for the CMSX-4 alloy. 33

Figure 1.12. Thermo-Calc equilibrium modeling of the effect of addition of 1, 2, and 3wt% Re to the composition of CMSX-4 on mole fraction of the Sigma phase. 34

Figure 1.13. Calculated solidification sequence of the alloy CMSX-4 predicted by Thermo-Calc Scheil model. 34

Figure 1.14. Logarithm of the interdiffusion coefficient of Al in the binary Ni-Al system versus the mole fraction of Al at different temperatures. The filled symbols represent experimental data and the DICTRA predictions are shown as continuous lines [113]. 36

Figure 1.15. Variation of the interdiffuion coefficient of Ni in Ternary Ni-Al-Cr alloy at 1200°C as a function of Cr content at three different concentrations (at%) of AL. The symbols and continuous line represent the experimental data and Dictra results [113]. 36

Figure 1.16. Schematic architecture of the MLP used in this study showing the input, hidden, and output layers. 41

Figure 1.17. PDAS shown in two different views in SEM photos of the crystals grown in this study. 48

Figure 1.18. SDAS from two top and side views. 49

Figure 1.19. Tertiary dendrite arms branching from the secondary dendrite arms (a, and b). Note the tertiary arms on the secondaries in the marked area. 50

Figure 1.20. Schematic of the vertical Bridgman method [145]. 51

Figure 1.21. The vertical Bridgman with a submerged baffle (VBSB) technique. The effective bulk melt height is shown by h and bounded between base of the baffle and the solid/liquid interface (top of dendrites). 52

Figure 1.22. Variation of the Rayleigh number with liquid fraction during solidification of (a) Pb-Sn, and (b) CMSX-11B alloys. εs and K are the solid fraction, and permeability [150]. For different formulations for Rayleigh numbers, the reader is referred to [144]. 53

Figure 1.23. Variation of the free energy with the size of a nucleus [153]. 57

Figure 1.24. A typical strain versus time plot in single crystal superalloys [79].....64

Figure 1.25. Effect of the temperature at constant stress of 137Mpa (a), and effect of stress at constant temperature of 1085°C (b), on the shape of the creep curve of a fourth generation single crystal alloy containing 4.5wt% Re and 3wt% Ru [165]. 65

Figure 2.1. Root mean square error for training and testing the networks with different number of hidden nodes for estimation of a) density, and b) rupture time. 68

Figure 2.2. Schematic of the transverse and longitudinal cut sections of the samples. 72

Figure 2.3. Schematic of dendritic pattern in the microstructure of a single crystal superalloy with marked areas showing locations of chemical composition measurements with electron probe microanalysis (EPMA). 74

Figure 2.4. The drawing of the machined sample for the creep test. 76

Figure 2.5. Picture of the creep test equipment. 76

Figure 3.1. The predicted density is plotted against the known density after training (a), and testing (b) of the network. The results of the training (c), and testing the network (d), compared with experimental values for rupture time.....79

Figure 3.2. The percentage of the alloys versus density (a), volume fraction of γ' (b), and M_d (c). 80

Figure 3.3. Percentage of alloys in given rupture time ranges are shown in (a-c). Rupture time versus density (d-f), volume fraction of γ' (g-i), and M_d (j-l) are plotted. The markings are explained in the text.....81

Figure 3.4. Scatter plots of M_d versus volume fraction of the γ' for different concentrations of Re. The triangle, circle, and diamond show the first (CMSX-2) [176], second (CMSX-4) [177], and third (CMSX-10) [178] generation alloys, respectively. 86

Figure 3.5. Percentage of alloys in given rupture time ranges are shown in (a-c). Rupture time versus density (d-f) are plotted. The markings are explained in the text. 87

Figure 3.6. Scatter plots of M_d versus volume fraction of the γ' for different concentrations of Cr. The triangle, circle, and diamond show the first (CMSX-2) [176], second (CMSX-4) [177], and third (CMSX-10) [178] generation alloys, respectively. 88

Figure 3.7. Percentage of alloys in given rupture times are shown in (a, c ,e and g). The scatter plot in red shows the alloy design space for different Al levels. b) 3%<Al≤4%, and d) 4%<Al≤5 %, f) 5%<Al≤6%, h) 6%<Al≤7%. The markings are explained in the text. 89

Figure 3.8. Variation of the M_d with volume fraction of γ' for different concentration of Al. a) 4.5%<Al≤5%, and b) 5%<Al≤5.5%, c) 5.5%<Al≤6%, d) 6%<Al≤6.5%. The markings are explained in the text. 90

Figure 3.9. Percentage of alloys in given rupture times are shown in (a,c ,e and g). The scatter plot in gray show the whole alloy design space. Red color shows the alloy design space for the Ta/W ratios as in the first column. The markings are explained in the text. 91

Figure 3.10. Rupture time vs. concentration of Re, Cr, and Al. The secondary top axis shows rupture time vs. ratio of Ta/W. 93

Figure 3.11. Density (a), and rupture time (b) of the CMSX-4 with concentration of the elements. Temperature-stress-rupture time plot for the CMSX-4 (c),

and Larson-Miller plots for selected alloys by NN (continuous lines), and experimental (filled symbols) (d). 94

Figure 3.12. Modeling of the solidification of the ERBALLOY by Thermo-Calc equilibrium model. The vertical axis shows the phase fraction of the phases. FCC_L12#1 is the γ matrix and FCC_L12#2 is the strengthening γ' phase. 96

Figure 3.13. Varying concentration of Re (a), and Al (b), during solidification of ERBALLOY, predicted by Thermo-Calc equilibrium model. The vertical axis shows the weight fraction of the elements. FCC_L12#1 is the γ matrix phase. 97

Figure 3.14. Mole fraction of solid versus temperature simulated by Scheil solidification model of Thermo-Calc. The dotted line shows the results of the equilibrium solidification. 98

Figure 3.15. Solid fraction versus temperature simulated by Scheil solidification model of Thermo-Calc, by considering only the three liquid, γ, and γ' phases. The dotted line shows the results of the equilibrium solidification. 99

Figure 3.16. Varying concentration of Re (a), and Al (b), during solidification of ERBALLOY, predicted by Thermo-Calc Scheil model. The vertical axis shows the weight fraction of the elements. FCC_L12#1 is the γ matrix and FCC_L12#2 is the γ' phase. 100

Figure 3.17. The sequence for nucleation of the interdendritic γ' [191]. 102

Figure 3.18. The longitudinal microphoto showing the position of the eutectic islands at interdendritic region (a), and the interdendritic γ' island at higher magnification (b). 103

Figure 3.19. Three different morphologies of the interdendritic region. Large islands of γ' (1), mosaic type eutectic (2), and elongated γ' with the fan shape eutectic morphology (3). 103

Figure 3.20. SEM photos at two different magnifications for the three morphologies of Figure 3.19. (a) and (b) represent morphology number 1, (c) and (d) represent morphology number 2, and (e) and (f) represent morphology number 3. 104

Figure 3.21. Microstructure of the interdendritic region showing the fan-like eutectics in the vicinity of the γ dendrites and impingement of large γ' (red circles) from two dendrites at the interdendritic region. 106

Figure 3.22. The solidified length (a), interfaces displacement (b), and interface velocity during solidification with different crucible pulling velocities. The dashed line in (a) shows the case when the solidified length would be equal to the pulling velocity. 107

Figure 3.23. The longitudinal microstructure of the samples VB12 (a) and, VBSB12 (b). 109

Figure 3.24. The XRD pattern obtained for the samples of (a) VB12, and (b) VBSB12. 110

Figure 3.25. The initial solidification interface, melt-back transition region, and the new dendrites above the interface of sample VB12 (a), and transverse microphotos at I-5 (b), I0 (c), and I+5 (d). 111

Figure 3.26. Nucleated dendrites at the start of the withdrawal process. The yellow box shows the transient stage at the start of the withdrawal process showing dendrites which are not well-aligned with the growth direction are suppressed after the transient stage. 112

Figure 3.27. The mushy zone length (a), and the transition length (b) for the ERBALLOY samples solidified with the vertical Bridgman (VB) and the vertical Bridgman with a submerged baffle (VBSB). Numbers following the method abbreviation in name labels show the pulling velocity.....114

Figure 3.28. Transverse microphotos of ERBALLOY samples grown with the VB and VBSB methods with different growth velocities, (a) VB12, (b) VBSB12, (c) VB30, and (d) VBSB30. Numbers following the method abbreviation in labels show the pulling velocity.....115

Figure 3.29. The primary dendrite arm spacing (a), and the dendrite core diameter (b) along the lengths of samples solidified with the VB and VBSB methods. Numbers following the method abbreviation in labels show the pulling velocity.....118

Figure 3.30. Longitudinal photos of the dendritic structure of the VB12 at elevations (a) 25, and (b) 65mm above the interface. 118

Figure 3.31. Solidification shrinkage microporosity (seen as dark) in the VB12, (a) transverse section, and (b) longitudinal section. 120

Figure 3.32. The pore diameter in the ERBALLOY, showing a general increase in pore diameter with the distance from initial interface. 121

Figure 3.33. Pore area fraction percentage for the four samples along the solidified length (a), and the average pore area fraction of the samples (b). 121

Figure 3.34. The top portion of the grown VBSB12 sample showing the interconnectivity in the interdendritic region resembling the fluid feeding path at the interdendritic region. 124

Figure 3.35. Variation of the interdendritic width along the grown samples. 124

Figure 3.36. SEM photos of the VB12 samples for the as-cast and solution treated samples. First column shows the dendrites. Second column shows precipitates in the dendrite core. Third and fourth column show precipitates in the interdendritic region. 128

Figure 3.37. Segregation coefficients in the solution treated samples..... 129

Figure 3.38. The incipient melting signs in the sample S4..... 130

Figure 3.39. Concentration profiles along secondary dendrite arms for the as-cast (a), and solution heat treated sample S6..... 131

Figure 3.40. The concentration profile during the solution treatment process simulated by Dictra by considering half SDA as characteristic diffusion length, and Schiele segregation pattern. a) Al, b) W, c) Re, and d) Co..... 132

Figure 3.41. The concentration profile during the solution treatment process simulated by Dictra by considering half PDAS as characteristic diffusion length, and experimental segregation pattern. a) Al, b) W, c) Re, and d) Co. 134

Figure 3.42. Comparison of the simulation (a) and experimental results (b)..... 135

Figure 3.43. Morphology of the coarse and fine γ'. All samples are first aged for 6 hours at 1140 ˚C and then aged at 870 °C for 2,4,16,48,500 and 1000 hours. The samples are quenched in water after aging treatment. 137

Figure 3.44. Fine precipitates observed in the dendrite core (a) for the sample A48, which are absent in the dendrite leaf (b) and in interdendritic regions (c). 138

Figure 3.45. Formation of the fine precipitates in the shared corner of the four neighbor coarse precipitates..... 139

Figure 3.46. Fine precipitates in the γ matrix in between the TCP phases..... 141

Figure 3.47. Size versus aging time for the coarse precipitates at 870 ˚C. 142

Figure 3.48. Natural logarithm of the size versus natural logarithm of time with a line fitted. All the alloys are first aged at 1140 ˚C for 6 hours. 143

Figure 3.49. Variation of the area fraction of the coarse precipitates with the aging time..... 144

Figure 3.50. Coarsening of the secondary γ' precipitates at 870 ˚C. All the alloys are first aged at 1140 ˚C for 6 hours. 145

Figure 3.51. Increasing size of γ' precipitates during aging process at 1140 ˚C. 146

Figure 3.52. Size distribution of the primary γ' precipitates after 2, 4, and 6 hours of aging at 1140 °C..... 146

Figure 3.53. Histogram of the primary precipitate size range for the sample aged at 1140 ˚C for 6 hours a) experimental and b) TC-Prisma modeling. 147

Figure 3.54. Morphology of the representative TCP phase formed at the dendrite core for different aging times. A0, A2, A4, A16, A46, A500, and A1000 samples are aged first at 1140 °C for 6 hours. Then they are aged at 870°C for 0, 2,4,16, 500 and 1000 hours respectively. 149

Figure 3.54. Morphology of the representative TCP phase formed at the dendrite core for different aging times. A0, A2, A4, A16, A46, A500, and A1000 samples are aged first at 1140 °C for 6 hours. Then they are aged at 870°C for 0, 2,4,16, 500 and 1000 hours respectively. (cont.) 150

Figure 3.55. Morphology of the Sigma, and Mu phase (a) and P phase (b) [217]. 150

Figure 3.56. The strain vs time curves (a, c, and e), and strain rate vs strain (b, d, and f) for the alloys grown in this study. 155

Figure 3.57. Creep test under intermediate and high temperature regime for the alloy CMSX-4 [222]. 156

Figure 3.58. Change in the morphology of the γ-γ' microstructure for a Re containing (3 to 5wt%) crystal superalloy. Solutionized and aged sample (a), microstructure after creep under 980°C-248 MPa (b), and microstructure after creep under 1100°C-120Mpa (c) [222]. 157

Figure 3.59. a) The interfacial dislocation network for alloy with rafted microstructure shown in Figure 3.58 (b), and b) the denser dislocation network for the microstructure of Figure 3.58 (c) [224]..... 159

Figure 3.60. The Larson Miller parameter for the CMSX-4 by Cannon Muskegon, CMSX-4 produced in this study and ERBALLOY. 161

LIST OF TABLES

Table 1.1. Crystal structure characteristics of the four main TCP phases in single crystal superalloys [62]. 10

Table 1.2. The M_d and B_o values of the alloying elements in Ni-base superalloys [75]..... 14

Table 1.3. Some examples of the polycrystalline and first to fifth generations single crystal superalloys compositions (wt%). 16

Table 2.1. Composition ranges used to generate the alloy design space. 67

Table 2.2. Table chemical composition of the designed alloy (ERBALLOY)..... 70

Table 2.3. Solution treatment procedures 73

Table 3.1. Chemical composition of the first, second, and third generation commercial alloys (CMSX-2, CMSX-4 and CMSX-10)..... 82

Table 3.2. Chemical composition of the Alloy X. 84

Table 3.3. Density, volume fraction of γ', M_d, and rupture time of the ERBALLOY and ALLOY X, compared to the CMSX-2, CMSX-4, CMSX-10..... 85

Table 3.4. Thermo-Calc modeling results for the composition of the first solidified γ and liquid phases and the resulting segregation coefficient..... 98

Table 3.5. Scheil modeling results for the segregation ratios of alloying elements. 101

Table 3.6. Segregation coefficient determined by simulation and experiments..... 133

Table 3.7. The composition (wt%) of the γ and γ' during isothermal aging at 870 °C. 140

Table 3.8. The minimum, maximum and average size of the precipitates in the aged samples. 144

Table 3.9. The chemical composition of the Sigma phase during aging at 870°C. 153

Table 3.10. The experimental rupture time and Larson Miller parameter for the CMSX-4 by Cannon Muskegon and this study. The last two raws is for the ERBALLOY. 161

LIST OF SYMBOLS

a	Neural network output in hidden layer
b	Bias value of the neural network
B_o	Electronic Bond order
d	Precipitate mean size
D	Diffusion coefficient
E_d	Cost function for the input of the neural network
E_w	Cost function for the weights of the neural network
f_l	Mole fraction of the liquid
f_s	Mole fraction of the solid
g	Gravity constant
G	Transfer function
G_L	Temperature gradient in the liquid
J	Concentration flux of the atoms
J_s	Steady state nucleation rate
J(t)	Time dependent nucleation rate
k	Segregation ratio
K	Coarsening constant
L	Mushy zone length
L'	Kinetic factor of the flux equation
M_{Creep}	Creep merit index

M_d	d orbital energy level
M_{kv_a}	Exchange rate of the atom and its neighbor vacancy
N_v	Electron vacancy of elements
N	Number of available sites for nucleation
O	Neural network output in output layer
p	Probability function
P	P phase
P_t	Total pressure in interdendritic region
P_A	Atmospheric pressure
P_ρ	Metallostatic head pressure
P_σ	Surface tension related pressure
Q	Activation energy of diffusion
R	R phase
r^*	Critical radius for nucleation
S_w	Cost function of the Bayesian neural network
t	Time
T	Temperature
T_L	Liquidus temperature
T_s	Solidus temperature
v	Interface velocity
V_m	Molar volume fraction
V_s	Withdrawal velocity

W	Connection weights between the inputs and hidden layer
X	Mole fraction
y_{va}	Vacant lattice fraction
Z	Zeldovich factor
Z_D	Normalizing constant of the probability equation
β	Connection weights between the hidden and output layer
γ	Gamma phase
γ'	Gamma prime phase
ΔG	Free energy change
ΔG^*	Critical free energy of the nucleation
ΔG_V	Free energy change per unit volume
ΔG_s	Surface energy per unit area
ΔP	Pressure drop in interdendritic region
ΔT	Solidification temperature interval
θ	Alloying angle
μ	Mu phase
ξ	Adjustment factor for diffusion distance
λ	Levenberg damping factor
σ	Sigma phase
τ	Incubation time before nucleation
Ω	Mobility

LIST OFACRONYMS/ABBREVIATIONS

CALPHAD	Calculation of phase diagrams
PDAS	Primary dendrite arm spacing
PHACOMP	Phase computation
NN	Neural network
SDAS	Secondary dendrite arm spacing
TCP	Topologically close packed phases
VB	Vertical Bridgman
VBSB	Vertical Bridgman with submerged baffle

1. INTRODUCTION

Nickel (Ni) based superalloys are used in applications that require excellent mechanical strength and good oxidation/corrosion resistance. They show a good microstructure stability while operating at high temperatures. They gain these outstanding properties from their unique microstructure which is strengthened by different mechanisms such as the solid solution, grain boundary, carbide, and precipitate strengthening [1,2].

As superalloys are classified into iron (Fe), nickel (Ni), and cobalt (Co) based and produced in poly, directional, and single crystalline forms, the Ni based single crystal superalloys are the exclusive candidates in the demanding hot sections of the aircraft and land based gas turbine engines. They are distinguished by the absence of grain boundaries and presence of a high volume fraction of the strengthening γ' precipitate phase in their microstructure. Technological advancement in the 1970s led to elimination of the grain boundaries and so production of articles as single grains after solidification [3]. Since the grain boundaries are not efficient strengtheners at high temperatures, their elimination is important for such applications. Following this achievement, the studies then are mainly focused on developing new compositions for enhanced alloy properties. Early alloy design studies were experimental and relied on trial and error [4–6]. However, the alloy design was too broad with many parameters which made this job very challenging [7].

Of course, these early studies broadened our understanding on the role of the alloying elements and yielded several high performance alloy compositions. However, the experimental alloy design and production cycle is very time consuming and costly. Computational methods and tools like the PHAse COMPutation (PHACOMP) approach [8,9], the alloy-by-design method by property merit indexing [10,11], and the modern software based on CALculation of PHAse Diagrams (CALPHAD), like Thermo-Calc [12], JMatPro [13], and Pandat [14], have aided the alloy designers. The PHACOMP approach relies on calculations of the energy of the molecular orbitals of the alloying elements for estimating the susceptibility to formation of the TCP phases [8,9]. The existing software for mechanical property predictions is based on simplified empirical approaches, and so they are unable to make a full correlation between influencing

parameters [11,15]. Mechanical properties depend not only on the atomic bonding and the atomic/molecular arrangement, but they are also strongly influenced by the morphology, distribution, and amount of multiple phases as well as the interface strength, which are all determined by the chemical composition of the alloy at given operating conditions. In fact, interdependence of all these makes it a challenging task to develop a unique, physically sound model to predict the long-term properties of superalloys.

Statistical approaches like the regression [16,17] and neural network (NN) [18,19] methods also have been used in design of superalloys. In the regression method, a number of experiments are performed on a single or a few number of alloys and the effect of the material and operating parameters (like the temperature and stress in creep testing) are modeled by linear regression formulas for a known group of alloys. On the other hand, the neural network method is a powerful tool with the capability of correlating the alloy chemistry and operating parameters and forecasting the required property for an arbitrary alloy composition. In fact, it has been shown that a well-structured neural network models are universal approximates for any function [20–22].

The commercially available single crystal alloys are classified as first, second, and third generation based on their Rhenium (Re) content, which is 0, 3, and more than 5wt%, respectively. The amount of other refractory elements like Tungsten (W), Molybdenum (Mo), Tantalum (Ta) has increased with generations, as well. These additions improved the creep resistance with a trade off in increased alloy density. Moreover, the additions made the microstructure susceptible for the topologically close packed (TCP) phases. Owing to the brittle nature of the TCP phases, they serve as a crack initiation sites. Furthermore, due to the accumulation of the refractory elements in the TCP phases, softening of the alloy occurs and the high temperature creep resistance is reduced [23,24]. Fourth and higher generation superalloys are being investigated by optimizing composition for improved mechanical properties [25].

This current study utilizes a combined Neural Network – CALPHAD – PHACOMP approach for design of low density and high creep resistance single crystal Ni base superalloys targeted for hot sections of aero-engines. NN modeling results for the density and creep rupture strength are combined with the volume fraction of γ’ and M_d (a

parameter for evaluating the tendency for formation of TCP phases) data obtained from PHACOMP to render very useful materials selection scatter plots to study the effect of alloying elements on the density, volume fraction of the γ', formation of the TCP phases, and their effect on the creep resistance. The solidification and phase analysis of a selected alloy (ERBALLOY) from NN-PHACOMP results is analyzed by Themo-Calc software to give the liquidus, solidus, γ' solvus temperature and phase factions of the γ' and TCP phases. It is shown that this method is capable of correlating the chemistry of the alloys and their operating conditions (stress and temperature) to the creep-rupture life. The NN model also provides very accurate density predictions. The promising results achieved in this study can aid designers/manufacturers to reduce the degree of empiricism inherent in many previous treatments and reduce the number of trial experiments when developing new alloys.

In the experimental part of the thesis, a new alloy composition (ERBALLOY), determined by NN-PHACOMP model, is grown as single crystal by the conventional vertical Bridgman (VB) and a new vertical Bridgman with a submerged baffle (VBSB) methods. The latter is a modification to the conventional method by positioning a submerged baffle inside the melt during growth [26–28]. The VBSB method is used in superalloy production during this current study for the first time in the world [29]. The effect of reduced melt height in the presence of the baffle on the solidification characteristics of the alloys is studied. The γ' and TCP phase evolution in the grown alloys were characterized by using microscopic techniques (optical and SEM), EDS, EPMA and XRD.

The grown alloys are heat treated to understand kinetics and the morphology of the γ' phase. The heat treatments include the solutionizing and aging. Different temperature and soaking times are tested in the solution treatment to achieve a reasonably homogenized microstructure. The coarsening of the precipitates is studied in the aging heat treatments. The solution and aging heat treatments are modeled by the Dictra and TC-Prisma software and compared to experimental results.

In the last step of the study, the rupture strength of the grown alloys is assessed by performing creep-rupture tests at high temperature/low stress regime of 1100°C/137MPa and intermediate stress / temperature regime of 982°C/248MPa.

1.1. Introduction to Superalloys

Superalloys are developed to perform under extreme conditions of high stress and temperature at corrosive and oxidizing environments. They are categorized as Fe, Co, and Ni base superalloys [30,31]. Fe base superalloys contain Fe as the base material with Ni content greater than 25wt%. These alloys have the FCC matrix strengthened by both the solid solutions and precipitates [32,33]. A high amount of chromium (Cr) gives the alloys a resistance to high temperature oxidation. Mo is added as a solid solution strengthening element and the Titanium (Ti), Aluminum (Al), and Niobium (Nb) from precipitates in the matrix to attain the high temperature strength of the alloy [34]. Cobalt base superalloys have Co as the base material with a high amount of Cr to gain the oxidation and hot corrosion resistance. The strengthening relies on the solid solution and the carbides provided by refractory elements like Mo and W [33]. However, recent studies focused on precipitate strengthening of Co base alloys [35,36]. The refractory metals in combination with the carbon form carbide networks in the grain boundaries and make the alloy stable up to temperatures close to the melting point of the alloy. They have lower strength compared to the Ni base superalloys, but they have higher oxidation and hot corrosion resistance than the Ni base superalloys [37].

Ni base superalloys are a group of alloys containing more than ten alloying elements, which are the best candidates in corrosive environments under high stress and high temperature. The main element is Ni with the FCC crystal structure. Ni is stable at high temperatures, and due to its crystal structure, it has a good ductility. A combination of Ni as a base materials with the alloying elements like Ti, Al, Cr, Co, W, Re, Ta, Hf, and Mo gives these alloys a unique characteristics of a combined high temperature creep resistance, long fatigue life, good microstructure stability, and high oxidation and corrosion resistance. All these characteristics make the Ni base superalloys unmatched materials for the high temperature critical parts of the aircraft and jet engine like the turbine blades and discs.

1.1.1. Nickel Base Superalloys

The first commercial Ni base superalloys were wrought Nimonic 75 and 80 alloys that were developed in 1940s in the USA [38]. The advent of the vacuum melting in the 1950s helped for better control of the chemical compositions of the superalloys and removed the limitations on addition of the refractory and other reactive elements [39]. Later, the polycrystalline cast Ni base superalloys were developed for demanding high temperature applications due to their unique γ' precipitate strengthening ability which gives these alloys the capability of retaining considerable amount of their room temperature strength at high temperatures [40]. At first, the equiaxed cast Ni base superalloys, like IN100 or MARM200, were used for manufacturing the turbine blades. Later in 1970, the directional solidification led to the elimination of undesirable grain boundaries transverse to the applied load direction and increased the fatigue and creep life significantly [41]. In the next step, all the grain boundaries were eliminated by single crystal growth of the superalloys. This led to considerable changes in the composition of the superalloys, and the grain boundary strengtheners like C, B, Zr, and Hf were totally removed from the composition of the superalloys [42]. The next activities mainly focused on developing alloys with increased creep and fatigue resistance, microstructure stability, and good corrosion and oxidation resistance. The first generation single crystal Ni base superalloys that were developed had no Re in their composition [43]. The chemical composition of these alloys were refined in the following years to increase the γ' content, solid solution strengthening, castability, and to reduce the undesirable TCP phases. Later, second and third generation alloys were developed which contained 3 and 6wt% of the Re, respectively [44–46]. The two major examples for second generation alloys are the CMSX-4 and René N5 [47]. It has been shown in several researches that Re increases the high temperature creep strength of the superalloys significantly [48–51]. The amount of Re increased to around 6wt% in the third generation alloys with the subsequent reduction in the level of Cr [52]. As an example, the two well-known third generation alloys are CMSX-10 and Rene N6 which include 5.4wt%and 6wt% of Re, respectively [47].

Fourth generation single crystal alloys are produced by introducing Ruthenium (Ru) (normally less than 4wt %) to the third generation alloys. The main problem that comes with the addition of Re in the third generation alloys is the high temperature instability of

the microstructure which weakens the mechanical properties. Fourth generation alloys, like EPM-102 and TMS-138, TMS-162, which were developed by Ru addition, have shown an improved high temperature structural stability [53]. Figure 1.1 shows schematically the general trend in variation of the alloying elements from the conventionally cast up to the fourth generation alloys.

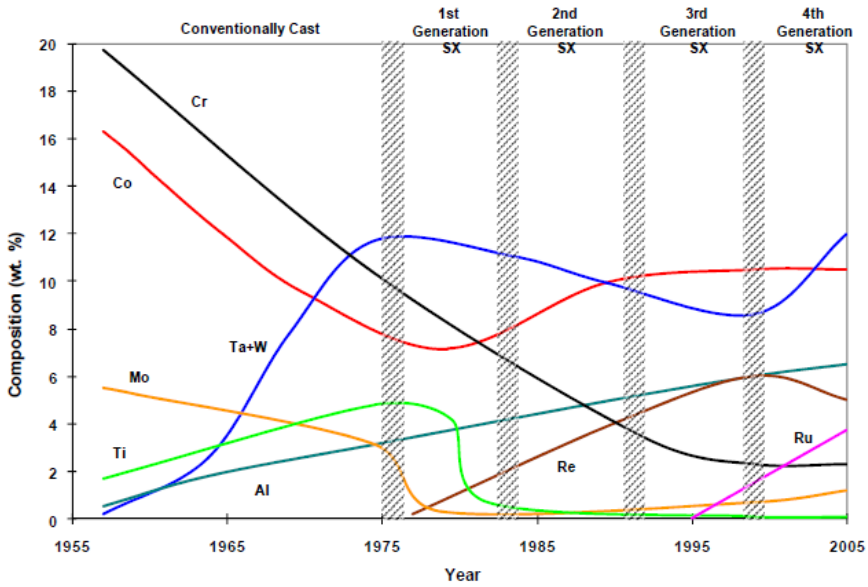

Figure 1.1. Variation of the alloying elements from the early conventional cast to the modern fourth generation superalloys [1].

Addition of more Ru, Re, and Mo than the amount in the fourth generation alloys led to development of the fifth generation superalloys. The higher amount of the mentioned alloying elements refines dislocation network at the interface between the matrix and the precipitates. Moreover, Re and Mo are the solid solution strengtheners in the alloys. Both of the mentioned characteristics along with the improved phase stability due to presence of high amount of Ru increases the high temperature creep properties of these alloys. In lower Cr alloys of these generation, like the TMS-162 and TMS-167, the poor oxidation resistance has been reported while the alloys with moderate Cr level, like TMS-192, show an acceptable oxidation resistance with a high creep resistance [53,54].

The high amount of the Re, W, and Mo in the fourth and fifth generation alloys destroys the continuity of the aluminum oxide film in the surface of the superalloys and

deteriorates the high temperature oxidation resistance of these alloys. This is due to their high vapor pressure and consequent vaporization of the oxides of these elements which disrupts the continuous aluminum oxide [25,55]. Therefore, even the high chromium ones have lower oxidation resistance than the previous generation alloys. The sixth generation superalloys were developed in the next step to overcome this problem. Thus, amount of the Mo and W was reduced, and the amount of the Co and Ta was increased. The sixth generation alloy TMS-238, developed at the National Institute for Materials Science (NIMS) in Japan, was reported to have the room and high temperature mechanical properties similar to the fourth generation alloy TMS-196 but with superior oxidation resistance. It was reported that the higher Ta and lower W and Mo might be a possible reason for the higher oxidation resistance of these alloys [56].

The microstructure of the Ni base superalloys generally includes the γ (matrix), γ' (precipitate), carbides, and TCP phases. These microstructural entities are detailed below.

1.1.1.1. Gamma (γ). The matrix of the Ni base superalloys is an austenitic phase named γ with the FCC crystal structure (Figure 1.2). The Ni and other solid solution forming elements occupy the corners and the center of the FCC structure in a random fashion. The matrix contains the solid solution strengthening elements like Re, Mo, Cr, Co, and W. Since these elements tend to segregate in the matrix during solidification, they are also said to be the γ forming elements and arbitrarily substitute for Ni positions in the FCC [30,57].

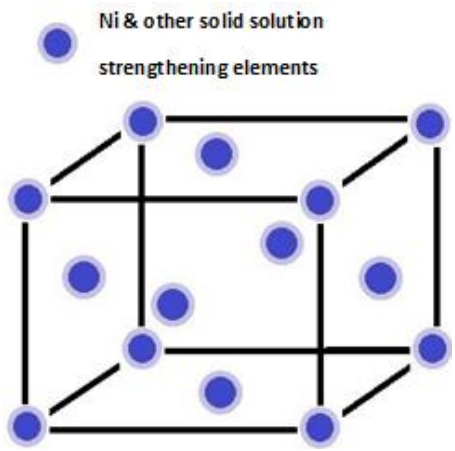

Figure 1.2. Crystal structure of the Gamma (γ) phase.

1.1.1.2. Gamma Prime (γ'). The major strengthening mechanism in the single crystal superalloys is the precipitation of the γ' phase within the matrix. The crystal structure of the γ' precipitate phase is the ordered $L1_2$ FCC. Ni occupies the corners and the Al takes the face-centered positions. This configuration gives rise to the Ni_3Al intermetallic composition. The Al positions may be substituted by Ti, Ta, and Nb [1].

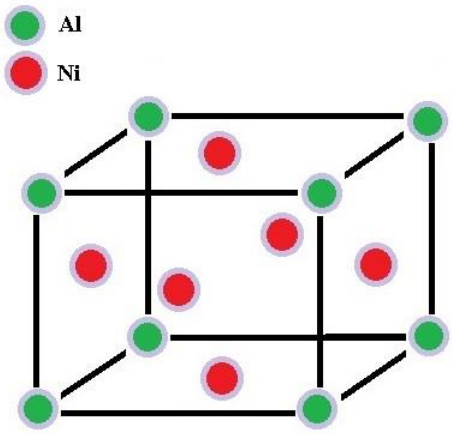

Figure 1.3. Crystal structure of the Gamma-prime (γ') phase.

Owing to the similarities of the crystal structures, the γ' precipitates form coherently in the matrix, but there is a strain energy in the structure due to a difference between the lattice constants of the two phases, a_γ for the matrix and $a_{\gamma'}$ for the precipitate. This difference is known as the misfit (δ) and often is calculated by the following formula [30]:

$$\delta=2\frac{(a_{\gamma'}-a_\gamma)}{(a_{\gamma'}-a_\gamma)} \tag{1.1}$$

This straining of the structure due to the presence of the misfit is the main strengthening mechanism in the γ' strengthened superalloys. The volume fraction, size, and morphology of the precipitate phase are the other important influencing parameters on the mechanical properties of the superalloys. Heat treatment has a major effect on the characteristics of the precipitates. The aging heat treatment allows for optimization of the distribution of the γ' precipitates. Depending on the chemical composition of the alloy, the morphology of the precipitates could change during heat treatment to spherical or

deteriorated cubic. Moreover, some fine precipitates could coexist with the most prevalent coarse γ' precipitates.

Directional coarsening of the precipitates parallel or normal to the applied load direction could occur, which is known as rafting. The sign and direction of the applied stress and the sign of the misfit are the parameters that determine the type and extent of the rafting. In superalloys with a negative misfit, under applied tensile stress, the rafting takes place normal to the direction of the applied stress, which is known as the N type rafting. The compressive stress, on the other hand, leads to directional coarsening of the precipitates parallel to the load direction, which is known as the P type rafting. The reverse is true for the superalloys with the positive misfit [58,59].

1.1.1.3. Carbides. Carbides are present in the microstructure of the Ni base superalloys mainly in the forms of MC, M6C, and M23C6 where M is one of the carbide forming alloying elements. The most prevalent form is MC that is normally rich in the strong carbide forming elements like Ta, Ti, or Hf and forms from liquid during solidification. During long time exposure at lower temperatures, these type of carbide tends to decompose into the M6C and M23C6 types [24,30]. These forms of carbides tend to segregate to the interdendritic regions or grain boundaries and the morphology of them determines their effect. The morphology of the M23C6 type carbide has a considerable effect on how it affects the strength of the alloy. If they are blocky shape, they prevent the sliding of the grain boundaries at high temperatures and have a strong effect in increasing the rupture strength of the polycrystalline superalloys. Nevertheless, if they are in the form of thin films along the grain boundaries, they will cause premature failure. Moreover, this type of carbides have been shown to have high level of Cr and due to depletion of the Cr from the neighboring precipitates, the oxidation resistance of those local areas is reduced [60]. In the modern single crystal superalloys, however, the carbon content is decreased or removed, as there is no need for any grain boundary strengthening mechanism. Elimination of carbon or other grain boundary strengthening elements, like Hf, reduces the complexity of the phases evolved at high temperatures and facilitates the heat treatment. The alloying elements which were already in the composition of the carbides now are free to partition between either the γ or γ' and act as solid solution strengthening of both the matrix and precipitates [61].

1.1.1.4. TCP Phases. A new generation single crystal superalloy contains a high level of the refractory elements like Cr, Mo, W, and Re for increased creep life under stress at high temperatures. Unfortunately, the high amount of these elements promotes the formation of undesirable intermetallic, hard compounds with complex crystal structures like tetragonal, rhombohedral, and orthorhombic. The most common form of the TCP phases in single crystal superalloys are Sigma (σ), Mu (μ), P, and R phases. Table 1.1 lists the crystal structure of the major TCP phases [62].

Table 1.1. Crystal structure characteristics of the four main TCP phases in single crystal superalloys [62].

TCP phase type	**Crystal structure**	**Atoms / Unit cell**	**Lattice Parameters**	**α**
σ	Tetragonal	30	a=b=0.878 nm, c=0.454 nm	90°
μ	Rhombohedral	13 (Hexagonal=39)	a=b=c=0.904 nm, a=b=0.4755 nm, c=2.583 nm	30.5° 120°
P	Orthorhombic	56	a=1.698 nm, b=0.475 nm, c=0.907 nm	90°
R	Rhombohedral	53 (Hexagonal=159)	a=b=1.093 nm, c=1.934 nm	120°

Figure 1.4 shows the crystal structure of these phases [63]. The composition of the TCP phases could vary by chemical composition of the base alloy and temperature. They generally have a high level of the Re, Cr, Co, W, and Mo. The other alloying elements like Al, Ti, and Ta do not show strong tendency towards formation of the TCP phases. Their structure includes the elements with small atomic radii, like Ni and Cr, in a close packed layer with the larger atoms like Re and W between the layers. These phases deplete the refractory elements from both the matrix and precipitate and leave a low melting, soft zone. Moreover, they decrease the ductility of the alloy [60,62]. Due to their complex crystal structure, they are brittle and mainly appear in the form of plate, needle, or lath. Their interface with the matrix is a place where the cracks could easily initiate. The major consequence is reduced fatigue life and tensile ductility [64]. In Re containing superalloys, this phase has a high percentage of the Re. In alloys with no Re content, the major alloying element is Cr [65].

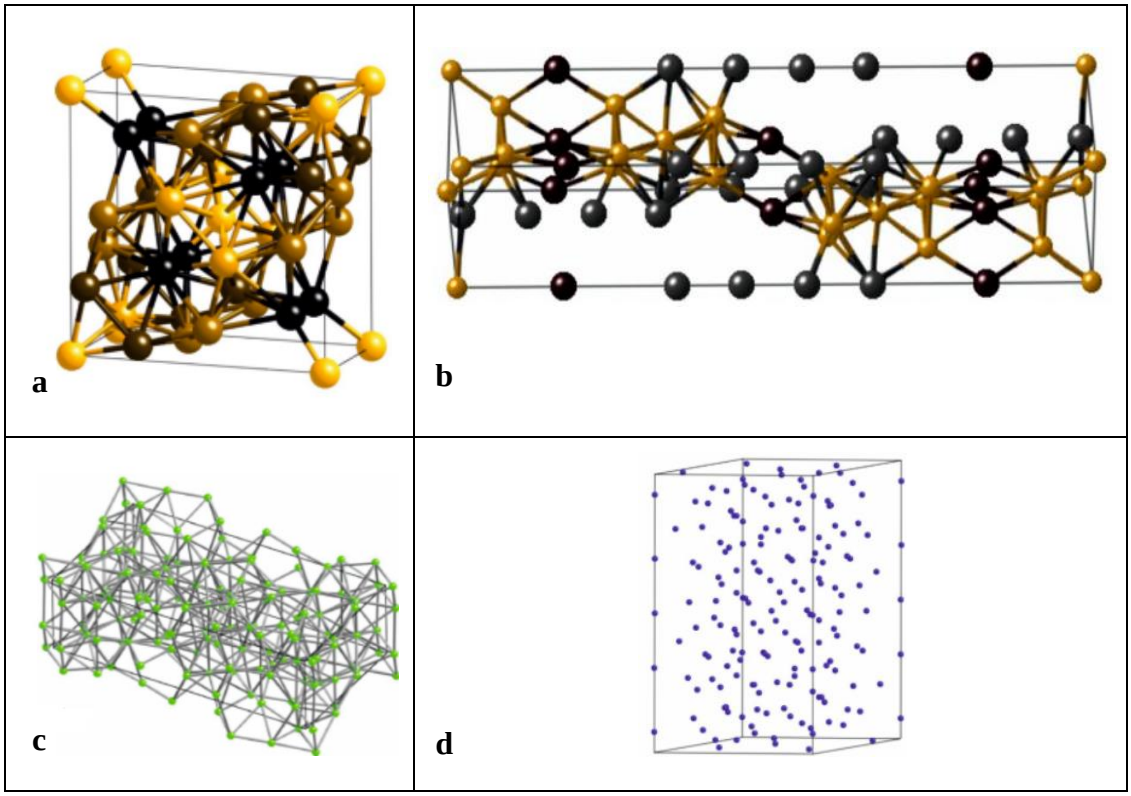

Figure 1.4. The crystal structure of the major TCP phases in single crystal superalloys a) σ, b) μ, c) P, and d) R [63].

The Sigma (σ) phase is the most well-known of the TCP phases seen in the superalloys. It can form after heat treatment or long time service at high temperatures. In case of strong segregation of the alloying elements, it can even form directly from the liquid during solidification [66]. The Sigma phase is a brittle phase with the tetragonal crystal structure. Evolution of this phase reduces the rupture strength and ductility of the superalloys significantly [23,24]. It precipitates in the stoichiometric form of $(Cr,Mo)_x(Ni,Co)_y$, where x and y are dependent of the chemical composition of the alloy and both can vary from 1 to 7. It forms in elongated plate-like morphology and generally is characterized by high level of the Cr and lower amount of the Re, Mo, and W. It has a deleterious effect on the mechanical properties of the alloys and the creep fracture has been reported to initiate from its interface with the matrix [62,67].

Mu (μ) phase is common in superalloys with high W and Mo elements and low Cr and Re elements. It can form either during solidification or during aging heat treatment or after long time exposure under stress at high temperatures. Like the other TCP phases, it

deteriorates the ductility, fatigue, and rupture life of the alloy. It is critical to prevent formation of this phase either in solidification, heat treatment, or service; yet it is hard to remove this phase during a solid solution treatment [68].

P phase has the orthorhombic crystal structure and generally forms with needle-like morphology. It mostly precipitates in alloys with high Mo content [69]. This phase is rich in refractory elements like Mo, W, and Re [70,71].

R phase is normally enriched by almost equal amount of Mo and Cr elements but depending on the chemical composition of the alloy its concentration could vary significantly. It could also originate from the Sigma phase. The crystallographic data of this phase is limited due the fact that it is rarely is observed in superalloys [63].

It is worthwhile to note that depending on the service temperature, different types of TCP phases may form. As an example, C.M.F. Rae et al. showed that in single crystal superalloy PR2071, the major TCP phase at temperatures between 800 and 900°C is μ with small percentage of the R and Sigma, but at temperatures above 950°C, P phase is predominant with small percentages of μ [62].

The addition of Ru in the fourth generation single crystal superalloys have been shown to suppress the evolution of the TCP phases. This has been attributed to several possible reasons, among them are the increase in solubility of the Re and W elements in the matrix and also change in the interfacial energy between the matrix and the TCP phase which reduces the nucleation and growth rate of the TCP phases [64,72]. It has also been reported that Ru increases the stress rupture strength of the superalloys by increasing the volume fraction of γ' [72].

The PHACOMP method is developed to predict the susceptibility to formation of the TCP phases from the chemical composition of the superalloys. This model relies on the interaction of the electronic structure of the alloying elements. The PHACOMP method was based on calculation of the total average electron vacancy (N_v) of the alloy. N_v is the number of electron vacancies above the Fermi level of the d orbital band. The theory of electron vacancy in the d-bond was first developed in 1938 by the L. Pauling[73].

According to Pauling, the orbitals in the d band could be divided as bonding or non-bonding orbitals. From the 5 d orbitals, only 2.56 take part in the bonding with hybridization with the other P and S orbitals for the formation of the metallic bonds. The remaining 2.44 orbitals are referred to as the nonbonding orbitals that could get 4.88 nonbonding electrons. Moreover, for the 3-d transition elements, the d band requires only 5.78 hybrid (spd) electrons for bonding. Then, for example, for the Cr with the 6electrons in the valence band, there will be 0.22 electrons remaining which will reside in the nonbonding orbitals. They will first occupy the positive spin bonds. The remaining of the non-bonding orbitals will be empty which is called vacancies or electron holes in the d-bond [8]. Later, this theory was extended to consider the other alloying elements. In 1951, Rideout *et al.* [74], calculated the average electron vacancy for ternary alloys according to the following:

$$N_v = \sum_{i=1}^{n} (N_v)_i . x_i \qquad (1.2)$$

where $(N_v)_i$ is the electron vacancy (N_v) of each of the n elements and x_i is the atomic fraction of that element. The iso-N_v lines were used then to determine the boundary between the TCP phases and the matrix. A critical value for the N_v is defined then which if exceeded there would be risk of evolution of the TCP phases. The critical N_v values changes with regard to the type of the TCP phase.

The PHACOMP method was then modified to consider not only the electronic structure of the elements but also the effect of the atomic size. Two other parameters, M_d and B_o, are defined for each element, and the behavior of the alloy is determined by averaging the effect of all elements. M_d is determined based on the d orbital energy level of the elements and B_o is the strength of the atomic bonds. Table 1.2 shows the M_d and B_o value of the d-transition alloying elements and the Al and Si [75].

By taking the zero as a reference energy level for the Ni_3Al, the M_d is calculated as the average value of the energy levels of the d bond for each alloying elements. In fact, by addition of the alloying elements to the composition of the pure Ni_3Al, new energy levels are introduced.

Table 1.2. The M_d and B_o values of the alloying elements in Ni-base superalloys [75].

electronic structure	**3d**					**4d**			**5d**				**3p**	
Element	Ti	V	Cr	Co	Ni	Zr	Nb	Mo	Hf	Ta	W	Re	Al	Si
M_d (eV)	2.271	1.543	1.142	0.777	0.717	2.944	2.117	1.550	3.020	2.224	1.655	1.267	1.900	1.900
B_o (eV)	1.098	1.140	1.278	0.697	0.514	1.479	1.594	1.611	1.518	1.670	1.730	1.692	0.533	0.589

The total M_d for an alloy is calculated by taking the average of the effect of the alloying elements as follows.

$$M_d = \sum_{i=1}^{n} (M_d)_i . x_i \tag{1.3}$$

where $(M_d)_i$ is the M_d value of ith alloying element and x_i is the atomic fraction of that element. M_d has been attributed to the electronegativity of the bonds and the atomic radius. A high M_d means a low electronegativity and large atomic radius. The alloying elements with the higher energy levels in their d orbitals increase the average M_d of the alloy and enhance formation of the TCP phases [75,76].

The other parameter, B_o, is a measure of the bond strength between the Ni and the other alloying elements. The main alloying elements in Ni base superalloys have generally a large Bo number. The total B_o for an alloy is then calculated by taking the average of the effect of the alloying elements.

$$B_o = \sum_{i=1}^{n} (B_o)_i . x_i \tag{1.4}$$

where again the $(B_o)_i$ is the B_o value of ith alloying element and x_i is the atomic fraction of that element [76].

1.1.2. Alloying Elements

The chemical composition of the Ni base superalloys includes many alloying elements. Table 1.3 shows some of the well-known polycrystal and single crystal alloys. It is seen that these alloys in general have around ten alloying elements. The polycrystal superalloys are distinguished by grain boundary strengthening elements like Nb, Zr, B, and C. Other than Re and Ru, the other alloying elements like Al, Ti, Cr, Co, Ta, W, Mo are seen in the composition of the single crystal superalloys.

Every alloying element is well designed for a single or multiple purposes. The effect of the alloying elements could be described by their position in the periodic table. The atomic radius and the number of electrons in the d orbital of the electronic structure are the important parameters that determine the behavior of the element in the alloy. The elements Cr, Co, Re, Ru, W, and Mo that have the atomic radii close to Ni and therefore partition to and stabilize the gamma (γ) phase. Moreover, these elements act as solid solution strengthening of the matrix. The elements Al, Ti, and Ta have larger atomic radii and stabilize the γ'. Elements like Zr, B, and C segregate to the grain boundaries and strengthen the alloy either by forming the carbide network in the grain boundary or by retarding the mobility of the grain boundary. The latter elements are not used in the composition of the modern single crystal superalloys as there is no grain boundary or the carbide strengthening mechanisms in these alloys.

The excessive usage of alloying elements may degrade the other characteristics of superalloys, and for this reason, the amount of each alloying element should be optimized carefully. For example, Re has been proven to enhance the creep rupture life of single crystal superalloys significantly; on the other hand, it promotes precipitation of the TCP phases. Moreover, it increases the density of alloys, which reduces the efficiency of the entire engine. To alleviate this effect in the third generation alloys with the high fraction of the Re, the amount of other refractory elements and Cr has been reduced. The Cr and Al provide a protective adherent oxide layer on the surface and increase the oxidation and hot corrosion resistance of the superalloys.

Table 1.3. Some examples of the polycrystalline and first to fifth generations single crystal superalloys compositions (wt%).

Alloying element / Alloy	Cr	Co	Mo	W	Ta	Al	Ti	Hf	Re	Ru	Nb	Zr	C	B
Polycrystals														
IN-713LC	12	-	4.3	-	-	5.8	0.7	-	-	-	2	0.06	0.06	0.07
Mar M200	9	10	-	12.5	-	5	2	-	-	-	1.8	0.05	0.15	0.015
Mar M246	9	10	2.5	10	1.5	5.5	1.5	-	-	-	-	0.05	0.15	0.015
First generation single crystals														
PWA1480	10	5	0	4	12	5	1.5	0	-	-	-	-	-	-
SRR99	8	5	0	10	3	5.5	2.2	0	-	-	-	-	-	-
AM1	8	6	2	6	9	5.2	1.2	0	-	-	-	-	-	-
AM3	8	6	2	5	4	6	2	0	-	-	-	-	-	-
CMSX2	8	5	0.6	8	6	5.6	1	0	-	-	-	-	-	-
CMSX3	8	5	0.6	8	6	5.6	1	0.1	-	-	-	-	-	-
CMSX6	10	5	3	0	2	4.8	4.7	0.1	-	-	-	-	-	-
AF56	12	8	2	4	5	3.4	4.2	0	-	-	-	-	-	-
Second generation single crystals														
CMSX-4	6.5	9	0.6	6	6.5	5.6	1	0.1	3	-	-	-	-	-
PWA1484	5	10	2	6	9	5.6	-	0.1	3	-	-	-	-	-
SC180	5	10	2	5	9	5.2	1	0.1	3	-	-	-	-	-
MC2	8	5	2	8	6	5	1.5	0	0	-	-	-	-	-
Rene'N5	7	8	2	5	7	6.2	-	0.2	3	-	-	-	-	-
Third generation single crystals														
CMSX-10	2	3	0.4	5	8	5.7	0.2	0.03	6	-	-	-	-	-
Rene'N6	4.2	12.5	1.4	6	7.2	5.75	-	0.15	5.4	-	0.1	-	-	-
TMS-75	3	12	2	6	6	6	-	0.1	5	-	-	-	-	-
TMS113	2.89	11.93	1.99	5.96	5.96	6.56	0	0.1	5.96	-	-	-	-	-
Fourth generation single crystals														
PWA1497	2	16.5	2	6	8.3	5.6	-	0.15	6	3	-	-	-	-
MC-NG	4	0	1	5	5	6	0.5	0.1	4	4	-	-	-	-
TMS-138	3.2	5.8	2.9	5.9	5.6	5.8	-	0.1	5	2	-	-	-	-
EPM-102	2	16.5	2	6	8.25	5.55	-	0.15	5.95	3	-	-	-	-
TMS-138A	3.2	5.8	2.9	5.6	5.6	5.7	-	0.1	5.8	3.6	-	-	-	-
Fifth generation single crystals														
TMS-162	3	5.8	3.9	5.8	5.6	5.8	-	0.1	4.9	6	-	-	-	-
TMS-173	3	5.6	2.8	5.6	5.6	5.6	-	0.1	6.9	5	-	-	-	-
TMS-196	4.6	5.6	2.4	5	5.6	5.6	-	0.1	6.4	5	-	-	-	-
TMS-238	4.6	6.5	1.1	4	7.6	5.9	-	0.1	6.4	5	-	-	-	-

1.1.3. Mechanical Properties

Ni base superalloys have a high yield and tensile strength along with a good fatigue and creep properties, which make them suitable for applications in the most critical parts of the aircraft engines. The yield and tensile strength could reach values in the range of 900-1300MPa and 1200-1600MPa at room temperature, respectively [76].

The yield strength of the superalloys is dependent of the microstructure variables and temperature. The reduced grain size, and the optimum γ' precipitate size are the parameters that increase the room temperature yield strength of the superalloys. The yield strength of the superalloys shows an unusual behavior with the increase of temperature. The yield strength shows an increase with temperature up to a peak temperature and then slows down. This behavior is shown for some alloys in the Figure 1.5. The peak temperature for the SR99 and RR2000 alloys is 760°C [1,76]. The peak temperature is 800°C for the CMSX-4 [77].

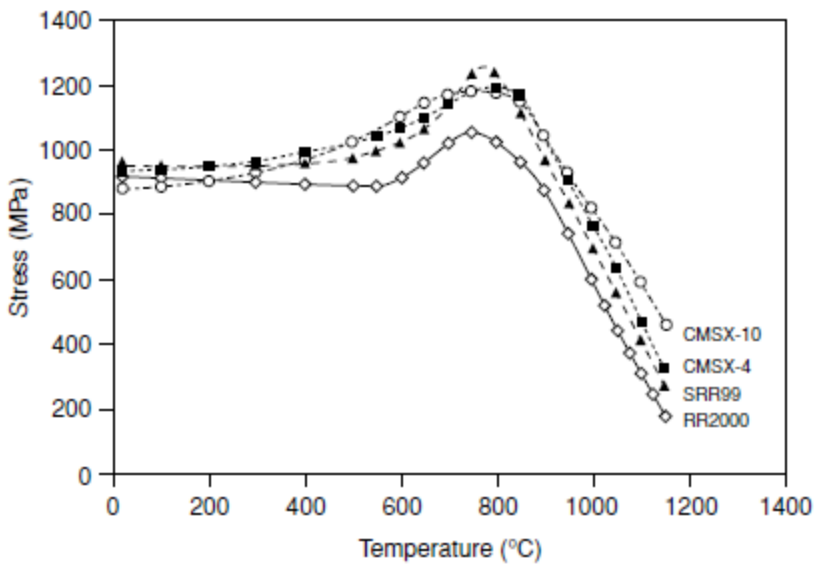

Figure 1.5. The yield stress behavior of some single crystal superalloys with temperature.

The increase in the tensile strength of the superalloys at the intermediate temperatures is due to the increase in the flow stress of the Ni_3Al (γ' phase) [78]. Below the peak temperature, the γ' precipitates are cut by the a/2<110> type dislocations on the

octahedral {111} slip planes. The superpartial dislocations cross lip from their {111} slip plane to the {100} planes. The further movement of these cross slip segments is associated with the antiphase boundaries. The microstructural features created this way are known as the Kear–Wilsdorf lock. The thermally activated process of the cross slip is the main reason for the temperature hardening.

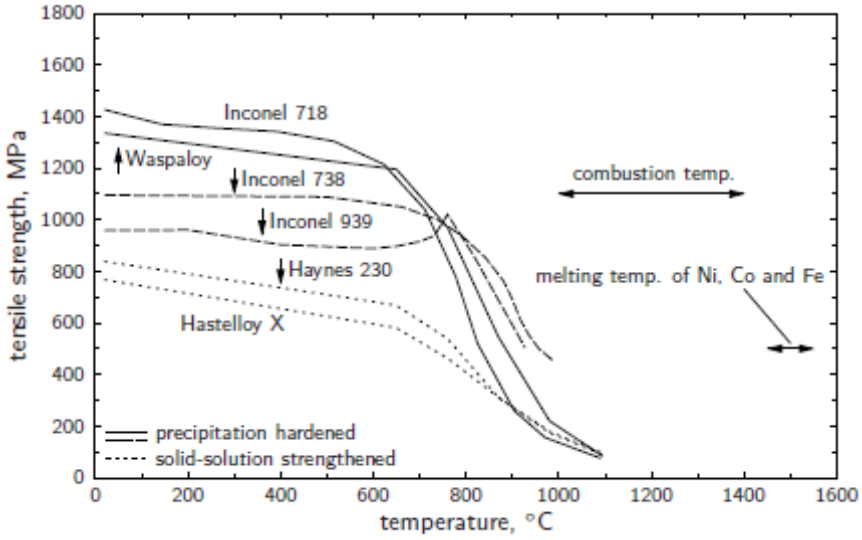

Figure 1.6. Tensile strength of some superalloys as a function of temperature.

Since superalloys are used at high temperatures, the time dependent deformation under stress at high temperatures (which is called creep) is of the greatest importance in the superalloys. It is generally said that metals are prone to creep deformation at temperatures above half their melting point. Creep deformation happens at stresses smaller than yield strength of alloy and for this reason, it is very important to consider it in design of the alloys, which are used under stress at high temperatures. Creep deformation is generally reported in strain versus time diagrams. Depending on the temperature and stress level, different creep mechanisms may be activated, which are classified in two main groups as diffusional and dislocation creep.

Diffusional creep occurs because of plastic deformation induced by movement of the vacancies. At a high temperature, the materials favor higher amount of thermodynamically stable vacancies. Vacancies then are able to move even at lower stress levels. The grain

boundaries are high-energy states that host the vacancies. The flux of the vacancies occurs because of the applied stress that is in fact a plastic deformation of the material. The diffusion of the vacancies through the crystal lattice is called the Nabarro–Herring creep. If the diffusion occurs through the grain boundaries, it is then called the Coble Creep.

Dislocation creep occurs due to movement of the dislocations in the crystal structure of the material. This is also known as the power-law creep. Dislocations move at relatively higher stresses than the vacancies by two mechanisms of dislocation gliding and climbing. In gliding, an edge dislocation moves in the crystal lattice in its plane. However, if a vacancy diffuses to the dislocation line, the edge dislocation can displace its plane of slip to another plane, which is called climbing. This happens when the dislocation faces an obstacle like a precipitate where the dislocation line has to move to another plane by diffusion of the vacancies to the root of the dislocations. Climbing is a time dependent process that is strongly dependent to the level of the stress. Dislocation creep could occur at intermediate temperatures where the diffusion processes are slow [79].

1.1.4. Processing of Superalloys

The three main processing techniques used in the production of superalloy parts are casting, forging, and powder processing. The processing techniques influence the macro and microstructural features such as the grain size and morphology, primary dendrite arm spacing (PDAS), microporosity, and segregation, which in turn significantly affect the physical and mechanical properties of superalloys parts.

Casting is the main processing method for production of small to large size superalloy products. Depending on the casting technique and solidification methodology, the microstructural features are altered significantly. The turbine blades are nowadays produced as single crystals in the ceramic molds. The casting allows for producing the parts with complicated shapes like the vanes and turbine blades with cooling channels [80,81]. The investment casting includes applying several layers of the refractory powders and slurries on a wax pattern. First, the pattern is produced by injecting the liquid wax into a metallic mold. Then the pattern is dipped into slurry of the refractory ceramics, like alumina, silica, or Zirconia, to build up the first inner layer of the mold with high surface

quality. The next step is coating the first layer with the coarser refractory ceramic powders. This process is repeated several times until the mold reaches the desired thickness. The wax is melted down in the next step and the molten metal is poured into the mold and allowed to solidify [82]. Melting and casting process in much of the nickel base superalloys is performed under vacuum or inert gas environment to prevent loss of the volatile and reactive elements and oxidation of the elements.

The solidification technique has been developed along with the advances in the casting technologies. Before the advent of the directional solidification, the parts were produced by conventional polycrystalline solidification technique. The advent of the unidirectional and later the single crystal solidification has revolutionized the superalloys industry by increasing the temperature capability and durability of the critical engine parts. The directional solidification eliminates the transverse grain boundaries by growing the grains along the solidification direction. Single crystal growth eliminates all the grain boundaries in the cast products that are the fatigue and creep crack initiation sites. The process includes withdrawal of the mold from the hot to cold zone of the furnace. The thermal gradient in the furnace induces an axial thermal gradient in the solidifying part. By withdrawal of the mold toward the older region, the interface moves towards the liquid. The typical thermal gradient and withdrawal velocity range from 10 to 100°C/cm and 5 to 40 cm/hours, respectively [83].

Solidification takes place through the nucleation and growth of the solid phase under favorable thermal conditions. When the temperature is reduced uniformly throughout the liquid, nucleation of the solid particles occurs throughout the liquid. Homogeneous nucleation, involves the formation and survival of solid nuclei whose radii are larger or equal to the critical radius. However, for the nucleation to take place, the temperature should be lowered below the equilibrium melting temperature. In other words, thermal undercooling is required to overcome the free energy barrier for the nucleation [84]. The homogenous nucleation is rather theoretical and heterogeneous nucleation always happens on the favorable nucleation sites in the liquid as the mold walls or other solid particles like the grain refiners. The practical conditions of heat flow promotes the formation of temperature gradients in the liquid, which induce initial nucleation on the mold walls, with grain growth taking place in the direction of the heat flow. Nucleated grains with the most

favorable orientation grow preferentially, advancing toward the bulk of the casting by progressive deposition of atoms in the solid-liquid interface [85].

The presences of grain boundaries in the cast part diminish the high temperature mechanical properties. The grain boundaries are potent sites for nucleation of high temperature creep and fatigue cracks. Since turbine blades are used in the hot section of the engine where the high temperature creep is active, they are produced via either directional solidification or preferably single crystal growth. Directional solidification with heat extraction only from the bottom of the mold produces a cast part with the grains aligned in the direction of heat flow. It is done by controlled withdrawal of the crucible in the furnace in the direction of heat flow. In directional solidification, heat is extracted from the mold in only one direction and the lateral growth is restricted by competitive growth, resulting in the aligned columnar and elongated grains in the direction of heat flow. This method produces cast parts, which have higher strength against high temperature creep in the axial direction. The ideal microstructure is the one without any grain boundaries. Such a microstructure is called single crystal (SC). Single crystal superalloys are used in hot section of turbine blades where the temperature is highest and the creep is highly probable. Casting in the form of single crystal requires fully controlled directional solidification with using either a single crystal seed or a grain selector in the bottom of the crucible as a starter. Single crystal seed allows for orienting the first solid crystals to adopt the crystal orientation of the single crystal seed and grow as a single crystal under controlled thermal gradient and heat flow. With the grain selector method, only one grain is permitted to enter the pigtail shaped spiral part of the mold after which only one grain survives to grow as a single crystal [85]. In Figure 1.7, simple drawing shows how investment casting leads to a single-crystal microstructure. In the process, the superalloy charge is melted in a vacuum furnace before being retracted from the furnace in a controlled direction. The front edge of the cast is cooled during the retraction. During cooling, columnar grains start to grow parallel to the direction of the retraction. By use of a grain selector, only one grain is permitted to grow any further within the component. After the grain selector, the single grain continues to grow through a pigtail shaped spiral. The spiral is followed by the actual blade form where the melt continues to solidify into one grain. After casting, the bottom part is cut from the actual single crystal blade.

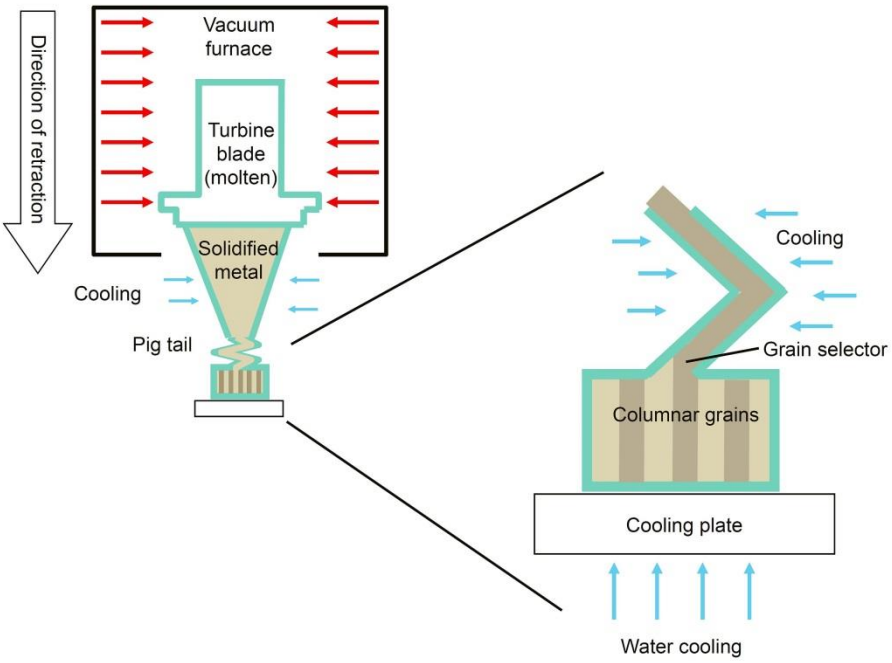

Figure 1.7. Directional solidification of a turbine blade in single crystal form [86].

As already mentioned, the solid nucleus whose radius is equal or larger than a critical radius, survives and grows inside the molten metal. As solidification advances, the interface may grow planar or the instabilities may occur which yields a dendritic microstructure. Morphology of the interface is determined by the solidification velocity and the temperature gradient. Figure 1.8 shows a typical plot of the solidification velocity versus thermal gradient for single crystal superalloys. It can be seen that for the solidification with oriented dendrites, the thermal gradient and withdrawal velocity should be between a specified limit. High thermal gradient-low withdrawal velocity and low thermal gradient-high withdrawal velocity couples may result in planar or equiaxed interfaces, respectively. Another point is that increasing the thermal gradient allows for higher rate of solidification which will give finer microstructure and increases the productivity.

Following initial solidification, castings are subjected to a series of heat-treatment cycles that serve to reduce segregation, establish one or more of the γ’ precipitate size population, modify the structure of grain boundary phases (particularly carbides), and/or assist in the application of coating [86–88].

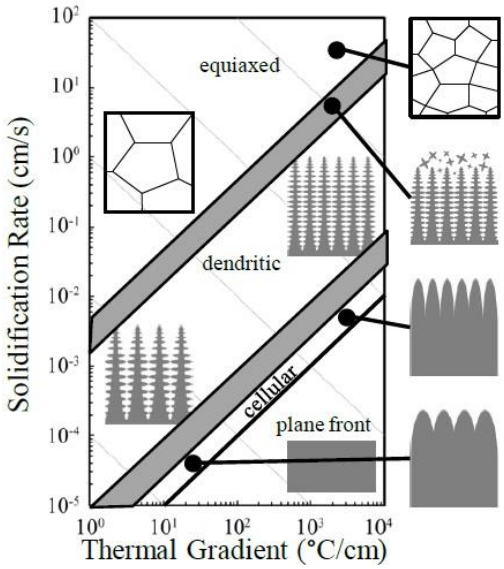

Figure 1.8. Typical plot of the solidification velocity versus thermal gradient for single crystal superalloys [71].

Powder metallurgy (P/M) methods are developed to overcome the drawbacks of the cast ingots for converting into wrought products. It is hard to attain a sound cast ingot free from solidification segregation and other solidification defects. P/M is applied for production of the high strength disc superalloys. The P/M method produces homogenized fine grain microstructure free from the macro segregation [89]. It also brings advantages like the higher strength and lower cost over the cast or forged parts. However the inclusions inherent to this method lowers the fatigue performance of the parts [90]. In addition, P/M parts are not suitable for hot section parts due to small grain size promoting creep. The forging is applied for hot or cold deformation of the billet of ingot superalloys or as a subsequent process for the P/M parts to modify the grain size of these superalloy parts [91].

Additive manufacturing is another promising cost effective method for producing near net shape superalloy parts without a need for excess tooling. Compared to the casting methods, the manufacturing time could be lowered 8-10 times lower [92]. Moreover, since additive manufacturing is a layer by layer manufacturing method, a high thermal gradient could be established in the melting zone which increases the solidification velocity compared to the casting. This will result in a finer structure with higher mechanical

properties. For example dendrite sizes of 15 times smaller than the investment casting of the CMSX-4 alloy is obtained in directional solidification of a 35.56mm x 10.16mm x 2.54mm CMSX-4 coupon by scanning laser epitaxy (SLE) on a single crystal CMSX-4 as-cast substrate [93].

This method allows for the lower fabrication costs [94,95]. A machined part may include several components and those components may be built up with various materials. This technology could help us in achieving the circular economy based business goal, which is to keep the components, materials and parts at their initial highest value and utility at all time. This is achieved by fast, reliable and low cost repair, refurbishment and remanufacturing of the products via additive manufacturing methods. Remanufacturing means the manufacturing of the used products to a new product with even better quality than the original one. The refurbishment means taking back the defected product to the quality of its original or less than the original by fast replacing or repairing the major malfunctions pieces. The repair is defined as a process for correcting the errors and faults in the products. Additive manufacturing enables fast manufacturing of the replacement components and also repairing the malfunctioned parts and therefore allows for manufacturing optimization to attain the circular economy based business goal with maintaining the quality and value of the products at their initial value [96,97]. As an example Laser additive deposition which is one of the branches of the powder-based systems is reported to be used for repair of the single crystal superalloys which reduces the cost of the replacing the blades and extends the life [98].

Additive manufacturing methods are still in their infancy, so they have a very limited use in aero-engine part production.

1.2. Superalloys Design

The development of a new nickel base superalloy for use in the high temperature turbine blades of a modern aircraft and gas turbine engine is one of the most expensive and lengthy exercises undertaken by metallurgists. This current study aims at contributing these efforts. More than 10 alloying elements are present in superalloys which makes the old experimental alloy design method very time consuming and costly. A typical complete

development cycle can take several years. This delay arises because not only the extensive mechanical testing and validation procedures, required for safe utilization of a critical part, but also because of the difficulty of finding a material chemistry that provides the correct degree of balance between mechanical properties and long-term material stability. However, significant improvement has been achieved in the high temperature performance and durability of Ni base superalloys despite an Edisonian alloy development approach that relies on the traditional, empirical method of extensive experimentation for various stages of alloy development from a concept to a validated part [99]. The oldest method for the design of superalloys comprises the systematic variations of an element in the composition, growing the alloy as a single crystal, and characterizing the microstructure and mechanical properties. The optimum composition of the alloy could be determined then which gives the optimum microstructure leading to improved mechanical properties [100].

Among the other approaches that are used for alloy design are the PHACOMP, linear regression, and merit indexing methods. In the PHACOMP method, the tendency of the alloy towards formation of the detrimental TCP phases [101], is determined by a magnitude of the average electron vacancy number, N_v. The electron vacancy number, N_v, is the number of vacancies or electron holes in the metal d band above the Fermi level. It is assumed that N_v value for a certain composition should not pass a threshold otherwise the detrimental second phase will appear in the matrix. The threshold depends on the second phase composition and structure and at the same time to temperature as a measure for solubility of that phase in the γ matrix. This method is improved to cover the d-orbital energy level (M_d) of transition alloying element and the bond order (B_o) between atoms. The M_d versus Bo is plotted, and the aim is to design the alloy chemistry such that it falls in the specified area of the plot that has been established to yield high creep resistance and low fraction of the TCP phases [8].

The linear regression method assumes that there is a linear relation between the input parameters and the output. This method is based on the experimental data to obtain formulae for the prediction of the physical or mechanical properties of superalloys like the density or rupture strength. Every parameter has a coefficient and the magnitude of that coefficient shows the impact of that parameter on the output [102].

In order to quantify the influence of alloy chemistry on alloy design, a new composition–microstructure–property approach has been recently proposed for the design of the single and poly crystal superalloys [103,104]. In this method, a composition dependent creep merit index is defined as a ranking scale of the creep resistance of the alloys. This index, defined in Equation (1.5), allows isolating compositions which are likely to be the optimal ones.

$$M_{Creep}=\sum_{i=1}^{n} D_i/x_i \tag{1.5}$$

The x_i is the atomic fraction of an alloying element in an alloy and D_i is the inter-diffusion coefficient of that element in the Ni. The creep Merit index relies on the sound assumption that the diffusion coefficients as rate controlling for dislocation movement during creep, but this method could be considered at best a qualitative measure of the creep resistance.

The uncertainty involved in the mentioned methods and the longtime needed to reveal the results of the tests made the alloy design cycle far behind the speed of product design cycle. To overcome this, the materials development and research community gave considerable attention to the new concept of Integrated Computational Materials Engineering (ICME) [105]. The aim was to use the advances in computer hardware and computational modeling to develop a set of computational tools for both fundamental materials research and design of new advanced materials. Using computational methods reduces the materials development cycle to keep pace with very fast developing product design and development and enables cost effective development to meet cost/performance requirements [106,107]. Computational thermodynamics known as CALPHAD helps for determining the thermodynamics properties and phase diagrams of the multicomponent alloys has a great place in the ICME approach. Through the reliable experimental thermodynamic databases for those of the binary and ternary subsystems, the set of stable and metastable phases, their thermodynamics properties and phase diagrams could be predicted in multicomponent alloys without conducting experiments. These data are invaluable especially for the alloy design. For example, in alloy design of the superalloys, density, volume fraction of gamma-prime, and TCP phases which are three major

parameters that influence the high temperature stability and creep resistance are predicted reliably via CALPHAD based tools like Thermo-Calc.

While optimizing the chemistry of the alloy to attain high creep resistance, a particular attention should be given to lowering the density of the alloy. Addition of heavy refractory elements in the later generations of superalloys to reduce diffusion has led to an increase in the density which adversely affects the energy efficiency of the blade and disk parts [108]. To have a measure of the density based on chemical composition, some methods like rule of mixtures and regression methods have been proposed [15,109], but they suffer either from lower accuracy or they do not include all the candidate alloying elements generally used in superalloys.

The formation of the TCP phases such as P, Sigma and Laves [110] puts another limit on the amount of the especially refractory alloying additions. It has been shown that TCP phases could have deleterious effects on the performance of the Ni-base superalloys. Owing to the brittle nature of the TCP phases, they serve as crack initiation sites. Moreover, due to the accumulation of the refractory elements in the TCP phases, softening of the alloy occurs and the high temperature creep resistance is reduced. Other than commercial thermodynamic software that directly determines the TCP phases in the alloys, the electronic approach gives a good measure of the susceptibility of the alloy to form the TCP phases.

1.2.1. Integrated Computational Materials Engineering (ICME)

The integrated computational materials engineering (ICME), aims at developing a set of modeling software for simulation of the solidification, phase diagrams, and physical/mechanical properties of the alloys. These models should consider several parameters that are interlinked in a complex way. A partial list of these parameters can include the size, distribution, and volume fraction of the precipitates, the ordered nature of the precipitates, lattice misfit between the precipitates and the matrix, temperature, stress, and environmental conditions. Recently, a number of software is developed to model thermodynamics, diffusion, microstructure, and mechanical properties. Among these are the software to predict solidification, phase transformation, and microstructure based on

thermodynamics and diffusion calculations such as Thermo-Calc [12], JMatPro [13], and Pandat [14]. The existing software for mechanical properties is based on simplified empirical approaches, and so they are unable to make a full correlation between influencing parameters [15,104,107,111]. Mechanical properties depend not only on the atomic bonding and on the atomic/molecular arrangement, but are also strongly influenced by the morphology, distribution and amount of multiple phases, and interface strength, which are all determined by the chemical composition of the alloy at given operating conditions. In fact, interdependence of all these makes it a challenging task to develop a unique, physically sound model to predict the long-term properties of superalloys. Even if the models are available, defining the optimum alloy chemistry for further assessment by modeling tools is a tedious task. For example, consider a single crystal superalloy containing 10 alloying elements. Given a concentration resolution of 1wt% and a concentration interval of 1 to 10 wt% for each alloying element, alloy design space will cover 10^5 different alloys to be modeled. The number of alloys in the design space increases further with decreasing the concentration resolution.

1.2.2. Alloy Design by Electronic Approach (PHACOMP)

PHACOMP (PHAse COMPutation) has always been a guide for estimating the interaction of the alloying elements in superalloys. In the PHACOMP method, the tendency of the alloy towards formation of the detrimental TCP phases is determined by the average energy level of d-orbitals (M_d) of transition alloying metals [9,75,112]. Murata et al. determined [113] another alloying parameter named Bo that is the bond order between atoms. In the plots of M_d versus Bo for various alloy compositions, the ones that have been established to yield high creep resistance and low fraction of the TCP phases are selected [76]. Figure 1.9 shows M_d-B_o plot for a set of commercial alloys. The related required stress for rupture times of 3.6 million seconds at 1255K strength of these alloys is shown in a table in the right side of the plot with their corresponding position in the M_d-B_o plot. The position of the alloys with more than 100 MPa rupture strength and some single crystal alloys (Hashed circle) shows that these alloys have the M_d and B_o values in the range of 0.95-1 and 0.6-0.7 respectively [114,115].

Murata et al. successfully extracted a parameter, named alloying angle (ɵ), from the M_d-Bo plot (Figure 1.9). A vector is defined for each element. The origin of each vector is the Ni position and end of the vector corresponds to M_d-B_o intersection for an element. Then, two parameters for this vectors are defined which are the length and the angle. Length of the vector is determined based on the mole fraction of the alloying elements. The angle is determined according to the position of the element in the periodic table. It has been shown [113] that the alloying elements in the same periodic group show more or less similar alloying angles. This is shown in Figure 1.9 for elements in the group 4A (Hf, Zr, and Ti), group 5A (Ta, Nb, and V), and group 6A (W, Mo and Cr). Obviously, the γ' stabilizing elements like Al, Ti, Ta, V, and Nb have the lower alloying vector.

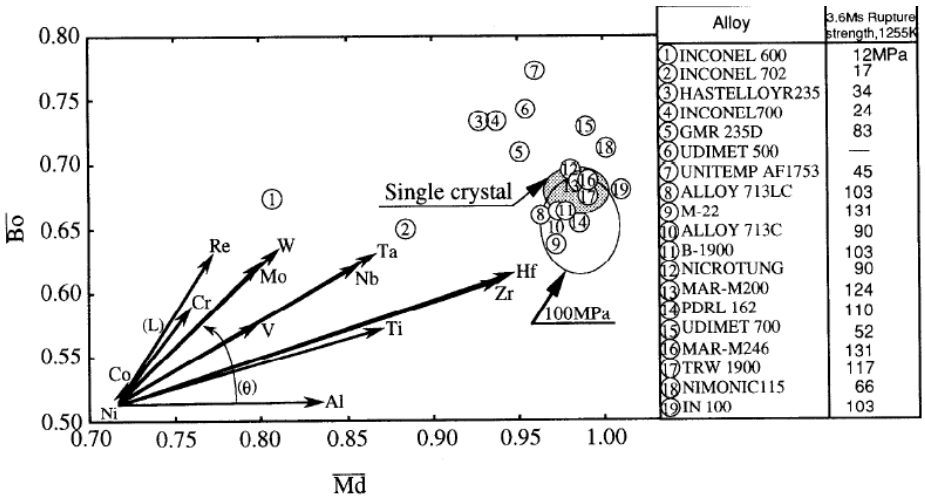

Figure 1.9. B_o versus M_d plot showing the alloying angle. Commercial alloys are shown with their position in the M_d-B_o plot.

For a multicomponent alloy, the vectors for each single alloying element is calculated and then summed together to give the overall length and angle for that alloy. Therefore for an alloy the alloying angle could be determined by the ratio of the average B_o and M_d (Equations 1.3 and 1.4 respectively) for an alloy:

$$\theta = \mathrm{Arctan}\left(\frac{\overline{B}_o}{\overline{M}_d}\right) \tag{1.6}$$

This observation is used by Murata [113] to find a relation between the alloying angle and the volume fraction of the γ' (Figure 1.10). The experimental data shows a good agreement between the calculated and actual volume fraction of γ'. Moreover, it is expected that by reducing the angle, the segregation of the γ' forming elements to the interdendritic region increases.

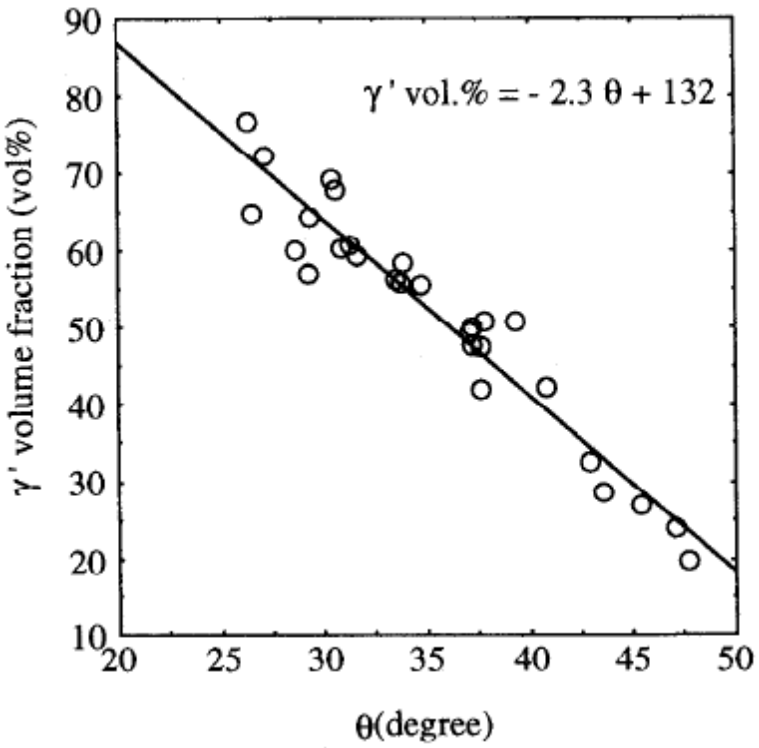

Figure 1.10. Dependence of the alloying angle and volume fraction of γ'.

1.2.3. Alloy Design by CALPHAD

Thanks to computational thermodynamics or the so-called CALPHAD (CALculation of PHAse Diagrams) technique, it is now possible to perform accurate calculations of phase diagrams even for rather complex alloys, and thereby speed up the alloy development time substantially [116]. In the CALPHAD method, the alloy system is divided to a set of binary and ternary subsystems and the results are generalized to multicomponent system. Thermodynamic calculations are performed for the system to calculate the phase equilibria. It can predict the evolution of the phase types and their

fractions by temperature and composition. The integration of the thermodynamics and kinetics makes this method successful in modeling the solidification and heat treatment and provides invaluable information about the segregation and heat evolution during solidification. Therefore, the effect of variation in the concentration of each alloying elements could be examined on phase stability of the alloy. This is really a considerable advantage especially for superalloys where the experimental determination of these parameters is expensive and even impossible in some cases. For this reason, phase diagram calculation software have been developed which are powerful and flexible with reliable databases for many phase equilibrium, phase diagram, and phase transformation calculations [116,117].

The CALPHAD method allows for calculating the phase diagram by knowing the temperature dependent thermodynamic properties of any composition. The Gibbs free energy is the most well-known and widely used state function for defining the thermodynamic equilibrium of the existing phases. This method is a semi-empirical method as it uses the experimental data to optimize the coefficient in the Gibbs free energy relation of the phases. Therefore, having a reliable database is the key factor in successful application of the CALPHAD method. The coefficients are then determined by the best fit between the parameters in the state function equation. Once the optimization of a system is done, it can be included in the already existing thermodynamic databases. The simple lower order relations then could be expanded to cover the thermodynamic relations describing the phase equilibrium of the multicomponent systems. For example combining the database of the Ni-Al and Ni-Cr, the CALPHAD method is able to determine the phase equilibrium of the ternary Ni-Al-Cr system. When reliable databases are provided, the system can model any composition and also any temperature which may be hard or impossible to determine experimentally [117,118].

Application of the CALPHAD method requires reliable database, which comes from extensive experiments. These databases should also include the temperature dependent phases. The database includes the following data input types:

- Thermodynamic data: The thermodynamic data includes the information such as the enthalpy of mixing, enthalpy of transformation, enthalpy of formation,

activity, and chemical potential. The enthalpies of mixing at different compositions and temperatures and enthalpies of formation of the stable phases can be determined experimentally with the help of calorimetric measurements.

- Phase diagram data: It includes the data related to the phase equilibria in a system such as liquidus temperatures, solidus temperatures, invariant reaction temperatures, invariant reaction compositions, tie lines, tie triangles, and phase boundaries.

- Crystallographic data: The information related to the crystal structure of the constituent phases such as space group, site occupancies and orientation of the crystals that are obtained from the structural characterization techniques such as X-ray or neutron diffraction, is very important in selection of the suitable thermodynamic models for the constituent phases.

- Physical measurements: It involves the data related to the specific heat or magnetism.

- Calculated Data: The information such as enthalpy of formation or enthalpy of mixing of different stable and metastable compounds can also be obtained with the help of density functional theory (DFT) calculations and are very useful in thermodynamic modeling of a system.

A CALPHAD based software Thermo-Calc is now well-developed and mature with reliable databases for modeling many kinds of phase equilibria, phase diagram, and phase transformation calculations and thermodynamic assessment in the fields of chemistry, metallurgy, material science, alloy development, geochemistry, and semiconductors [119,120]. This software was developed at the department for physical metallurgy at the Royal Institute of Technology in Stockholm, Sweden, by professor Mats Hillert and his PhD students Bo Sundman, Bo Jansson, and John Ågren [121]. The most common application of the Thermo-Calc software is its ability to predict the stable phases at different temperatures. This is of critical importance especially in the field of alloy design that relies on accurate understanding of the evolution of the stable phases at different

temperatures. The below example (Figure 1.11) shows the calculation of the equilibrium phases of the CMSX-4 with temperature.

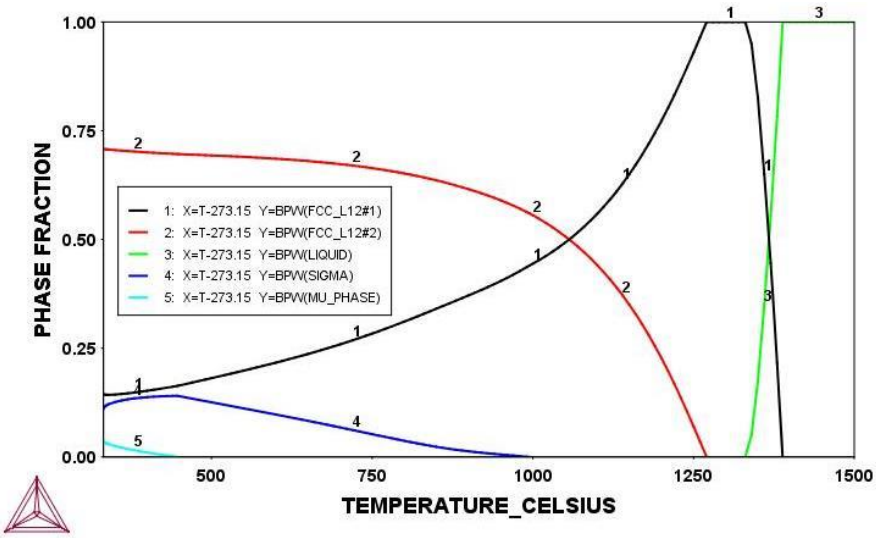

Figure 1.11. Amount of phases vs. temperature for the CMSX-4 alloy.

The diagram shows melting temperature for the alloy CMSX-4 and possible phases that can form during solidification. It also indicates the risk of forming detrimental secondary phases such as Sigma or Mu at temperatures below the solidification temperature. Therefore, Thermo-Calc is a powerful tool in the hands of alloy designers to study the effect of each individual alloying elements on the phase equilibrium. Alloying elements greatly affect stabilization of γ' phase and its content. More importantly, they alter the formation of TCP brittle phases in superalloys. This effect is shown in Figure 1.12 for the effect of increasing the Re content in the composition of the CMSX-4 on phase fraction of the Sigma (TCP) phase.

The software is also able to model the equilibrium and non-equilibrium Scheil solidification [122]. The equilibrium module simulates the diffusion processes, such as compositional variation in segregation occurring when an alloy solidifies, by utilizing local equilibrium approximation. The Scheil module within Thermo-Calc applies the Scheil-Gulliver model to deal with solidification problems of alloys. This assumes that the diffusion coefficients in the liquid phase are equal to infinity whereas in the solid phases

they are equal to zero, and that local equilibrium is always held at the phase interface between the liquid and solid phases [123].

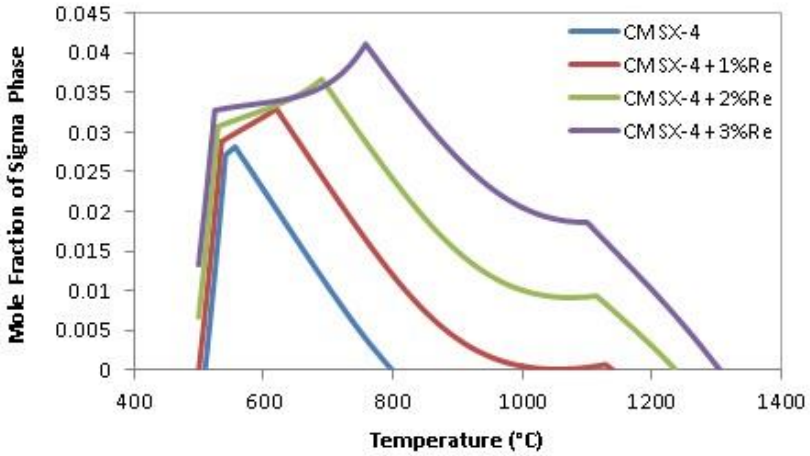

Figure 1.12. Thermo-Calc equilibrium modeling of the effect of addition of 1, 2, and 3wt% Re to the composition of CMSX-4 on mole fraction of the Sigma phase.

An example of solidification sequence of alloys CMSX-4 by the Scheil method is shown in Figure 1.13.

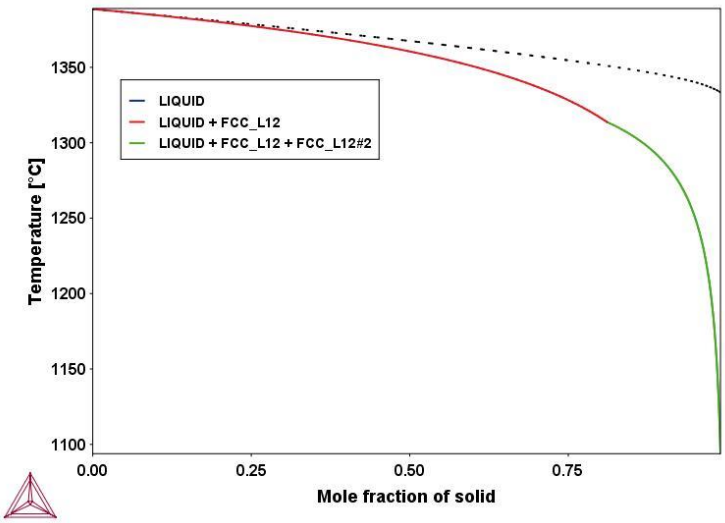

Figure 1.13. Calculated solidification sequence of the alloy CMSX-4 predicted by Thermo-Calc Scheil model.

The plotted diagram shows how the mole fraction of solid material varies with temperature. The calculated liquidus temperature is thus 1390°C and the material is completely solidified at 1140°C. The solidification sequence also is observed. In the first segment of the curve, liquid is transformed to the Gamma and Gamma prime phases and in 1140°C, all the liquid is solidified into these two phases.

Linking the thermodynamics and kinetic databases, the time dependent diffusion controlled phase transformations also could be modeled which especially are suitable for modeling the heat treatment processes. DICTRA is software developed by Thermo-Calc Company for simulation of diffusion controlled phase transformations in multicomponent alloys by numerical simulation of the diffusion equations [115]. DICTRA has the limitation of handling diffusion problems in 1-d. Three geometries could be defined, the planar, cylindrical, and spherical. The planar geometry is a boundless plane with a certain width that is specified by the user. The cylindrical geometry is a long cylinder with a radius, and the spherical geometry is a sphere with a radius. The radius in cylindrical and spherical geometries again is defined by the user dependent on the problem to be solved.

The basic formulations behind this software is described in the following [124]: The 1-d diffusion of a component k in a multicomponent alloy with n components in the diction x could be described by the Fick's first law of diffusion as following:

$$J_k = -\sum_{j=1}^{n} D_{kj} \frac{\partial C_j}{\partial x} \tag{1.7}$$

where J_k (kg/s.m^2) is the flux of the species of k which is the amount of the mass (kg) of the species k transferred by diffusion per unit time (Seconds) per unit area (m^2) perpendicular to the direction x. D_{kj} is the diffusion coefficient, C_j is the concentration of the components and therefore $\frac{\partial C_j}{\partial x}$ is the concentration gradient of the components in the x direction. The diffusivity term in this equation is only temperature and concentration dependent. This is for example shown for diffusion of Al for Ni–Al as a function of Al composition and temperature in Figure 1.14. The filled symbols are the experimental data and the lines show the Dictra calculations. The above plot shows that the interdiffusivity

increases with increasing the Al content. Moreover, the diffusion coefficient is higher at higher temperatures.

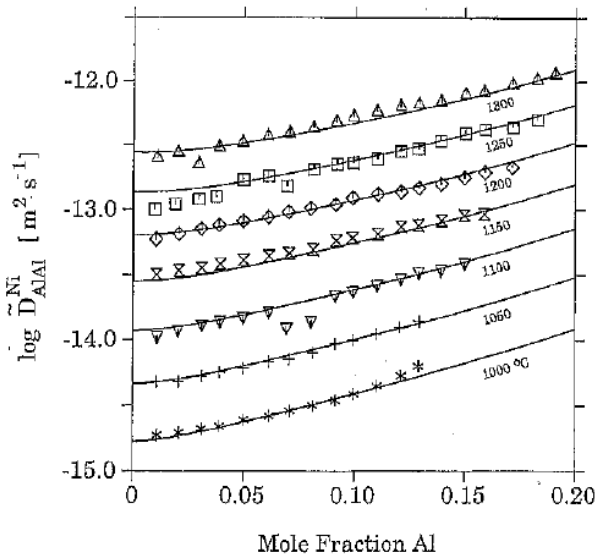

Figure 1.14. Logarithm of the interdiffusion coefficient of Al in the binary Ni-Al system versus the mole fraction of Al at different temperatures. The filled symbols represent experimental data and the DICTRA predictions are shown as continuous lines [113].

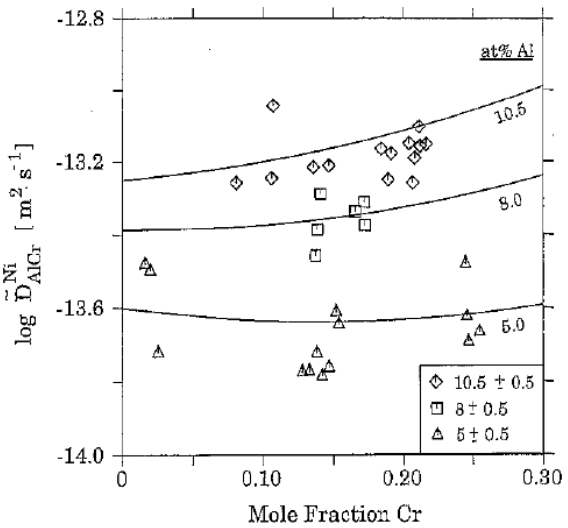

Figure 1.15. Variation of the interdiffuion coefficient of Ni in Ternary Ni-Al-Cr alloy at 1200°C as a function of Cr content at three different concentrations (at%) of AL. The symbols and continuous line represent the experimental data and Dictra results [113].

However, in multicomponent alloys with more than one species, the diffusivity will depend on the concentration gradient of all the species as well. This is for example shown for the interdiffusivity of Ni in the Ternary Ni-Al-Cr alloy at different concentrations of Cr and Al in Figure 1.15. It is seen that Al increase the diffusivity of the Ni, however the effect of Cr depends on the concentration of Al.

Fick's second law of diffusion is the combination of the first law and continuity equation, which yields the time dependent flux of the atoms as following:

$$\frac{\partial C_k}{\partial t} = -\frac{\partial}{\partial x}(J_k) \tag{1.8}$$

Onsager [66] adopted the Fick's second law for solving the diffusion problems in multicomponent alloys by introducing the phenomenological force term (L'_{ki}) which relates the flux to the driving force for diffusion. Then, the first law now could be described as:

$$J_k = -\sum_{i=1}^{n} L'_{ki} \frac{\partial \mu_i}{\partial x} \tag{1.9}$$

where μ_i is the chemical potential for the component i which is a thermodynamic state function and is a function of the concentration of all the species. It defines the change in the Gibbs energy and other thermodynamic state functions with the change in the number of the particles of i. In terms of the Gibbs free energy it can be written as.

$$\mu_i = \left(\frac{\sigma G}{\partial n_i}\right)_{p,T} \tag{1.10}$$

where μ_i is the chemical potential of the component i (partial molar Gibbs energy), G is the Gibbs energy of the phase, n_i is the number of moles of the component i, T is the absolute temperature, and p is the pressure. Thus the term $\left(\frac{\partial \mu_i}{\sigma c_j}\right)$ is in fatt the second derivative of the molar Gibbs free energy with respect to the concentration and therefore is a pure thermodynamic quantity which can be calculated from the thermodynamic description of

the system. The Thermo-Calc software could determine this value. L'_{ki} on other hand is a kinetic factor which is a proportional factor depending on the mobility of a species.

Equation 1.10 could be rearranged to describe the flux equation based on the concentration gradient that is a measurable value rather than the chemical potential gradient.

$$J_k = -\sum_{i=1}^{n} L'_{ki} \cdot \sum_{j=1}^{n} \frac{\partial \mu_i}{\partial C_j} \cdot \frac{\partial C_j}{\partial x} \tag{1.11}$$

This equation could be rewritten as;

$$J_k = -\sum_{j=1}^{n-1} D_{kj}^{n} \frac{\partial C_j}{\partial x} \tag{1.12}$$

where the coefficient D_{kj}^{n} is known as diffusion coefficient:

$$D_{kj}^{n} = -\sum_{i=1}^{n} L'_{ki} \cdot \frac{\partial \mu_i}{\partial C_j} \tag{1.13}$$

The diffusivity matrix for n component will be a matrix of (n-1) × (n-1). The reason is that in a system with n component, there will be n-1 independent concentration while the concentration of the solvent is dependent to the other components.

In the volume frame fixed references where the volume of the species does not change during diffusion, the diffusivity matrix could be expressed as:

$$D_{kj}^{n} = D_{kj} - D_{kn} \tag{1.14}$$

where the nth species which is the solvent is excluded from the diffusion matrix. This way the interdifusion coefficient is described in terms of a thermodynamic function $\frac{\partial \mu_k}{\partial C_j}$ (called thermodynamic factor) and the kinetic term L'_{kj} (called kinetic factor).

In 1992, Andersson and Agren [66] suggested a method for calculating the kinetic parameters in multicomponent alloys based on vacancy exchange mechanism. The model assumes that atoms diffuse by jumping to their neighboring vacant sites. They suggested that

$$J_k=-c_k y_{v_a} M_{kv_a}\left(\frac{\partial \mu_k}{\partial C_j}\right) \tag{1.15}$$

where y_{va} is the fraction of lattice vacant sites and M_{kva} is a kinetic parameter expressing the rate of exchange of an atom and its neighboring vacancy. The expressed the term $y_{v_a} M_{kv_a}$ with the symbol Ω which is called mobility which is a function of composition, temperature and pressure. Therefore equation 1.15 could be written as:

$$J_k=-x_k \Omega_k \frac{\partial \mu_k}{\partial C_j} \tag{1.16}$$

Compared to Equation 1.9, the kinetic parameter expressed as:

$$L_{kk}=x_k \Omega_k \tag{1.17}$$

By combining Equations 1.9, 1.14 and 1.17, the following equation can be written for diffusivity

$$D_{kj}=\sum_{i=1}^{n} (\delta_{ik}-c_k V_s) x_i \Omega_i \frac{\partial \mu_i}{\partial c_j} \tag{1.18}$$

where δ_{ik} is the kronecker delta, c_k and c_i are the concentration of the k and i, V_s is the total molar volume of the species and y_{va} is the vacant lattice fraction. This way, the Equation 1.9 could be expressed as:

$$J_k=-x_k \Omega_k \frac{\partial \mu_k}{\partial c_j} \tag{1.19}$$

The term mobility then is described as

$$\Omega_k = \Omega_k^0 . \exp\left(-\frac{Q_k}{RT}\right) \tag{1.20}$$

where R is the gas constant and T is the absolute temperature. Ω^0_k and Q_k are the frequency factor and activation energy that are dependent on the temperature, pressure and composition. The composition dependency of these parameters (Ω^0_k and Q_k) could be expressed based on the CALPHAD method as following:

$$\emptyset_k = \sum_i^n x_i \emptyset_k^i + \sum_i^n \sum_{j>1}^n x_i x_j \left\{ \sum_{r=0}^m \emptyset_k^{ij} (x_i - x_j)^r \right\} \tag{1.21}$$

where Ω_B and Q_B could be replaced by $\emptyset$.

Therefore, $\emptyset_B^i$ is the value of $\emptyset$ for the pure state of the element i, and $\emptyset_B^{ij}$ is the interaction parameter dependent on the value of r. The value of r determines if the solution of the components is regular or sub-regular. x_i and x_j are the mole fraction of the elements i and j.

In the kinetic database of the Dictra software necessary for most diffusion simulations, the mobility expressions mobilities are stored instead of expressions for the diffusivities. In summary by coupling the thermodynamic data from the Thermo-Calc software and the mobility terms via the kinetic database, the Dictra software is able to solve the multicomponent diffusion equations for phase transformations.

In working with Dictra, first, the alloy composition is defined in the program. Then, the size of the system and the initial condition are defined. The thermodynamic data is called from the Thermo-Calc software and is linked to the mobility database of the Dictra. After defining the boundary condition, based on the problem to be solved, the appropriate module of the program is run for solving the problem. Dictra could be used in several metallurgical and materials science applications, like the solidification microsegregation, different heat treatment processes like the homogenization, coarsening, post weld heat

treatment, carburizing, nitriding, and also the interdiffusion in coupled compounds. However, unfortunately, the application of this software in alloys with large number of the alloying elements, like in single crystal superalloys, is limited due to the very low speed. Therefore, it is preferred to simplify the chemistry of the alloy to the equivalent lower order alloy systems.

1.2.4. Alloy Design by Neural Network (NN)

Neural network (NN) models are exceptionally useful in complex pattern recognition and function approximation tasks where other techniques are not able to notice the trend. Therefore, they are especially used in places where there is not a physically sound model such as alloy design with multiple components. Among various types of neural networks, the multilayer perceptron (MLP) feed-forward network is the most commonly used one due to relative ease in implementation and lower number of required training samples [125]. Architecture of a sample MLP, which is also used in the current study, is schematically shown in Fig. 1.16, which includes an input layer (Xi), a processing unit called hidden layer (a_j), and an output layer (O).

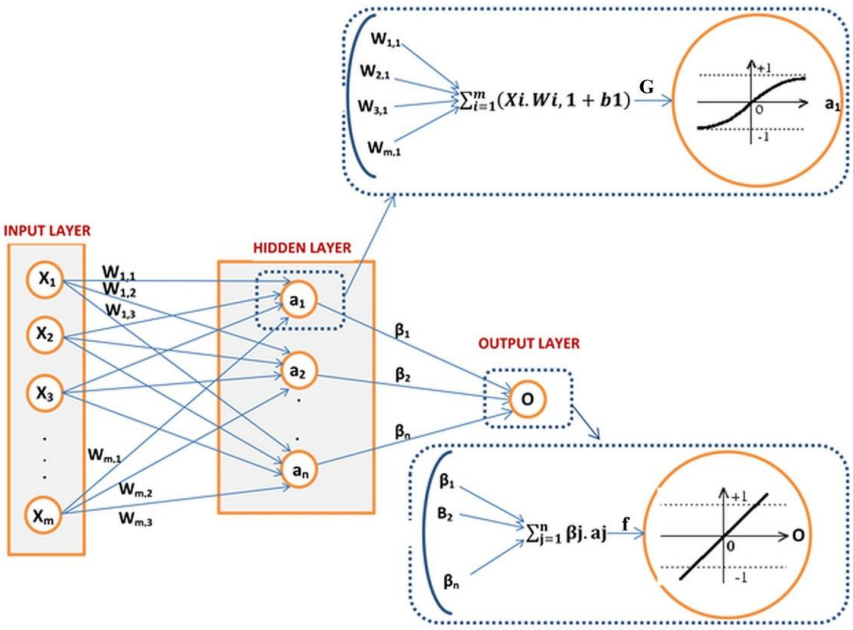

Figure 1.16. Schematic architecture of the MLP used in this study showing the input, hidden, and output layers.

The hyperbolic tangent and linear transfer functions [126] are used respectively in the hidden and output layers. The weights $W_{i,j}$ are assigned for the connections between the input and the hidden layers and the β_j are between the hidden and output layers. The Bayesian Regularization (BR) [127] backpropagation algorithm is used to adjust the weights in neurons in order to increase the accuracy in the output.

Multiple perceptron (MLP) is a kind of neural networks that receive one or several inputs and produce outputs. The architecture of the MLP includes the input layer, the processing unit that is called the hidden layer(s), and the output layer (Figure 1.16). The data are received and processed in nodes present in all the layers. Nodes in the input layer receive the inputs. The inputs are then processed through the hidden layers, and a yield is output. Input layer includes m input nodes ($X_1,\ldots,X_m$), each of them is related to a particular input variable. The hidden layer is composed of n nodes which are connected to all the input nodes and a single output node of the network by a set of connection strengths labeled as $W_{i.j}$ and β_j respectively. The $W_j= (W_{j,1},\ldots..,W_{j,m})$ represents the vector of the connection weights between the jth hidden node and all of the m input units. Similarly, β_j is a scalar value for the connection of the jth hidden layer to the single output neuron. After feeding the inputs into the first layer of the network, they are sent to all hidden node with a random weight ($W_{i,j}$). The summation of all weighted inputs in each unit together with a constant bias of b is passed through a transfer function (G) in the hidden layer to yield an output for that hidden node.

$$aj=G\left(\sum_{i=1}^{m} Wi,j.Xi+bj\right) \tag{1.22}$$

The output from all hidden units is assigned the output unit connection weights (β_j) and then transformed to the output by the output layer activation function f. This way, the output that is a scalar value is obtained as:

$$O=f\left(\sum_{j=1}^{n} \beta j.aj\right) \tag{1.23}$$

The transfer functions (G and f) transform the input of a neuron to an output in the hidden and output layers, respectively. Theoretically, any differentiable function can be used as a transfer function; however, in practice a few number of functions, which have the mixed characteristics of continuous, bounded, and differentiable, are preferred. Among these functions, the threshold, linear, sigmoid (logistic), and hyperbolic tangent (tanh) functions are the most widely used. The threshold function sets the output to 0 if the summed input is less than a certain threshold value or 1 if the summed input is greater than or equal to the threshold value. Due to the nature of the threshold function, it is mainly used in classification and machine learning activities. The logistic and hyperbolic functions outputs between 0 to 1 and –1 to +1, respectively. The nonlinearity of these functions allows the network to learn nonlinear relationships between input and output vectors in the hidden layers. For modeling purposes, with continuous target values, the linear transfer function is preferred in the output layer. In fact, it has been shown that multilayer feedforward networks with a single hidden layer and an arbitrary bounded and non-constant transfer function in the hidden layer and a linear output transfer function are universal approximates for any function [20–22]. Kurt Hornik [128], showed that for an arbitrary choice of the non-constant and bounded transfer function for hidden layer and linear transfer function for the output layer, the architecture of a multilayer feedforward network is potentially a universal approximate to map any arbitrary input space to the output.

The number of nodes in the input and output layers depends on the number of input and output variables respectively. The number of hidden layers and the number of nodes in each hidden layer affect the accuracy of the output; however, a large number of hidden layers and nodes may lead to overfitting [129]. The number of nodes in the hidden layer is determined according to the lowest error of the network.

MLPs are layered feed-forward neural networks where the flow between nodes is unidirectional and the output from one layer is used as an input to the next layer. MLP is applied in three steps; the network is first trained by feedforward backpropagation algorithm, then the trained network is tested. Finally, the trained and tested network is used to detect the pattern between a vast number of input and output data. The backpropagation algorithm is used in layered feedforward NN to adjust the weights in neurons during

training in order to reduce the error of training and increase the accuracy in the output. The network is trained first by a known set of input-output pairs and then the cost function which is generally chosen to be the sum of square of the difference between calculated and expected results (E_d) is calculated as following for the single output network [18]:

$$E_d = \frac{1}{2}\sum_{k=1}^{N}[O(k) - t(k)]\,2 \tag{1.24}$$

where N is the number of training datasets, t the target output of the network and O the predicted output of the network. The gradient of the cost function with respect to all the connection weights is calculated according to the chain rule and the new output is calculated by updating the weights in the backward pass by back propagating the error to the former layers and adjusting their weights. This operation is repeated until the calculated error between the predicted and desired outputs is reduced to an acceptable minimum value. Various training algorithms can be implemented in the framework of the backpropagation methodology like Gradient Descent algorithm (GD), Conjugate Gradient Descent, Levenberg-Marquardt algorithm (LM), and Bayesian Regularization (BR). The Bayesian Regularization is the most widely used one for the cases that the overfitting of the training data is probable due to a large number of input variables and limited number of the training dataset. The process is called Bayesian regularization backpropagation [127]. It minimizes a combination of squared errors and weights, and then determines the correct combination to produce a network that generalizes well. Bayesian regularization expands the cost function to search for the minimum error using the minimum number of the weight connections. By forcing the weights and bias of the network to the smaller values, it reduces the number of parameters involved in the training and avoids the overfitting of the training data and poor estimation for the test data which is a usual drawback for the other training algorithms. The cost function is defined as a combination of squared error and weight functions multiplied by two Bayesian hyperparameters, alpha and beta. Then the aim is to find a direction for minimizing the cost function by without overfitting the network. Therefore, the cost function will take the form [18]:

$$S(w)= \beta E_d+\alpha E_w \tag{1.25}$$

where E_d (given in Equation 1.9) and E_w are the sum of the squared network errors and the sum of weights respectively. The E_w is defined as:

$$E_w=\frac{1}{2}\sum_{k=1}^{w}[w(k)] \tag{1.26}$$

The detailed formulation then is:

$$S(w)=\frac{\beta}{2}\sum_{k=1}^{N}(O(x(k),w)-t(k))^2+\frac{\alpha}{2}\sum_{k=1}^{W}w(k)^2 \tag{1.27}$$

where the x(k) and t(k) are the training pairs of the input and output respectively and w € R^W is the training weights and biases. The O(x(k),w) is the output of the network for the corresponding x and w. In the BR framework, the weights of the network are viewed as random variables, and then the distribution of the network weights and training set are considered as Gaussian distribution. The hyper parameters, α and β are determined by the Bayes' theorem. This theory calculates the posterior probability of occurrence of network weights (W) in a network with given input dataset D,$\left(P\left(W|D,\alpha,\beta\right)\right)$ [130]:

$$P(W|D,\alpha,\beta)=\frac{P\left(D|W,\beta\right)P(W|\alpha)}{P(D|\alpha,\beta)} \tag{1.28}$$

where $P(W|\alpha)$ is called the prior probability of $P(W)$ without knowing the value for α. $P\left(D|\alpha,\beta\right)$ is the prior known probability of the known dataset D, which functions as a normalizing constant. The term $P\left(D|W,\beta\right)$ is the initial probability density for the input data, which is also called the likelihood function and determines the probability of occurrence of any dataset for that specified set of weights. Assuming the error function has a Gaussian distribution:

$$P\left(D|W,\beta\right)=\frac{1}{Z_D(\beta)}\exp(-\beta E_d) \tag{1.29}$$

where $Z_D(\beta)$ is the normalizing constant. Similarly for P (W),

$$P(W|\alpha)=\frac{1}{Z_D(\alpha)}\exp(-\alpha E_w) \tag{1.30}$$

and the $Z_D(\alpha)$ is the normalizing constant.

The maximum posterior probability is equal to maximizing the probability of the likelihood function $P(D|W,\beta)$ and $P(W|\alpha)$, which is attained by minimum value of the error function (E_d and E_w). This way, considering a Gaussian distribution of the error, the standard choice for the weights is the maximum likelihood estimate for which the optimum values for α and β are found. The next step is to solve the S(w) with the Levenberg-Marquardt algorithm where the Hessian matrix calculations take place and updates the weight space in order to minimize the cost function. The Levenberg-Marquardt algorithm is simply solving the equation [130]:

$$(J^TJ + \lambda I)\delta = J^TE \tag{1.31}$$

where J is the Jacobian matrix for the first order derivatives of the errors with regard to the weight connections, E is the error vector, λ is the Levenberg's damping factor and δ is the weight update vector. The term J^TJ forms the Hessian matrix.

The λ damping factor is adjusted at each iteration based on the rate of reduction of the error. This value is added to the diagonal members of the Hessian matrix and then, the Levenberg - Marquardt equation is solved to find the value of δ. The next step is adjusting the weights using δ and recalculating the error. If the error is decreased, the λ is decreased and if not the new weights are discarded and the method is repeated with a higher value for λ. The process is repeated until the error decreases to any determined acceptable level [127,131].

1.3. Production of Single Crystal Superalloys

Solidification takes place through the nucleation and growth of the solid phase under favorable thermal conditions. When the temperature is reduced uniformly throughout the liquid, extensive random nucleation occurs in the liquid. Homogeneous nucleation involves

the formation and survival of solid nuclei whose radii are larger or equal to a critical radius. However, for the nucleation to take place, the temperature should be lowered below the melting temperature in equilibrium, characterizing the occurrence of thermal undercooling [85]. The homogenous nucleation is rather theoretical, and heterogeneous nucleation always happens on the favorable nucleation sites in the liquid such as the mold walls or other solid particles like the grain refiners. The practical conditions of heat flow promotes the formation of temperature gradients in the liquid, which induce initial nucleation on the mold's walls, with grain growth taking place in the direction of the heat flow. Nucleated grains grow in the favorable crystallographic orientation and heat direction, advancing toward the bulk of the casting.

The presence of grain boundaries in the cast part weakens the high temperature mechanical properties. The grain boundaries are potent sites for nucleation of high temperature creep and fatigue cracks [30]. Since turbine blades are to be used in the hot sections of the engine where the creep and fatigue mechanisms are active, they are produced by directional solidification (DS) or single crystal (SC) growth methods. Both methods are accomplished by controlled withdrawal of a crucible in a temperature gradient generated by a furnace. In directional solidification, heat is extracted from the mold in only one direction, but due to solid/liquid (s/l) interface instability, several grains form and grow unidirectionally. The lateral growth of these grains is restricted by eliminated or limited radial heat extraction, resulting in the aligned columnar and elongated grains and prevention of the equiaxed grains. The ideal microstructure for high temperature applications is the one without any grain boundaries. Such a microstructure is called single crystal (SC). Casting in the form of single crystal requires fully controlled directional solidification with using either a single crystal seed or a grain selector or combination of the both in the bottom of the mold. Single crystal seed allows for orienting the first solid crystals to adopt its crystal orientation and grow as a single crystal. The grain selector allows for surviving only one grain to grow as a single crystal part. Of course, s/l interface stability must be preserved during the entire solidification by carefully controlled temperature gradient and solidification velocity.

As already said, the solid nuclei with a radius equal or greater than a critical radius survive and grow inside the molten metal. As solidification advances, the interface may

grow planar or the instabilities may occur which yields a dendrite microstructure. Morphology of the interface is determined by the solidification velocity and the temperature gradient. The solidification velocity and thermal gradient along with the level of convection in the melt have a pronounced effect on the solidification characteristics of the superalloys like the mushy zone length, primary dendrite arm spacing (PDAS), and microporosity. In dendritic solidification, the convection is usually defined for the interdendritic melt. However, it has been reported that flow characteristics of this region can be influenced by the flow in the bulk melt [132]. Hence, reduced convection in the bulk melt can decrease interdendritic convection. The mushy zone length is directly affected by the thermal gradient and the heat extraction rate from the system. High thermal gradients and heat transfer rates will tend to reduce its length. On the other hand, a turbulent mixing in the bulk melt can smear out the thermal field which can increase the mush length due to a reduced thermal gradient [133]. Moreover, when solidification is initiated on a single crystal seed, any disturbance in the mushy zone can destroy the dendritic morphology and cause formation of misoriented dendrites before and at the start of pulling the crucible to initiate solidification. This region of the misoriented dendrites is called the melt-back transition region [134–136]. Still, the new axially oriented dendrites form as extensions of the dendrites in the mushy seed.

Two main features of the dendrites are the primary and secondary dendritic arm spacing which affect the mechanical properties of the solidified alloys. The distance between the primary trunks is called primary dendrite arm spacing (PDAS). Figures 1.17a and b shows a three dimensional representation of the PDAS from two different views.

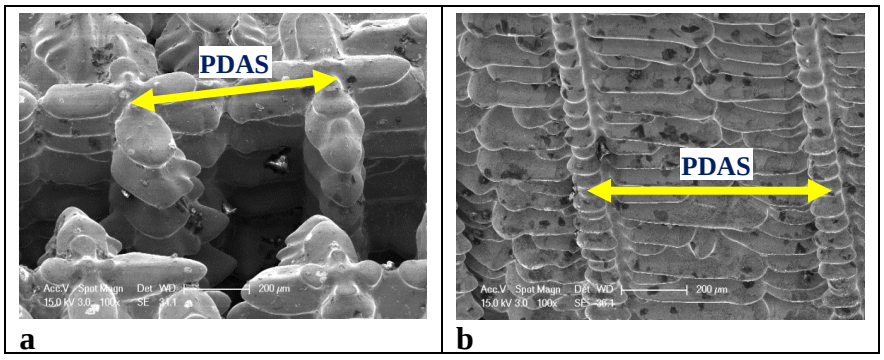

Figure 1.17. PDAS shown in two different views in SEM photos of the crystals grown in this study.

One of the critical parameters that have to be considered for producing a high quality single crystal is the cooling rate that depends on the rate of the heat transfer from the mold cavity to the atmosphere through the mold. There are three modes of heat transfer, namely conduction, convection, and radiation. Conduction focuses on the transfer of heat through a solid medium, convection results from the energy transfer through the motion of a fluid, and radiation focuses on the transmission of energy through electromagnetic waves [137]. In directional solidification, the axial heat flow by conduction to the baffle that will be described in the next section or bottom cooled pedestal is increased. On the other hand, the radial heat transfer by radiation and convection is limited to prevent a lateral temperature gradient.

Primary dendrite arm spacing (PDAS) is dependent of the thermal gradient, withdrawal velocity, and convection in the melt. For high axial thermal gradients (GL > 28°C/cm), [138] the radial thermal gradients in the melt is negligible and the primary dendrite arm spacing decreases with increasing withdrawal rates [139]. In contrast, GL < 28°C/cm, even a very low radial thermal gradient may become dominant leading to the growth of secondary dendrite arms and to a larger PDAS. Furthermore, low gravity experiments have yielded a larger PDAS [140]. Secondary dendrite arms grow vertical to the direction of the primary dendrite trunks. Figures 1.18a and b shows a three dimensional representation of the SDAS from two different views.

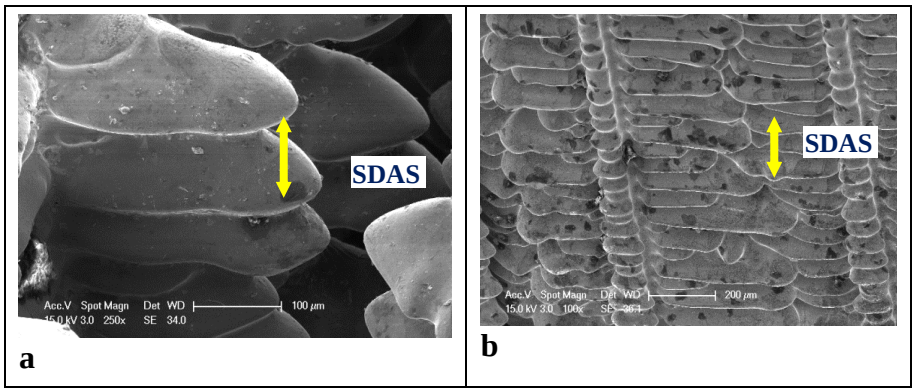

Figure 1.18. SDAS from two top and side views.

Tertiary dendrite arms also may nucleate and start to grow on the secondary dendrite arms. The two images in Figure 1.19 show them. They are even observed to grow from

secondary arms and act as the source for the new primary dendrite trunks [141]. Tertiary arm formation is commonly related to the branching mechanism in steady-state growth experiments where they are observed to grow from secondary branches in the direction of the temperature gradient to form new primary trunks [142]. The alignment of the dendrites will influence the interdendritic flow pattern between dendrites, which consequently determines the other solidification characteristics like the amount and distribution of the microporosities in the solidified part. That will also influence the segregation pattern. The mechanical properties of the material will be affected as well.

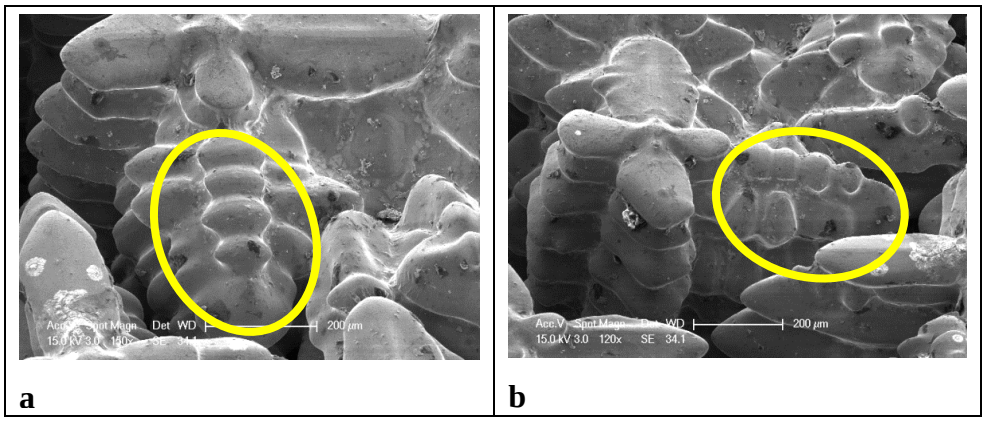

Figure 1.19. Tertiary dendrite arms branching from the secondary dendrite arms (a, and b). Note the tertiary arms on the secondaries in the marked area.

The level of microporosity in a solidified part is affected by the mushy zone characteristics. A fine dendritic microstructure decreases the permeation of the bulk melt into the interdendritic region that can cause microporosity. On the other hand, in a dendritic structure with secondary and tertiary dendrite arms, pores may be isolated and hence their limited growth can reduce the microporosity. In fact, these two competing effects determine the final pore content in a dendritically solidified part [143].

1.3.1. Vertical Bridgman (VB) Method

The turbine blades are produced in very closely controlled directional solidification process in a protective environment. The vertical Bridgman (VB) method is the major technique used for single crystal growth of superalloys [144]. In this technique, a crucible

is translated along a furnace with a thermal gradient. The mold is cooled by radiation heat transfer to walls of the furnace. The furnace has two hot and cold zones that are isolated from each other by a baffle (Figure 1.20). The baffle serves to isolate the upper hot zone from the bottom colder zone. The temperature gradient is adjusted so that the solidification interface is established at the baffle. A seed is introduced at the bottom of the crucible and the crucible is slowly lowered into the freezing zone, where upon the single crystal grows from the melt. The charge is first melted completely in the hot zone and then the crucible is moved towards the freezing zone so that the melted charge gets in contact with the single crystal seed in the cold zone. After setting the initial interface, the crucible is translated downwards through the freezing zone to solidify the entire part. The directional heat transfer creates a vertical thermal gradient and promotes nucleation and growth of the dendrites in the direction of the heat flow. The crystallographic orientation of the seed along with the thermal gradient determines the crystallographic texture of the epitaxially grown dendrites from the single crystal seed.

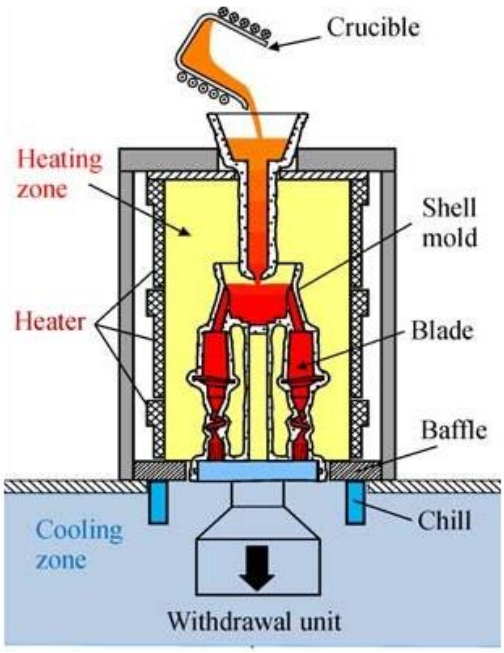

Figure 1.20. Schematic of the vertical Bridgman method [145].

The heat extraction rate from the solidified casting part mainly depends on the thermal conduction through the mold to the chilled plate. To achieve higher thermal gradient, the cooling system of the conventional Bridgman process is modified to include

LMC (Liquid Metal Cooling) [146], and the GCC (Gas Cooling Casting) processes [147]. However, application of these processes is limited due to the complicated process and economic issues.

1.3.2. Vertical Bridgman with Submerged Baffle (VBSB) Method

Vertical Bridgman system is modified by positioning a baffle immersed inside the melt during growth (Figure 1.21). This modified technique is called vertical Bridgman with a Submerged Baffle (VBSB). Note that the baffle in VBSB is submerged in the melt and is different from the baffle used in conventional VB to separate the hot and cold regions. The baffle may be made of a material with conductivity similar to that of the melt, and it may have a heater inside to supply heat axially to the s/l interface of a growing crystal. It also reduces the axial and radial segregation in crystal growth of semiconductors. Due to reduced melt height, the level of buoyancy driven convection in the bulk melt is decreased [26–28]. These effects have been reported to promote stability of the planar interface in single crystal growth of different semiconductors [148]. The application of this method in directional solidification of aluminum alloys has led to considerable reduction in the level of microporosity [149].

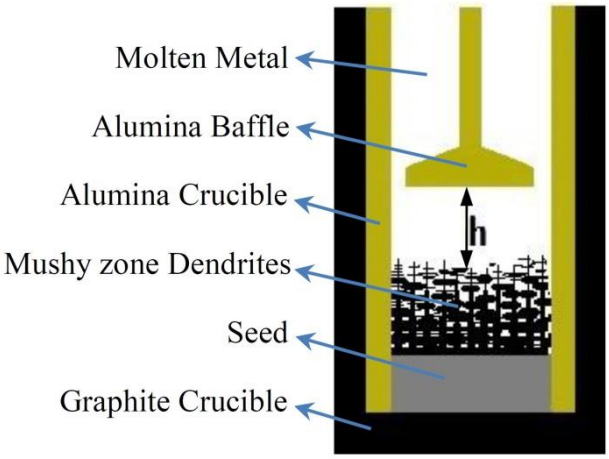

Figure 1.21. The vertical Bridgman with a submerged baffle (VBSB) technique. The effective bulk melt height is shown by h and bounded between base of the baffle and the solid/liquid interface (top of dendrites).

A reduced melt height can decrease convection in the bulk melt which is given by the Rayleigh number and is proportional to the fourth power of the melt height [26,149]. Rayleigh number is the ratio of the driving buoyancy force to the retarding frictional forces. In fact, Rayleigh number is the property of a fluid that determines how heat is transferred throughout the fluid. When you have a mass of fluid with an uneven temperature distribution, it is natural for this temperature distribution to be evened out, and that takes place through heat transfer. Heat transfer itself can take place through multiple modes as conduction, convection, and radiation. In fluids, it happens only via the first two methods. This is where the Rayleigh number comes into play. This number helps to determine how a fluid will transfer heat amongst itself if a temperature gradient is introduced. Different types and flows of fluids have their own threshold Rayleigh's number. If the Rayleigh number falls below this threshold, heat transfer takes place through conduction; however, if the Rayleigh number exceeds the threshold, heat transfer is predominantly through convection. Figure 1-22 shows the Rayleigh number variations with the liquid fraction during solidification of CMSX-11B and binary Pb-Sn alloys [150]. This figure shows that there is a critical Rayleigh number for a specified solid fraction. Moreover, the superalloys solidification is with the low Rayleigh number.

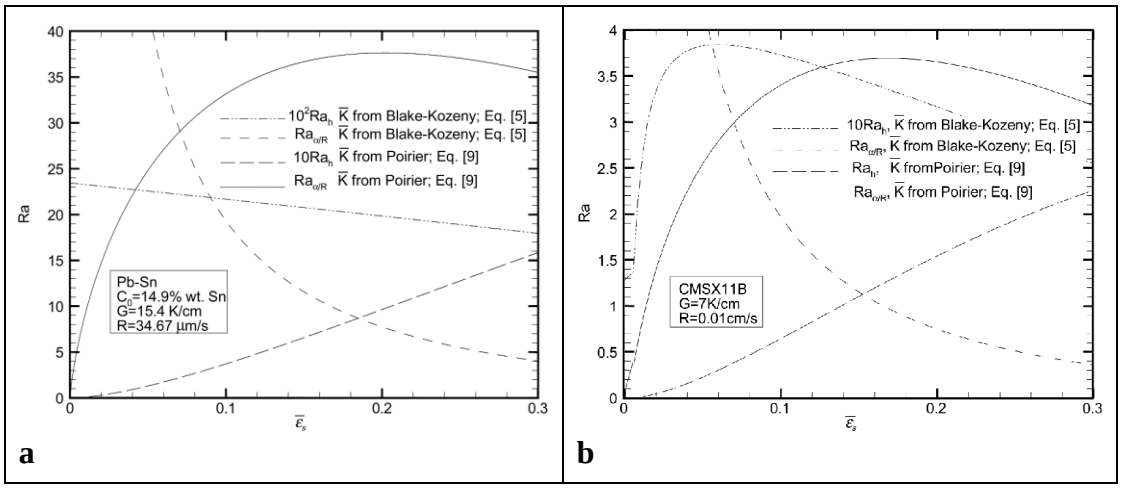

Figure 1.22. Variation of the Rayleigh number with liquid fraction during solidification of (a) Pb-Sn, and (b) CMSX-11B alloys. $\bar{\varepsilon}_s$ and $\bar{K}$ are the solid fraction, and permeability [150]. For different formulations for Rayleigh numbers, the reader is referred to [144].

While the bulk metal Rayleigh number depends mainly on the height of the liquid metal above the interface, the mushy zone Rayleigh number depends on the density and permeability in the mushy region. The segregation during solidification of the superalloys leads to density variation in the mushy zone, which alters the Rayleigh number and fluid flow behavior in the interdendritic region. To have a measure of the change of Ra number in the mushy zone, the density variation of the liquid phase in the mushy zone should be calculated first. Since the density is directly determined by the alloy compositing, the varying composition of the liquid along the mushy zone should be determined first.

1.4. Heat Treatments of Single Crystal Superalloys

1.4.1. Solution Treatment

Single crystal superalloys have compositions with as many as ten different elements present in significantly varying proportions. The segregation is inherent in solidification processes because of different segregation coefficient of the elements. Therefore, single crystal superalloys possess a high degree of segregation in the dendrite core and interdendritic region after their production. The problem is augmented by the presence of the heavy, slow diffusing elements. Moreover, for most of the single crystal compositions, the very last stages of solidification occur via one or possibly more eutectic reactions. These eutectic reactions give rise to a low melting eutectic which contains a large volume fraction of the γ’ phase due to segregation of precipitate forming elements. A homogenization (solution) treatment is then necessary to remove heavy segregation. In practice, a care should be given to prevent the occurrence of an incipient melting of the eutectic regions during the homogenization and, if not completely removed, during the high temperature service [30].

To perform a suitable heat treatment, a number of critical temperatures should be determined. They are the liquidus, solidus, and γ’ solvus temperatures. During the solution heat treatment, the temperature should be above that of the γ’ solvus temperature to dissolve the γ’ phases in the matrix. On the other hand, temperature should not be above the solidus temperature to prevent the incipient melting. Hence, the solution treatment

temperature should be between the γ' solvus and the solidus. This is known as the heat treatment window.

1.4.2. Aging Heat Treatment

After homogenization of the microstructure, aging process is applied for the evolution of the strengthening γ' precipitate phase. This is done by heating a homogenized sample to a predetermined temperature for a predetermined time. The process is finished by water quenching the sample. The resulting microstructure is a homogenized structure of the γ matrix with uniformly dispersed γ' precipitates. The aging of the single crystal superalloys is usually a double aging process as this produces a microstructure with evenly distributed γ' phase [151].

Since the TC-Pisma software is used for modeling the precipitates evolution and coarsening in the aging, the formulations used in that software is described in this section for the nucleation and coarsening.

1.4.2.1. Nucleation. TC-Prisma follows the classical nucleation theory for precipitation of supersaturated precipitates inside the matrix. Normally the nucleation happens after an incubation period. After nucleation, the precipitates should reach a critical size to get stable and grow in the next stage. The free energy after nucleation increases until this critical size and after that, the free energy decreases. However, the interfacial energy increases always. Nucleation occurs either homogenously or heterogeneously. The homogenous nucleation occurs in the bulk of a single crystal alloy. Heterogeneous nucleation occurs in the microstructure imperfections like the grain boundaries, dislocations, or the edges or the grin corners. In the presence of the crystallographic imperfections, the free energy barrier reduces and the critical radius for the stable precipitates decreases as well. The classical theory of the solid-state nucleation assumes that a spherical second phase precipitate could form inside the matrix with the rate that is frequency related to the mobility of the atoms [152]:

$$J(t)=J_s \cdot \exp\left(-\frac{\tau}{t}\right) \tag{1.32}$$

where J(t) and J_s are the time dependent and steady state nucleation rates respectively, τ is the incubation time before the nucleation and t is the time. The steady state nucleation rate is described as:

$$J_s = Z\beta N \exp\left(-\frac{\Delta G^*}{kT}\right) \tag{1.33}$$

where Z is the Zeldovich factor, β is the rate of attaching the atoms from the matrix to the precipitates, N is the number of available nucleation sites on the precipitate, ΔG^* is the free energy change due to precipitate, k is Boltzmann constant, and T is the temperature. The Zeldovich factor Z is a thermodynamic parameter of the nucleation process which is related to the probability of the formation of the embryos with radius greater than the r* in stochastic manner. On the other hand, is the term hat considers the kinetic of transportation in the interface between the matrix and precipitates.

For the precipitation of a precipitate γ' inside a supersaturated matrix of γ, the diffusion of element should occur to form a small volume of γ' composition with the crystal structure of the γ'. The creation of a new surface creates an interfacial energy barrier.

The free energy for nucleation (ΔG_t) is composed of two parts, a volume free energy (ΔG_v) and a surface energy (ΔG_s). ΔG_v is the reduction in free energy per unit volume for nucleation of the new phase, and ΔG_s is the strain energy per unit volume associated with creation of the new precipitate due to a misfit between the size of the structure of the matrix and precipitate. The amount of ΔG_s is dependent on the amount of the coherency between the precipitate and the matrix. ΔG_v is negative and stabilizes the nuclei. On the other hand, G_s is positive and destabilizes the nuclei. Therefore the total free energy for precipitation of a volume of V of the precipitate γ' inside a matrix of γ will be:

$$\Delta G_t = -V\Delta G_v + A\sigma + V\Delta G_s \tag{1.34}$$

For a spherical shape of precipitate with radius of curvature r, the equation takes the form as:

$$\Delta G_t = -\frac{4}{3}\pi r^3(\Delta G_v - V\Delta G_s) + 4\pi r^2\sigma \tag{1.35}$$

The variation of the terms in this equation is shown in Figure 1.23. Differentiation of the Equation 1.35 will give the critical free energy (ΔG*), known as the energy barrier for the transformation or the activation energy for nucleation [152]:

$$\Delta G^* = \frac{16\pi\sigma^3}{3(\Delta G_v - \Delta G_s)^2} \tag{1.36}$$

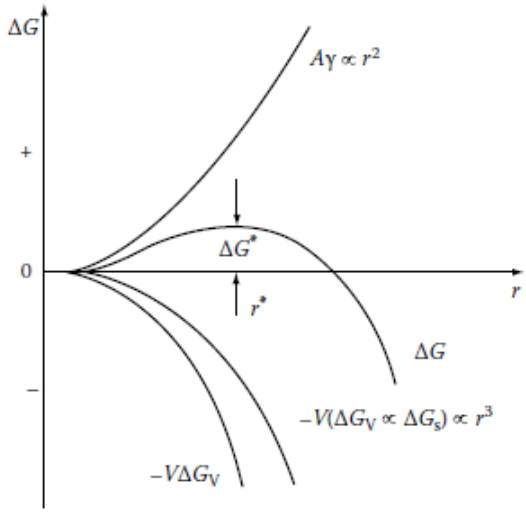

Figure 1.23. Variation of the free energy with the size of a nucleus [153].

The radius at which the total free energy of the transformation reaches a maximum is known as the critical radius, r*.

$$r^* = \frac{2\sigma}{(\Delta G_v - \Delta G_s)} \tag{1.37}$$

Embryos with the radius less than r* are unstable and will be dissolve in the matrix while the embryos with radius larger than the r* will grow as stable precipitates.

The homogenous nucleation happens very rare in real alloys as there are always heterogeneous nucleation sites originating from the heterogeneous defect sites like the

vacancies, inclusions, dislocations, grain boundaries, stacking faults and free surfaces exist in the material which increases the free energy of the material. Nucleation on these sites results in release of some free energy (ΔG_s) which reduces the activation energy required for the nucleation. However, in nickel base superalloys the γ' could form from the homogenous nucleation at a very low value of undercooling in the range of tens of degree. This is due to the low associated misfit and interfacial energy due to nucleation. The equations for the heterogeneous nucleation are the same as the homogenous nucleation, however the available nucleation sites and the activation energy is different.

1.4.2.2. Growth. If the concentration of the interface for the precipitate and the matrix is c_p and c_m respectively, the mass balance equation for the diffusive interface could be written as following [154].

$$\vartheta\left(c_p - c_m\right) = D\nabla c \tag{1.38}$$

where ϑ is the interface velocity, D is the diffusivity of the components in the matrix and ∇c is the concentration gradient of the element in the interface. This equation has been solved analytically [154], and the growth rate is defined as:

$$v = \frac{2D\lambda^2}{R} \tag{1.39}$$

where R is the radius of the precipitate and λ is defined as following:

$$2\lambda^2 - 2\lambda^3\sqrt{\pi}e^{\lambda^2}\mathrm{erfc}(\lambda) = \Omega \tag{1.40}$$

where $\Omega = \frac{(c^M - c^I)}{(c^P - c^I)}$ is the dimensionless supersaturation.

By introducing an effective diffusion distance, Equation 1.40 is rewritten as:

$$\vartheta\left(c_p - c_m\right) = \frac{D\,(c_0 - c_m)}{d} \tag{1.41}$$

and d could be written as:

$$d=\frac{\Omega R}{2\lambda^2} \tag{1.42}$$

The term $\frac{\Omega}{2\lambda^2}$ is shown with ξ and is the adjustment factor for the diffusion distance. By inserting Equation 1.42 in Equation 1.41, the following formula is obtained:

$$\vartheta\left(c_p-c_m\right)=\frac{D(c_0-c_m)}{\xi R} \tag{1.43}$$

The approach for solving the diffusional transformation in the interface of dilute binary alloys has been extended and modified by Chen, Jeppsson, and Agren for the growth of precipitates in multicomponent alloys [154]. This approach is adopted for the TC-Prisma software. In modeling of the growth by TC-Prisma, a spherical particle of stoichiometric composition is assumed under the local equilibrium condition. The governing equations are given in the following. This approach considers the cross diffusional terms in the diffusivity matrix and allows for high supersaturation in the interface. Large supersaturations occur when there are elements with very low diffusivities in the matrix. The flux balance for the solutes in the interface between the matrix and the precipitate could be written as following:

$$\vartheta\left(c_i^p-c_i^m\right)=\sum_{j=1}^{n-1} D_{ij}\nabla c_j \tag{1.44}$$

where ϑ is the interface velocity, D_{ij} is the diffusivity of the components in the matrix and $\nabla c_j$is the concentration gradient of the element in the interface. The indices i and j vary between 1and n-1 since there are n independent component in the n-component system. The diffusivity matrix is composed of the thermodynamic and kinetic parameters as following:

$$\vartheta\left(c_i^p-c_i^m\right)=\sum_{j=1}^{n-1} D_{ij}\nabla c_j \tag{1.45}$$

where M_{ij} is the mobility and $\frac{\partial \mu_j}{\partial c_k}$ is the thermodynamic term related to the gradient of the chemical potential term in the interface. Therefore, there will be n-1 equation for the n component system to be solved. However, the number of the unknowns is 2n-1. Other sets of equations will come from the local equilibrium assumption at the interface.

$$\mu_i^p = \mu_i^m + \frac{2\delta V_m}{R} \tag{1.46}$$

where μ_i^p and μ_i^m are the chemical potential of the element i in the precipitate and matrix respectively. The second term in the left hand of Equation 1.46 comes from the Gibbs-Thomson effect due to the pressure difference across the sides of a precipitate with radius R and its effect on the free energy of the precipitate.

By assuming the effective diffusion distance depends only on its superstition factor, a general equation similar to Equation 1.43 is obtained for the alloy with n elements:

$$\vartheta\left(c_i^p - c_i^m\right) = \sum_{j=1}^{n-1} \frac{D_{ij}(c_j^0 - c_j^i)}{\xi_{ij} R} \tag{1.47}$$

By inserting Equation 1.41, we get the equation as:

$$\vartheta\left(c_i^p - c_i^m\right) = \frac{c_i^I M_i(\mu_i^m - \mu_i^I)}{\xi_{ij} R} \tag{1.48}$$

Finally the non-liner equations of 1.48 and 1.46 are solved simultaneously for every precipitates with the radius R to render the growth of the interface.

<u>1.4.2.3. Coarsening.</u> Coarsening or Ostwald ripening happens where the large precipitates grow in the expense of shrinking and annihilating small precipitates. The driving force for the coarsening is the reduction of the free energy of the system due to decrease in the interfacial energy. In thermodynamics point of view, there is a gradient of the chemical potential in the system due to the difference in precipitates radius and related Gibbs–Thomson effect on the free energy. This leads to diffusion of solutes across the matrix

towards the larger precipitates. The formulations behind the coarsening in TC-Prisma are the same as the growth with considering the absolute value of Ω to calculate the interface velocity for all sizes of the particles. Now if r<r*, then $\mu_i^I > \mu_i^M$ and the interface velocity will be negative which will cause the precipitates to shrink. The reverse is true if r>r* and this particles will grow. In summary, the dissolution is the reverse of the growth and coarsening is concurrent with the nucleation and growth or as a dominant process in the final stage of the phase transformation.

Ardell and Nicholson studied the coarsening of the γ' (Ni_3Al) precipitates in the binary Ni-Al and showed that the coarsening could start at low temperatures as 645°C [155]. The addition of the other alloying elements influences the coarsening rate in multicomponent alloys. For example, the work of Giamei and Anton on the effect of refractory elements on the coarsening of Ni base sueralloys proved that Re could reduce the coarsening rate considerably [155].

Coarsening phenomenon has been formulated by Lifshitz and Slyozov [9], and by Wagner [10] under the name of LSW theory. Coarsening kinetics is then determined by solving the classical equation of the coarsening as following [156]:

$$d^n - d_0^n = kt \tag{1.49}$$

where d_0 is the initial precipitates size and d is the average precipitates size at time t. k is a constant, which considers the thermodynamics and kinetics effects and is described by the following formula:

$$k = \frac{8(\sigma V_m^2 D c_e)}{9RT} \tag{1.50}$$

where σ is the interfacial energy, V_m is the volume fraction of the precipitate, C_e is the equilibrium concentration of the precipitates, D is the diffusivity, R is the gas constant, T is the temperature, and t is the time.

Equation 1.50 shows that the coarsening rate constant k is directly proportional to the diffusivity of solutes in the matrix. Therefore, addition of elements with low diffusivity in the matrix, like Re, could have considerable impact on reducing the coarsening rate in superalloys. The parameters in this equation are very hard to determine experimentally.
The diffusivity has the Arrhenius relation with temperature.

$$D=D_0 \exp\left(-\frac{Q}{RT}\right) \tag{1.51}$$

where Q is the activation energy for diffusion of the solutes. If the equilibrium concentration of the solute does not vary with the aging temperature, the activation energy (Q) could be determined by the slope of the plot of the Log (k) with (1/T) using Equation 1.51. The value of the Q for any special alloy could be determined experimentally by calculating the coarsening rate in at least two different temperatures. This value has been shown [157] to generally vary between 250 and 290kJ/mole for the Ni base superalloys. This value is close to the activation energy for diffusion of the Al in pure Ni [158]. The parameters in Equation 1.50 are very hard to determine and for this reason, very little data is available in the literature. For example, the values for the interfacial energy for precipitation of γ' inside matrix for the Ni base superalloys varies between 6 to 90mJm^{-2} [159]. It is dependent on a large number of parameters like the volume fraction of precipitates, temperature, and concentration of the matrix. The solid solubility of the elements in the matrix is also hard to be determined experimentally. An example of the analytical determination of the coarsening rate is performed by J. Lapin on the CMSX-4. Due to a limited data on CMSX-4, they used the values of the solid solubility of the Al for Udimet 700 alloy and relation for the interfacial energy variation with temperature of the Nimonic 115 alloy. Finally, they determined the diffusion coefficient by fitting their data to the experimental coarsening plot. Although their results showed a very good fitting of the experimental and analytical results, since the diffusion coefficient is obtained by fitting the analytical and experimental results and using the interfacial energy and solid solubility for different alloys, it could be considered in best a way to fit the data.

The coarsening, involves diffusional redistribution of different alloying elements, so the effect of the alloying elements and their diffusion rate is of great importance in determining the kinetics of the coarsening. The closed form of the analytical solution for

the diffusion controlled dissolution and growth of the precipitates is not possible for the multicomponent alloys. Therefore, numerical modeling is required with linking to the thermodynamic property database to solve the time dependent dissolution and evolution of the precipitates. All of these modeling steps are embedded in the TC-Prisma software [160]. TC-Prisma solves the equations for concurrent nucleation, growth/dissolution, and coarsening under using Langer-Schwartz theory and the Kampmann-Wagner numerical approach. A set of equations for nucleation and growth rates of the particles are solved as a function of the particle size distribution (PSD) to yield the temporal evolution of the size and particle size density of the precipitates during the precipitation stage. By discretizing the PSD and solving the continuity and mass balance equations, the time dependent evolution of the PSD, number density, mean radius and the volume fraction of the precipitates are determined. The PSD equations are nonlinear and need to be solved numerically. TC-Prisma is integrated with the Thermo-Calc software to get all necessary thermodynamics and kinetics data such as the driving force for the nucleation, atomic motilities and diffusivities in different phases, and interface composition. More details about the nucleation, growth and coarsening modeling could be found in [154,161,162].

1.5. Creep Rupture Behavior of Single Crystal Ni Base Superalloys

Creep is a time dependent plastic deformation which occurs at a stress lower than the yield strength of a material provided that the temperature is high enough to let the diffusion and/or dislocations motion occurs [163].

A typical creep curve in single crystals is shown in Figure 1.24 and shows 4 regions.

(i) An initial sudden strain that happens as the load is applied. This term is more elastic but depending on the level of the applied load, plastic strain also may contribute to it.

(ii) A region of primary creep where the strain rate decreases with time. Dislocations are created and move to deform the material but strain hardening mechanisms are activated as dislocations form a three-dimensional networks [164].

(iii) A steady state region, where hardening processes are balanced by dynamic recovery processes and the material deforms under a nearly constant strain rate. This stage of the creep curve is the most important step in creep that dominates the creep life. In the alloys where no rupture expected, the steady state creep rate is considered in the design stage, which is equal to accumulation of the creep stress with service time. The final portion of the creep curve is known as the tertiary stage where the strain rate increases. The localized failure known as necking occurs due to accumulation of the voids and finally the rupture occurs at the region of the necking.

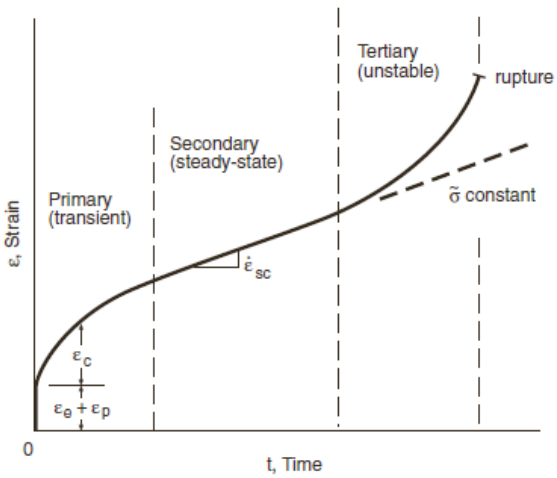

Figure 1.24. A typical strain versus time plot in single crystal superalloys [79].

The stress and temperature could shorten or lengthen each of the regions defined. Increasing the level of stress increases the strain rate and rupture occurs at lower times. The steady state creep also decreases. The same is true for the temperature and the effects are illustrated for a fourth generation single crystal alloy containing 4.5wt% Re and 3wt% Ru in Figures 1.25a and b.

Since the main strengthening mechanism in single crystal Ni base superalloys is due to the ordered γ' phase, the volume fraction of it has a great impact on the creep resistance. It has been generally approved that the optimum volume fraction of the γ' to attain the high creep resistivity is between 55 to 70vol% [98,165,166].

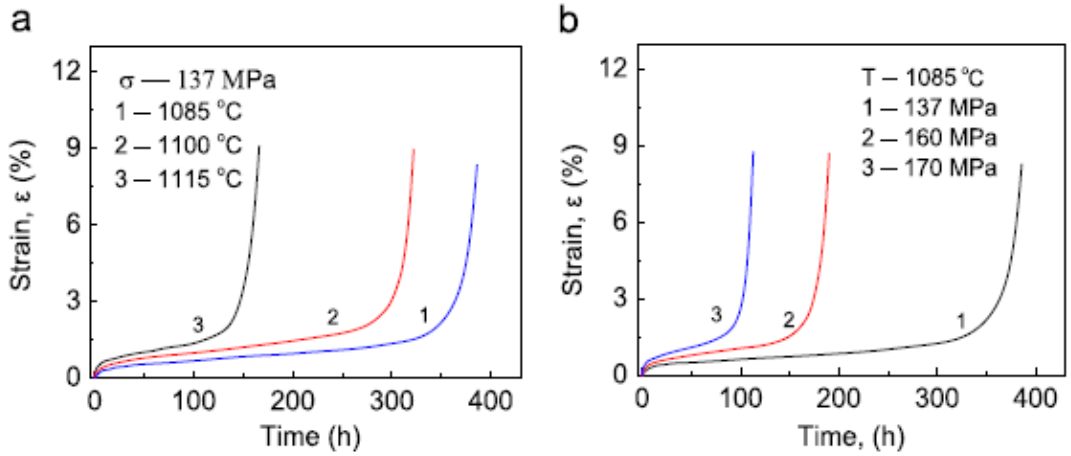

Figure 1.25. Effect of the temperature at constant stress of 137Mpa (a), and effect of stress at constant temperature of 1085°C (b), on the shape of the creep curve of a fourth generation single crystal alloy containing 4.5wt% Re and 3wt% Ru [167].

1.6. Objectives

The purpose of this study is to develop knowledge and capabilities for designing, production, and characterization of high temperature alloys, specifically the Ni base superalloys.

Objectives of this study are itemized as following:

- Utilize integrated computational materials engineering (ICME) tools for alloy design of third generation Ni base superalloys. To this end, a combined Neural Network (NN) – PHAse COMPutation (PHACOMP) – CALculation of PHAse Diagrams (CALPHAD) method is used, which is an original approach in the field.

- Produce the designed alloy as single crystal with conventional vertical Bridgman (VB) and novel vertical Bridgman with submerged baffle (VBSB) methods. The latter one is used for the first time in the world for superalloy single crystal growth.

- Compare crystal characteristics obtained via the two methods (VB and VBSB) to determine the effect of baffle.

- Apply full heat treatment cycle to the alloy.
- Determine the creep life of the alloy.
- Fully characterize the microstructure after single crystal growth and heat treatments.

2. MATERIALS AND METHODS

2.1. Alloy Design of Ni Base Superalloys

2.1.1. Neural Network Modeling

Neural network approach is used to model the density and rupture strength of the nickel base single crystal superalloys. A Ni base superalloy database for the training and testing of the neural network model is formed by collecting data from the open literature, articles and patents. The database contains 260 single crystal superalloys for the density modeling and 1250 datasets for the rupture time. The test temperature ranges from 800 to 1200 ^{o}C and the test stress ranges from 30 to 845 MPa in the alloy database for the rupture time which itself ranges from 15 to 1050 hours. Eighty percent of the literature data is selected randomly to train the network and the remaining twenty percent is used to test the performance of the trained network. The input data are first linearly normalized in the range of -0.5 to 0.5. The output data are normalized in the range of 0.2 to 0.6. Normalization equalizes the influence of the variation of the network weights on the input variables, which increases the efficiency of the backpropagation algorithm in adjusting the weights of the connections [168]. For the NN modeling, sixty thousand (60,000) alloy compositions are generated, limited only by the allowed number of rows in the excel spreadsheet. The volume fraction of the γ' phase [101], and the M_d value [113] for each alloy in the generated design space are determined according to PHACOMP model.

Considering the input data range in Table 2.1, an alloy design space can cover infinite number of alloy datasets depending on the resolution.

Table 2.1. Composition ranges used to generate the alloy design space.

Element	Ni	Re	Cr	W	Co	Mo	Hf	Ti	Al	Ta
Range, wt.%	Bal.	0-6	0-10	0-10	0-10	0.6	0.1	1.0	3.7	0-10

For the NN modeling, sixty thousand (60,000) datasets are generated randomly, which reasonably covers the entire alloy design space for the rupture strength at 982°C and 248MPa.

The MLP architectures of 10-8-1 and 14-10-1 are developed for modeling the density and rupture time, respectively. The network has 10 input nodes (concentration of 10 alloying elements) for density modeling and 14 input nodes (concentration of 10 alloying elements, volume fraction of the γ' phase, density, temperature, and stress) for rupture time modeling. The number of neurons (nodes) for the hidden layer (8 for the density and 10 for the rupture time) is selected based on the error level of the network. The RMS (root mean square) error of the network is determined for the training and testing of the network for both the density and rupture life estimation as seen in Figs. 2.1 (a) and (b). It is seen that by increasing the number of nodes in the hidden layer, the network error decreases. Beyond 8 nodes in the density modeling and 10 nodes in the rupture time modeling, the error of the network is stable.

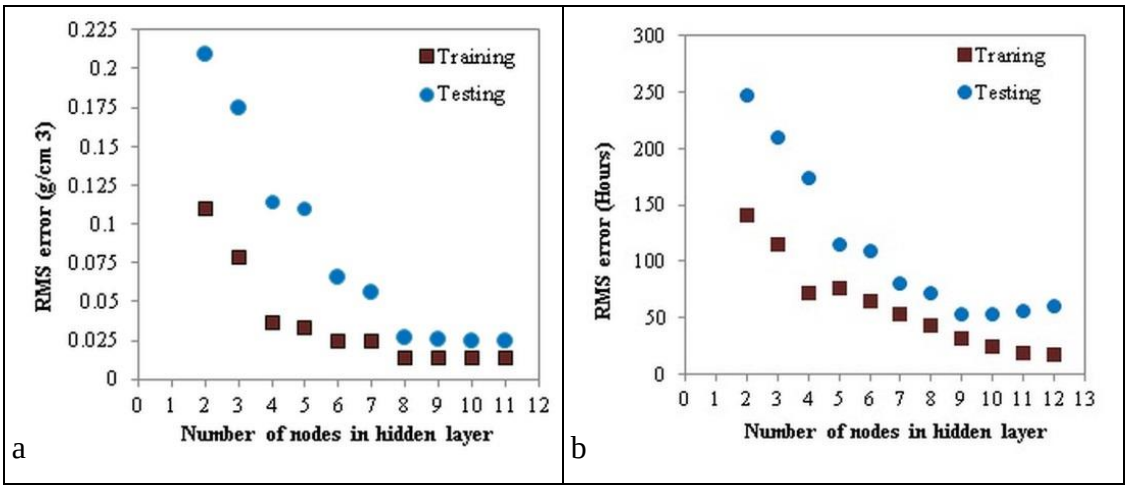

Figure 2.1. Root mean square error for training and testing the networks with different number of hidden nodes for estimation of a) density, and b) rupture time.

2.1.2. CALPHAD Modeling

CALPHAD is a method for modeling the thermodynamic properties of various phases in multicomponent systems. It is based on reliable databases of experimentally

determined thermodynamics properties of binary and ternary systems. Since the modern single crystal superalloys contain a large number of the elements, the thermodynamic data is rarely available for modeling the evolution of phases at different temperatures. The CALPHAD is a powerful tool which allows for estimation of the thermodynamic data from those of the binary and ternary alloys by extrapolations to the higher order systems [169]. Appropriate software packages are developed in this context like the Thermo-Calc [12], JMatPro [13], and Pandat [14] among which the Thermo-Calc is the most preferred choice by people in the academy and industry. Thermo-Calc software was used in this study to model the solidification of the alloys. The equilibrium and Scheil solidification modules were used and the results were compared. From the Scheil solidification module, the concentrations of the alloying elements were calculated for the solid and liquid phases.

The Dictra is another software [170] developed by Thermo-Calc company that simulates the diffusion controlled transformations by solving the diffusion equations for a multicomponent system. Other than the thermodynamic database (TCNI7 used in this study), which is used in Thermo-Calc, the kinetic database (MOBNI3 used in this study) is used in Dictra. The kinetic database includes the atomic mobility information for individual elements in different phases. It is used in this study for modeling the homogenization heat treatment of the grown alloys.

TC-Prisma precipitation software [160] developed jointly by Thermo-Calc Software AB, Stockholm, Sweden and Questek Innovations, Northwestern University, Evanston, IL, USA. TC-Prisma is a user-friendly graphical approach, which has specialized applications in modeling the concurrent solid-state nucleation, growth, and coarsening of precipitates. It is based on using Langer-Schwartz theory and the Kampmann-Wagner numerical approach [66,171]. In this work, it is used for modeling the aging heat treatment of the grown alloys. Same as Dictra, the TC-Prisma uses both the thermodynamic (TCNI7) and kinetic (MOBNI3) databases.

2.2. Single Crystal Growth of Designed Ni Base Suepralloys

2.2.1. Experimental Setup

Before growing the single crystals in this study, a thorough study was done to analyze the solidification behavior of the alloys in the designed furnace. The main question was that if the withdrawal velocity is equal to the solidification velocity or not and if they were different how the difference varies by the withdrawal velocity. To answer these questions, a set of experiments were designed to measure the solidification velocity at different withdrawal velocities. The alloy CMSX-4 was used in the experiments. The s/l interface displacement was determined during solidification with the crucible pulling velocities of 6, 12, 18, and 30 cm/h. A 3mm diameter alumina dipstick was immersed in the melt. At certain time intervals during the solidification, this stick was pushed down until it touched the solid. With respect to a reference point in the solidification system, it was possible to determine the current interface position. The temperature also was measured during solidification by a thermocouple fixed at the initial s/l interface position.

2.2.2. Growth of the Alloys by the VB and VBSB Methods

Based on the results of the NN-PHACOMP and CALPHAD, an alloy, labeled ERBALLOY, with the following chemical composition was developed and solidified in the form of single crystal alloys.

Table 2.2. Table chemical composition of the designed alloy (ERBALLOY).

Element→ Alloy↓	Ni	Cr	Co	Re	W	Mo	Hf	Al	Ta	Ti
ERBALLOY	Bal.	7.1	9.31	4.98	6.43	0.5	-	5.06	5.5	0.73

The designed alloy was solidified by two methods, vertical Bridgman (VB) and the vertical Bridgman with a submerged baffle (VBSB), with the velocities of 12 and 30 cm/h in each method. Thus, four samples were solidified. The grown single crystal bars had a diameter of 15 mm and a length of 70 mm. A bottom seeding technique was used. A single

crystal cylindrical seed with <001> orientation was placed at the bottom of a 99.8 % purity alumina crucible, and a polycrystalline alloy charge was placed on top of the seed. The seed diameter was equal to the crucible diameter. The alumina crucible was encased within a graphite tube to prevent cracking of the alumina and to protect the system for any liquid metal leaks, but luckily, no such problems occurred. The melting/solidification were carried out inside a four-zone resistive heating furnace and in a high purity (99.999 %), continuously flowing argon atmosphere. The furnace was first heated to 800 °C under ~ 10^{-2}mBar vacuum and then purged with argon three times to remove degassing impurities. Afterwards, the four zones were heated to their set temperatures to establish a stable, positive temperature gradient in the system. Then, the crucible, initially staying in the cold zone, was elevated into the hot zone of the furnace until all of the charge and a portion (~ 5 mm) of the seed melted. The melting/solidification and position of the interface were controlled by four thermocouples, which were placed at different longitudinal positions on the graphite encasing. After melting, the system was put to rest for about 20 minutes. Then, the solidification was started by pulling down the crucible under a constant temperature gradient of 24 °C/cm with two different pulling velocities of 12 and 30 cm/h. The solidified bars had a length of 70 mm above the initial s/l interface. In case of the VBSB solidifications, a specially produced baffle made of a 99.8 % purity alumina was inserted in the melt, and the effective melt height (h) between the baffle and the solidifying interface was set to 10 mm, see Figure 1.21. There was a 1mm annular gap between the baffle and the crucible. The baffle was fixed to the top of the solidification chamber via a high purity alumina rod.

After solidification, the samples were longitudinally halved and one of them was further sectioned transversely at distances of -5, 0, 5, 10, 15, 25, 35, and 45 mm from the initial solid/liquid (s/l) interface (Figure 2.2). The grain scale structures of the samples were characterized by an optical microscope. After grinding and polishing, unetched sample images were used to determine the area fraction of the pores on transverse sections using the ImageJ software [172], and their length averaged value was used as an overall estimate of the microporosity in a sample. This averaging was justified on the basis that the pore content did not vary much along a solidified bar, although equivalent pore diameter slightly increased. No distinction was made between the shrinkage and gas porosities in the analysis. Afterwards, the samples were etched with a solution of 4g $CuSO_4$ + 20cc HCl +

20cc H_2O. The longitudinal cuts were used to determine the length of the mushy zone and melt-back transition region, and the transverse cuts were used to determine the dendrite core size and primary dendrite arm spacing. When determining lengths of the mushy zone and melt-back transition region, the longitudinal cuts of the samples were scanned from the s/l interface down to the seed base by an optical microscope. The transition region was characterized by melted/blunted and sometimes broken/bent secondary dendrite arms. It started from the s/l interface and extended down toward the seed base to a point where the blunted secondary dendrite arms disappeared. From this point downward, the local melting in the interdendritic region in the seed was still seen until a distance from the seed base. This point marked the end of the mushy zone, which also started from the s/l interface and included the transition region.

To assess the orientation of the dendrites, 10 mm samples were cut from the longitudinal section of the cast samples and then prepared by polishing for the analysis using x-ray diffraction.

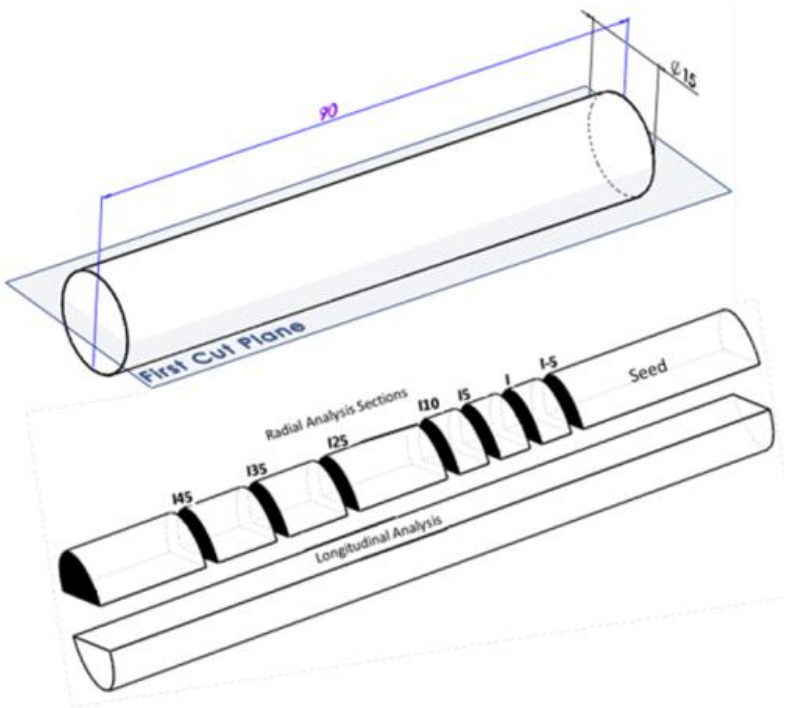

Figure 2.2. Schematic of the transverse and longitudinal cut sections of the samples.

2.3. Heat Treatment of the Grown Alloys

The heat treatment of the ERBALLOY includes the solution and subsequent aging heat treatments. The solution heat treatment is sometimes used as homogenizing heat treatment, which dissolves the existing precipitates and carbides into the matrix and removes the solidification induced macro and microsegregation of the alloying elements. The aging heat treatment on the other hand is to precipitate uniform and modified distribution of the strengthening γ' phases. The experimental details of these two processes are described in the following.

2.3.1. Solution Treatments

An optimum solution heat treatment is designed for the ERBALLOY to homogenize the microstructure and to give a uniform distribution of the γ' precipitates in the microstructure. Since the ERBALLOY is developed based on the CMSX-4, the heat treatments are benchmarked to that of the CMSX-4. A typical solution heat treatment for the CMSX-4 alloy involves heating the alloy 8 hours at 1314 ˚C [173]. The aging is accomplished in two steps. The primary aging is carried out at 1140 ˚C for 4 hours and the secondary aging at 870 ˚C for 16 h. Considering the critical temperatures (liquidus, solidus, and γ' solvus) determined by Thermo-Calc software, six samples are solution treated by different procedures (Table 2.3), and the related samples are labeled from S1 to S6.

Table 2.3. Solution treatment procedures

S1	1270 ˚C/4 hours,
S2	1290 ˚C/4 hours
S3	1315 ˚C/4 hours,
S4	1280 ˚C/2 hours + 1290 ˚C/2 hours + 1315 ˚C/2 hours + 1320 ˚C/2 hours,
S5	1280 ˚C/2 hours + 1290 ˚C/3 hours + 1315 ˚C/5 hours.
S6	1280 ˚C/2 hours + 1290 ˚C/2 hours +1300 ˚C/2 hours + 1305 ˚C/2 hours + 1315 ˚C/4 hours.

To determine the extent of the segregation, the chemical composition is analyzed at 5 points along an SDA by electron probe microanalysis (EPMA). Figure 2.3 shows a schematic of the SDA with the points marked 1 to 5 indicating points of chemical

composition measurements. A new solution treatment schedule is designed iteratively after analyzing the microstructure and segregation in a previous sample. Finally, a solution treatment of 1280˚C/2 h + 1290˚C/2h +1300˚C/2h + 1305˚C/2h + 1315˚C/4h is chosen, which dissolves all of the γ' islands in the interdendritic region and renders the segregation coefficient close to unity for the alloying elements. This solution treatment is adopted for the grown samples for aging.

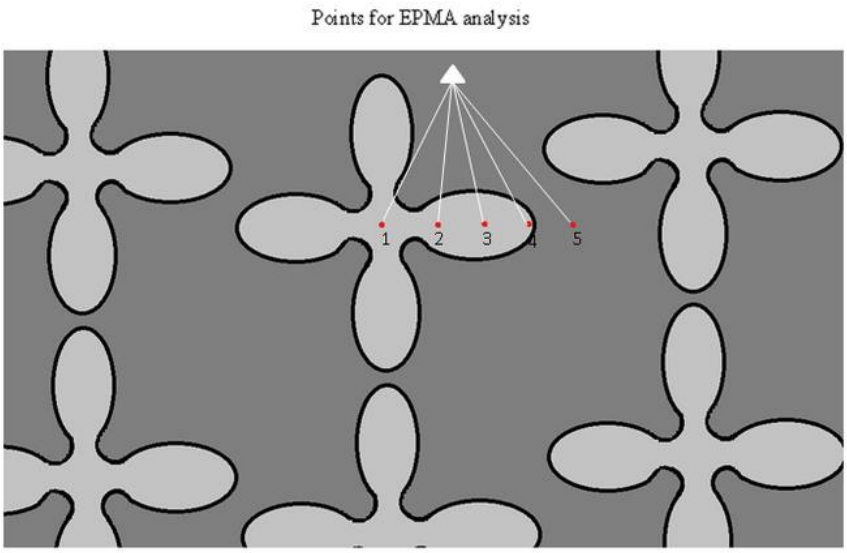

Figure 2.3. Schematic of dendritic pattern in the microstructure of a single crystal superalloy with marked areas showing locations of chemical composition measurements with electron probe microanalysis (EPMA).

In all of the heat treatment processes, the samples are encapsulated inside a quartz tube in vacuum. Samples are first inserted inside a quartz tube and then one end of the quartz tube is sealed by oxyacetylene torch. Moreover, to protect the samples from excessive heating, the samples are rapped with a stainless steel sheet. Then, the tube is purged with 99.999% pure argon gas three times by successive argon filling and 10 minutes vacuuming each time. The open end of the quartz tube is then closed while the tube is under vacuum. This creative method allows environmental protection to samples during high temperature heat treatments in a time and cost-effective manner instead of using expensive vacuum heat treatment furnaces. After the solution treatment, the samples

are quenched into water at room temperature. The mentioned sealing process is repeated for every sample for the subsequent primary and secondary aging heat treatments.

For the grown single crystal samples in this current study, solution heat treatment procedure is developed to achieve a homogenous microstructure with all the γ' eutectic islands in the interdendritic regions dissolved. This process also reduces the segregation of the elements between the dendrite core and the interdendritic region. Following this treatment, the γ' is dissolved in the matrix and in a subsequent lower temperature holding below the γ' solvus temperature, new uniformly dispersed γ' precipitates are formed inside the γ matrix. Mass transport by bulk diffusion also acts to reduce the scale and extent of the microsegregation and eutectic regions that are inherited from the casting process.

2.3.2. Aging Treatments

The primary aging treatment is accomplished at 1140˚C for 6 hours, and the secondary aging treatment is accomplished at 870˚C for various duration of times to study the coarsening behavior of the γ' precipitates. Samples are again sealed into a quartz tube under vacuum and argon as for the solution treatment process. This was to protect the sample from oxidation. After aging process, the samples were ground and polished for observation of the microstructure with the SEM. Moreover, the concentration profile of the elements was determined by EPMA for observation of the elementals segregation.

2.4. Creep Rupture Behavior of the Grown Alloys

Three samples (one VB12.CMSX-4, and two VB12.ERBALLOY) were machined to dimensions shown in Figure 2.4 adopted from ASTM E139. Due to a hardness of 40 HRC, the machining of the samples was very hard and finally they were machined on a lathe equipped with a grinding disk at a very low speed. The samples were then solution treated according to S6. Following the solution treatment, the samples were aged at 1140˚C for 6 hours and 870˚C for 24 hours.

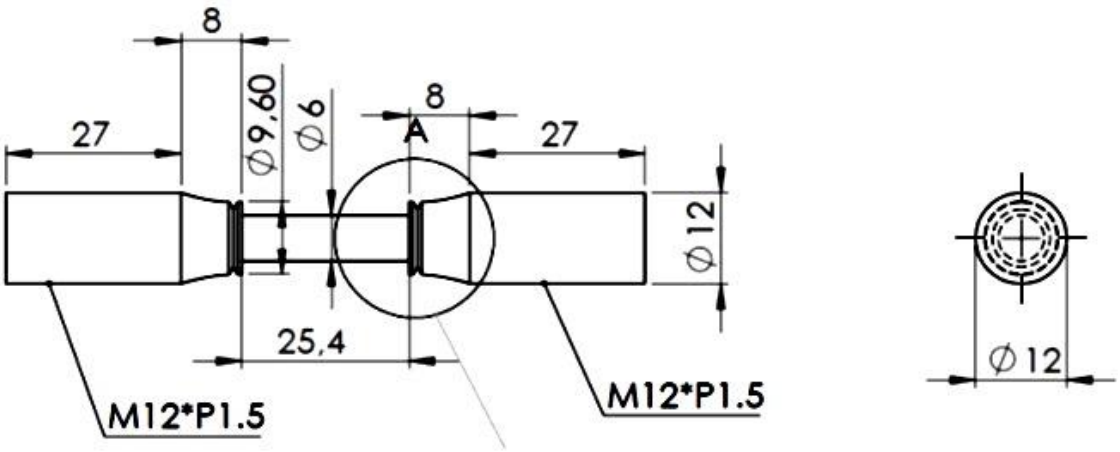

Figure 2.4. The drawing of the machined sample for the creep test.

Figure 2.5 shows a picture of the rupture test equipment. An Instron model 5982 model test system is used for the creep tests. The system is equipped with a three-zone furnace.

Figure 2.5. Picture of the creep test equipment.

A set up is prepared for the creep test under inert argon gas. For this reason, the creep testing system is equipped with a quartz tube to protect the sample from oxidation by purging argon gas from the bottom of the quartz tube. This setup provides means to conduct experiments under inert atmosphere. Holes were drilled in the middle of the quartz tube for inserting the extensometer to touch the sample. The extensimeter was cooled down during the test by a chiller to prevent the high temperature damage. The exact temperature of the sample in the middle of the furnace was monitored separately by a K-type thermocouple inserted at that position. After heating the sample to a desired temperature, the constant load creep tests are performed at 982°C under the load of 8008 N that generates 248MPa stress and 1100°C under the load of 3875N that generates 137MPa stress at the reduced section of the samples.

2.5. Composition and Microstructure Characterization

After growing the single crystals, the dendritic microstructure, the length of the mushy and met-back region and the microporosity content of the samples is analyzed by using the optical microscopy. The SEM photos of the microstructure of the as-cast samples are obtained at the dendrites core and interdendritic region to analyze the distribution and morphology and the area fraction of the precipitates. The concentration profile of the alloying elements is determined by the Electron probe microanalysis (EPMA).

The microstructure analysis of the solution treated and aged samples is characterized by the SEM. Similar to the cast samples, the size and morphology of the precipitates are determined by analyzing the SEM photos with ImageJ software [172]. The segregation profile is determined by analyzing the concentration of the alloying elements from dendrite core to the interdendritic region by EPMA.

3. RESULTS AND DISCUSSION

3.1. Alloy Design of Ni Base Superalloys

This chapter discusses the results obtained for the alloy design of the single crystal Ni base superalloys by combination of the neural network, PHACOMP, and CALPHAD approaches. First, the results of modeling the density of the alloys by neural network are described. It then continues by the results of modeling the rupture strength, volume fraction of the γ', and susceptibility for TCP phase formation by combined NN-PHACOMP methods. Finally, the results of modeling the solidification, homogenization heat treatment, and aging heat treatment by CALPHAD tools (Thermo-Calc, Dictra, and TC-Prisma) are presented and discussed.

3.1.1. Neural Network Modeling of the Density and Rupture Life

A major objective in the design of superalloys used in hot sections of the turbine engines is to come up with alloy compositions that provide a high creep life with a low alloy density and no TCP phases. There are other equally important parameters like the oxidation resistance, hot corrosion resistance, castability, and cost which are affected by the chemical composition of the alloy [15,30] but they are out of the scope of this study. The density of an alloy is calculated simply based on the amount of the elements forming the alloy, while the creep life is related to the elements in the alloy, volume fraction of the γ', density, and M_d values.

The training and testing of the network are accomplished by comparing the predicted values and the experimental ones, Figure 3.1. It is apparent that the neural network model performs very well in modeling the density (Figures 3.1a and b) and rupture time Figure 3.1c and d with the confidence levels of 99.3% and 92.7%, respectively. Clearly, the prediction accuracy for the rupture time is lower. The rupture time depends on other parameters (i.e.; temperature and stress) than the chemistry of the alloy, which increases the sensitivity of the experiments and increases the fluctuations in the experimental data.

Since the input data is gathered from published papers and patents, the unknown inaccuracy of the input data is conveyed to the network.

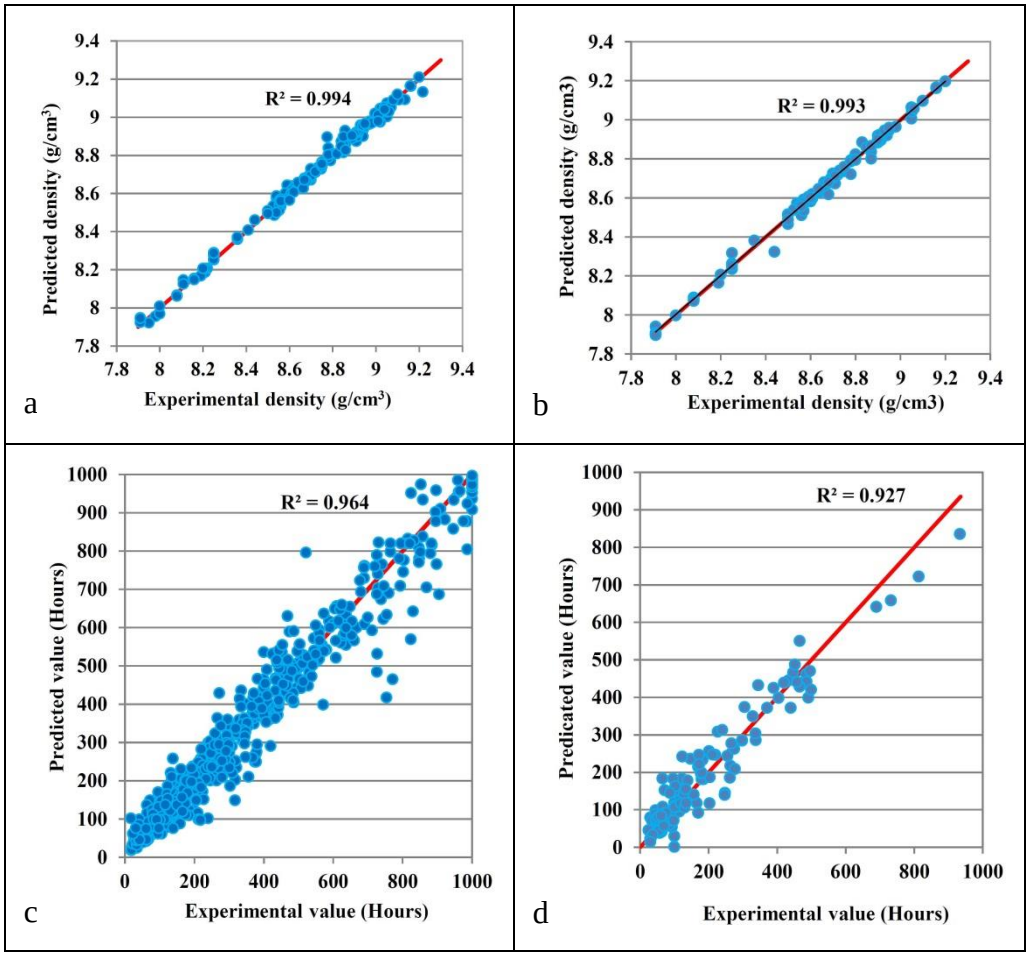

Figure 3.1. The predicted density is plotted against the known density after training (a), and testing (b) of the network. The results of the training (c), and testing the network (d), compared with experimental values for rupture time.

The density, volume fraction of the γ', and M_d distributions of the alloys in the entire design space are shown in Figure 3.2. The spread is between 8 and 9.6 g/cm^3 for the density, 40 and 95% for the γ' volume fraction and 0.9 and 1.08 eV for M_d. The respective peaks occur at 8.5-8.7g/cm^3, 60-65%, and 0.97-0.98 eV. These histograms show symmetric distributions of the input data, and the typical (peak) values match the properties of the commonly known single crystal superalloys, which indicate a well-representing alloy design space.

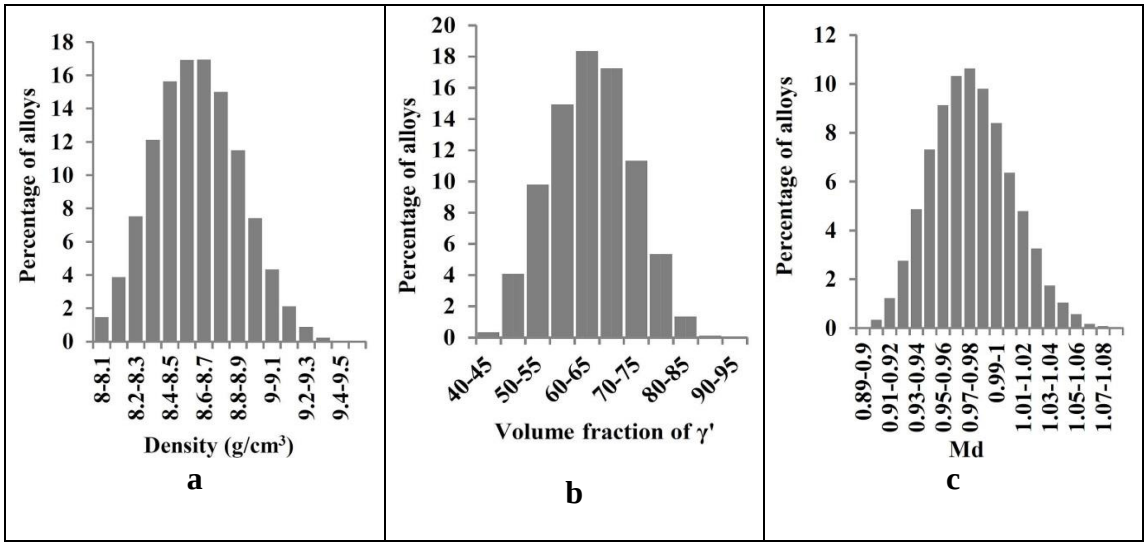

Figure 3.2. The percentage of the alloys versus density (a), volume fraction of γ' (b), and M_d (c).

In the following, the effect of the major alloying elements (Re, Cr, Ta/W, or Al) on the density, TCP phase formation, and creep life will be disused in detail:

3.1.1.1. Re. Among the alloying elements in the composition of superalloys, the positive effect of expensive Re is dominant in the rupture life, and for this reason it has been added in the second (3wt% Re) and third (5–6wt% Re) generation nickel base single crystal superalloys [174]. However, due to its limited resources in the world and consequently its high price, recent activities have focused on developing high creep resistant alloys with low levels of Re [175]. Thus, the fourth, fifth, and sixth generation alloys have lower Re, replaced with Ru in their compositions [53,54]. This study, however, focuses on the first, second, and third generation alloys as they are the most widely used industrial superalloys.

To investigate the effect of Re on the creep resistance of the single crystal Ni base superalloys, the composition space for the rupture time at 982˚C and 248 MPa versus density, volume fraction of γ' and M_d are plotted in a series of scatter plots in Figure 3.3. The first raw of the figure shows the histogram of the percentage of alloys versus rupture times. The gray background regions show the entire alloy design space, and the red regions show the alloys with Re content similar to that in the 1st, 2nd, and 3rd generation single crystal superalloys in the respective columns.

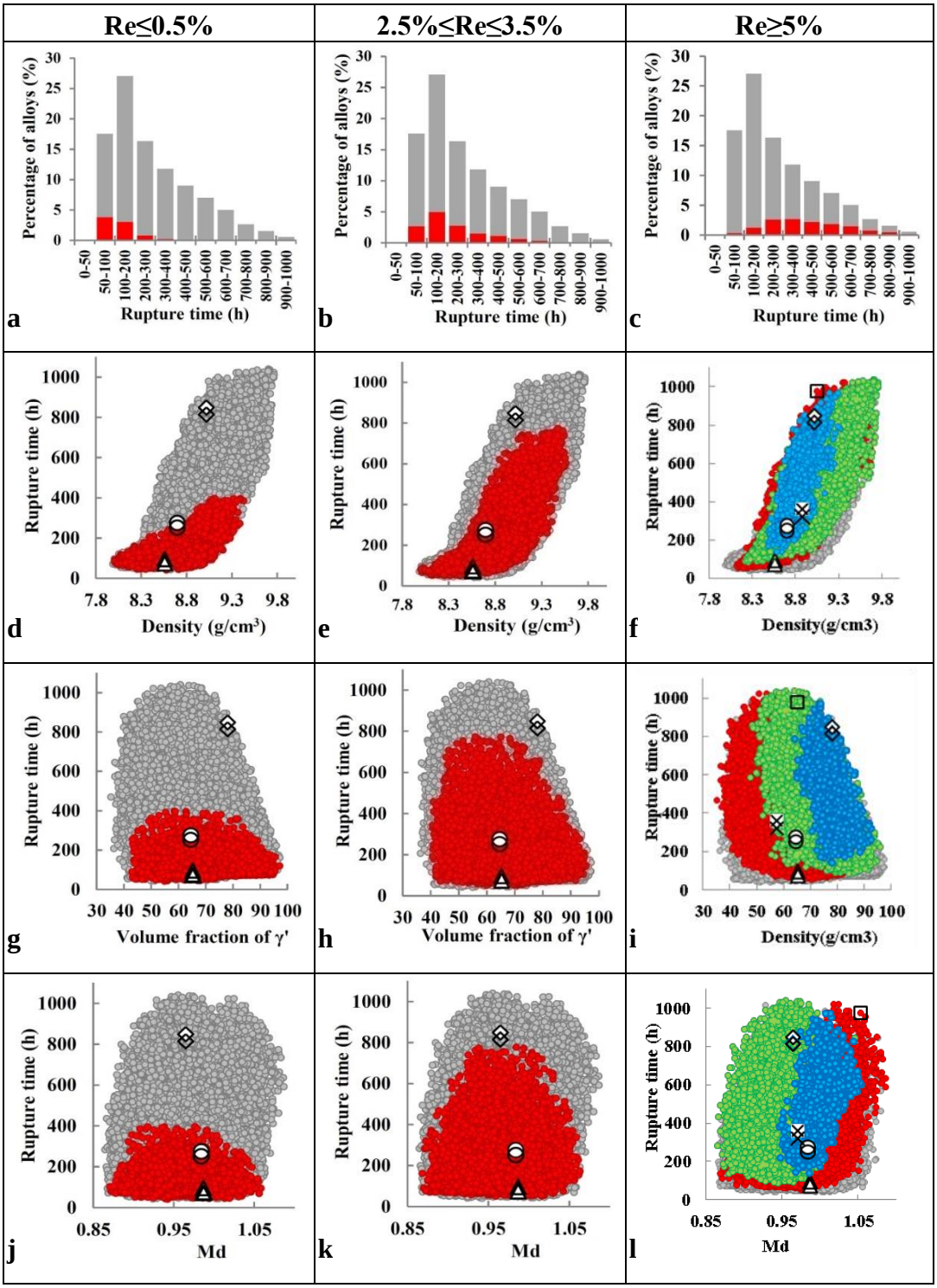

Figure 3.3. Percentage of alloys in given rupture time ranges are shown in (a-c). Rupture time versus density (d-f), volume fraction of γ' (g-i), and M_d (j-l) are plotted. The markings are explained in the text.

The first raw (Figure 3.3a-c) shows distribution of the alloys with respect to the rupture time for varying Re contents. While interpreting these histograms, the shape of the histogram and the maximum percentage are more important parameters than the ratio of the total red to the total gray bars. It is seen that the histograms of the rupture time do not follow a Gaussian distribution. The typical value (maximum likelihood) falls within the 100-200 hours for the overall alloy design space of this study. However, the typical value changes when alloys are classified based on their Re content (red areas). In the alloys with Re content less than 0.5, the typical value falls between 50-100MPa. By increasing the Re to the ranges between 2.5 and 3.5wt%, the typical value increases to the range of 100-200 hours. The typical value increases to 200-300 hours for the alloys with Re content greater than 5wt%. Moreover, the distribution pattern is very different between these groups of alloys tending to be more normal as the Re content increases.

Figures 3.3d-f shows an overall sigmoid relationship between the rupture life and the alloy density with a large variation in both the axes. The overall trend of the data indicates about 1000 hours increase in the creep life for a 1 g/cm^3 density rise. However, the creep life exists in a large band for a given density. Closeness of the experimental data (filled symbols) [176–178] presented in the design space with the neural network predictions (empty symbols) for well-known first (CMSX-2: triangle), second (CMSX-4: circle), third (CMSX-10: diamond) generation commercial alloys and designed alloy in this study (ERBALLOY: multiplication), displays the prediction accuracy of the neural network. The chemical composition of these alloys is presented in Table 3.1.

Table 3.1. Chemical composition of the first, second, and third generation commercial alloys (CMSX-2, CMSX-4 and CMSX-10).

Element→ Alloy↓	Ni	Cr	Co	Re	W	Mo	Hf	Al	Ta	Ti	Density (g/cm^3)
CMSX-2	Bal.	8.0	5.0	-	8.0	0.6	-	5.6	6.0	1.0	8.56
CMSX-4	Bal.	6.5	9.0	3.0	6.0	0.6	0.1	5.6	6.5	1.0	8.70
CMSX-10	Bal.	2.0	3.0	6.0	5.0	0.4	-	5.7	8.0	0.2	9.05

The rupture life increases with addition of the Re (red regions). A striking observation is, however, that alloys with a high amount of the Re (Figure 3.3c, and f) are not necessarily the best creep resistant ones and the rupture life spans a large range from about 100 to 1000 hours. This shows the unavoidable effect of the other elements than the Re, and the neural network model demonstrates this nicely.

Figures 3.3g to i show the effect of Re addition on the volume fraction of γ'. For high rupture strength alloys, the range within which the γ' volume fraction varies gets narrower. The results show that alloys with gamma prime volume fractions around 55 to 65% have higher rupture strength which is in accordance with the data published for some advanced single crystal nickel based superalloys [1,2,179]. The rupture strength decreases when moving away from these values. It is noteworthy that dependency of the rupture life on the γ' volume fraction is minimal on the low fraction boundary (left) while it is significant on the high fraction boundary (right). The role of the Re addition on the rupture life is prevalent in Figures 3.3g-i, but that on the γ' volume fraction is vague. The gray background shows the entire alloy design space, and the red regions show the alloys with different Re content. The green and light blue regions in Figures 3.3f, i, and l show respectively alloys with Re≥5% and Cr≤4% and Re≥5%, Cr≤4%, Ta≥5%, and 5≥Al ≥7%. The triangle, circle, diamond, and multiplication markings show the first (CMSX-2) [176], second (CMSX-4) [177], third (CMSX-10) [178] generation alloys and ERBALLOY, respectively. Filled symbols are experimental data and the open symbols are the neural network predictions. The square symbol in Figures 3.3f, i, and l is for Alloy X. Figures 3.3j-l show the effect of addition of Re on the M_d which is the parameter representing the propensity of an alloy to the formation of the TCP phases. The trend in the figure shows that in general, alloys with M_d value of about 0.98 yield the highest higher creep lives in the design space. Again, while the role of the Re addition on the rupture strength is obvious, it is not so for the M_d effect.

The combined effect of elements are shown for two groups of alloys in Figures 3.3 f,i, and l. The green and light blue regions show respectively alloys with Re≥5% and Cr≤4% and Re≥5%, Cr≤4%, Ta≥5%, and 5≥Al ≥7%. The first group contains the Re and Cr and is shown by the color green. The second group contains the Re, Cr, Ta, and Al and is shown by the color light blue. The element contents in both the groups are equivalent to

those in the 3rd generation superalloys. It is clearly illustrated by these figures that the neural network results can be post processed to highlight any alloy composition ranges for any investigated property. In fact, definite alloy compositions are outlined for well-known commercial superalloys are illustrated in these figures.

The ERBALLOY designed in this study, is also shown in these figures with the modeling and experimental rupture results. The chemical composition of the alloy is already shown in Table 2.2. As it will be shown in the section 3.4, the rupture testing of this alloy showed rupture time of 361 hours at 982°C/248MPa. The modeling results, however shows the value of 310 hours. The difference between the modeling and experimental results may arise from the uncertainty in the modeling results and also measurement errors in chemical composition of the alloy by bulk WDS method. ERBALLOY was designed based on modification of the Re content of the second generation CMSX-4 alloy to manufacture a third generation alloy. Considering the density of the ERBALLOY (~8.88 g/cm^3) ,the scatter plots show that there are alloys with the same density as for the ERBALLOY but with higher rupture strength which could be selected for the experimental rupture test, however due to limitations in alloy making, the chemical composition of the designed alloy was adjusted according to Table 2.2.

To compare the ERBALLOY with the alloys with higher rupture strength, an arbitrary alloy (Alloy X) is chosen and shown by the empty rectangle symbol in Figures 3.3f,i, and l. It is seen that this alloy has the same density as for the CMSX-10 but with a higher rupture strength. The scatter plots for the Alloy X shows a slight improvement in the rupture life over the CMSX-10 without an increase in the density, see also Figures 3.3f, i, l. The composition for Alloy X is similar to those in the 3rd generation superalloys and is given in Table 3.2.

Table 3.2. Chemical composition of the Alloy X.

Element	Ni	Re	Cr	W	Co	Mo	Hf	Ti	Al	Ta
Range, wt.%	Bal.	6	4.5	9.5	9.10	0.6	0.1	1	6.30	10

Table 3.3 compares the density, volume fraction of γ', M_d, and rupture strength of the CMSX-2, CMSX-4, and CMSX-10 with that of the ERBALLOY and Alloy X. Except for the Alloy X, the experimental values for the rupture strength at 982°C and 248MPa are used in this table. For the hypothetical alloy X, the modeling results is presented.

Table 3.3. Density, volume fraction of γ', M_d, and rupture time of the ERBALLOY and ALLOY X, compared to the CMSX-2, CMSX-4, CMSX-10.

Alloy	Density (g/Cm3)	Volume fraction of γ'	M_d	Rupture time (h)
CMSX-2	8.56	65	0.983	74
CMSX-4	8.7	65	0.984	275
CMSX-10	9.05	77	0.96	849
ERBALLOY	8.88	58	0.971	361
Alloy X	9.05	65	1.048	969

It is seen that ERBALLOY has a density in between the second generation (CMSX-4), and modern third generation (CMSX-10) alloys. Compared to the other alloys in Table 3.3, ERBALLOY has lower volume fraction of γ', mainly due to lower Al content. The M_d value of the ERBALLOY which is an index for tendency towards formation of the TCP phases is almost the same for all alloys in the Table 3.3 except the Alloy X. The rupture strength of the ERBALLOY is in between the CMSX-4, and CMSX-10. It is seen that ERBALLOY is advancement in the second generation alloys in terms of creep resistance by a slight increase in the density. Comparing the chemical composition of the ERBALLOY (Table 2.2) with Alloy X (Table 3.2), it is seen that the Alloy X has higher Re, W, Al and Ta content with a lower Cr content. The density of the Alloy X, is 9.05 g/cm^3 which is almost 2% heavier than the ERBALLOY with density of 8.88 g/cm3. Moreover the M_d parameter for the ERBALLOY is 0.97 which compared to the alloy X (1.048) shows a considerable lower tendency towards TCP phases.

Unfortunately, like other refractory elements, the Re increases the tendency for the TCP phase formation which is predicted in this study by utilizing the M_d [76]. A high M_d

number increases the propensity. Due to the Re's high M_d number, the overall M_d number of the alloy increases [180]. Figures 3.4a-c plots the M_d versus the volume fraction of the γ'. The gray background regions here show the entire alloy design space, and the red regions show the alloys with various contents of the Re. The values for the well-known commercial superalloys are also provided. Although very weak, a shift toward a lower volume fraction of the γ' and a higher M_d number is observed in alloys with higher Re content.

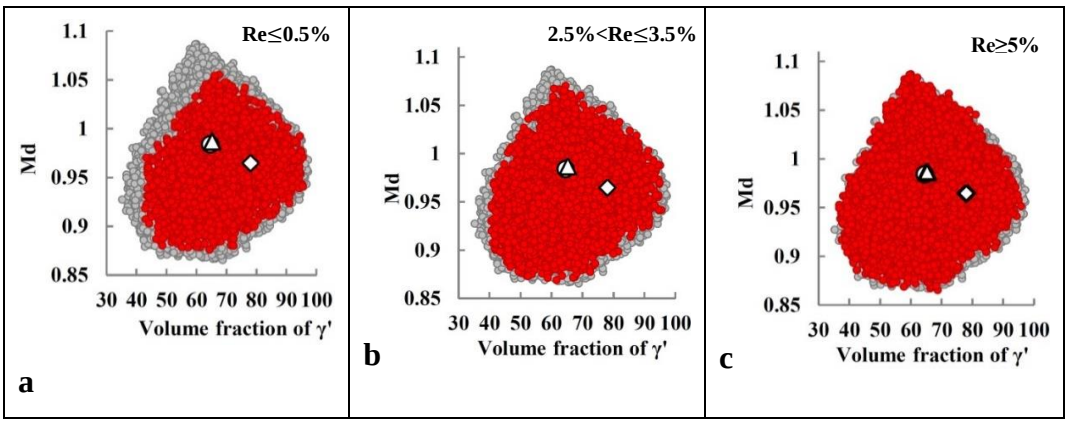

Figure 3.4. Scatter plots of M_d versus volume fraction of the γ' for different concentrations of Re. The triangle, circle, and diamond show the first (CMSX-2) [176], second (CMSX-4) [177], and third (CMSX-10) [178] generation alloys, respectively.

<u>3.1.1.2. Cr.</u> Cr is another element whose content in the single crystal Ni base superalloys varies significantly from the first to third generations. Figure 3.5 shows the effect of varying the Cr content on the density and the rupture life. Like the graphs for the Re, the gray background shows the entire alloy design space, and the red regions show the alloys with different Cr content. The triangle, circle, and diamond show the experimental data for the first (CMSX-2), second (CMSX-4), and third (CMSX-10) generation alloys, respectively. The histograms (Figure 3.5a-c) give the percentage of the alloys in given rupture time intervals. It is observed that increased Cr shifts the alloy design space to a lower rupture life. The typical value is constant between 100-200 hours in all the Cr contents but more importantly, it is seen that by increasing the Cr content, the number of alloys with the capability of achieving longer rupture lives decreases. Cr has lower density than Nickel and reduces the density of Ni base superalloys. Moreover, it is a γ-forming and

fast diffusing element [1], clearly decreases the rupture life. These effects are seen in Figure 3.5d-f.

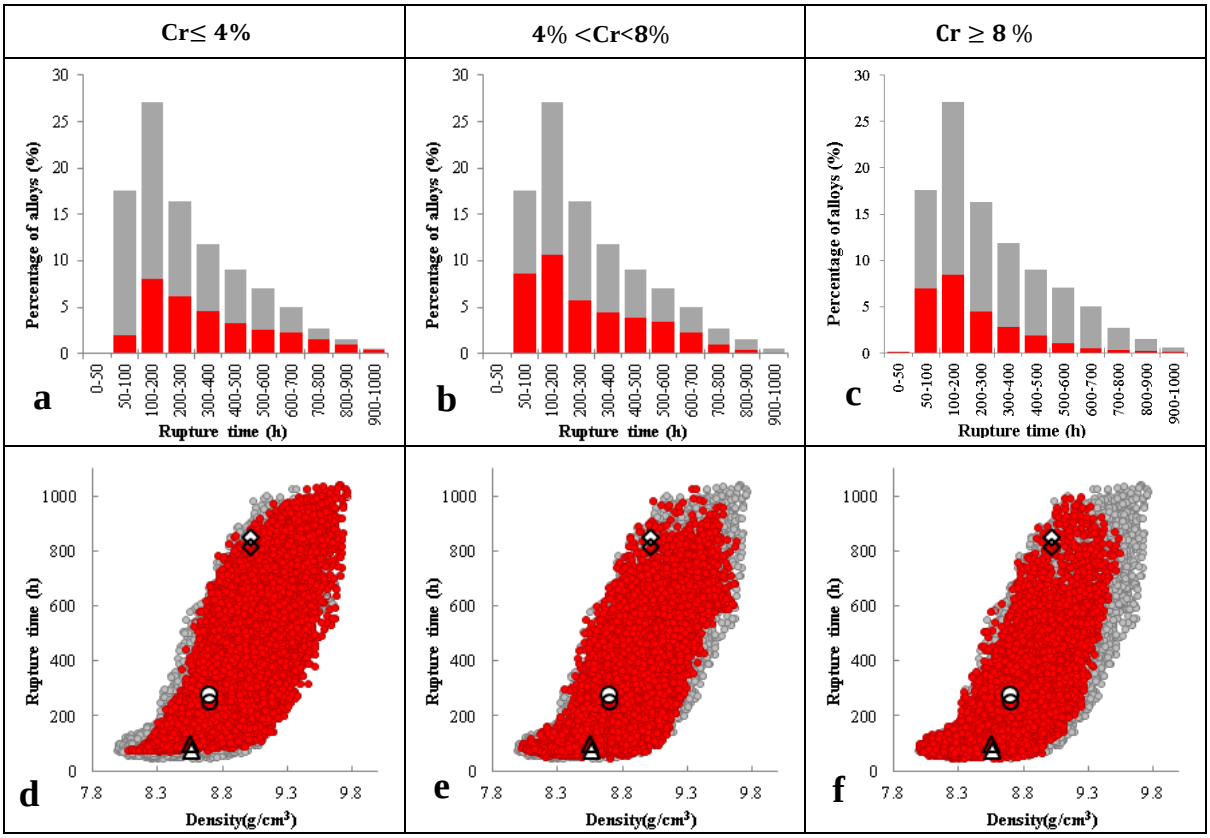

Figure 3.5. Percentage of alloys in given rupture time ranges are shown in (a-c). Rupture time versus density (d-f) are plotted. The markings are explained in the text.

Similar to the Re, the Cr has a high propensity to form the brittle TCP phases, which reduce the creep resistance of an alloy. Presence of the Cr in an alloy increases the partitioning of the refractory elements to the matrix [181] and so enhances the formation of the TCP phases. This claim is supported by the M_d versus the volume fraction of the γ' scatter plots for the alloys with various Cr contents as seen in Figure 3.6a-c. Increasing amount of the Cr shifts the alloy design space toward the region with lower volume fraction of the γ' and higher values of the M_d. The observed shift is more discerned with the Cr than the Re. While the presence of Cr is necessary for the hot corrosion and oxidation resistance, yet a low Cr content is beneficial for the rupture strength and stability of the microstructure. Hence, in later generation superalloys, the Cr level is reduced to less than 4wt% to accommodate more Re [181,182].

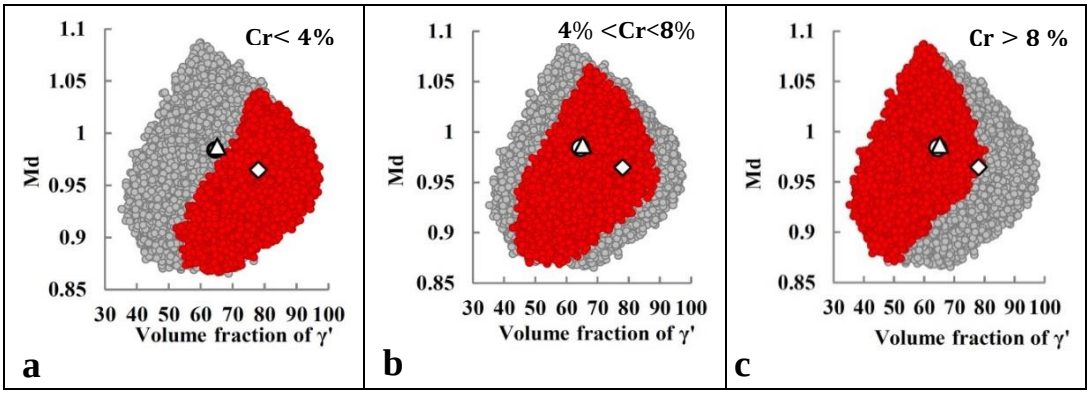

Figure 3.6. Scatter plots of M_d versus volume fraction of the γ' for different concentrations of Cr. The triangle, circle, and diamond show the first (CMSX-2) [176], second (CMSX-4) [177], and third (CMSX-10) [178] generation alloys, respectively.

3.1.1.3. Al. The Al is an essential element for oxidation resistance due to formation of the Al_2O_3 oxide layer. Moreover, it is the major element in the strengthening γ' phase and is a solid solution strengthener in the matrix, yet the effect of Al on both the density and rupture time is shown in the scatter plots in Figures 3.7. Alloys containing higher level of Al tend to have lower densities, yet the alloy design space shifts towards the lower rupture strength.

Figure 3.8a-d shows the plots of M_d versus volume fraction of the γ' for various Al concentrations. Alloys with higher Al content have higher volume fraction of the γ' and higher M_d values. Moreover, the plots show a very discernible increase in the M_d value with a slight increase in the Al content. Although the Al is the main γ' forming element, its excessive usage diminishes the high temperature stability of the alloys by making them prone to precipitation of the TCP phases. With the Al segregating into the γ', the matrix is enriched by the refractory elements, which promote the precipitation of the TCP phases in the matrix [183]. Therefore, increasing the Al content increases both the volume fraction of the γ' and the M_d values.

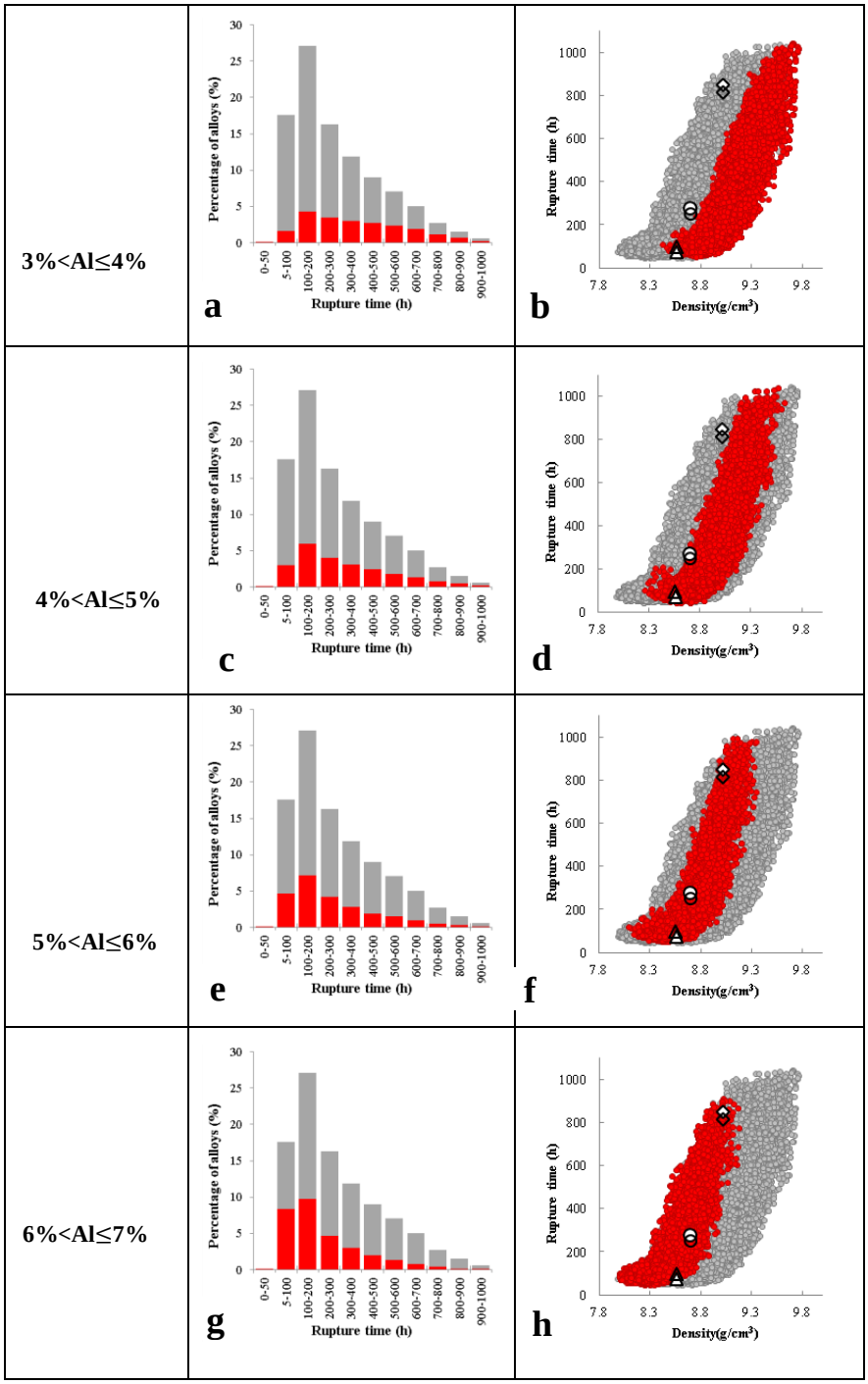

Figure 3.7. Percentage of alloys in given rupture times are shown in (a, c ,e and g). The scatter plot in red shows the alloy design space for different Al levels. b) 3%<Al≤4%, and d) 4%<Al≤5 %, f) 5%<Al≤6%, h) 6%<Al≤7%. The markings are explained in the text.

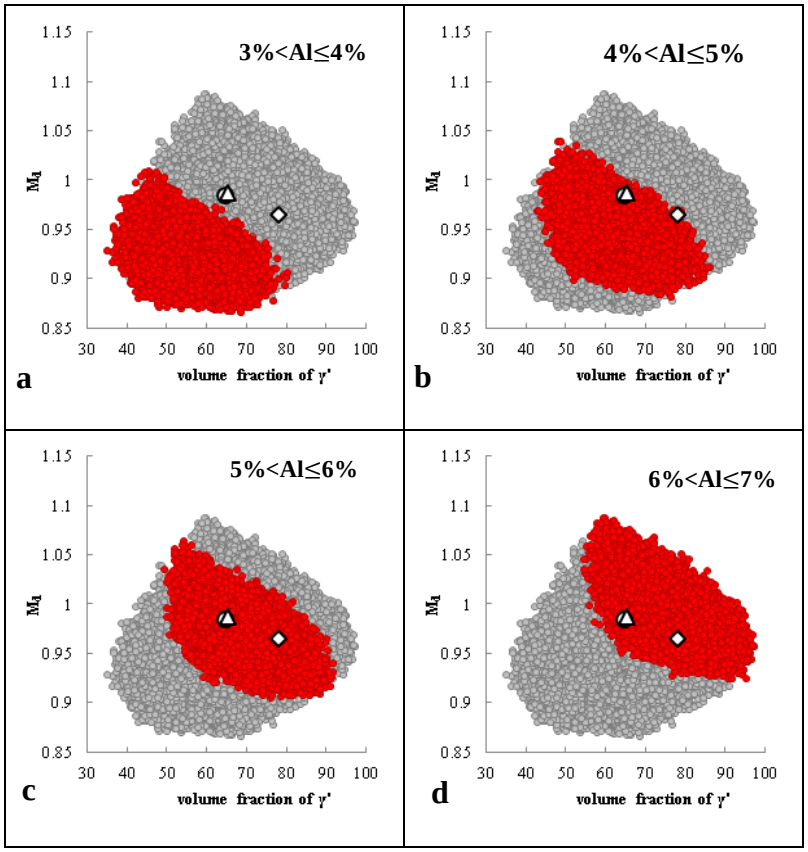

Figure 3.8. Variation of the M_d with volume fraction of γ' for different concentration of Al. a) 4.5%<Al≤5%, and b) 5%<Al≤5.5%, c) 5.5%<Al≤6%, d) 6%<Al≤6.5%. The markings are explained in the text.

3.1.1.4. Ta/W. Two other major refractory elements used in superalloys are the W and Ta and the ratio of the Ta/W is important in alloy design. From the processing point of view, a high Ta/W ratio is reported to increase the interface stability and reduce the extent of the freckling type casting defects caused by convective instabilities during solidification processing [184]. The Ta, by segregating into the interdendritic regions, alleviates density inversion in these regions induced by the W segregation to the dendritic cores. Thus, Ta/W≈1 is beneficial. Hence, the Ta/W ratio can give a hint on the manufacturability of alloys as single crystals. In addition, it has been reported that the ratios close to the unity have the best hot corrosion resistance [19]. The NN modeling results of the current study predicts these experimental findings. The average rupture strength in Figure 3.5 increases until this ratio becomes unity and then it decreases. Due to a nonlinear relation of the rupture life with the T/W ratio and to be able to detect the slight changes, the narrow Ta/W

ratio of 0.1 was chosen for this figure. Figure 3.9 shows the scatter plots of the rupture life with density.

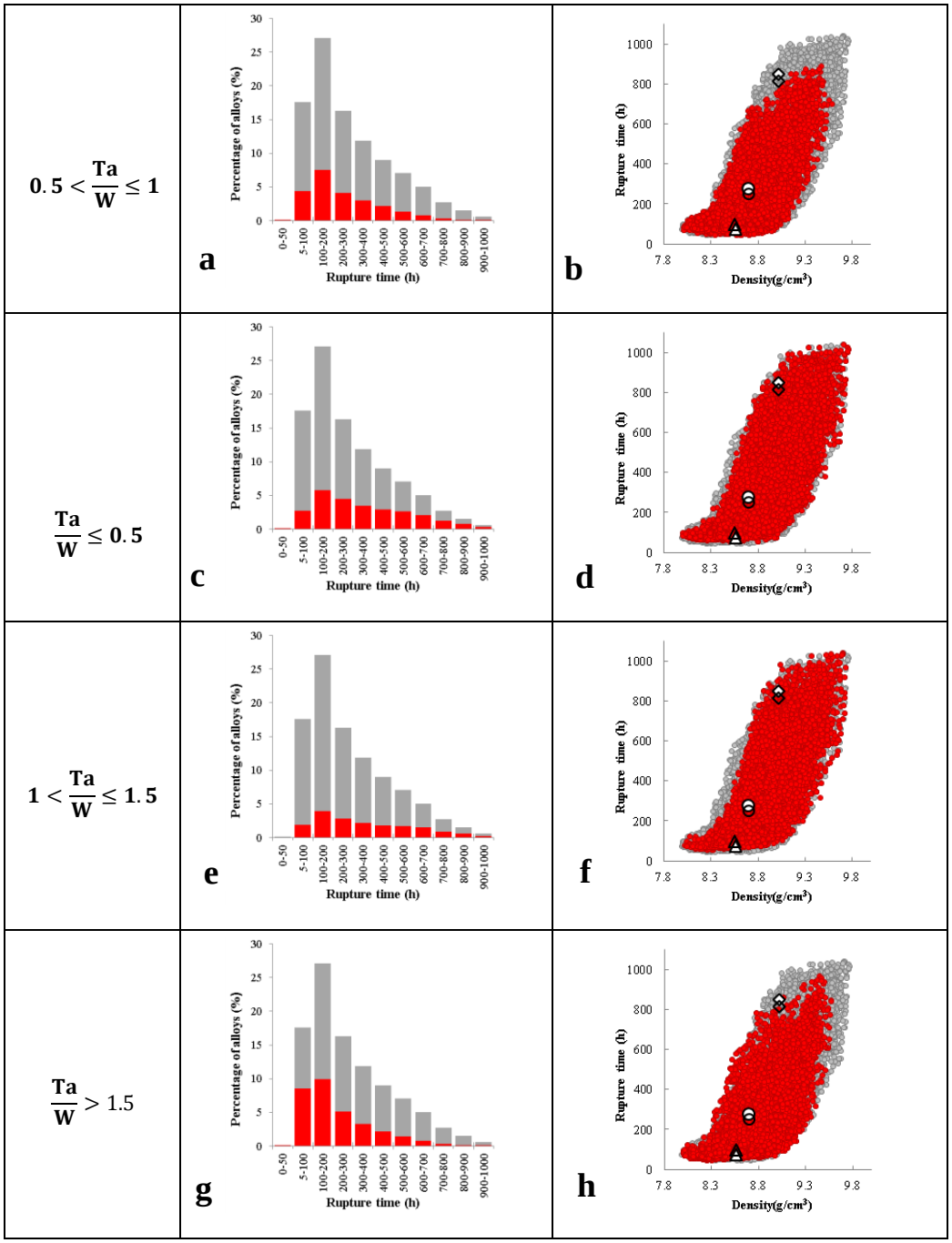

Figure 3.9. Percentage of alloys in given rupture times are shown in (a,c ,e and g). The scatter plot in gray show the whole alloy design space. Red color shows the alloy design space for the Ta/W ratios as in the first column. The markings are explained in the text.

The results show that alloys with a Ta/W ratio less than 0.5 have rupture life spanning from low values to about 800 hours. The Ta/W ratio between 0.5 and 1 (Figure 3.9b) increases the rupture life to the maximum of the design space. The ratio between 1 and 1.5 shows the similar behavior s for the ratio between 0.5 and 1 (Figure 3.9c). Increasing this ratio beyond 1.5, further reduces the number of alloys with a high rupture life (Figure 3.9d). The effect of this ratio on the creep properties relies also on the Ta/W relation to the γ' phase fraction. At a given Al concentration, Ta increases the volume fraction of the γ' while alloying elements like W, Mo, Cr, and Re decrease it [1]. It has been also shown that the variation of the Ta/W ratio has a significant effect on the size and morphology of the γ' phase in single crystal superalloys, both of which are a strong function of the test temperature and misfit that determine the creep strength of the alloys [16]. Increasing this ratio may lead to changing the shape from the cuboidal to the spherical one which reduces the rupture life.

The average creep lives of the alloys in the design space are determined for various composition ranges of Re, Cr, Ta/W, and Al and plotted in Figure 3.10. Obviously, these plots can be generated for any other element too. It is seen that the increased Re content substantially increases the rupture life. Re partitions preferentially to the matrix (γ) and is the strong solid solution strengthener of the matrix in the Ni base single crystal superalloys [185]. The Re is also a slow diffusing element in the matrix which is the main reason for the rhenium effect increasing the rupture strength [175,186,187]. The average rupture life of the alloys in a small concentration range (1wt%) from 0 to 10wt% of Cr content clearly shows the decreasing trend for the rupture life with increasing Cr content.

The results in Figure 3.10 suggest that the Cr content should be adjusted carefully for an increased rupture life. Figure 3.10 shows the rupture life for the Al content in between 3 to 7%. The concentration resolution is defined smaller than Re and Cr to detect the nonlinear influence of the Al. The results show that the maximum average ruptures time occurs at 4.7-5.5wt% range. To gain the maximum rupture strength, the Ta/W ratio should be adjusted to be close to 1.

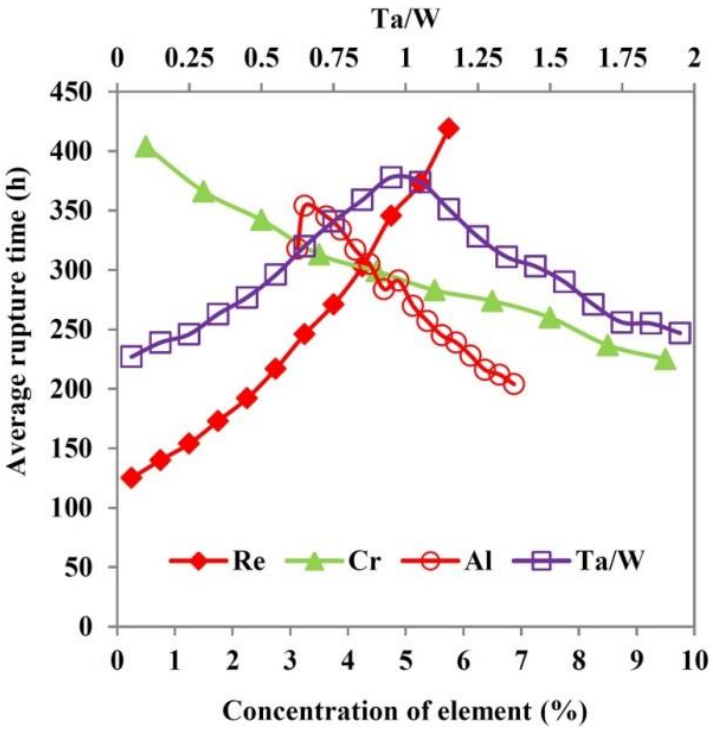

Figure 3.10. Rupture time vs. concentration of Re, Cr, and Al. The secondary top axis shows rupture time vs. ratio of Ta/W.

Influence of the major elements in the superalloys on the rupture life is shown altogether in Figure 3.11 for the superalloy CMSX-4. The effect of an alloying element is studied by varying the concentration of that element only, compensated by the Ni content while keeping the content of the other elements fixed. These plots are generated to show the capabilities of the neural network model and can obviously be generated for any alloy composition. Figure 3.11a shows variation in the density, which is related to the amount of the elements in the alloy and their atomic weights. The data point symbol corresponding to an element's concentration in the CMSX-4 is made larger in Figure 3.11a. A careful look will discern that the larger symbols all are at correct density value of 8.7 g/cm^3 for the CMSX-4, which again indicates the prediction accuracy of the NN model. Figure 3.11b displays influence of element content on the creep rupture life. Influence of some of the plotted elements is explained earlier, and non-linear influence of the Al is seen in the CMSX-4, too.

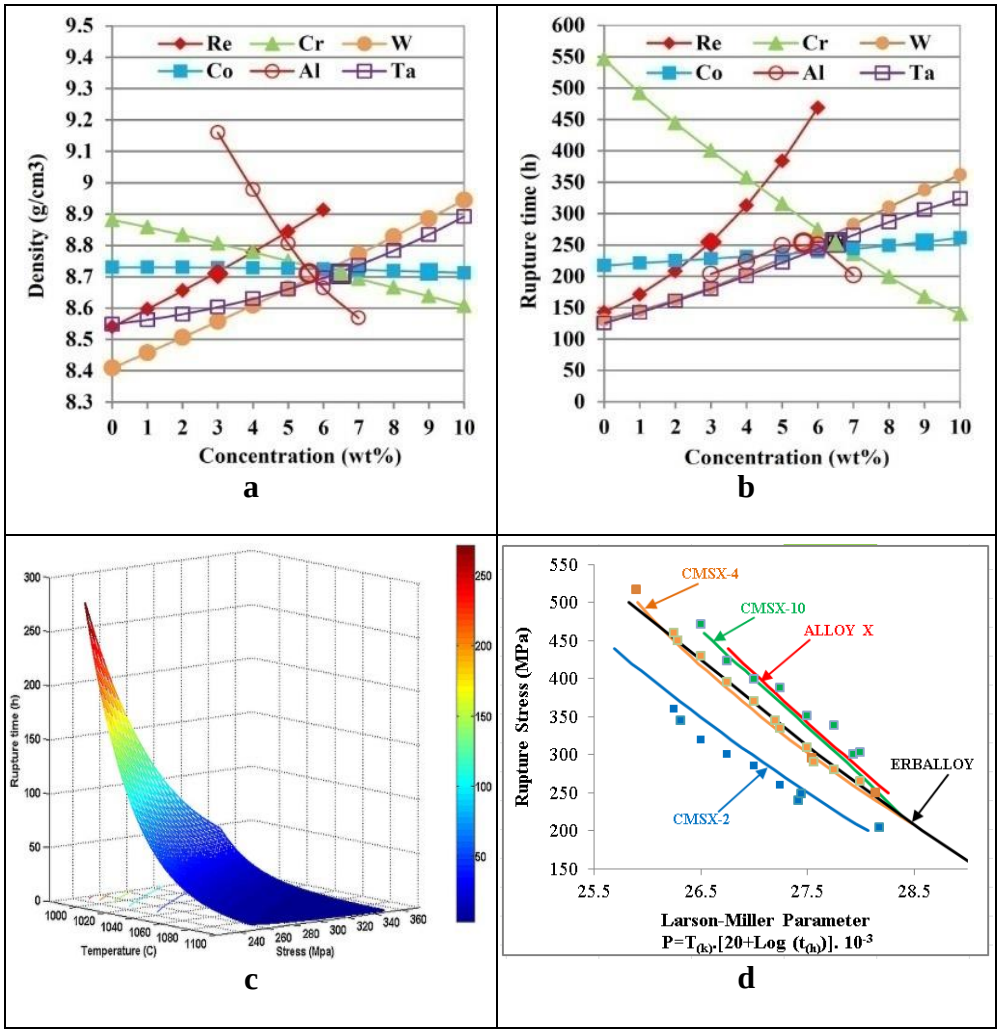

Figure 3.11. Density (a), and rupture time (b) of the CMSX-4 with concentration of the elements. Temperature-stress-rupture time plot for the CMSX-4 (c), and Larson-Miller plots for selected alloys by NN (continuous lines), and experimental (filled symbols) (d).

In this study, we have limited the NN predictions within the available experimental data ranges. Other work utilizing the NN [36] makes prediction outside the experimental data ranges, which we believe are incorrect or at best should be taken with very high caution. Of course, the NN model is used for forecasting [18]; however, this should be done for alloy design in the vicinity of the available experimental data. Figure 3.11c shows the neural network predicted influence of temperature and stress on the rupture time of the alloy CMSX-4. It is observed that with increasing temperature, time to rupture decreases at all stress values. The rate of decrease, however, is lower at higher stresses. The same is true for the effect of the stress and the results show that at higher temperatures, the dependency of the rupture strength to the stress decreases. The interactions between the

temperature, stress, and rupture time are better shown by the Larson-Miller plots. Figure 3.11d shows the neural network modeled Larson-Miller plots (continuous lines) for the first (CMSX-2), second (CMSX-4), and third (CMSX-10) generation alloys. The dotted lines are the experimental values from the literature [37]. A close agreement is evident between the experimental and neural network modeled Larson-Miller plots.

The foregoing has presented that the NN alloy design is a powerful method with highly accurate prediction of alloy properties. The NN method can use results from PHACOMP and CALPHAD base methods as inputs. Alternatively, the results of the three methods can be utilized in the post-processing step to establish correlations between the microstructure, property, and performance. In addition, the NN results can be transferred to CALPHAD type modeling to predict solidification and heat-treated microstructures. Evidently, an integrated NN modeling can facilitate finding the correct composition window and final microstructure / properties of a validated component.

3.2. CALPHAD Modeling of the Phase Evolution and Critical Temperatures

The solidification and evolution of the phases during cooling from liquidus temperature of the designed alloy (ERBALLOY) with the chemical composition of Table 2.2 is modeled by Thermo-Calc equilibrium and non-equilibrium Schiele module. Simulations were performed to reveal the liquidus, solidus, and γ' solvus temperatures and the composition of the evolving phases during solidification and subsequent cooling to room temperature. Scheil solidification model is based on the assumption that there is a complete mixing in the liquid and no diffusion in the solid. In contrast, the equilibrium modeling considers local equilibrium between the existing phases. Therefore, there is a complete mixing in both the solid and liquid phases. Both of these models are embedded in the Thermo-Calc software.

3.2.1. Equilibrium Module.

Equilibrium module calculates the state of the system with the minimum Gibbs free energy. In the present work, the thermodynamics database TCNI7 for the multicomponent Ni base alloys was used. The result of the modeling is shown in Figure 3.12. Thermo-Calc

equilibrium model predicts that the primary γ phase forms at 1403 °C from the liquid and the solidification terminates at 1354 °C with 100% γ in the microstructure without formation of any other phases.

$$\text{LIQUID} \rightarrow \text{LIQUID} + \gamma \qquad 1354°C < T \leq 1403°C \tag{3.1}$$

Moreover, it predicts that the γ' forms from γ by a solid state phase transformation below 1250°C. In other words, the γ' solvus temperature is estimated to be below 1250 °C.

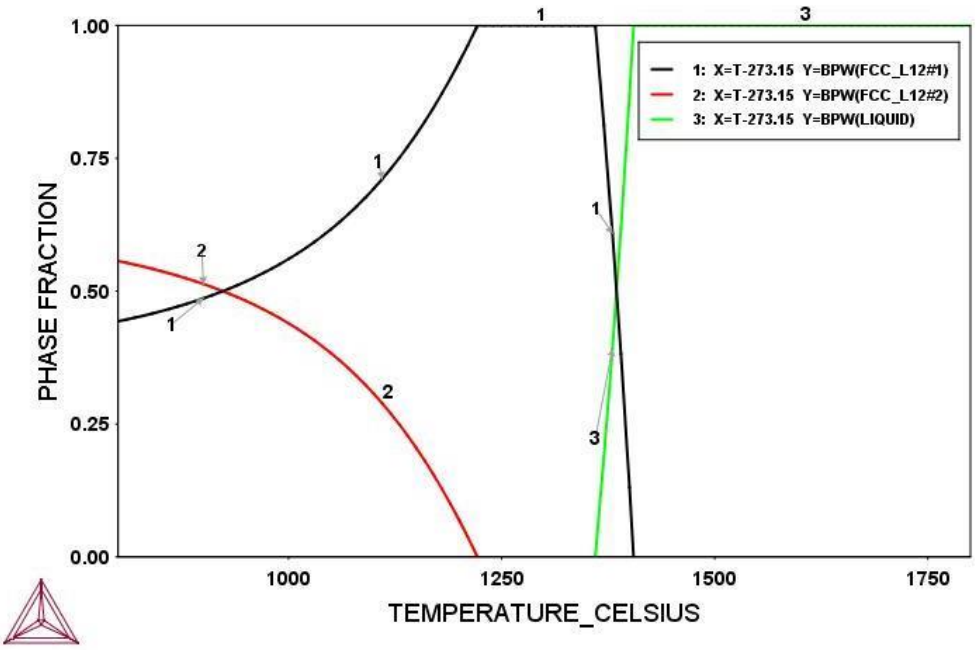

Figure 3.12. Modeling of the solidification of the ERBALLOY by Thermo-Calc equilibrium model. The vertical axis shows the phase fraction of the phases. FCC_L12#1 is the γ matrix and FCC_L12#2 is the strengthening γ' phase.

The simulation predicts that the volume fraction of the precipitate will be around 58% at room temperature. The volume fraction of the precipitates is calculated by ImageJ software which is around 70%.

The distribution of the alloying elements is not the same between the freezing solid and remaining liquid. W and Re tend to segregate to the solid while Ta, Ti, and Al are enriched in the remaining liquid. As an example, Figures 3.13 shows Thermo-Calc

predictions of the variation in the concentration of Re and Al elements in the liquid and γ phases during solidification. Re segregates to the γ in the core of the dendrite. Then, as solidification advances, its value decreases in the remaining liquid, and for this reason, the Re content of the γ is decreased continuously. On the other hand, Al is rejected to the liquid in front of the solidification interface, segregates towards the interdendritic region.

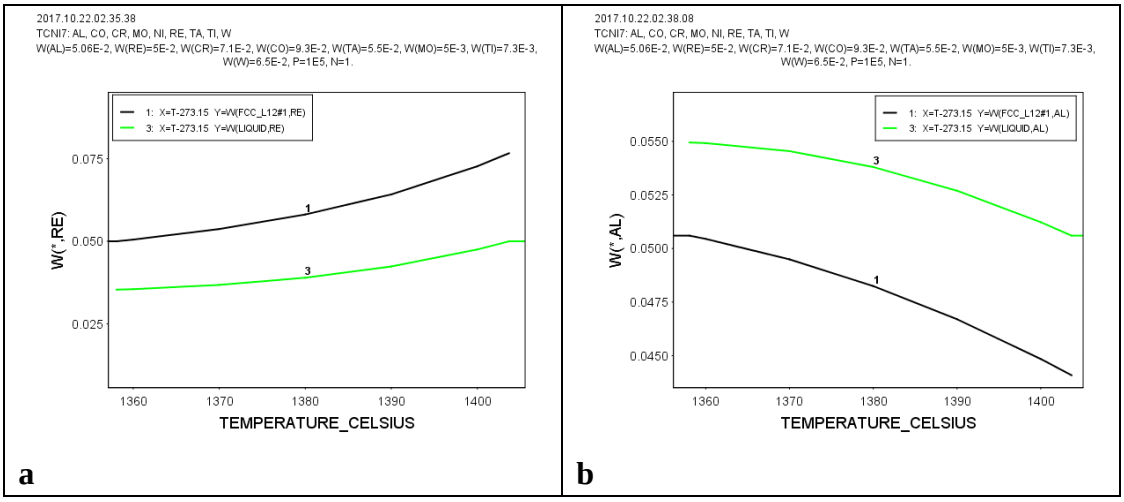

Figure 3.13. Varying concentration of Re (a), and Al (b), during solidification of ERBALLOY, predicted by Thermo-Calc equilibrium model. The vertical axis shows the weight fraction of the elements. FCC_L12#1 is the γ matrix phase.

The overall effect of the segregation of the alloying elements leads to the as-cast structure with elemental segregation to the dendrite core and interdendritic region. The extent of segregation is usually defined by the segregation coefficient (k) as follows:

$$k = Cs/Cl \tag{3.2}$$

where the C_s is the average concentration of an element in the dendrite core and the C_l is the concentration of that element in the interdendritic region. The equilibrium modeling results is used for calculation of the segregation coefficient and the results are shown in Table 3.3. In calculation of the segregation coefficient, the concentration of the first formed solid γ is divided by the concentration of the last solidifying liquid.

Table 3.4. Thermo-Calc modeling results for the composition of the first solidified γ and liquid phases and the resulting segregation coefficient.

Element	Ni	Al	Cr	Mo	Co	W	Re	Ti	Ta
First γ (wt%)	59.6	4.36	6.63	0.03	10.74	7.18	7.6	0.03	2.67
Last liquid (wt%)	58.6	5.47	7.05	0.6	7.95	5.9	3.6	1.5	9.14
k	1.02	0.80	0.94	0.05	1.36	1.22	2.11	0.02	0.29

3.2.2. Scheil Module.

Figure 3.14 shows the results of Scheil solidification model by Thermo-Calc software. Solidification starts at 1403°C by forming γ from the liquid. As solidification advances, the liquid fraction decreases and the amount of γ phase increases. After the mole faction of the liquid fraction reduces to 0.12at 1320°C, the γ' phase starts to form from the remaining liquid. Finally, the TCP Sigma and Mu phases form.

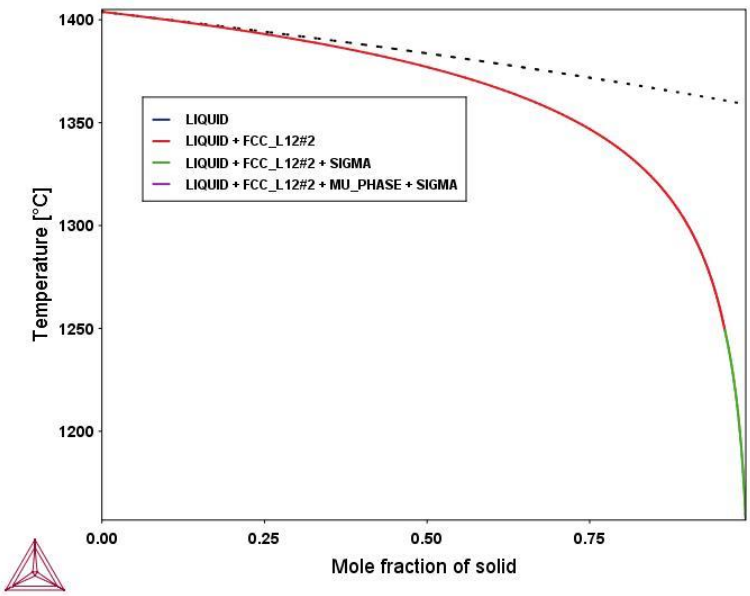

Figure 3.14. Mole fraction of solid versus temperature simulated by Scheil solidification model of Thermo-Calc. The dotted line shows the results of the equilibrium solidification.

Since no TCP phase was seen in the as-cast microstructure of the grown samples, solidification is modeled by considering only the liquid, gamma, and gamma prime phases and the other phases are excluded from the list of the phases. The results are shown in Figure 3.15.

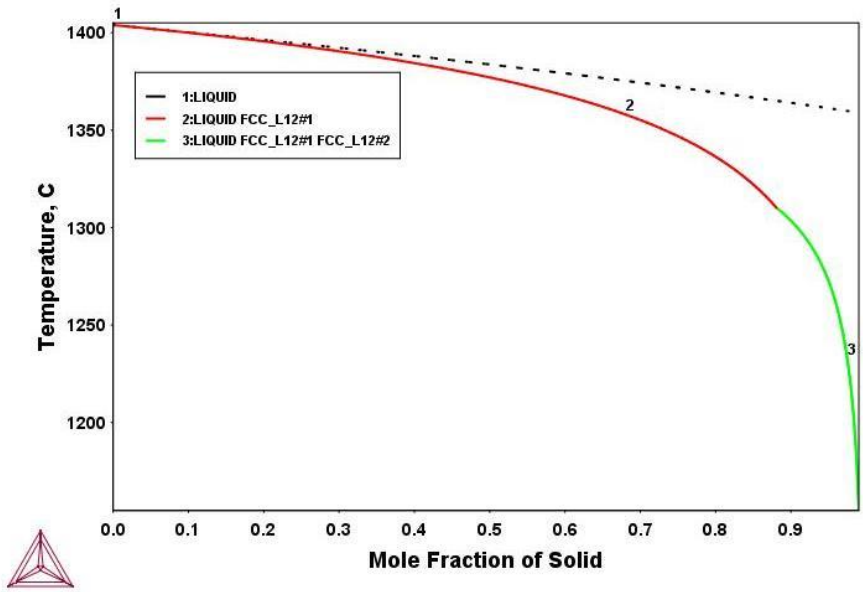

Figure 3.15. Solid fraction versus temperature simulated by Scheil solidification model of Thermo-Calc, by considering only the three liquid, γ, and γ' phases. The dotted line shows the results of the equilibrium solidification.

Scheil model predicts the liquids temperature to be 1403 °C. The primary solidification path corresponds to freezing of the γ phase at the core of the dendrite:

$$\text{LIQUID} \rightarrow \gamma \qquad T \leq 1403°C \tag{3.3}$$

In the final stages of the solidification when temperature falls below 1310°C, the γ' phase forms from the liquid and γ phase with the following equation.

$$\text{LIQUID} + \gamma \rightarrow \gamma + \gamma' \tag{3.4}$$

Scheil solidification predicts that γ' is formed at 1310°C. However, it does not give any information about type of the phase transformation leading to evolution of γ' phase. It will be discussed later that the last stage solidification could have characteristics of peritectic or eutectic reactions. It should be noted that in multicomponent alloys, the eutectic or peritectic reaction could happen in a range of temperatures until solidification is terminated. Scheil model considers full diffusion in the liquid and no diffusion in the solid. This is maybe correct for the liquid; however, since the solidus temperature of the alloy (1354°C in the equilibrium modeling and 1150°C by Scheil modeling) is high, some extent of diffusion exists in the solid. Since the Scheil solidification ignores diffusion in the solid phase, the concentration of the low melting eutectic forming elements get to a high values as solid fraction increases. Therefore the solidification temperature of the remaining liquid falls down. For this reason, Scheil model estimates wide solidification interval. In reality, some diffusion occurs in the solid and the solidification lies between the equilibrium and Scheil models. The concentration of the Al and Re in the formed γ phase during solidification is shown in Figures 3.16a and b, respectively.

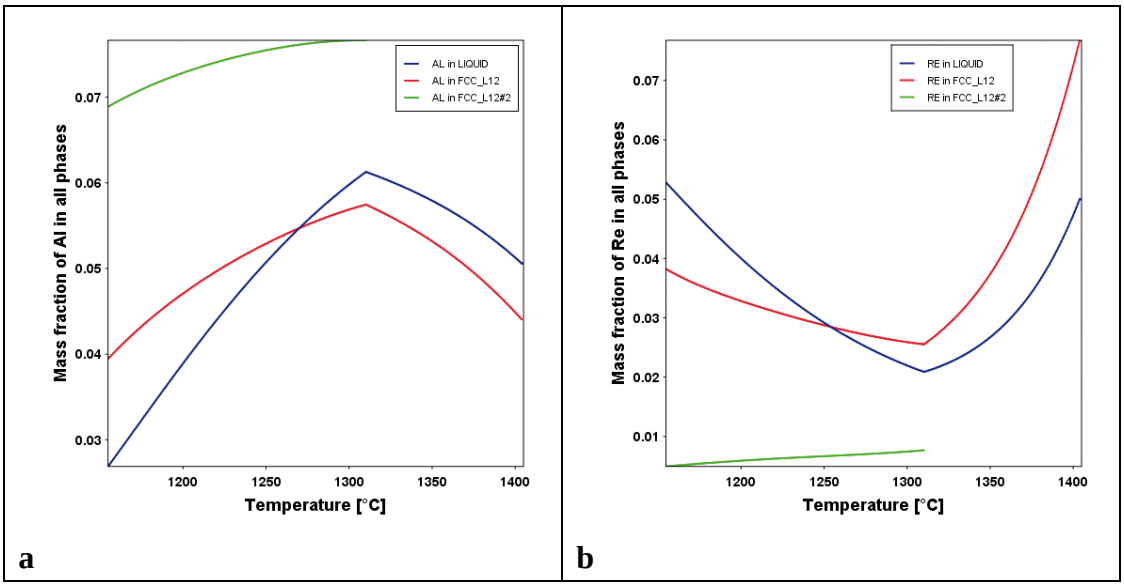

Figure 3.16. Varying concentration of Re (a), and Al (b), during solidification of ERBALLOY, predicted by Thermo-Calc Scheil model. The vertical axis shows the weight fraction of the elements. FCC_L12#1 is the γ matrix and FCC_L12#2 is the γ' phase.

The γ phase is rich in elements like Re, W and Cr that typically segregate to the solid. The remaining liquid then is enriched with the elements like Al, Ti, and Ta that are

the γ' forming elements. Formation of the γ' consumes γ' forming elements and hence the concentration of these elements in the liquid and γ decreases. This is shown for Al in Figure 3.16a. On the contrary, γ' has low concentration of the γ forming elements and the remaining liquid and γ are enriched with these elements. This is shown for Re in Figure 3.16b.

The segregation coefficients calculated by Scheil modeling is shown in Table 3.5. Compared to the values calculated by the equilibrium modeling, it is seen that the Scheil model gives higher segregation ratios for elements with segregation ratios far from the unit. This is due to ignoring diffusion in the solid.

Table 3.5. Scheil modeling results for the segregation ratios of alloying elements.

Element	**Ni**	**Al**	**Cr**	**Mo**	**Co**	**W**	**Re**	**Ti**	**Ta**
First γ (wt%)	60.1	4.45	6.72	0.37	10.81	7.06	7.67	0.29	2.65
Last liquid (wt%)	59.33	6.42	6.74	0.65	6.2	4.47	1.73	1.64	13.2
k	1.01	0.69	1	0.57	1.74	1.58	4.43	0.18	0.20

The as-cast microstructure of the Re containing third generation single crystal superalloys is composed of a matrix of γ phase and the γ' precipitates with the cuboidal morphology distributed in it. Large islands of γ' are seen in the interdendritic region. The γ' morphology is dependent on the lattice misfit which itself is a function of the chemistry of the alloy. The lattice misfit values close to zero results in the near spherical morphology; however, larger positive or negative misfit values lead to cuboidal morphology. What is of particular interest is the solidification of the last solidifying liquid in the interdendritic region. The formation of the γ' phase whether by the eutectic or peritectic reaction has been a controversy. Claudia Walter et al. [146] proposed that at the last stage of the solidification, large γ' islands are formed as a product of a eutectic reaction in the interdendritic region. N. Warnken et al. [189] suggested that the solidification of the interdendritic region is a eutectic reaction of L → γ + γ' with the fine lamellar (γ + γ') morphology. The reaction only occurs at the dendrite-melt interface. The coarse γ′ islands later grow to a finer lamellar structure towards the interdendritic region. However, some

other studies suggested the peritectic nature for the solidification of the interdendritic region. Mathieu Terner et al. [190] proposed that solidification of the interdendritic region starts with forming of the nucleus of the γ' on the surface of the existing γ phase. Solidification continues with formation of the fine network of γ–γ' with peritectic nature in the core of the interdendritic region. Towards the end of the solidification, the large γ' islands forming the edge of the dendrite. The peritectic reaction is three-phase equilibrium between a liquid and two different solids at peritectic temperature. Above peritectic temperature, there is a stable equilibrium between the liquid and existing solid phase. At peritectic temperature, the two solid phases are in stable equilibrium. The peritectic nature for solidification of the interdendritic region is also proposed by N. D'Souza and H. B. Dong. The sequence for nucleation of the interdendritic γ' according their theory is shown schematically by in Figure 3-17 [191].

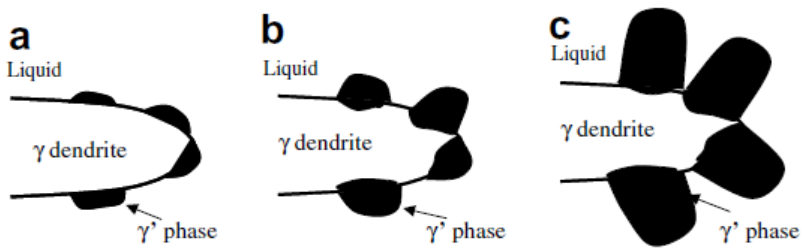

Figure 3.17. The sequence for nucleation of the interdendritic γ' [191].

During solidification, the first solid to form is the γ dendrites. Then the γ' nucleates on the primary γ (Figure 3.17a). In the next stage, the γ' grows into both the γ and the remaining liquid in the interdendritic region (Figure 3.17b) but the growth rate is higher in the liquid due to the higher diffusivity of the solute in the liquid than the solid. If viewed from the dendrite core, the edge of the dendrite has taken the convex shape, which shows that the γ phase has been one of the main parts of the reaction. The growth of the γ' into both the liquid and solid γ is a sign of a peritectic reaction. Solidification terminates with the solidification of fine lamellar eutectics.

Figure 3.18a shows a typical optical microstructure of the dendritic morphology of the as-cast alloys. Figure 3.18b shows that the large islands of γ' is located at the center of the interdendritic region.

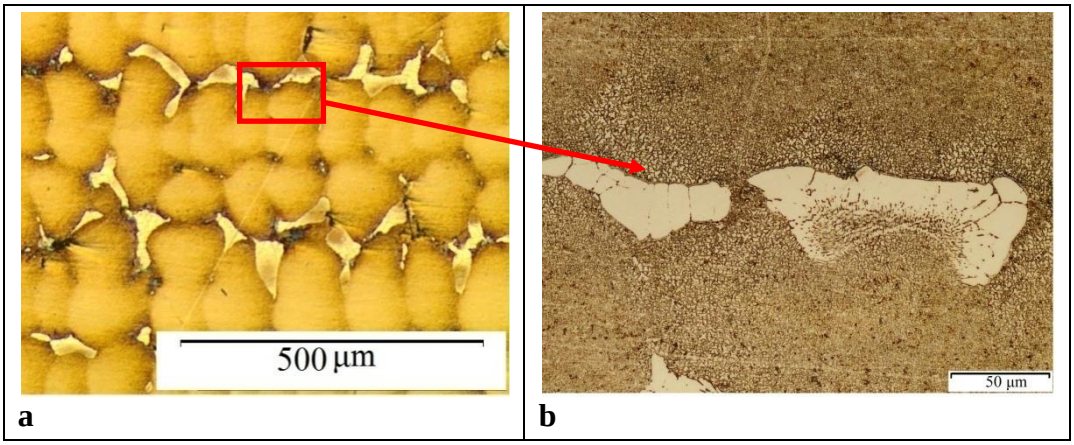

Figure 3.18. The longitudinal microphoto showing the position of the eutectic islands at interdendritic region (a), and the interdendritic γ' island at higher magnification (b).

The SEM photo of the interdendritic microstructure of the ERBLLOY VB12 is shown in Figure 3.19. Three different morphologies are seen in the interdendritic region of the alloys of this study (Figure 3.19) which are numbered 1, 2, and 3.

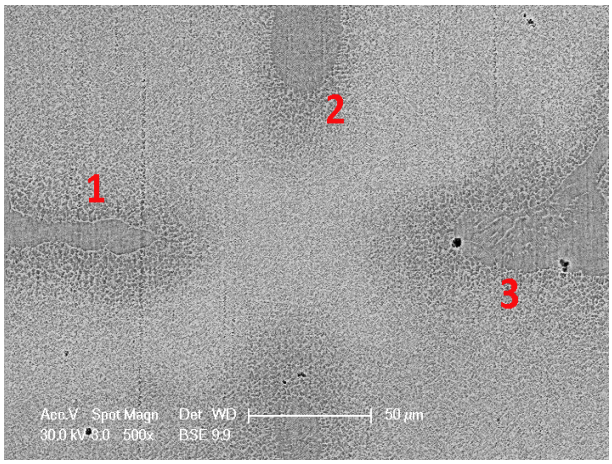

Figure 3.19. Three different morphologies of the interdendritic region. Large islands of γ' (1), mosaic type eutectic (2), and elongated γ' with the fan shape eutectic morphology (3).

In all three morphologies, the solidification starts with nucleation of the matrix γ phase from the liquid and lasts with the solidification of the eutectic pools at interdendritic regions. The shape of the precipitates in the dendrite is cuboidal in as-cast structure of all

the samples of this study. However, different morphologies are observed for the interdendritic region. The morphology in region 1 is shown in Figures 3.20a and b.

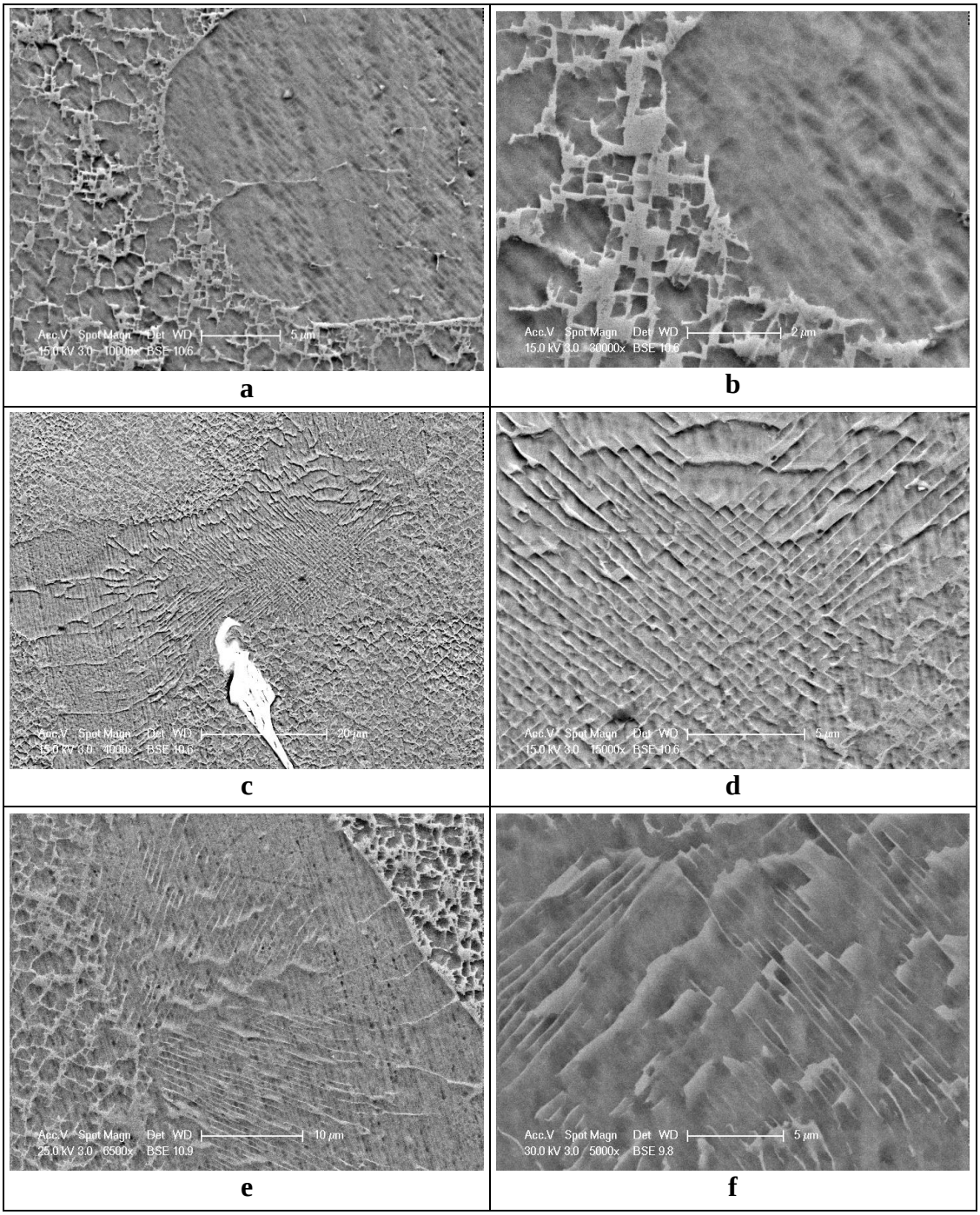

Figure 3.20. SEM photos at two different magnifications for the three morphologies of Figure 3.19. (a) and (b) represent morphology number 1, (c) and (d) represent morphology number 2, and (e) and (f) represent morphology number 3.

The first solid that forms is the γ phase that nucleates directly from the liquid. After formation of the γ dendrites, the large γ' islands are formed in the interdendritic region. Towards the end of the solidification, the large islands of γ' forms from the remaining liquid and γ via eutectic reaction. Then in the next stage, the γ' thickens towards the center of the interdendritic zone.

These γ' islands (Figures 3-20a and b) are the most prevalent type of the γ' that are solely seen in the interdendritic regions. They are undesirable, as long time is needed for dissolution of these large precipitates during homogenization heat treatment.

The other structure which is seen sometimes is a mosaic shaped γ–γ' eutectic, which is numbered 2 in Figure 3.19. Fine eutectic structure forms from a large number of solid nucleus on the primary γ. They grow fan out into the melt towards the center of the interdendritic region while the remaining liquid is progressively enriched with the γ' forming elements. The larger γ' are formed in the center of the interdendritic region. A higher magnification revealed a faceted/non-faceted eutectic growth morphology (Figure 3.20d). These regions include eutectic mixture, which contain a large volume fraction, around 90%, of the γ' phase. In the end, when the supersaturation of the γ' forming elements increases, the large γ' islands forming the center of interdendritic region.

The precipitate morphology in region 3 is shown in Figures 3.20e and f. This is the fan-shape eutectic with the fine network of the γ–γ' continued by large elongated γ' islands. Since the optical microscope images are taken at 2-d, the shape of the eutectic region is determined based on the cut plane from the interdendritic region. Therefore, this morphology is not different from the mosaic eutectic. Again, solidification starts with formation of the γ phase. The non-equilibrium solidification of the interdendritic region due to segregation of the alloying elements creates regions of fine and coarse γ' in the interdendritic region. Fine fan-like precipitates start to form first on the γ phase followed by growth of the coarse precipitates. The reason for nucleation and growth of these fan-like precipitates on γ is to reduce the interfacial energy for nucleation on the solid γ rather than the liquid. The coarse precipitates impinge to the periphery lobe of the adjacent dendrite or to another coarse precipitates originating from the neighbor dendrite (Figure 3.21). The

fan-like eutectics have been proved experimentally to form first by quenching the interdendritic liquid [192].

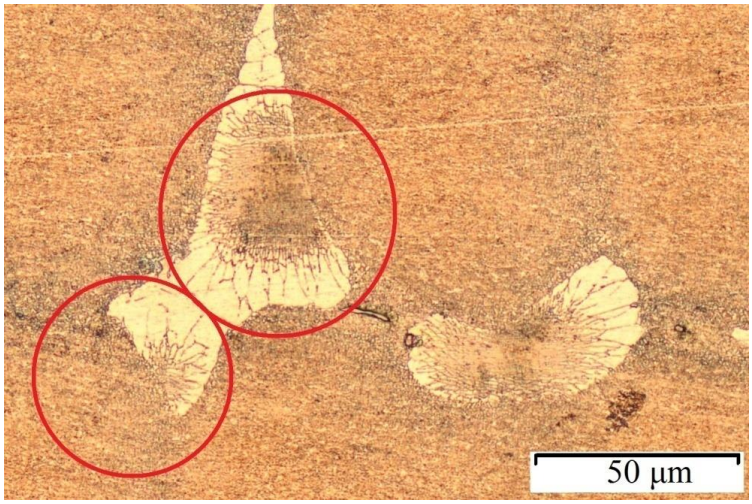

Figure 3.21. Microstructure of the interdendritic region showing the fan-like eutectics in the vicinity of the γ dendrites and impingement of large γ' (red circles) from two dendrites at the interdendritic region.

3.3. Microstructure of the Grown Single Crystal Superalloys

In this section, the microstructure characteristics of the as-cast samples of ERBALLOY will be discussed based on the growth velocity and method. The microstructure characteristics to be considered are the single crystallinity, dendrite core size, primary dendrite arm spacing (PDAS), mushy and melt-back transition region length, and microporosity content. Prior to the solidification of the designed ERBALLOY, the solidification system was investigated by using the CMSX-4 commercial alloy.

3.3.1. Solidification versus Withdrawal Velocity

To gain an insight into the solidification of the superalloys, in four separate solidification experiments, a thermocouple is placed in a one-end-closed alumina tube and positioned near the solidification interface. This has allowed recording of the temperature profile before and during the solidification. Moreover, the position of the interface was identified by dipping an alumina rod to touch the solid interface at different time intervals.

The solidified length, interface displacement, interface velocity, and initial interface temperature per distance traveled by the moving crucible are shown in Figures 3.22a to d.

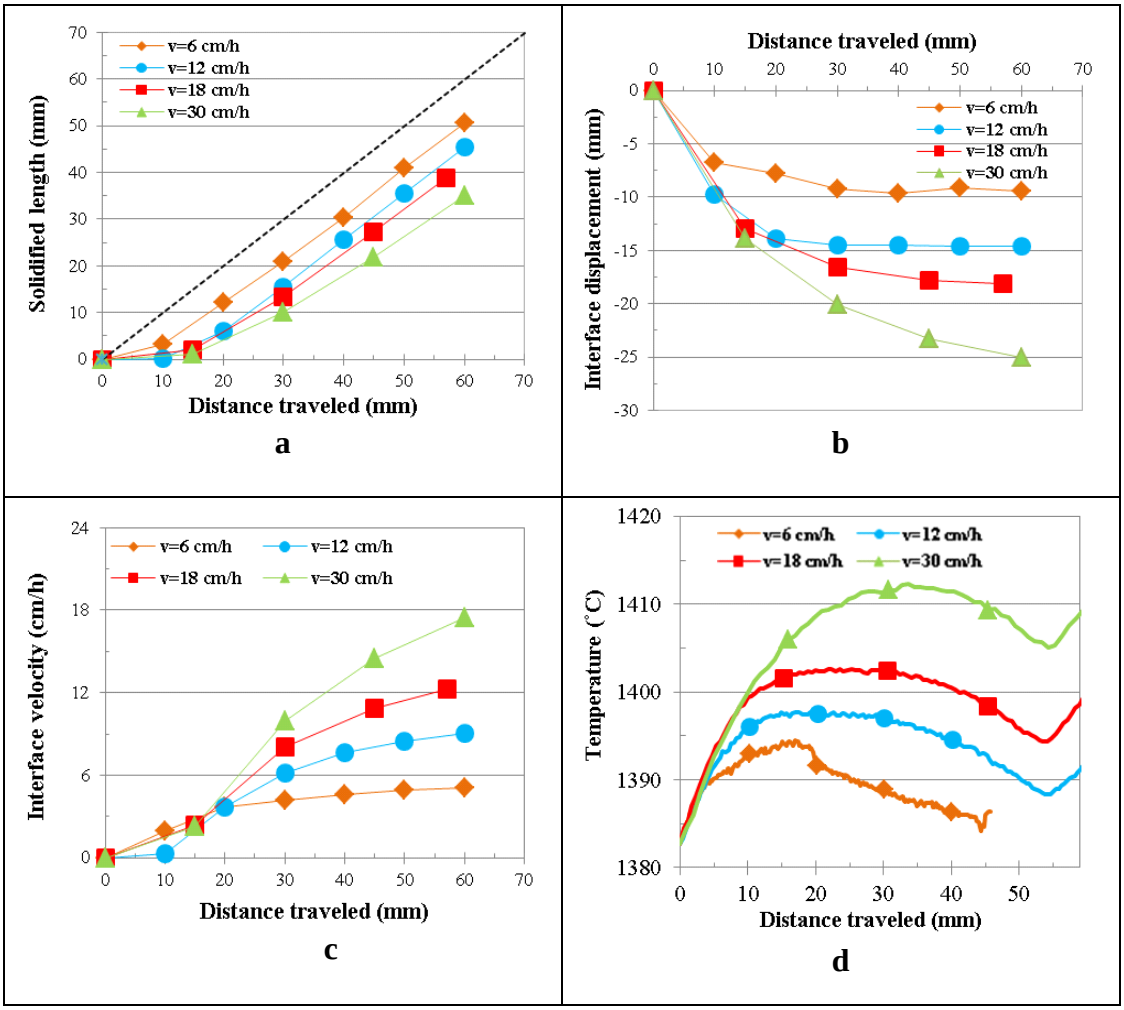

Figure 3.22. The solidified length (a), interfaces displacement (b), and interface velocity during solidification with different crucible pulling velocities. The dashed line in (a) shows the case when the solidified length would be equal to the pulling velocity.

As seen in Figures 3.22a to c, at the early stages of the withdrawal process, the solidification rate is very slow. Similar to that reported in [192], greatest crucible displacement rate in this current study (30 cm/h) produces the lowest crystal growth (solidification) rate (Figure 3.22a), and so the highest interface displacement backward (Figure 3.22b). At travelled distances up to about 15 mm, the solidification velocities are all less than 3 cm/h at all withdrawal velocities (Figure 3.22c). The thermocouple inserted to record the temperature shows a sharp increase in the temperature at the earlier stage of

the solidification. The rate of increase is dependent of the withdrawal velocity, and it is lower for the low withdrawal velocities. It reaches a maximum, and then there is a drop in the temperature. There is a sharp drop at around 20 mm for 6 cm/h experiment that is due to a thermocouple failure, but the trend is still seen. This increase in the temperature of the initial interface shows that the latent heat of the solidification is not effectively extracted from the system at the start of the solidification. Therefore, there is a transient period during the withdrawal. This transient stage affects the microstructure, as it will be shown in the following sections.

3.3.2. Orientation of Dendrites

Figure 3.23 shows the longitudinal microstructure of the ERBALLOY samples VB12 and VBSB12. It is seen that the structure shows well-aligned dendrites in the growth direction. The interface is apparent in both figures separating the mushy zone of the seed and newly grown crystals. Misoriented dendrites are observed above the initial interface. They disappear from the structure as solidification continues because their growth is hindered by growth of the dendrites well aligned with the growth direction. There is a unique region below the initial interface that shows a cellular microstructure which is known as the melt-back transition region. The length and characteristics of the melt-back transition and mushy zone will be discussed in the next section.

The quality of the single crystals is assessed by the x-ray diffraction (XRD) method. This technique provides overall orientation of the grown crystals. A single diffraction peak present in the XRD pattern indicates a single crystal.

Figure 3.24 shows the XRD pattern of the two samples VB12 and VBSB12 at four different elevations (-5, 0, 5, and 10 mm) from the initial interface. These elevations are numbered I-5, I0, I+5, and I+10, respectively. It is seen that both of the figures show the peaks at 2ɵ angle of around 50° for the I-5, I+5, and I+10. The corresponding plane is then determined to be the (200) which belongs to the family of planes {100}. This peak has the greatest intensity in the plot. The strong texture observed for the grown crystals shows that the dendrites are well aligned in the direction of the growth [001]. A small peak observed for the I0 samples corresponds to the (111). Since I0 is a sample from the interface, the

XRD pattern shows the characteristics of the transition region that contains misoriented dendrites as stated before.

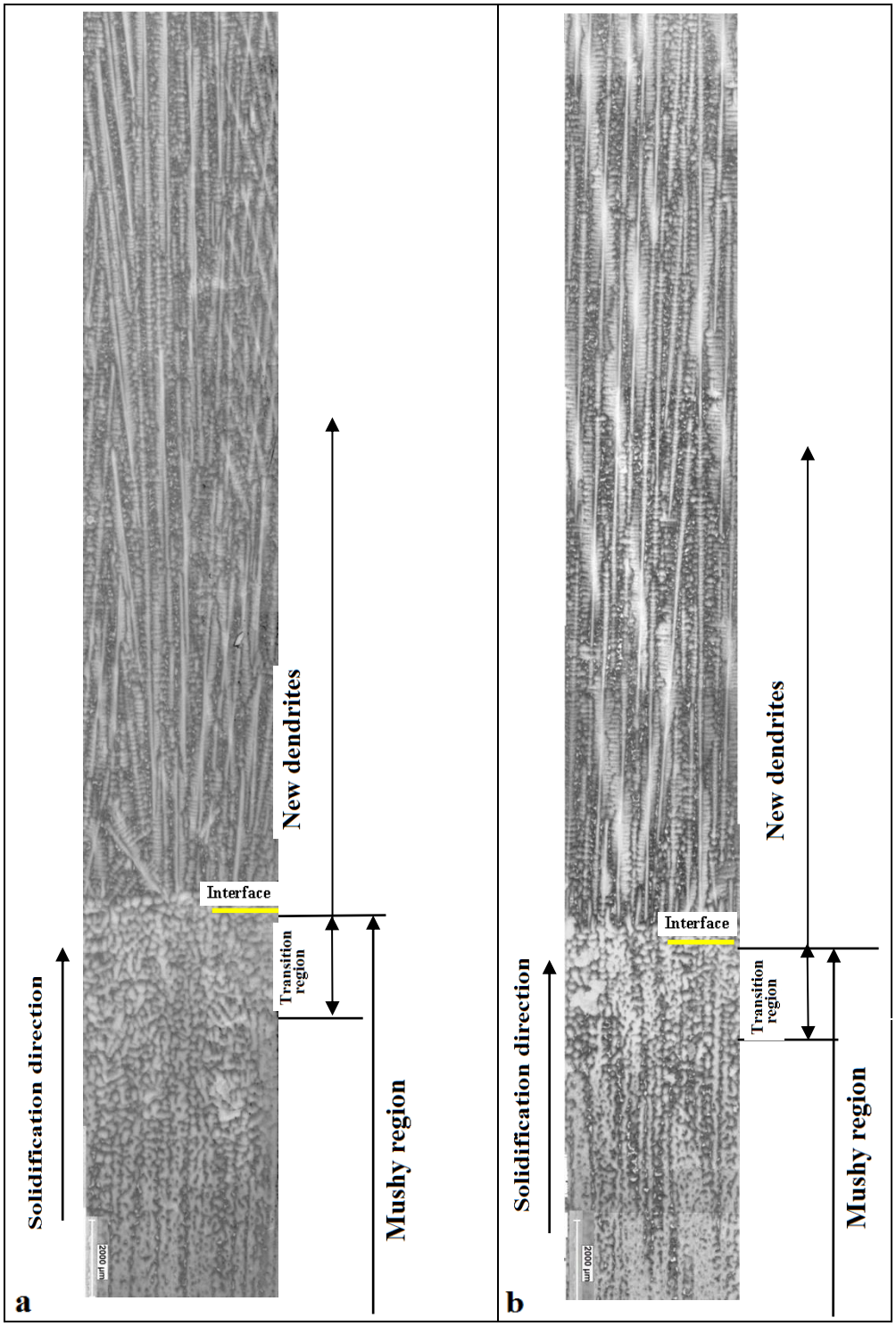

Figure 3.23. The longitudinal microstructure of the samples VB12 (a) and, VBSB12 (b).

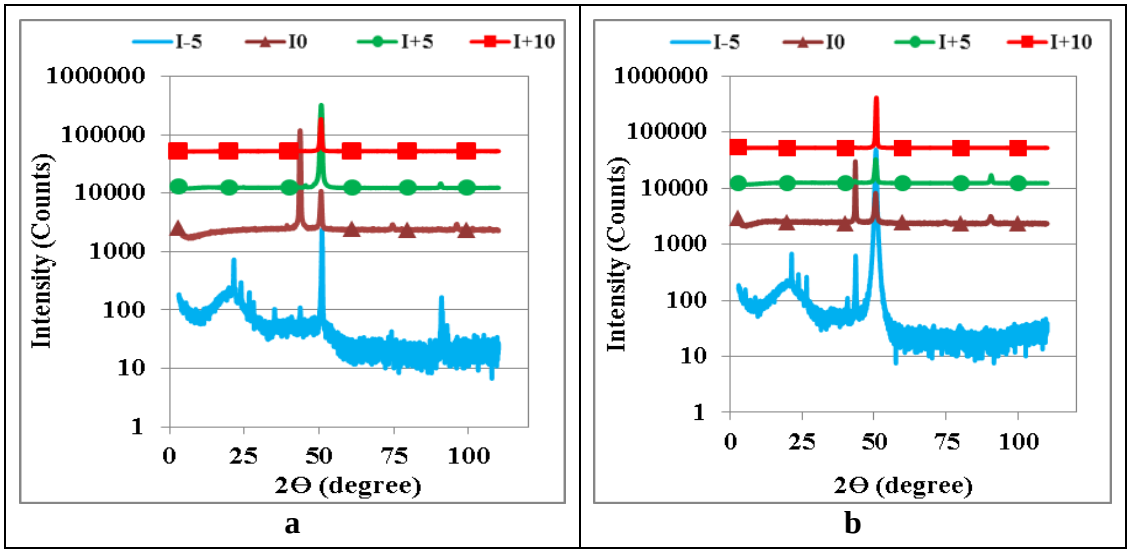

Figure 3.24. The XRD pattern obtained for the samples of (a) VB12, and (b) VBSB12.

3.3.3. Mushy Zone and Melt Back Transition Region

There is usually an undercooled region ahead of the solid/liquid interface during solidification of superalloys with commercially viable velocities. This undercooled region allows the solid to protrude into the liquid that leads to formation of a cellular or dendritic structure. The temperature varies from the tip to the root of a dendrite. As such, the liquid and solid coexist in the undercooled region that is named as the mushy region. Solidification starts at the liquidus temperature of an alloy that is dependent of the chemical composition. As temperature decreases, the fraction of the solid increases and it reaches 100% below the solidus temperature. To investigate the microstructure of the mushy region at any specified liquid fraction, the solidifying sample can be quenched [193,194]. By this approach, the mushy region and its dendritic and interdendritic patterns could be observed and analyzed. If the part is allowed to solidify and cool down to the room temperature, the initial mushy region at the single crystal seed could still be observed and analyzed, which is the case in the present study. The microstructure of the mushy region of the seed is analyzed by means of optical microscopes. A typical microstructure of this region for the sample ERBALLOY VB12 solidified at the withdrawal velocity of 12 cm/hour is shown in Figure 3.25. Figure 3.25a shows the initial interface for the solidification of the seed. The aligned dendrites are visible just above the interface. However, the microstructure of the region below the initial interface is not perfectly

dendritic. Figure 3.25b shows the transverse microstructure of the VB12 sample at 5 mm below the initial solidification interface (I-5). The microstructure shows that the preexisting dendritic microstructure of the seed is destroyed at this region. This region is called the melt-back transition region where the volume fraction of the liquid could reach more than 90%. Since this region is exposed to the flow of the bulk fluid, the secondary dendrite arms have been dissolved and the columnar trunks of the dendrites have remained. This effect extends to some depth inside the mushy region and gives this region a characteristic of a melt back transition region.

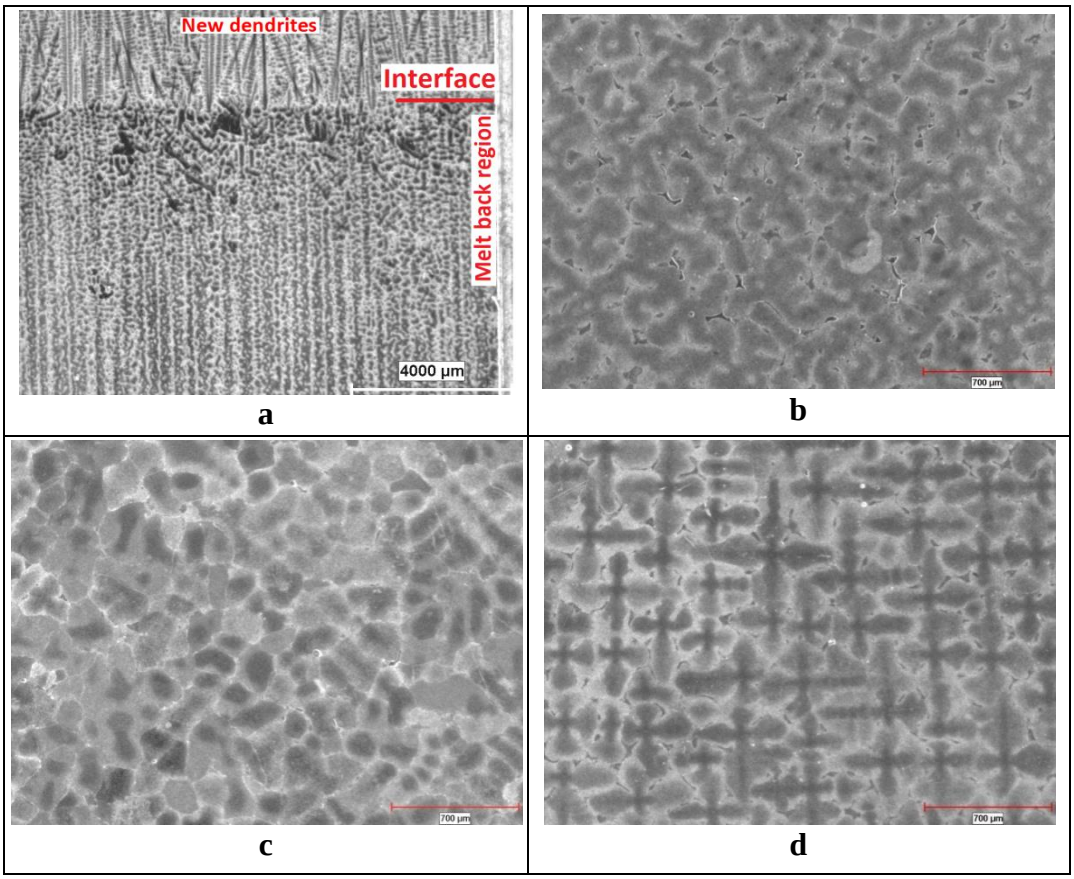

Figure 3.25. The initial solidification interface, melt-back transition region, and the new dendrites above the interface of sample VB12 (a), and transverse microphotos at I-5 (b), I0 (c), and I+5 (d).

The disturbance in the mushy zone due to the flow of the bulk liquid destroys the dendritic morphology of the seed and creates a region with misoriented dendrites before and at the start of pulling the crucible. Figure 3.25c shows the transverse microstructure of

the sample exactly at the interface (I0). At the interface, most of the secondaries are melted and the microstructure adopts a cellular structure. The primaries are the last to melt, but in the top portion of the melt-back transition region, melting and dissolving of the secondaries and even primaries is apparent. Figure 3.25d shows the dendritic microstructure of the sample at I+5 position. After the initial transient stage of solidification, the steady state solidification governs the rest of the solidification.

Close observation of the new dendrites above the initial interface shows that many dendrites nucleate at start of the solidification, but after a few millimeters, the number of the dendrites is decreased as seen in Figure 3-25 and will be disused later in primary dendrite arm spacing. Moreover, the dendrites, which are not well aligned with the growth direction <001>, are suppressed in this interval. This is more apparent at distances up to almost 1mm above the interface. It might be possible that as solidification starts, sparsely spaced primaries in the melt-back transition region may grow their secondary dendrites. Then new primary dendrites may form as tertiaries on these secondary dendrites.

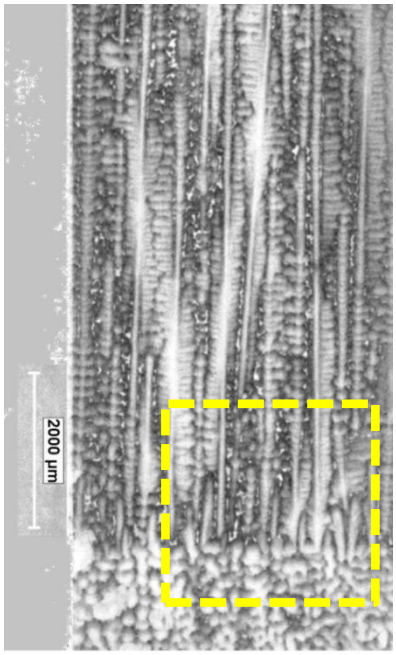

Figure 3.26. Nucleated dendrites at the start of the withdrawal process. The yellow box shows the transient stage at the start of the withdrawal process showing dendrites which are not well-aligned with the growth direction are suppressed after the transient stage.

The other parameters that affect the solidification characteristic and especially the extent of the melt-back and mushy regions, are the thermal gradient and withdrawal velocity. High thermal gradient and withdrawal velocity will decrease the length of the mushy region.

The experimental results for solidification of the CMSX-4 showed [29] that the length of the mushy zone and the transition region is pulling velocity dependent and increases with increasing the pulling velocity. Similar results are observed with the solidification of the ERBALLOY with two withdrawal velocities of 12 and 30 cm/h in Figure 3-27. The melt-back transition region and mushy region lengths increase with the withdrawal velocity. It is seen in Figure 3.20d that at the earlier stage of the solidification there is a heat release towards the liquid that increases the temperature of the liquid close to the interface. This increases the fluidity of the liquid and hence the liquid could flow more easily in the interdendritic region. This could dissolve the secondary dendrite arms of the seed region close to the interface to some depth and leave the transition region. This liquid could also flow to some deeper depth and leave the mushy region. This effect is higher for the velocity of 30 cm/h, and for this reason, the transition and mushy regions are longer for this sample. The results of Figure 3.22d showed that at the same values for the travelled distance, the heat release is higher in the velocity of 30 cm/h compared to 12 cm/h. Thus for a given crucible displacement, 30 cm/h experiment shows the lowest growth (Figure 3.22a) and so the highest interface displacement backward (Figure 3.22b). Since the solidification is sluggish for the fastest velocity, the hot melt flow can penetrate deeper into the mushy region in the beginning, which yields the data given in Figures 3.20a and b. Furthermore, when Figure 3.20c is considered, it is seen that a faster velocity brings down a hotter liquid from the bulk to the interface. This hot liquid should influence the sluggishly growing mushy region more. Furthermore, Figure 3.27 demonstrates that the VBSB samples show a lower length for the mushy zone and the melt-back transition region which may point to a convective melt flow for the VB samples and a diffusive (conductive ≈ tranquil) flow for the VBSB ones. The low gravity (less convection) experiments have already showed thinner mushy layers compared to the terrestrial samples with similar growth parameters [195,196]. Hence, the VBSB method mimics the diffusional growth mode, which is dominant in the low gravity space environments. Of course, a lowered

mushy layer thickness has its benefits in terms of reducing the formation of stray grains, freckles, and pores in a directionally solidified sample.

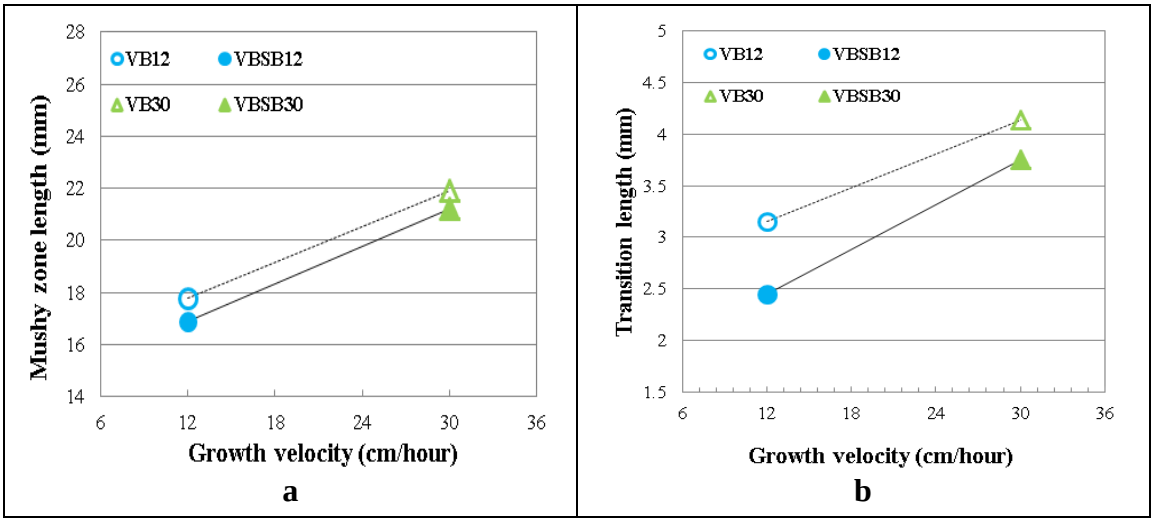

Figure 3.27. The mushy zone length (a), and the transition length (b) for the ERBALLOY samples solidified with the vertical Bridgman (VB) and the vertical Bridgman with a submerged baffle (VBSB). Numbers following the method abbreviation in name labels show the pulling velocity

3.3.4. Primary Dendrite Arm Spacing and Core Size

The microstructure of the ERBALLOY at velocities of 12 and 30 cm/hours are shown in Figure 3.28. The dendritic microstructure is observed for these samples. In fact, the combined effect of the thermal gradient and the solidification velocity has yielded the dendritic microstructure.

Our previous experiments with the alloy CMSX-4 [197], showed the columnar microstructures formed at withdrawal velocity of 6 cm/h. At a higher velocity of 12, 18 and 30 cm/h the microstructure was dendritic similar to ERBALLOY. Since no alloy was solidified at the velocities in between these 6 and 12 cm/h, the threshold withdrawal velocity for dendritic to columnar morphology was not detected at that experiment. Based on that experience and since similar solidification furnace was used for the CMSX-4 and ERBALLOY, the withdrawal velocities greater than 12 cm/h was chosen for ERBALLOY to yield the dendritic microstructure. Figure 3.28 shows also that ERBALLOYS solidified

at higher velocity (30 cm/h) have more tertiary arms grown on the secondaries. The reduced longitudinal directional heat extraction from the bottom of the seed at higher withdrawal velocities, results in radial heat transfer and growth of the tertiary arms and elongation of the secondary dendrite arms.

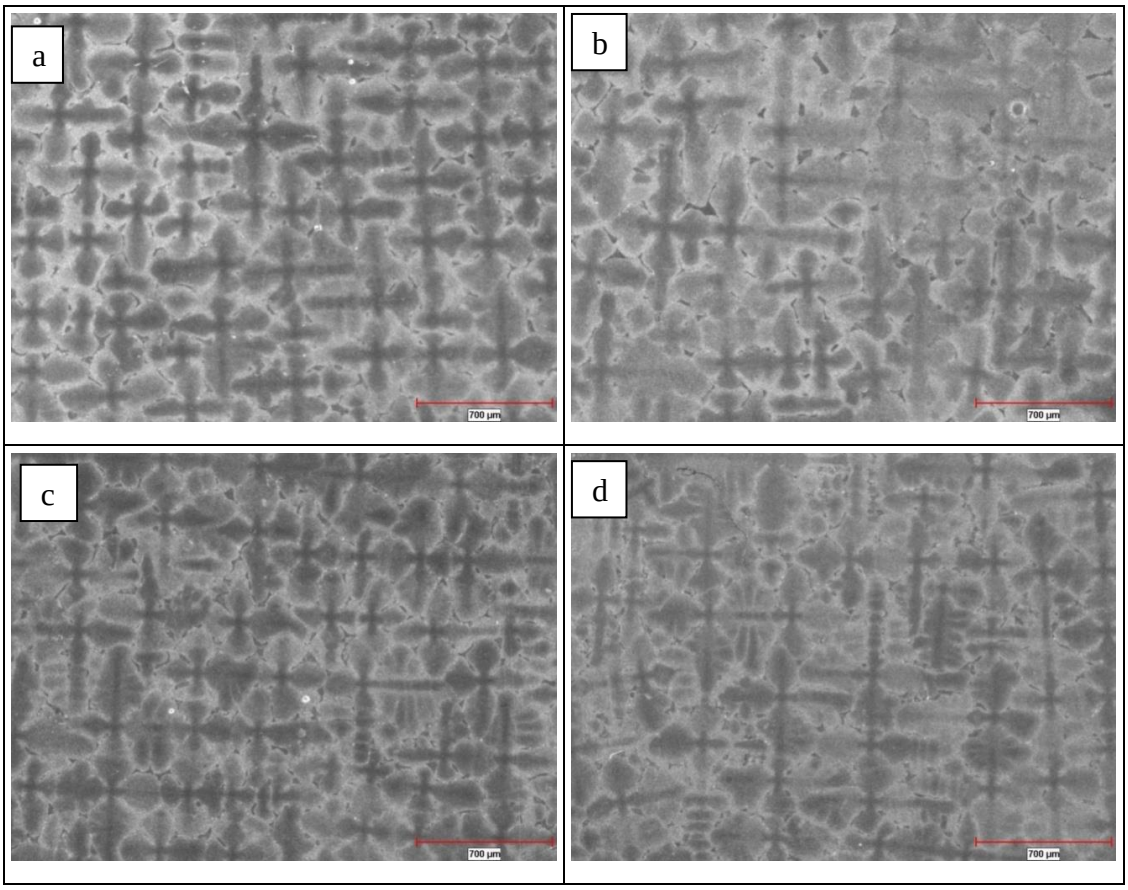

Figure 3.28. Transverse microphotos of ERBALLOY samples grown with the VB and VBSB methods with different growth velocities, (a) VB12, (b) VBSB12, (c) VB30, and (d) VBSB30. Numbers following the method abbreviation in labels show the pulling velocity.

The three important parameters that determine the solidification mode of the alloys are the temperature gradient in the liquid, solidification velocity, and extent of the segregation in front of the solidification interface. The solidification velocity is directly related to the cooling rate, which depends on the withdrawal velocity of the crucible in the furnace and cooling capacity of the system. Temperature gradient is directly imposed via furnace. The segregation of the alloying elements differs based on the alloys studied and is determined from the phase diagram. In a specific alloy, alloying elements are divided in

three groups. Alloying elements with segregation ratio less than 1 tend to segregate to the liquid while solidification. On the other hand, alloying elements with segregation ration greater than1 segregate to the solid. Alloying elements with segregation ratio close to 1 do not show strong segregation tendency either to the solid or to the liquid. The situation will be more complicated for single crystal superalloys with more than ten alloying elements. For Example, in ERBALLOY, the refractory elements Re and W show apparent segregation towards the solid, while Ta and Al have the segregation coefficients below 1 and segregate to the liquid. The different segregation ratios for the alloying elements will create solute redistribution profile in front of solidification interface. This profile will exist up to a distance inside the liquid. The higher thermal gradient and in the liquid ahead of the solidification interface will reduce the length of the undercooled region. The presence of the undercooled region will change the equilibrium liquidus temperature of the alloy in this zone. If sufficient concentration of alloying elements is accumulated in front of the interface, even under sufficient positive thermal gradients, a constitutional undercooling will exist in front of the interface. In other words, redistribution of the solutes will cause the liquid ahead of the solidification interface be cooler than the equilibrium liquidus temperature. Any instability in the interface towards the liquid will experience an undercooling which leads towards formation of the primary, secondary and even the tertiary dendrite arms. Huijuan Dai [198], showed that in a typical binary alloy of Ni and Ta with segregation ratio less than 1, undercooling is highest at the groove between the two primary dendrites and decreases by distance from the dendrite tip. He also showed that the maximum undercooling increases linearly with the growth velocity because of increased rate of solute rejection to the interface. The transition from columnar (cellular) to dendritic structure is closely related to the concentration profile of the alloying elements in front of the solidification interface. Although main solidification direction may be axial, radial temperature gradients and solute accumulations, with creation of the constitutional undercooling, allows for nucleation and growth of the secondary dendrite arms. Further undercooling on the surface of the secondary dendrite arms can trigger a tertiary dendrite formation. The tertiary dendrites are especially seen in Figure 3.28d at the velocity of 30 cm/h.

A minimum of six photos from different radial locations in a transverse section have been used to determine an average PDAS for a section, knowing that the PDAS may vary

within a size band [199,200].The results for the dendrite core size and PDAS variation along the sample is shown in Figure 3.29.

The core size and PDAS at elevations 5mm below the interface and at the interface could not be measured exactly due to dissolution of the secondaries and impinging of the primaries into each other, therefore the results of Figure 3.29 is presented for elevations after 5mm. Despite the observed fluctuations, the PDAS increases both in the VB and VBSB samples along the solidified length. Moreover, the PDAS is larger for the higher growth rates. In addition, compared to the VB samples, the VBSB samples show a slightly larger PDAS at velocity of 12 and the average PDAS value is almost the same in both the methods.

A close observation of the longitudinal micrograph a VB12 sample (Figure 3.30) shows that many dendrites are suppressed during the early stage of solidification due to competitive growth, and for this reason, the PDAS should have the lowest value at the interface. The survived dendrites again compete with each other and this is more apparent in the initial stages of the solidification. The dendritic spacing then may evolve towards a stable [199], and in the current samples, a larger spacing. The fluctuations in measured dendrite core and PDAS then could be related the competitive growth of the dendrites which is more apparent at transient stage.

A larger PDAS with a higher growth velocity is in agreement with the literature [199] for a low axial temperature gradient (<28 °C/cm). As solidification proceeds by pulling the crystals downward inside the furnace, the interface position may also shift down into cooler regions as shown in Figure 3.22b. This is more apparent in the highest pulling velocity. Once the interface is shifted down, radial temperature gradients may become influential since the axial gradient in the current growth system is low (~24 °C/cm). Then, the growth of the secondary/tertiary dendrite arms in the radial direction can increase the PDAS more in the faster grown samples.

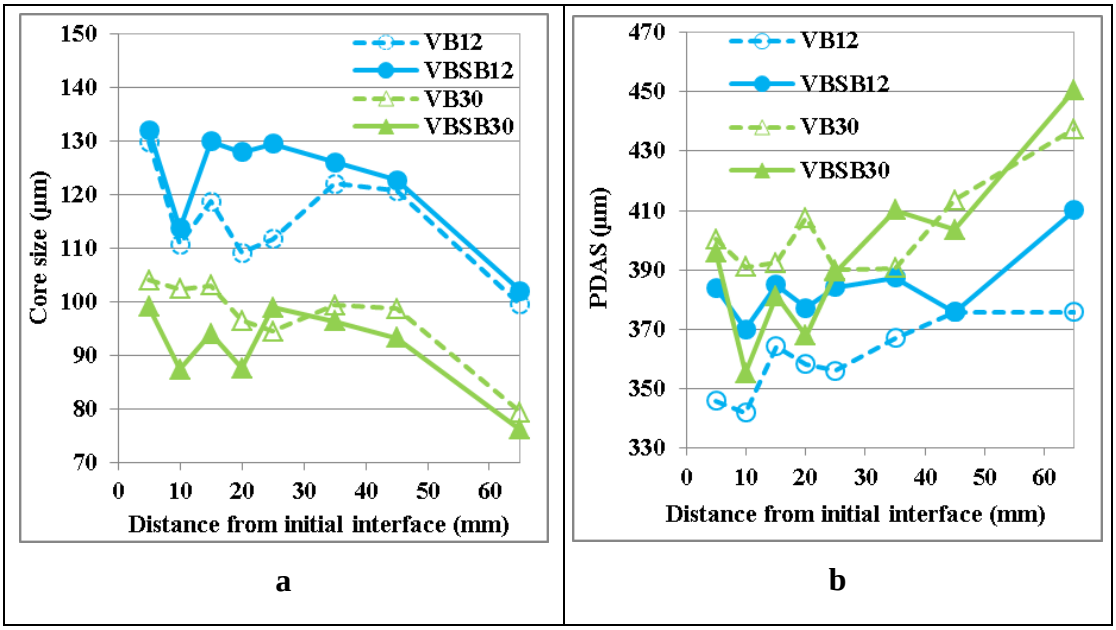

Figure 3.29. The primary dendrite arm spacing (a), and the dendrite core diameter (b) along the lengths of samples solidified with the VB and VBSB methods. Numbers following the method abbreviation in labels show the pulling velocity.

The overgrown tertiaries and its effect on the distance between primaries are shown in Figure 3.30.

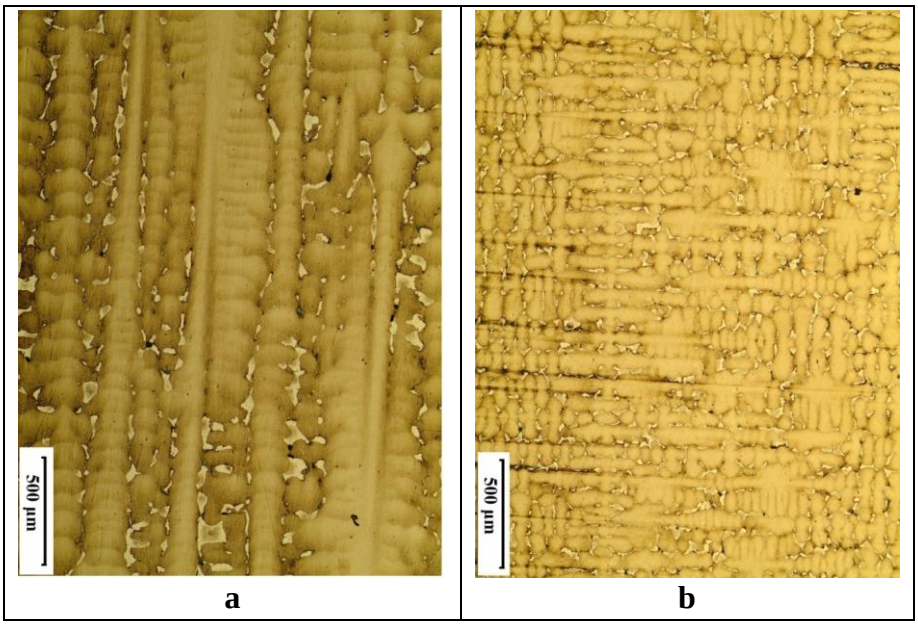

Figure 3.30. Longitudinal photos of the dendritic structure of the VB12 at elevations (a) 25, and (b) 65mm above the interface.

Figure 3.30 a, and b show the longitudinal photo of the dendritic structure of the VB12 at elevations 25 and 65mm above the interface. The overgrown tertiaries are apparent in Figure 3.30 b. Towards the end of the withdrawal process and when the crucible moved down 65mm, then the furnace was shut down, and for this reason, the heat transfer occurred in the radial direction which caused fast growth of the secondaries in this direction. The overall effect is considerable increase of the PDAS.

In addition, the dendrite core size, shown in Figure 3.31a, is higher for the velocity of 12 cm/h than 30 cm/h for the both methods. Indeed, to adjust to a faster growth rate, the dendrite tips get sharper to have increased s/l interface for higher rejection of the solutes. That yields thinner dendrite cores. These results are consistent with diffusional growth modes [201].

The larger PDAS value for VBSB samples is attributed to a suppressed convection due to reduced melt height in the VBSB samples. A suppressed convection enables diffusional growth. In contrast, convection could decrease the PDAS by forming new primary dendrites from the tertiary dendrites [201]. The effect of reduced convection on the core size is not as obvious, although it is evident in the lowest growth velocity of 12 cm/h; the VBSB12 sample shows the greatest core size. It seems that velocity determines the core diameter as stated above.

3.3.5. Porosity

The microporosity in a solidified part is determined by the solidification parameters. Microporosity is classified into two main groups as the solidification shrinkage and gas porosities. Shrinkage microporosity forms during the last stage of the solidification where there is not enough liquid flow to compensate for the solidification shrinkage due to phase change from the liquid to the solid. The other source of the microporosity is the gasses that are released due to the lower solubility of the gases in solid than the liquid. The released gases will form micropores if they reach a critical radius required for nucleation of the gas bubbles, which generally takes a spherical shape. Microporosity is one of the main reasons for rejection of the Ni base turbine blades. Moreover, the presence of microporosity gives a high scattering on the creep rupture test results [189].

Although there are many studies [202,203] regarding the effect of withdrawal velocity on the dendritic characteristics of the superalloys, there are few studies for the effect of the withdrawal velocity on the interaction of the microstructural features (primary dendrite arm spacing, mushy and melt-back zone length) and the porosity level. Some researchers [204,205] have shown that there is an optimum withdrawal velocity to attain the lowest porosity. This optimum velocity depends on the alloy composition. Our previous research with the alloy CMSX-4 with three withdrawal velocities of 12, 18 and 30 cm/h with the thermal gradient of 24°C/cm showed that the porosity increases from 12 to 18 cm/h and then decreases for the withdrawal velocity of 30 cm/h [29]. The current study addresses the mentioned items on the third generation ERBALLOY.

Figure 3.31 a, and b shows that the microporosity (black areas) is located mainly in the interdendritic regions. Moreover, they are irregular in shape, which indicates the fact that they are solidification shrinkage microporosities concurrent to the formation of the eutectics at the end of the solidification.

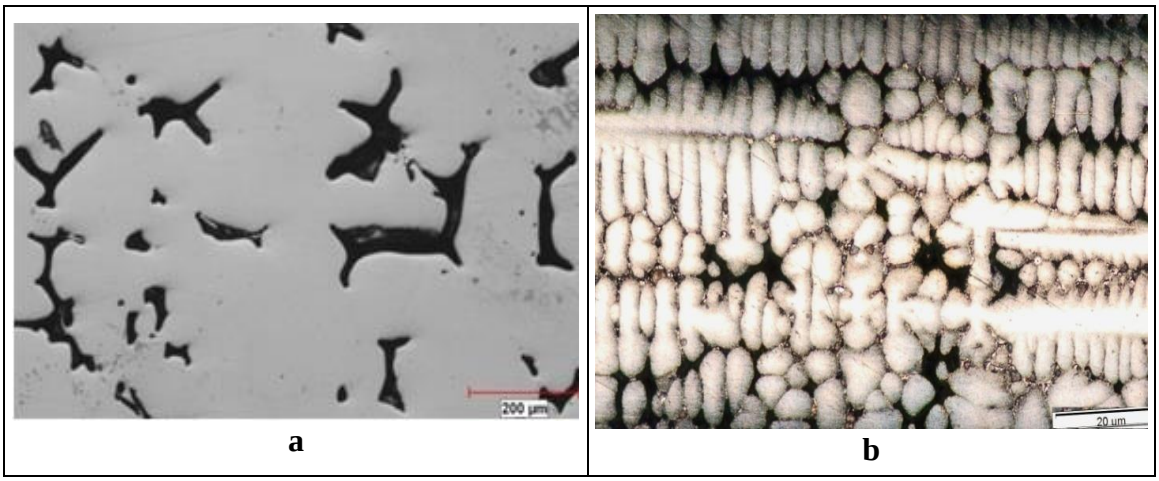

Figure 3.31. Solidification shrinkage microporosity (seen as dark) in the VB12, (a) transverse section, and (b) longitudinal section.

Analysis of the pore size along the solidified bar is shown in Figure 3.32. It is seen that the pore size generally varies between 5 and 10 µm. Moreover, the pore size in general increases slightly from the initial interface towards the top of the sample. Due to the

presence of the large solidification microvoids at the top end of the solidified bar (65 mm from the interface), the analysis of these areas is excluded.

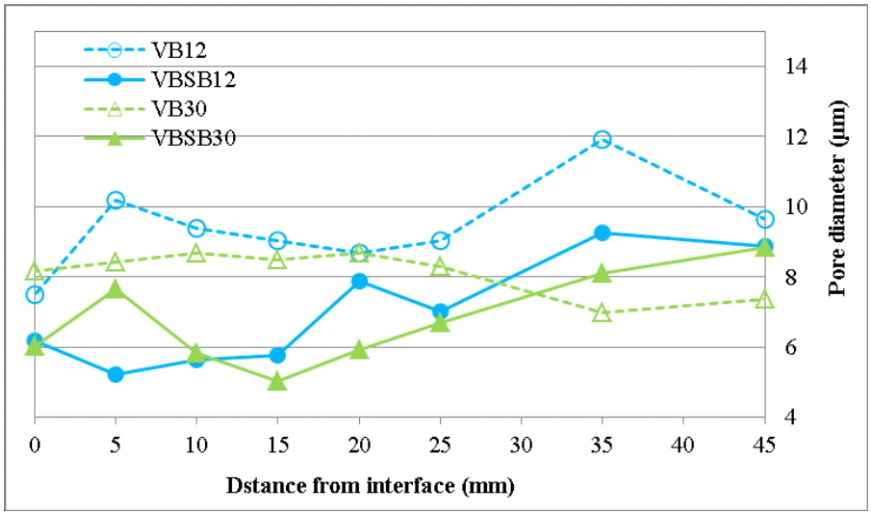

Figure 3.32. The pore diameter in the ERBALLOY, showing a general increase in pore diameter with the distance from initial interface.

The average pore area fraction in the samples is shown in Figure 3.33.

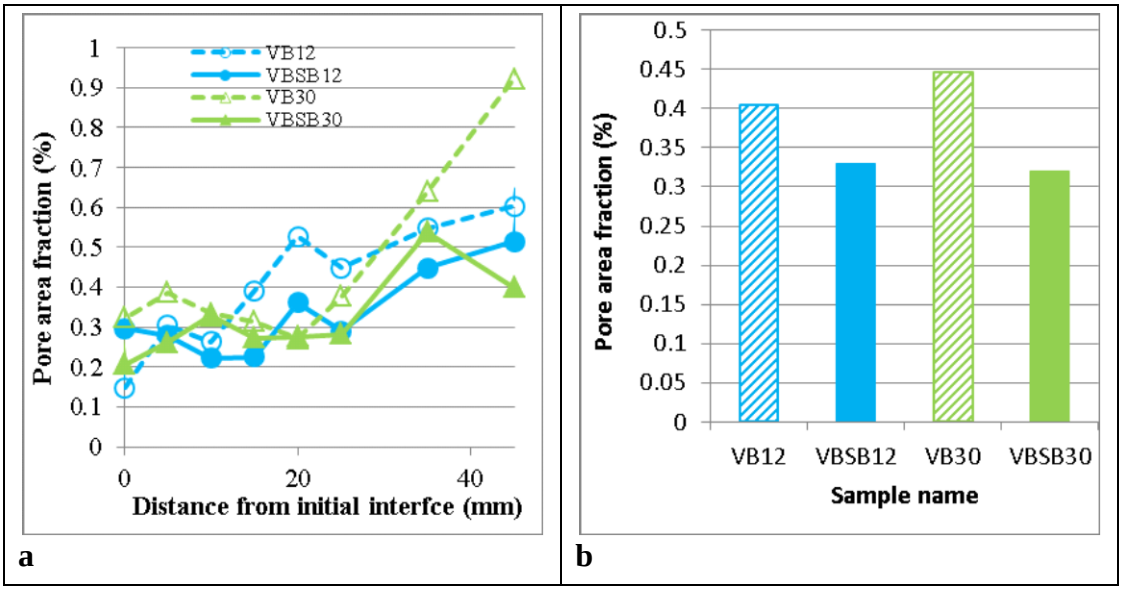

Figure 3.33. Pore area fraction percentage for the four samples along the solidified length (a), and the average pore area fraction of the samples (b).

The porosity content increased from the velocity of 12 cm/h to 30 cm/h. The results for comparison of the VB and VBSB methods showed that VBSB method yields lower microporosity level.

The porosity content varies with the solidification mode. There i no definite acceptance criteria for the porosity level in superalloys. However, the average volume fraction of the pores has been found to be 0.145% for the columnar alloy CMSX-6, 0.3% for the single crystal CMSX-10, and 0.28% for the single crystal MC-NG superalloys [206]. The difference between these two methods is the presence of the grain boundaries in the columnar growth. The other main parameters that could affect these values are the thermal gradient, growth velocity, and the permeability of the interdendritic region [207]. Among the many parameters, the withdrawal velocity is a more important parameter.

Microporosity occurs when the total pressure in the liquid is less than a critical pressure that is necessary to move the liquid through the capillary feeding in interdendritic regions. The total pressure could be written as following [189].

$$P_t=P_A+P_\rho+P_\sigma-\Delta P-P_G \tag{3.5}$$

Dissolved gas pressure (P_G) and pressure drop (ΔP) due to solidification within the mushy region are the parameters that help for nucleation of the pores. On the other hand, atmospheric pressure (P_A), metallostatic head pressure (P_ρ), and surface tension related pressure (P_σ) [202,203] try to annihilate a pore. An imbalance of the pressure between the mentioned parameters leads to formation of the micropores. To avoid the pores to form, the P_G and ΔP should be minimized. P_G is proportional to amount of dissolved gas in the melt. The main parameter to consider in this formula is the pressure drop in the mushy zone or ΔP. As solidification proceeds, the solid fraction in the interdendritic region increases and the value of ΔP increases due to reduced permeability of the interdendritic region, which may lead to a case where the P_t becomes negative. Gas porosities could arise from the argon gas. Pressure drop (ΔP) in the capillary interdendritic tubes is determined by the Darcy's law [202,203] as given in Equation 3.6.

$$\Delta P=\frac{24\pi\mu\beta\Delta T\tau^3 V_s}{\rho_L gG} \tag{3.6}$$

where μ is the kinematic viscosity of the liquid, β is the density difference ratio along the mushy region, ΔT is the solidification interval, G is the thermal gradient, τ is the tortuosity factor of the interdendritic region, V_s is the withdrawal velocity, ρ_L is the liquid density and g is the gravity constant. The term ΔT could be expressed in terms of the L (length of the mushy region), and G_L (the thermal gradient in the liquid).

$$\Delta P=\frac{24\pi\mu\beta L\tau^3 V_s}{\rho_L g} \tag{3.7}$$

Considering a single alloy, the only variables in this equation are τ, L and V_s and the other parameters could be considered as constant. Viscosity (μ) and liquid density (ρ_L) is determined by the chemical composition of the alloy [1].Therefore, the equation could be written as:

$$\Delta P=A.L.\tau^3 V_s \tag{3.8}$$

where A is a material related constant and described as:

$$A=\frac{24\pi\mu\beta}{\rho_L g} \tag{3.9}$$

Equation 3.8 states that a reduced mushy zone length (L), solidification velocity (V_s), and tortuosity factor (τ) can reduce the pressure drop that tries to form a pore; consequently, the porosity may be reduced. The tortuosity factor of the interdendritic region is a dominant parameter that determines the pressure drop and affects the occurrence of the microporosity. The tortuosity of the interdendritic region is directly related to the fraction of the liquid, which varies along the mushy zone. Increased permeability of the interdendritic region decreases the tortuosity of this region. The fluid flow in the interdendritic region determines the distribution of the microporosity in the final part. Hence, the morphology of the dendritic microstructure and the characteristic of the mushy region are of great importance for the microporosity level. The low permeability of the fine dendritic microstructure could increase pressure drop and reduce the interdendritic liquid flow and increases the risk of nucleation and growth of the microspores. On the other hand, in a coarse dendritic structure with secondary and tertiary

dendrite arms, pores may be isolated and hence their limited growth can reduce the microporosity. In fact, these two competing effects determine the final pore content in a dendritically solidified part [208]. Figure 3.34 shows transverse view of the dendritic structure of the VBSB12 sample. The last solidified slag at the interdendritic region could be representative of the interconnectivity of the interdendritic region and the path that liquid should flow to feed the area.

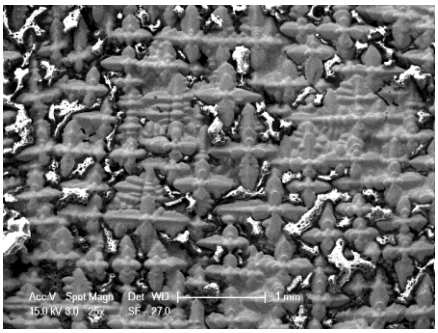

Figure 3.34. The top portion of the grown VBSB12 sample showing the interconnectivity in the interdendritic region resembling the fluid feeding path at the interdendritic region.

As discussed, the permeability of the mushy zone is an important factor in liquid feeding of the interdendritic region and annihilation of the pores, so the width of the interdendritic zone, estimated by subtracting the dendrite core size from the PDAS, is used to judge the permeability of the mushy zone (Figure 3.35).

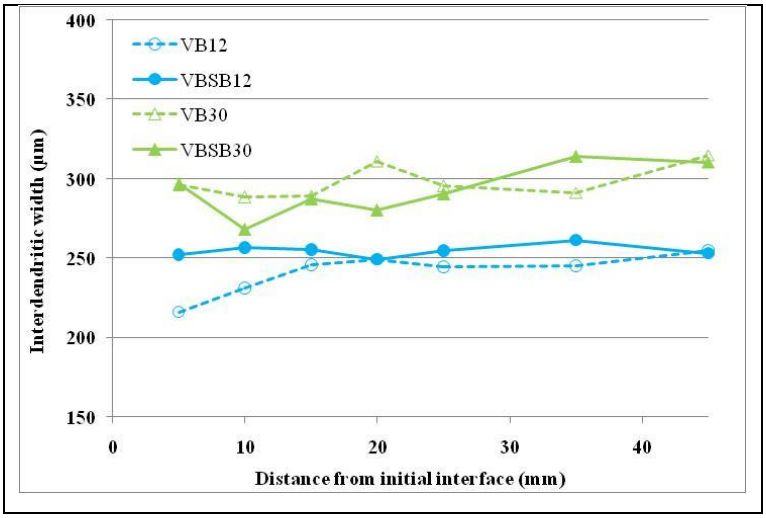

Figure 3.35. Variation of the interdendritic width along the grown samples.

Of course, this is a rough estimate, as it does not consider the secondary arm length and three dimensionality of the system. In fact, long secondary arms may prevent melt flow, but in a three dimensional space, the melt can flow around the dendrites. The interdendritic channel width increases with the growth velocity, which may indicate a higher permeability of the mushy zone with higher growth rates. Figure 3.35 also shows that the interdendritic zone width and consequently the permeability of the mushy zone are usually higher for the VBSB samples especially at the lower growth velocities.

The larger pores with distance from the initial interface show the exact influence of the dendritic characteristics on pore formation. This is an important finding, since considering each sample, all the material characteristics and also the solidification velocity is constant at all distances from the interface, however the porosity content and pore diameter increases with distance from the initial interface. In other words, all the parameters in Equation 3.9 are constant except the tortuosity factor and the metallostatic pressure of the remaining liquid. Therefore, considering the variation of the dendrite core size and PDAS with the distance from the initial interface, the dendritic characteristics are a determining factor on the microporosity level. The larger PDAS will lead to formation of the larger pores. On the other hand, it supports the very well liquid supply to mushy zone and hence reduces porosity. However, the metallostatic pressure of the remaining liquid is continuously decreasing which maybe the main reason for increased porosity content by distance from the initial interface.

The other observation is the effect of the growth velocity on the porosity level. According to Equation 3.9, the lower solidification velocity will lead to lower pressure drop. The lower porosity is observed for the samples grown with the velocity of 12 cm/h as seen in Figure 3.33. This can be interpreted by considering the core size and PDAS. Samples grown with this velocity have larger cores and lower PDAS that may imply a reduced permeability of the mushy zone. Nevertheless, a low level of porosity in this sample should be because of shorter secondary dendrites. By increasing the growth velocity to 30 cm/h, there is an increase in the width of the interdendritic channels; and there is a considerable increase in the microporosity. It seems that permeability of the structure has reduced considerably with this velocity. This might be due to an increase in

the mush length (Figure 3-27a) and especially due to elongated secondary dendrite arms as seen in Figure 3-25d.

Moreover, in all elevations from the initial interface, the VBSB samples show a lower porosity. The VBSB samples show up to 38 % reduction in the pore content, see Figure 3-33b. The interdendritic width is larger for the VBSB samples, which means more permeability of the dendritic structure of the mushy zone. Additionally, a larger spacing between the primary dendrites provides less nucleation sites for pores [19] and a better melt filling to the interdendritic region. The interdendritic feeding is also easier for the VBSB samples because of a lower mushy zone length (Figure 3-27a). In addition, a shallow mushy zone can allow annihilation of the gas pores. Indeed, in the presence of a gas in the melt, gas bubbles attach themselves to the baffle base and move with it out of the melt [29]. A similar behavior has been reported for the gas bubbles in the VBSB solidification of Al-4.5 % Cu alloy [209]. Hence, the content of the gas in the interdendritic region is lowered which subsequently reduces the P_G. Furthermore, as stated by 3.9, a reduced mushy zone length (L) in the VBSB samples decreases the ΔP. This equation also shows that a reduced melt flow velocity (V) can reduce the ΔP. In fact, the VBSB technique lowers the natural convection in the melt by a lowered melt height [5, 8, 24]. Consequently, the melt flow velocity in the interdendritic region decreases [9-12]. Thus, the VBSB method makes it possible to reduce porosity by weakening the effects of the two factors favoring pore formation, namely the P_G and ΔP in the interdendritic region. Kim and Abbaschian [209] have investigated the influence of both the P_G and ΔP on pore formation in their experimental study where a baffle has been employed to reduce the melt height. They have reported benefits of the baffle in reducing the porosity.

3.4. Heat Treatments of the Grown Single Crystal Superalloys

3.4.1. Solution Treatments

The solution treatment temperatures are selected to be between the solidus and solvus temperatures of the alloy. These two critical temperatures are calculated by Thermo-Calc in section 3.1.2 to be 1354 and 1230°C, respectively. Six different solution treatments are applied on cubic samples of the ERBALLOY with 3mm edge length taken

from 25mm above the initial s/l interface of the samples grown with the vertical Bridgman (VB) system with the withdrawal velocity of 12 cm/h. The mentioned solution treatments are designed to dissolve the γ' islands and remove the large elemental segregation between the dendrite core and interdendritic regions while avoiding incipient melting. After every solution treatment process, SEM microphotos are taken at different magnifications and are shown in Figure 3.36. The first column of this figure shows a low magnification of a typical dendritic structure. The second column shows the precipitate microstructure of the dendrite core. The third column shows the interdendritic region, and the fourth column shows the precipitates in the interdendritic region. The concentration profile of the samples is determined by means of EPMA along the secondary dendrite arms and extending into dendrite spacing. Moreover, the segregation coefficient is determined by dividing the average composition of the element at the core of the dendrite to the interdendritic region. The segregation ratios are shown in Figure 3.37.

The first raw of Figure 3.36 shows the as-cast-cast microstructure of the sample as a reference. As already discussed the as-cast structure composed of cubic γ' precipitates in the dendrite cores and large islands of γ' are seen in the interdendritic region. The interdendritic regions in the as-cast microstructure are interconnected and continuous around the lube periphery of the dendrite which will turn to fragmented isolated areas after solution treatment. The concentration profile shows a large gradient for the alloying elements from dendrite to interdendritic regions. The largest segregation is observed for the refractory elements (Re and W). On the other hand, Ta and Al have the smallest segregation coefficients (Figure 3.37a).

The first solution treatment that is tested is a single isothermal solutionizing of a sample. It is a short solution treatment for 4 hours at 1270 ˚C which is 40˚C above the solvus temperature of the γ' and the sample is named S1. The SEM microphotos show that the dissolution of the large islands of γ' phase s started in the interdendritic region (third column of the second raw). Compared to the as-cast structure, the segregation coefficient shows a sharp change towards the unity. To dissolve the γ' islands more and reduce the segregation, in the next step, the temperature is increased to 1290°C and the sample is named S2. The rise in temperature increased the dissolution rate of the coarse precipitates, but still huge γ' islands are seen in the interdendritic region (third raw of Figure 3.36).

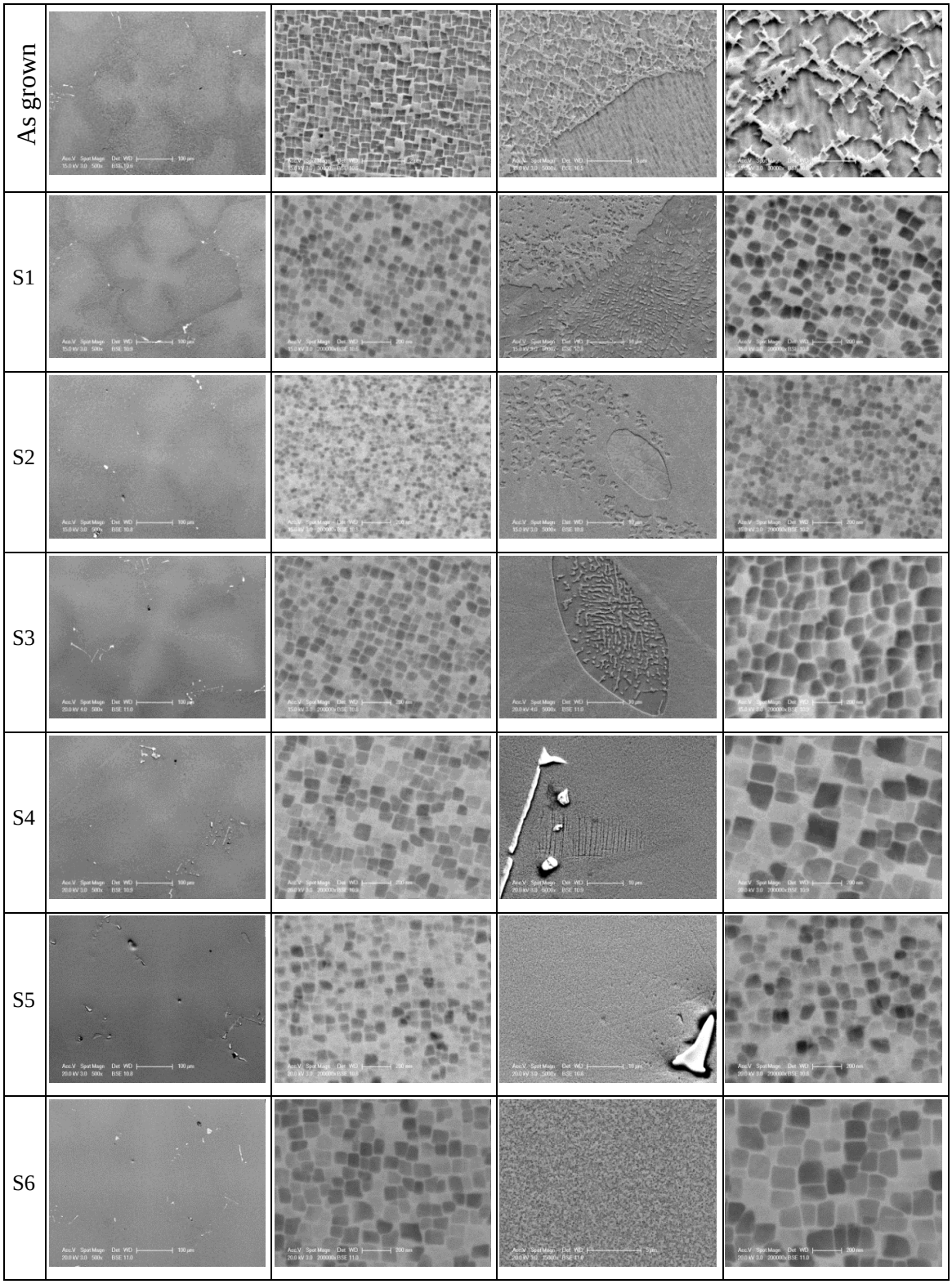

Figure 3.36. SEM photos of the VB12 samples for the as-cast and solution treated samples. First column shows the dendrites. Second column shows precipitates in the dendrite core. Third and fourth column show precipitates in the interdendritic region.

The concentration plots and segregation coefficients show a much better homogenization in the microstructure than S1 but still the segregation ratios are high. In the next stage, the temperature is increased up to 1315°C. In this sample, the heat treatment time is kept to be 4 hours similar to the samples S1 and S2 .This sample is named S3. The microstructure of the sample in different regions is shown in the fourth raw of Figure 3.36. It is seen that by increasing the solution treatment temperature, the strong segregation of the elements diminishes and becomes weaker. The concentration profile of the alloying elements along the SDA shows a segregation ratios get closer to the unity (Figure 3.37).

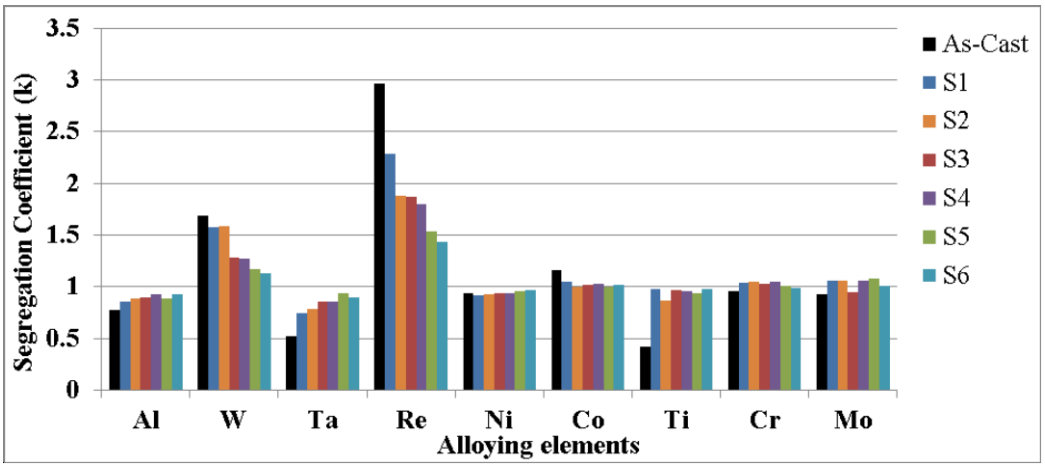

Figure 3.37. Segregation coefficients in the solution treated samples.

For the fourth sample (S4), a stepwise increase in temperature is applied as 1280 ˚C/2 h + 1290 ˚C/2 h + 1315 ˚C/2 h + 1320 ˚C/2 h. This sample shows more dissolution of the γ' eutectic islands (fifth raw in Figure 3.36) and the segregation is reduced significantly (Figure 3.37). It also shows signs of incipient melting (Figures 3.38), which causes the melting and recrystallization of low melting point regions (eutectics) which then appear mainly as porosities in the interdendritic zone. The ramped solution treatment is especially designed in this study to gradually dissolve these eutectic pools and homogenize the microstructure to avoid the incipient melting of the alloy. The obtained results suggest that the solution temperature should not be greater than 1315˚C. It is worthwhile to mention that increasing the temperature is more effective parameter for increasing the rate of the dissolution and homogenization of the alloy rather than the time.

This is due to the fact that these processes involve the diffusion of the alloying elements the diffusion coefficient follows an exponential relationship with the temperature.

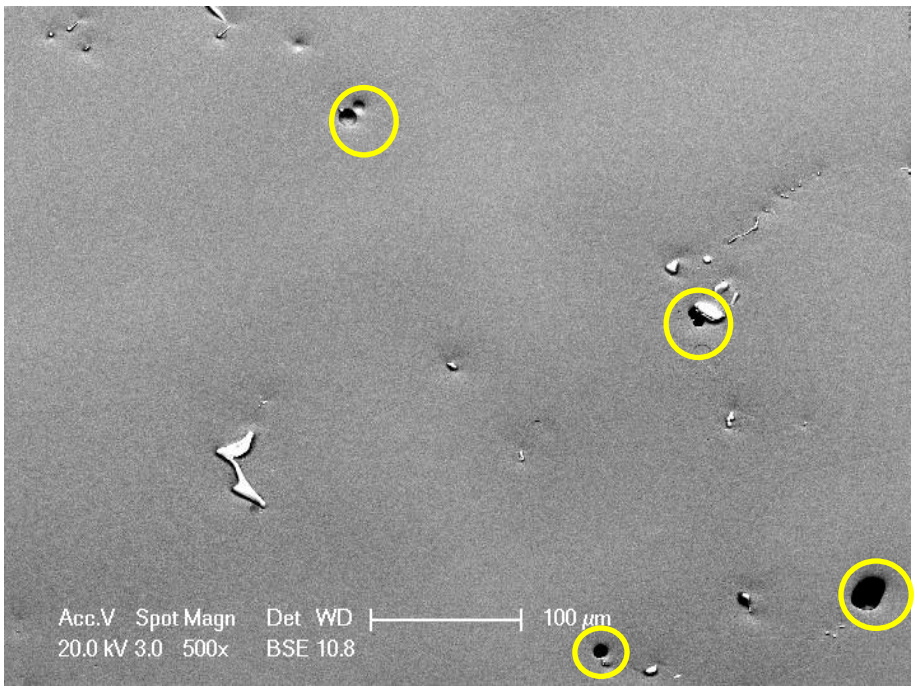

Figure 3.38. The incipient melting signs in the sample S4.

For the next sample (S5), again a stepwise increase in the temperature is proposed but also it is designed to be longer (5 hours at 1315 ˚C) to help for dissolution of the γ' islands and reducing the segregation. Thus, the solution treatment is chosen as 1280 ˚C/2 h + 1290 ˚C/3 h + 1315 ˚C/5 h. For this sample, it is observed that all the γ' islands are dissolved and the segregation is reduced more, but again there was signs of incipient melting in a few interdendritic region. Based on the obtained results, the final solution treatment is designed to be a longer, stepwise heating of the sample at 1280˚C/2 h + 1290˚C/2h +1300˚C/2h + 1305˚C/2h + 1315˚C/4h. This sample shows no sign of the undissolved γ' islands. No sign of incipient melting was observed in the interdendritic regions. Moreover, the segregation coefficient is close to 1 for most of the alloying elements. The highest improvement in segregation is observed for Re and W. Figure 3.39 compares the concentration profile of the as-cast structure with S_6. Figure 3.37 and 3.39 clearly show that an iterative design of the heat treatments has resulted in pushing the segregation coefficient closer to the unity, which indicates a homogenized microstructure.

Finally, the procedure (S6) is chosen as the solution treatment for the aged samples. This solution treatment is used for aged samples and for the creep tested samples.

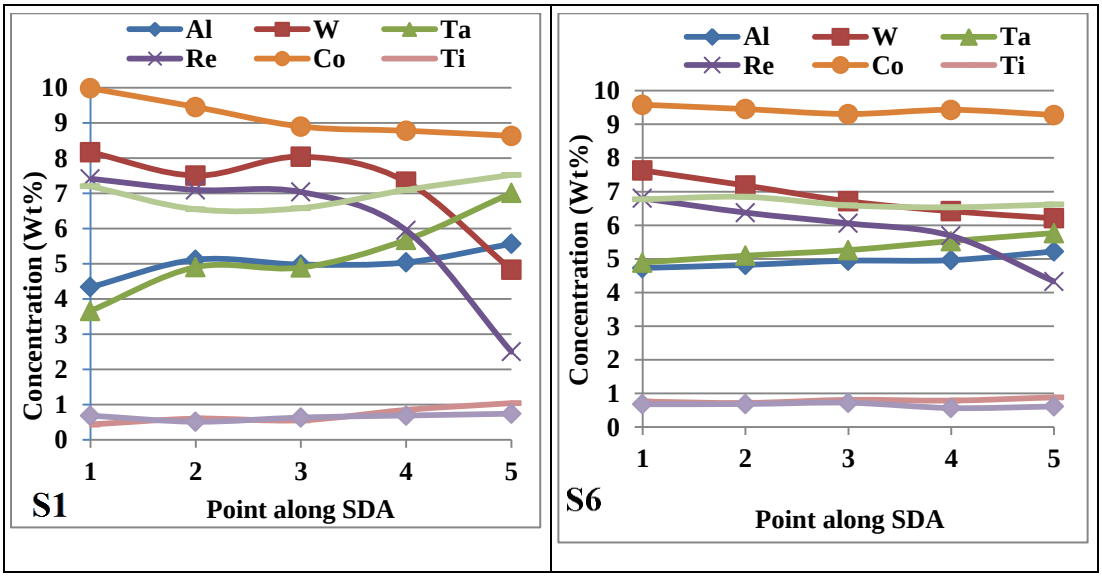

Figure 3.39. Concentration profiles along secondary dendrite arms for the as-cast (a), and solution heat treated sample S6.

<u>3.4.1.1. Modeling Results.</u> Due to the large number of the alloying elements in the composition of the single crystal superalloys and their different segregation behavior, non-equilibrium eutectics pools will solidify at the interdendritic region. Moreover, there will be high segregation in dendritic scale in the as-cast structure. Lengthy solution treatment at temperatures close to the solidus temperature of the alloy is then required for eliminating the non-equilibrium eutectics and homogenizing the composition of the alloy. This results in a significant increase in the cost. Moreover, there is always a risk of incipient melting. Dictra as software with the ability of solving diffusional equations could be an effective tool to optimize the solution treatment. However, using Dictra requires the previous knowledge of the composition of the alloy and also defining the characteristic length for diffusion of the elements. The steps for modeling the solution treatment by Dictra will be discussed next.

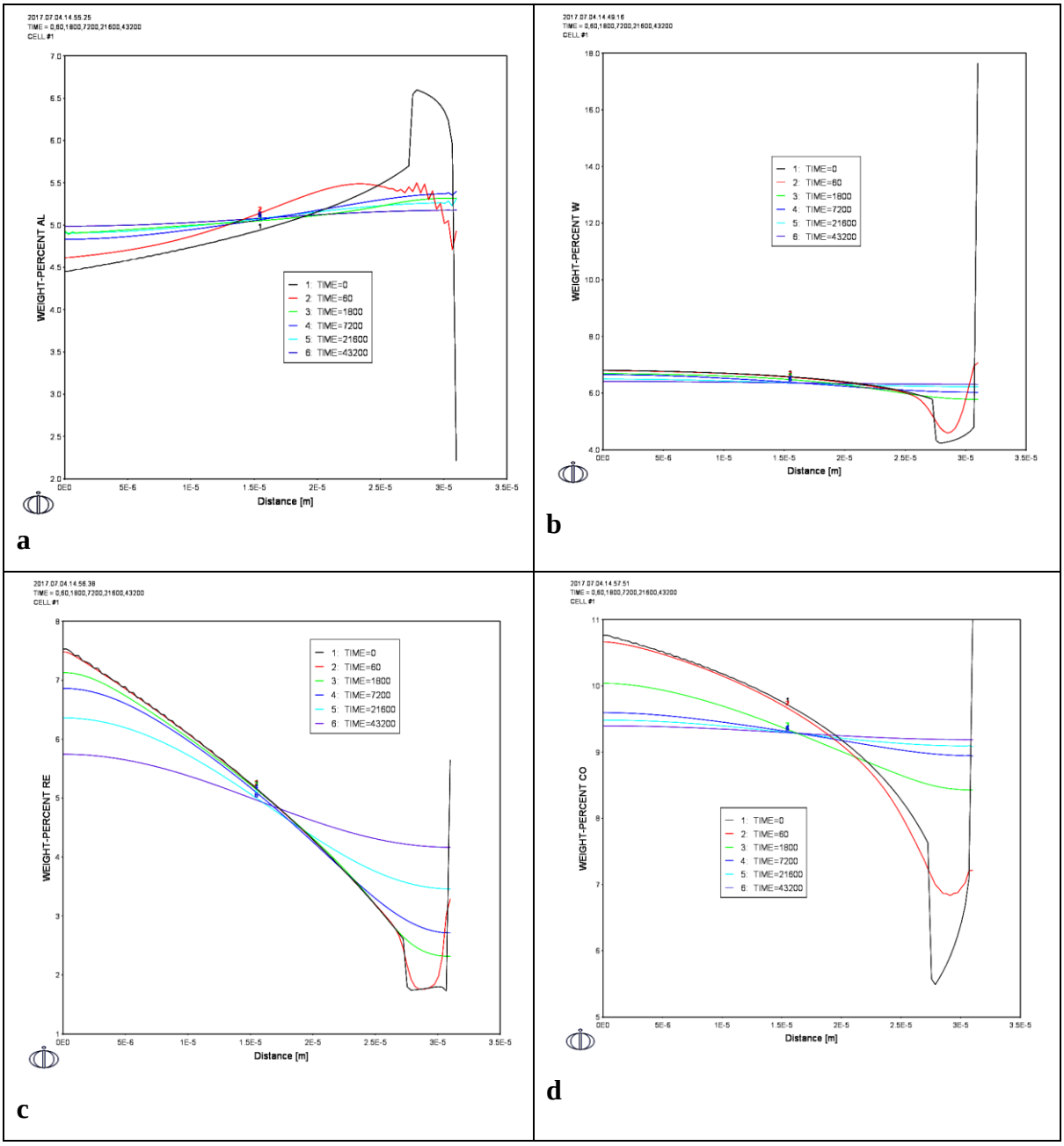

Figure 3.40. The concentration profile during the solution treatment process simulated by Dictra by considering half SDA as characteristic diffusion length, and Schiele segregation pattern. a) Al, b) W, c) Re, and d) Co.

Modeling of the solution (homogenization) treatment is performed by using the Dictra software for the S6 solution treatment. In the modeling of the solution treatment, the dendritic structures of alloys were simplified as planar regions. Moreover, the characteristic length for diffusion of the alloying elements is designed to be half the secondary dendrite arm spacing. The concentration of the alloying elements in the as-cast,

initial structure is set to be determined from the Scheil solidification module. The Scheil module of the Thermo-Calc software gives the concentration of the alloying elements at all solid fractions. Since the core of the dendrite is the first to solidify (f_s=0) and the last to solidify is the interdendritic region (f_s=1), then it is a good assumption that the segregation along the SDA follows the Scheil model. Figures 3.40a to d show the concentration profile of the four main elements Al, Ti, Re and Cr at different times after starting the solution treatment considering the half of secondary dendrite arm spacing as characteristic diffusion length. These Figures show continuous reduction in segregation amount of the alloying elements after solution treatment. The results indicate that the solution treatment labeled S6 is able to eliminate the concentration gradient in the as-cast structures and yield a homogenous alloy for subsequent aging process. However, for the Re element, the software estimates a longer time needed for full homogenization of the alloy.

The experimental segregation coefficient and the simulation results are compared in Table 3.6.

Table 3.6. Segregation coefficient determined by simulation and experiments.

Element	**Al**	**W**	**Ta**	**Re**	**Co**	**Ti**	**Cr**	**Mo**
K (Dictra simulation by considering Scheil solidification segregation profile)	0.96	1.03	0.95	1.33	1.03	1	1.02	1
K (Dictra simulation by considering EPMA measured segregation profile)	0.91	1.21	0.81	1.95	1.08	1	1.05	1
K (Experimental)	0.91	1.22	0.85	1.57	1.04	0.86	1.04	1.1

It is seen that the experimental segregation ratios are higher than the simulation ones, except for Ta. This suggests that the diffusion distance needs to be modified in the simulation. Moreover, determining the as-cast concentration profile with the Scheil model may also introduce some errors in the simulation. In the next step, the simulation was modified by considering the experimental concentration profile determined by EPMA instead of determining it by Scheil model. The experimental data are fed to the program in a DAT format as the initial condition of the simulation. Since the diffusion gradient due to the segregation exists in three dimensions in the as-cast structure and this gradient is the

highest from the core of the dendrite to the interdendritic region, then considering half the PDAS as characteristic diffusion distance is more realistic assumption for the third generation superalloys. Figure 3.41 shows the concentration profile at different stages of the solution treatment S6.

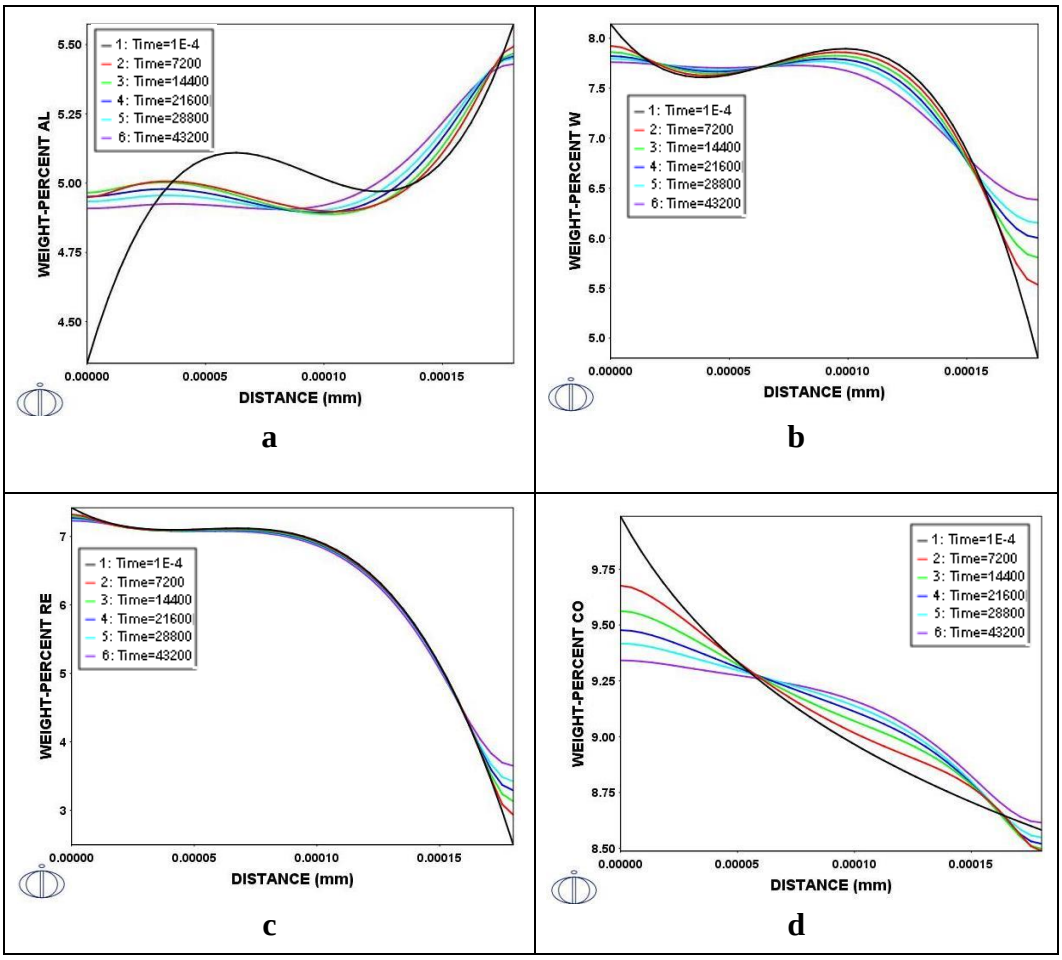

Figure 3.41. The concentration profile during the solution treatment process simulated by Dictra by considering half PDAS as characteristic diffusion length, and experimental segregation pattern. a) Al, b) W, c) Re, and d) Co.

The simulation determined concentration profile is compared to the experimental results in Figure 3.42. A reasonable agreement is seen between the results except for the Re element. This is due to considering a low diffusivity of the Re element in the calculations.

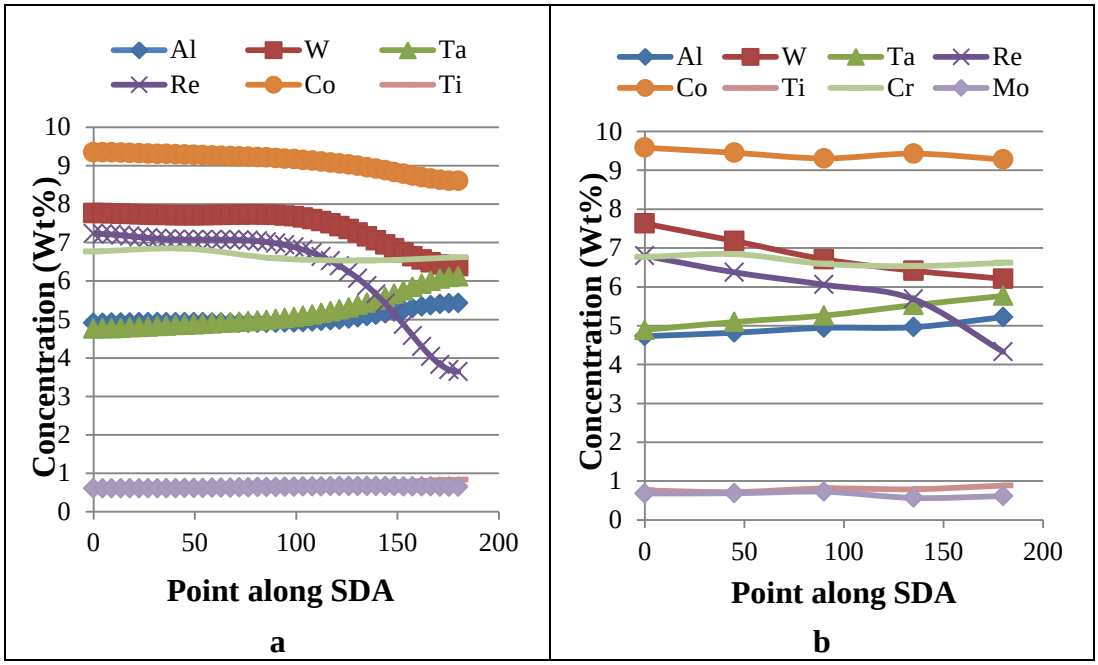

Figure 3.42. Comparison of the simulation (a) and experimental results (b).

The segregation ratios are compared in Table 3.6. It is seen that the simulation segregation ratios are closer to the experimental results for almost all the elements. The closer agreement with the experimental results is mainly due to the more accurate definition of the characteristic length for diffusion of the elements. This could also suggest that the diffusion distance could be a value between the PDAS and SDAS.

3.4.2. Aging Treatments

In the previous chapter it was observed that, after solution treatment (S6), the coarse eutectics are eliminated from the interdendritic regions of the as-cast structure. The solution treatment (S6) was observed to yield no incipient melting. The microstructure was comprised of fine precipitates in the dendrite and interdendritic regions with the interdendritic ones being larger due to still present elemental segregation effect. It was shown that the 12 hours of solution treatment has not been enough to eliminate the segregation effect. The longer times of 25 hours even have been reported not to completely remove the segregation [209].Therefore, the main parameter for the successful solution treatment considered to be the full dissolution of the coarse eutectic pools in the

interdendritic region. The designed solution treatment also showed that is free from the incipient melting.

Aging treatment is another step after solution treatment which is especially designed for optimization of the microstructure of the solution treated alloy to yield a high volume fraction of the precipitate with uniform morphology inside the matrix. Compared to the solution treatment studies, the number of studies related to the aging treatment is limited, and standard aging treatments are mainly followed in various modern single crystal superalloys. However, a very high service temperature of the advanced nickel based superalloys and the subsequent effect of the aging process on the microstructural evolution could have considerable effect on the mechanical properties and life of the alloy. Therefore the effect of aging temperature and time on the size, morphology and different phase evolution need to be studied more in detail.

The aging treatment can be treated in three stages as the nucleation, growth, and coarsening. These three stages occur consequentially (sometimes concurrently) and controlled by the interfacial energy between the matrix and precipitates and the free energy change during precipitation. The next section discusses the type of the precipitates and their morphology after aging treatment of the ERBALLOY at different times. In the last part of this chapter the effect of heat treatment on TCP phases evolution will be discussed.

3.4.2.1. Precipitate Size and Morphology. The samples are double aged at two different temperatures following the solution treatment procedure S6. The primary aging is conducted at 1140 ˚C for 6 hours, and then the secondary aging is done at 870 ˚C for 0, 2, 4, 16, 48, 500, and 1000 hours. After each aging step, the samples are quenched in water to preserve the microstructure of that temperature after the mentioned time. The samples are named A0, A2, A4, A16, A48, A500, and A1000, respectively where A means aging and the following number gives the aging time in hours at 870 ˚C. Figure 3.43 shows the precipitate microstructure in the dendrite core for the mentioned samples. The same scale bar (except for as-cast sample) in the figure is used for a comparison purpose. The microstructure of the as-cast sample at 200KX shows just the γ’ and for better representation of the as-cast structure, the lower magnification SEM photo at 60KX is chosen. The microstructure of the samples shows both the unimodal and bimodal size

distribution of the precipitates for the single aging process (A0).In addition to the coarse cuboidal precipitates, a large number of fine precipitates with near spherical shape are formed in the channels between the large precipitates.

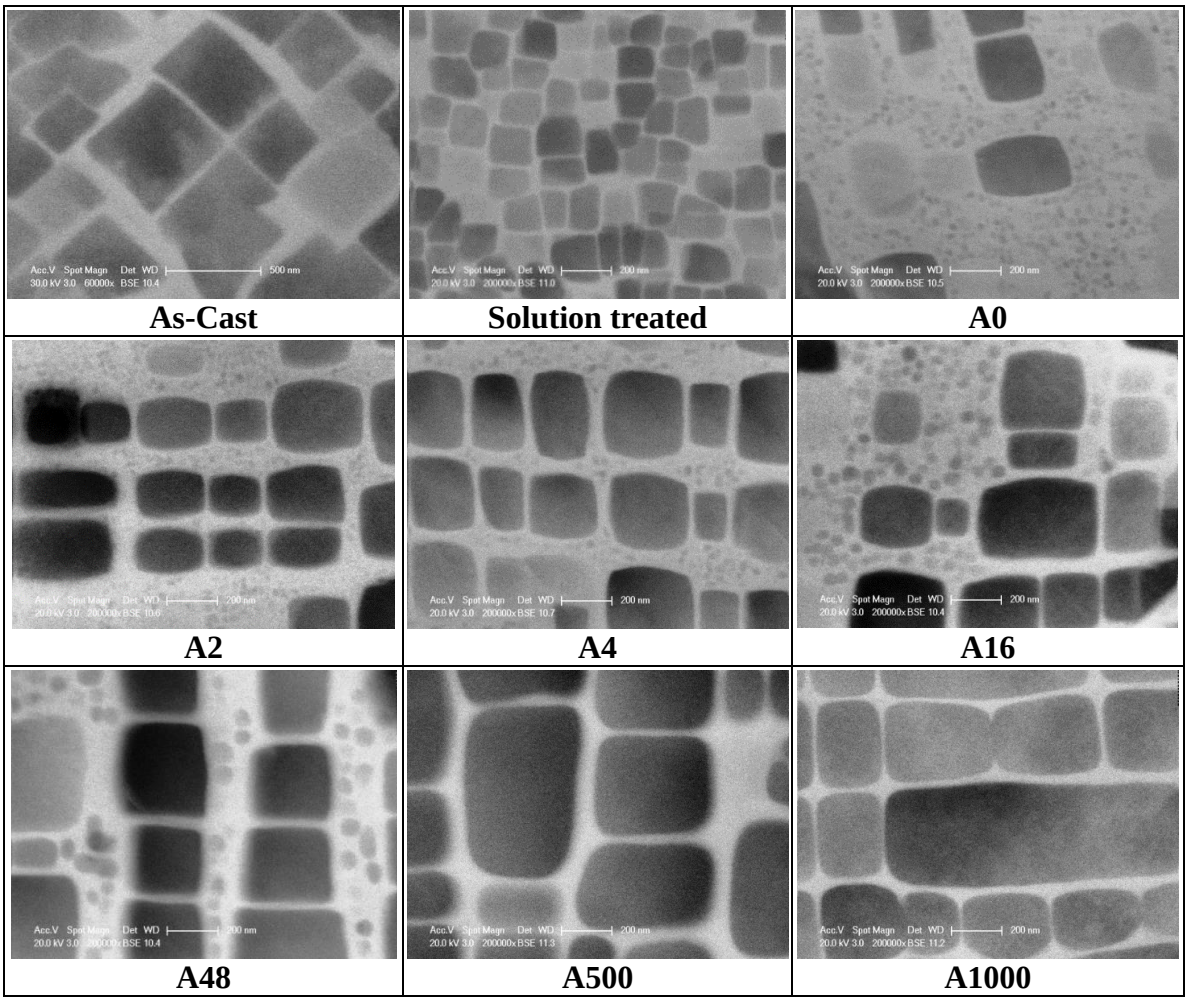

Figure 3.43. Morphology of the coarse and fine γ'. All samples are first aged for 6 hours at 1140 ˚C and then aged at 870 °C for 2,4,16,48,500 and 1000 hours. The samples are quenched in water after aging treatment.

The bimodal size distribution is mainly observed in the dendrite core where the concentration of the W and Re elements is high. The dendrite leafs and interdendritic regions show mainly the coarse precipitates. As an example, the microstructure of the dendrite core, leaf, and interdendritic region for the sample A48 is shown in Figure 3.44. The fine precipitates are present in the dendrite core while they are absent in the dendrite leaf and interdendritic regions.

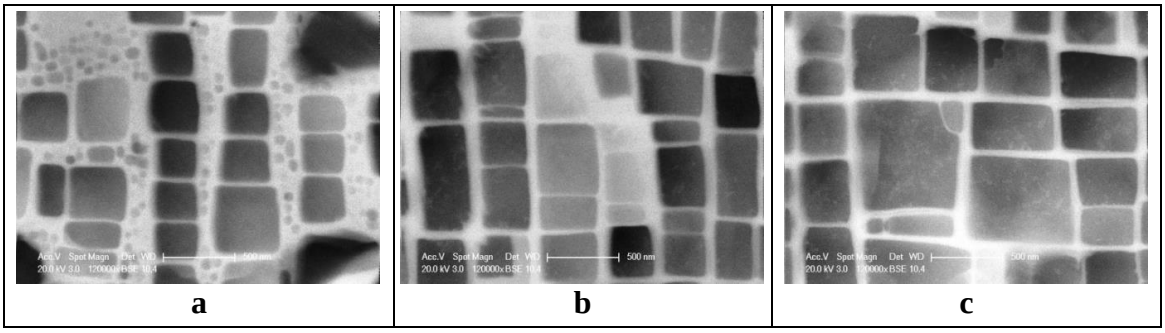

Figure 3.44. Fine precipitates observed in the dendrite core (a) for the sample A48, which are absent in the dendrite leaf (b) and in interdendritic regions (c).

Secondary aging at 870°C for two hours (A2) renders a similar microstructure as inA0sample with the bimodal size distribution of the precipitates in the dendrite core and mainly the single coarse precipitate in the dendrite leafs and interdendritic regions. The similar microstructure is observed for the 4 (A4), 16 (A16) and 48 (A48) hours of secondary aging. A500 and A1000 show only coarse precipitates in the microstructure with no sign of the fine precipitates. The coarsening and coalescence of the coarse γ' is evident at samples A500 and A1000. Moreover, they show rather rounded corners at the edge of the cubes.

The results for different aging times then indicate that the first step aging at 1140°C leads to growth and coarsening of the precipitates already existed in the solutionized microstructure. In addition to the coarse precipitates, fine size precipitates are observed to form in the matrix channels between the coarse ones. It is also observed that fine precipitates preferred to form in the matrix shared by four precipitate corners (Figure 3.45). Moreover, they are mainly located at the wide matrix channels.

The bimodal size distribution is related to multiple nucleations due to different undercooling at temperatures below the solvus temperature of the alloy. The interplay between the thermodynamic and kinetic parameters is determining the rate of the multiple nucleation mechanisms during continuous cooling. With the continuous cooling from the solvus temperature, the driving force for nucleation increases due to increased undercooling, but on the other hand the diffusion coefficient of the elements for the diffusional phase transformations declines due to reduction in temperature. With this

explanation, lower undercooling below the solvus temperature (aging at higher temperatures) would result in coarser precipitates. The aging time led to coarsening of the coarse and fine precipitates. Coarsening of the initially large precipitates and formation of the fine ones have already been reported [210,211]. Large precipitates coarsen due to the Ostwald ripening mechanism. Fine precipitates may form due to still present supersaturation in the matrix phase. When such a matrix is held at a lower temperature, in this case 1140°C, new precipitates nucleate in the favorable matrix sites, which then grow again due to coarsening principles [211]. In fact, coarsening of the fine precipitates is observed in this study during the double aging temperature of 870°C. Coarsening of the fine precipitates results in their disappearance from the matrix after 500 hours in this study (Figure 3.44). It is stated in the literature that [212,213] high cooling rates form the secondary precipitates in the microstructure of the single crystal superalloys. Nevertheless, disappearance of the fine precipitates at long aging times (> 500 h) in this study shows that the fine precipitates in this specific alloy do not form during fast cooling.

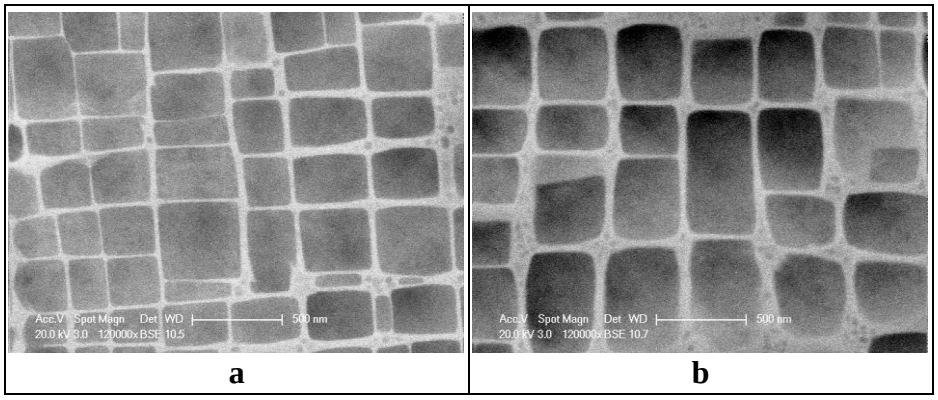

Figure 3.45. Formation of the fine precipitates in the shared corner of the four neighbor coarse precipitates.

It was already discussed that the fine precipitates prefer to form in the wider channels. Moreover they preferentially form at the shared corners of the four primary precipitates because of again wide matrix space. The chemical composition analysis of the fine and coarse precipitates and matrix in vicinity of them may help to understand this behavior [153].The coarse precipitates have been shown that are rich in γ' forming elements like Al and Ta while depleted from the γ forming elements like Re, Co and Cr. However, the composition of the fine ones have shown to include more amounts of Cr and

especially very low amount of Al compared to the primary precipitates. The chemical composition analysis in the channels including the fine precipitates for a Re containing single crystal superalloy shows that compared to the coarse precipitates, these fine precipitates are rich in Re, Co, Cr and Mo while depleted from the Al elements. Similar observation is seen for Rene88DT with the fine precipitates showing almost double Cr content and much lower Al content than the primary ones for the fast cooling experiments. The overall result is that the composition of the primary coarse precipitates is near equilibrium. This is due the fact that the primary precipitates tend to form at high temperatures where the high diffusion rate of the elements allows for them to reach the equilibrium composition. However, fine precipitates tend to form at lower temperatures where the diffusion process is limited. Therefore, the diffusion coefficient of the elements will play an important role. The low diffusion coefficient of the Cr and Co compared to Al and Ti therefore will be the reason for the composition difference between the primary and the fine precipitates [153].

The compositional analysis for the γ around the primaries and far from the primaries has shown that the regions near the primaries are close to the equilibrium composition while the regions far from the primaries are far from equilibrium. Therefore the latter one will be the main sites for nucleation of the fine precipitates. In other words while the thermodynamic local equilibrium may held at the interface between the primary precipitates and the matrix, this does not happen at distances far from the interface due to limited diffusion of the elements. The equilibrium concentration of the γ and γ’ during aging at 870 °C is simulated for the ERBALLOY by using Thermo-Calc and the results are shown in table 3.7. It is seen that under equilibrium condition the γ’ will be rich in Al, Ta and Ti and consequently will have lower content of the other alloying elements.

Table 3.7. The composition (wt%) of the γ and γ’ during isothermal aging at 870 °C.

Element	Ni	Co	Cr	W	Re	Al	Mo	Ta	Ti
γ	50.35	16.46	12.90	9.41	7.69	1.82	0.84	0.44	0.09
γ’	72.05	3.55	2.36	2.31	0.26	8.01	0.20	9.96	1.29

The fine precipitates have a great impact on the creep strength of the Ni base superalloys [209]. This is attributed to their effect in reducing the net width of the matrix

channels between the coarse precipitates. Therefore, the disappearance of them at longer times may have a negative impact on the creep resistance if the channels width in the matrix and increases.

A problem arises with the presence of the TCP phases in the dendrite core for the Re containing alloys. The presence of these phases is especially attributed to the low diffusivity of the Re and its accumulation in the dendrite core due to solidification segregation [209]. TCP phases in general contain high amount of refractory elements like Re, W, and Mo. Formation of these phases creates a local composition inhomogeneity in the dendrite core. As it will be shown in Section 3.3.3, the TCP phases are generally surrounded by a continuous layer of the γ'. As already discussed in the introduction, the presence of the TCP phases reduces the creep rupture life of the alloys by depleting the solid solution strengthening elements from the matrix. The formation of the TCP phase in Figure 3.47 is associated with depletion of the huge amount of the Re and W from the matrix. Moreover, the TCP phases are poor in the gamma prime forming elements like Al, and Ta. Therefore, TCP phases while form, reject these elements and uptake the gamma forming elements from the surrounding matrix. The consequence is formation of the continuous layer of the γ' around the TCP phase. A region with mainly γ phase surrounds the continuous layer of the γ' where the fine precipitates form (ovals specified in Figure 3.46 a).This may influence the creep resistivity of the alloy which needs to be investigated in separate study. The fine precipitates are also observed to form inside the γ matrix where the probable dissolution of the coarse precipitates has occurred (Figure 3.46 b).

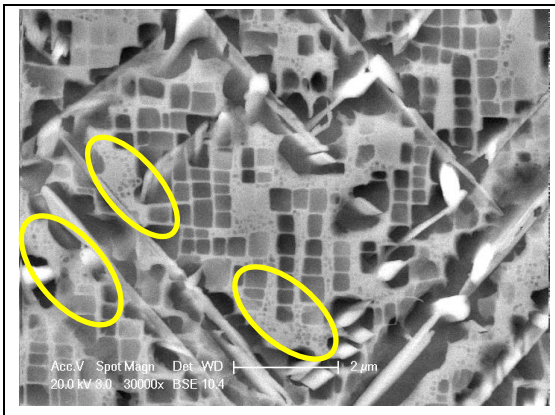

a

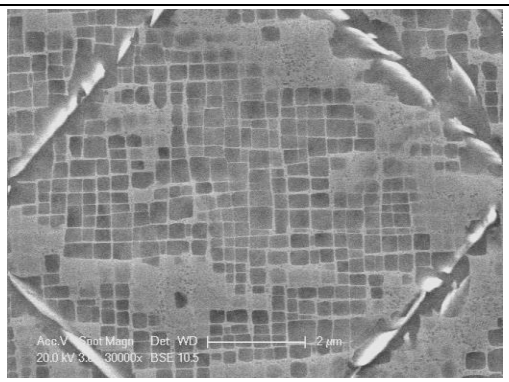

b

Figure 3.46. Fine precipitates in the γ matrix in between the TCP phases.

To obtain the size of the precipitates, five pictures are taken from the core of the dendrites in every sample in magnification of 60,000X and analyzed by ImageJ software[214] to determine the size of the γ' precipitates. Then considering the sphere shape for the precipitates, the equivalent diameter of the precipitates is determined and plotted. Figure 3.47 shows the results for the coarse precipitates.

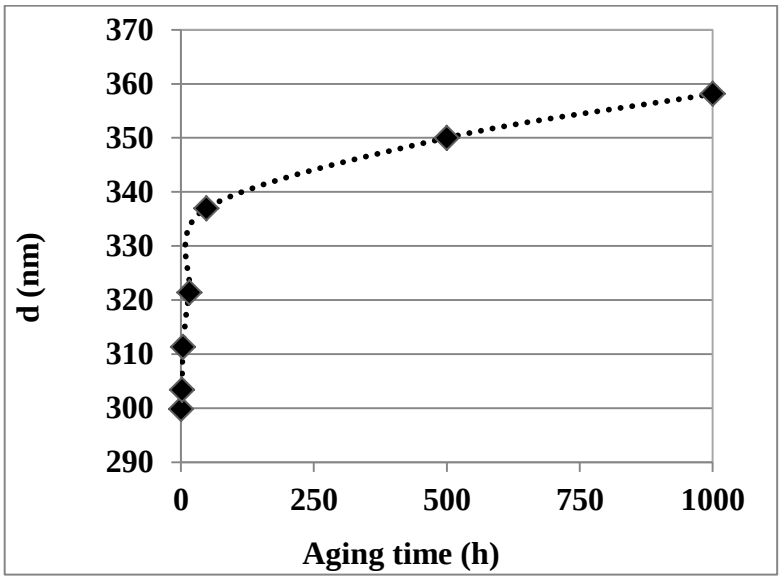

Figure 3.47. Size versus aging time for the coarse precipitates at 870 ˚C.

The plot in Figure 3.47 shows continuous increase in size of the primary precipitates; however, it is seen that the plot is composed of two different regions with different slopes that may be attributed to the growth and coarsening regimes [215].

Coarsening of the precipitates in Nickel base superalloys involves coarsening of the large precipitates due to the diffusion of the species from the small shrinking precipitates. The volume fraction of the precipitates hence remains constant during this process. The diffusion of the precipitate forming elements occurs from matrix to the precipitate. The parameters involved in the coarsening are the size and distribution function of the precipitates which are formulated by Lifshitz, Slyozov and Wagner under the LSW theory [216]. The LSW formulation for this time dependent process is described as:

$$d^n = k.t \tag{3.10}$$

where d is the size after time t, and k is the coarsening rate constant. The mass transport mechanism defines the value for the power n.

By taking the natural logarithm of the terms in equation 3.10, the following is obtained:

$$Ln\ (d) = \frac{1}{n}.Ln(k) + \frac{1}{n}.Ln\ (t) \tag{3.11}$$

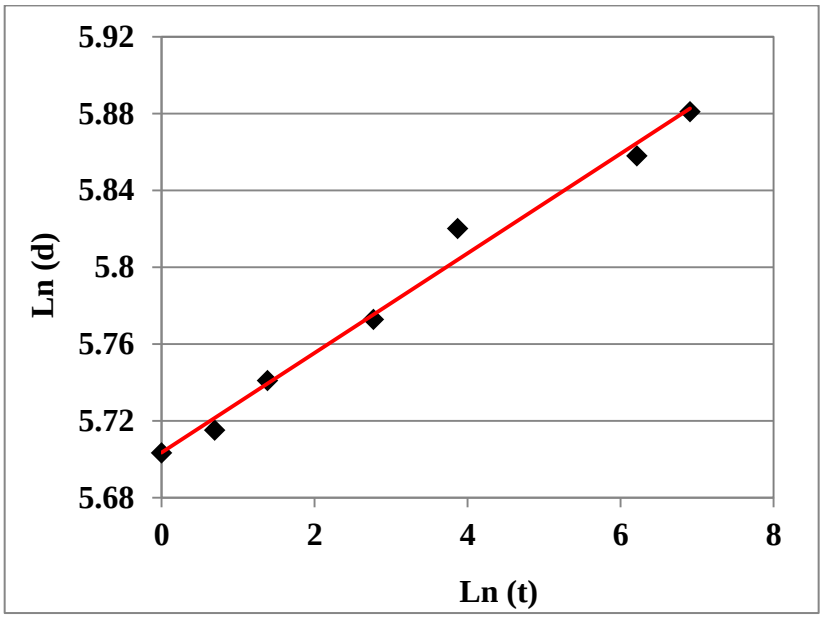

Figure 3.48. Natural logarithm of the size versus natural logarithm of time with a line fitted. All the alloys are first aged at 1140 ˚C for 6 hours.

Therefore if plotted, the natural logarithm of the size of the precipitate should show a linear relation with the natural logarithm of the time and the slope of the plot gives the value of 1/n. Figure 3.48 shows this plot for different times of aging at 870 °C. Linear trend is observed and the value of n is calculated to be 4.

The minimum and maximum size of the precipitates is presented in table 3.8**.** It is seen that the precipitates size changes in a broad range spanning from minimum 200 to 465 nm. The minimum and maximum shift to higher values as the aging time increases.

Table 3.8. The minimum, maximum and average size of the precipitates in the aged samples.

Sample name	**A0**	**A2**	**A4**	**A16**	**A48**	**A500**	**A1000**
Minimum size (nm)	200	220	220	250	250	270	260
Average size (nm)	300	303	311	321	340	350	358
Maximum size (nm)	440	440	460	440	450	460	465

In order to discern between the growth and coarsening stages, the area fraction of the precipitates is measured from the SEM images of the precipitates in the dendrite core and the results are plotted in Figure 3.49. The precipitate area fraction is about 71% after the primary aging treatment at 1140°C. The fraction then gradually increases toward about 74% during the secondary aging at 870°C up to 16 hours, which may mark the growth regime. Beyond 16 hours, the area fraction stays almost constant; this may indicate the coarsening regime.

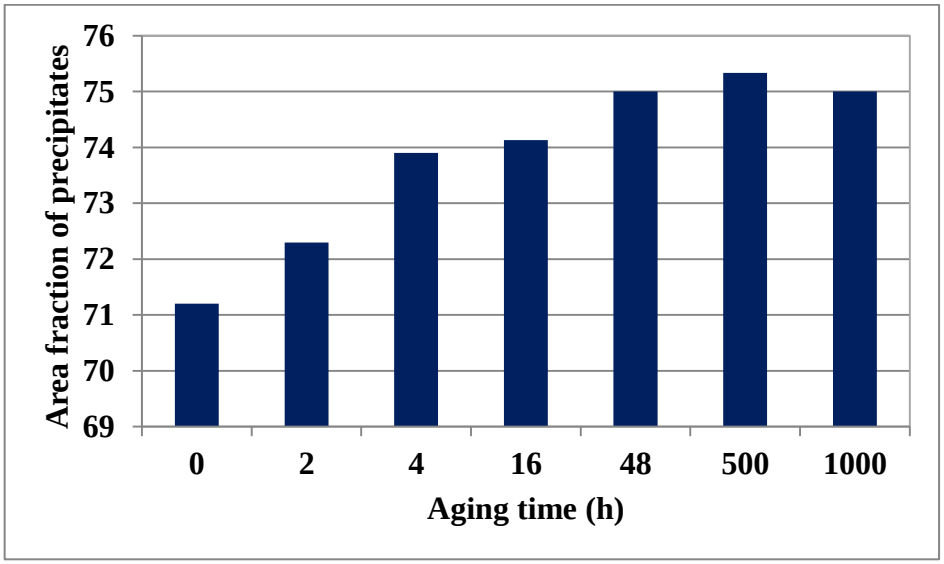

Figure 3.49. Variation of the area fraction of the coarse precipitates with the aging time.

Figure 3.50 shows the size variation of the fine precipitates during the secondary aging. The high rate coarsening of the fine precipitates happens up to 48 hours.

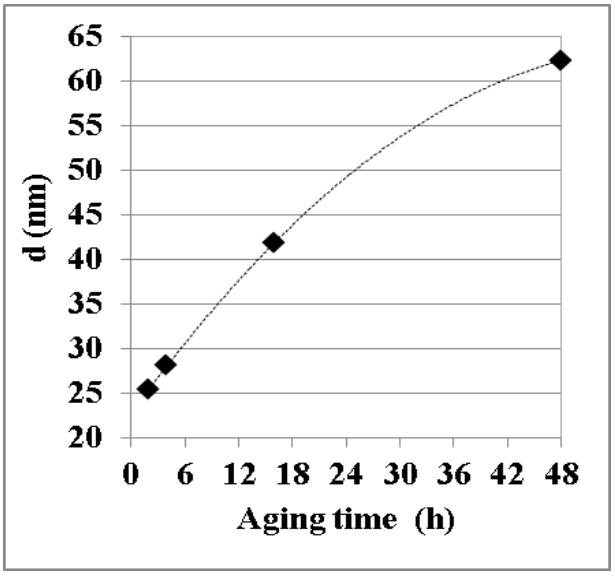

Figure 3.50. Coarsening of the secondary γ' precipitates at 870 ˚C. All the alloys are first aged at 1140 ˚C for 6 hours.

<u>3.4.2.2. TC-Prsima Predictions of the Precipitate Size.</u> The volume fraction and size evolution of the primary γ' precipitates during the primary aging at 1140°C are modeled with the TC-Prisma software (Figure 3.51).

The results show that under isothermal equilibrium condition with zero volume fraction of the precipitate at the beginning of the aging process, a small volume fraction of precipitate will evolve at the end of the primary aging, however more γ' in the experimental aged samples (around 71%) was observed which is because of the pre-existing small size γ' in the microstructure of the solution heat treated samples which is not considered in TC-Prisma calculations.

TC-Prisma prediction shows that when aging at 1140 °C for 6 hours, the size of the γ' precipitates reaches around 350 nm, which is found to be 300 nm experimentally.

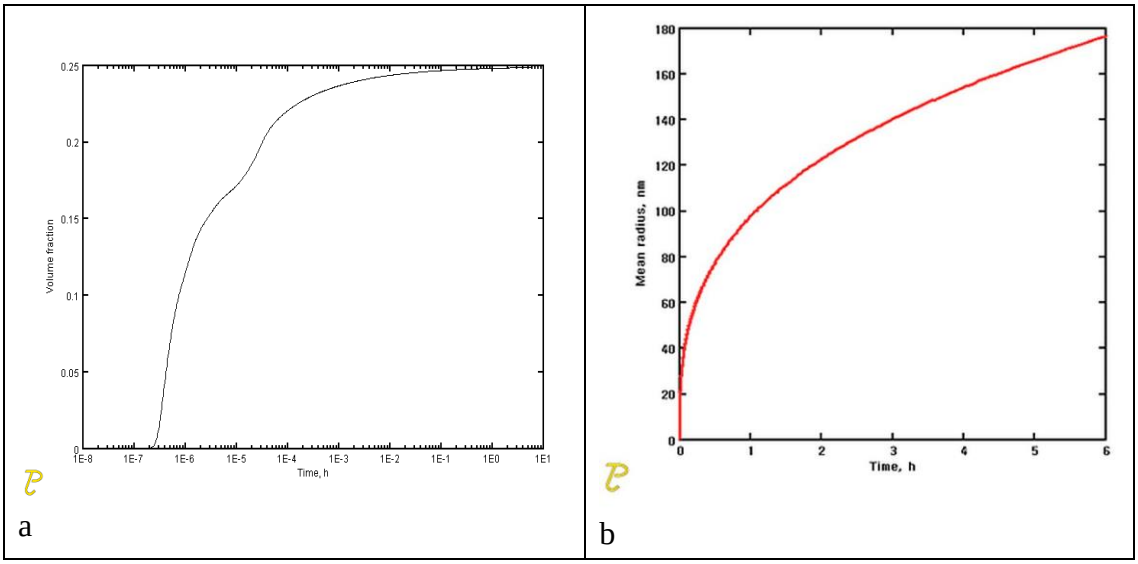

Figure 3.51. Increasing size of γ' precipitates during aging process at 1140 ˚C.

The simulation results show that the growth rate is high at the beginning of the aging and then decreases. Experimental aging is conducted only for 6 hours at 1140°C, so only the final stage of the simulation may be compared to the experimental data. The particle size distribution obtained by modeling is shown in Figure 3.52 for 2, 4, and 6 hours of aging. It is seen that as precipitates grow in size with longer aging times, the size distribution is normal Gaussian with slight shift of the peak towards large sizes.

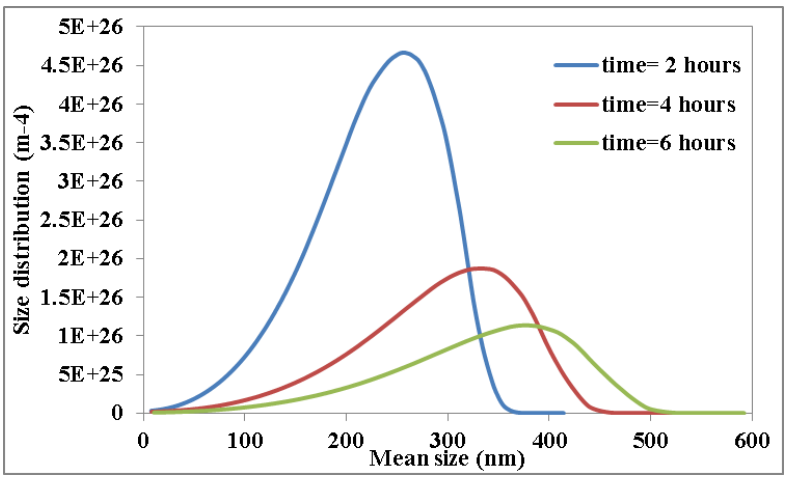

Figure 3.52. Size distribution of the primary γ' precipitates after 2, 4, and 6 hours of aging at 1140 °C.

The size frequency of the precipitates after first stage of the experimental aging is determined by analyzing the micro photos taken from the sample aged at 1140 ˚C for 6 hours. The results are shown in Figure 3.53 a.

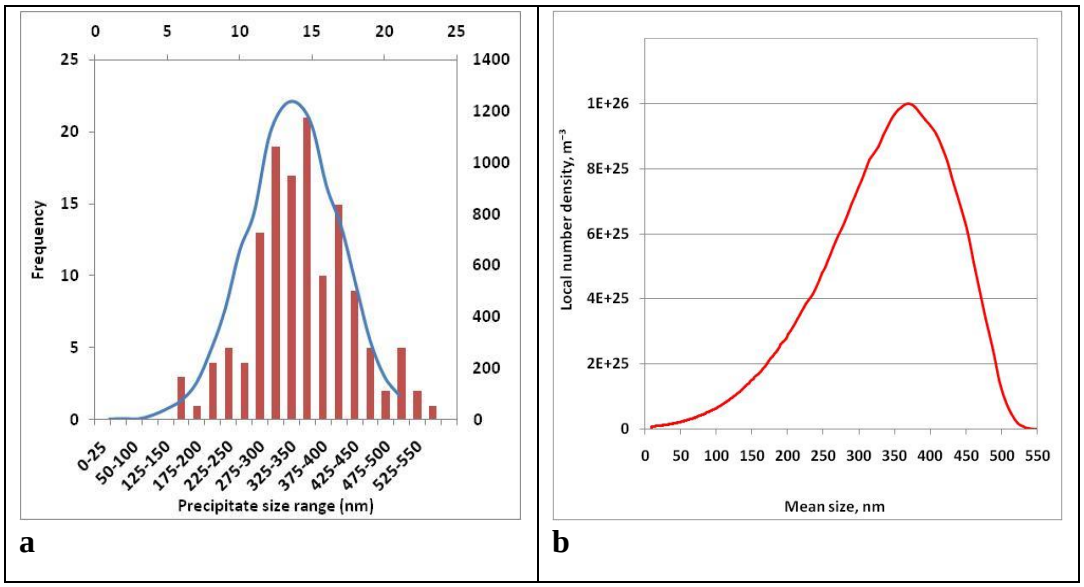

Figure 3.53. Histogram of the primary precipitate size range for the sample aged at 1140 ˚C for 6 hours a) experimental and b) TC-Prisma modeling.

A normal distribution curve is fitted to the data. It is shown that the precipitates have the size range of 150-550 nm with the maximum frequency occurring around 300 nm. The TC-Prisma simulation results (Figure 3.53b) show a very similar distribution curve to the experimental one. The results of the simulation at lower aging temperature (870 °C), yielded erroneous results and shows that the software is not able to handle the multiple aging.

3.4.3. TCP Phases

Ni base superalloys have high concentration of the refractory elements like Mo, W, Re, and Ta, which act as solid solution strengtheners in both the γ and γ' phases. On the other hand, high concentration of these alloying elements makes the alloy prone to precipitation of the TCP phases. The TCP phases are rich in these elements, which make the matrix depleted from potent solid-solution strengthening elements. Moreover, the

formation of these phases in high amount is detrimental to the mechanical performance of these alloys because of their brittle nature.

The main change in the composition of the ERBALLOY compared to the second generation CMSX-4 alloy is the introduction of 2% more Re which puts ERBALLOY in the third generation superalloy category. It is already discussed that more Re in the composition of the superalloys makes them more prone towards formation of the TCP phases. In the following, the morphology and type of the phases formed in the microstructure of the ERBALLOY will be discussed more in detail. ERBALLOY VB12 (grown with vertical Bridgman a withdrawal velocity of 12 cm/h) is selected for the study. This is to focus mainly on the chemical composition rather than both the chemical composition and method of manufacturing. TCP phase, which was absent in the as-cast and solution treated structure, appear after double aging heat treatment. They are mainly observed to form in dendrite core. Therefore the dendrite core is the preferential site for nucleation of the TCP phases. This is because the concentration of the refractory elements is high at the core of the dendrite. In a few dendrites, TCP phases also observed to form along the dendrite leaves.

Figure 3.54 shows the morphology of the representative TCP phase formed at the dendrite core for different aging times. A0 is the sample aged only at 1140 ^{o}C for 6 hours. A2, A4, A16, A46, A500, and A1000 are the samples which are first aged at 1140 ^{o}C for 6 hours and then aged at 870°C for 2,4, 16, 500, and 1000 hours, respectively. Close observation of Figure 3.54 reveals that TCP phases are formed in three different morphologies, which are the Sigma, Mu, and P phases. They are seen mainly in the needle and plate morphologies, but in few areas, the blocky morphology is also observed. The difference between these morphologies is shown by TEM microphotos in Figure 3.55. Depending on the orientation of the cut plane, P phase is distinguished from the Mu phase by its circular or lenticular cross section [217]. The Mu phase, on the other hand, shows a blocky shape. The needle like morphology is prone to formation of cracks with no loss in the interface cohesion with the matrix [218]. This is achieved due to a special orientations relationship with the matrix that causes a semi-coherent interface with the matrix. In other words, the TCP phases with the needle like morphology act as brittle short fibers which cause internal cracking; however, the interface decohesion does not happen. On the other hand, the globular

morphology is not prone to crack formation but loss of cohesion with the matrix has been reported [218].Connecting the cracks by several such globular interfacial cracks, could cause the failure in the structure.

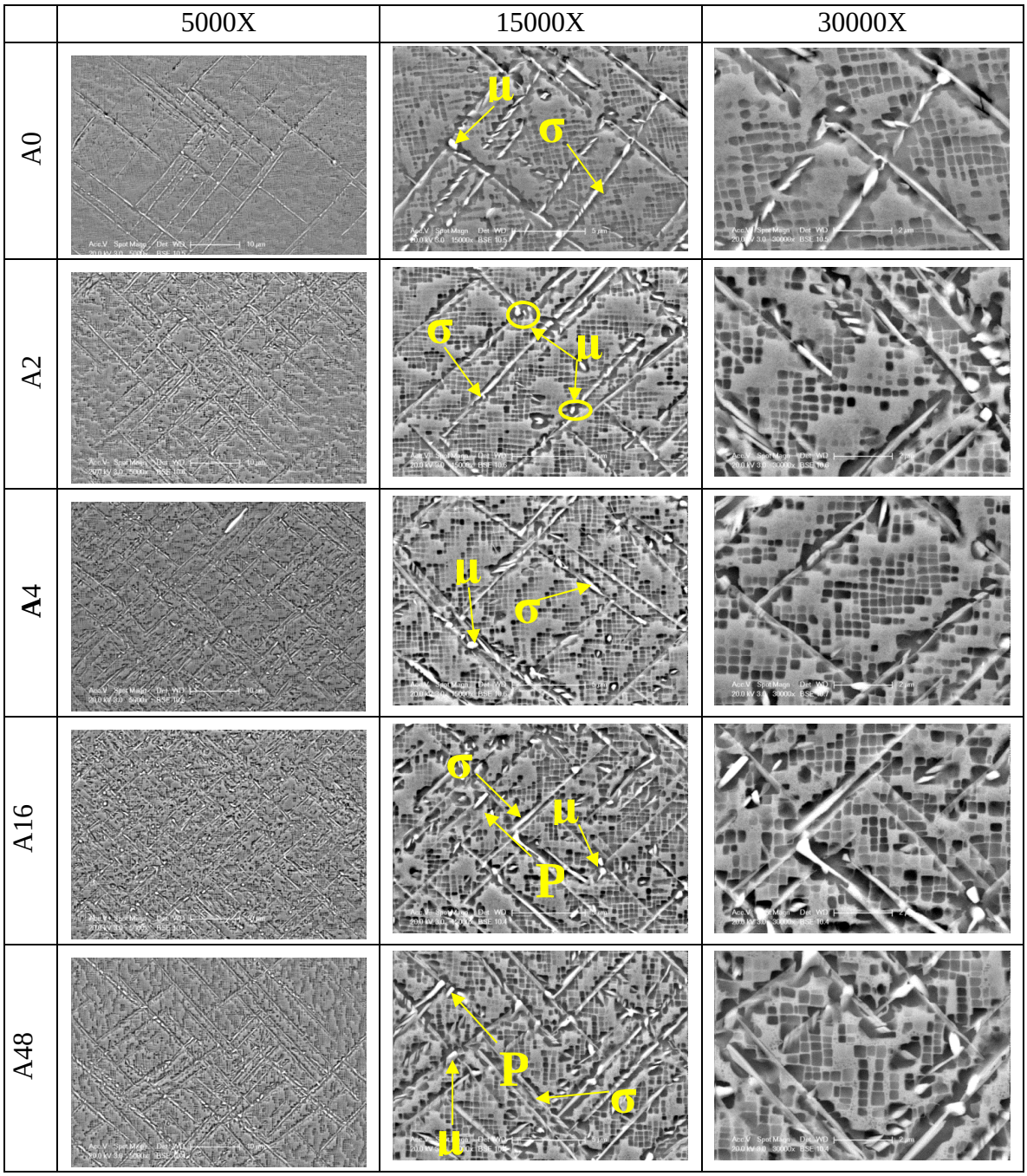

Figure 3.54. Morphology of the representative TCP phase formed at the dendrite core for different aging times. A0, A2, A4, A16, A46, A500, and A1000 samples are aged first at 1140 °C for 6 hours. Then they are aged at 870°C for 0, 2,4,16, 500 and 1000 hours respectively.

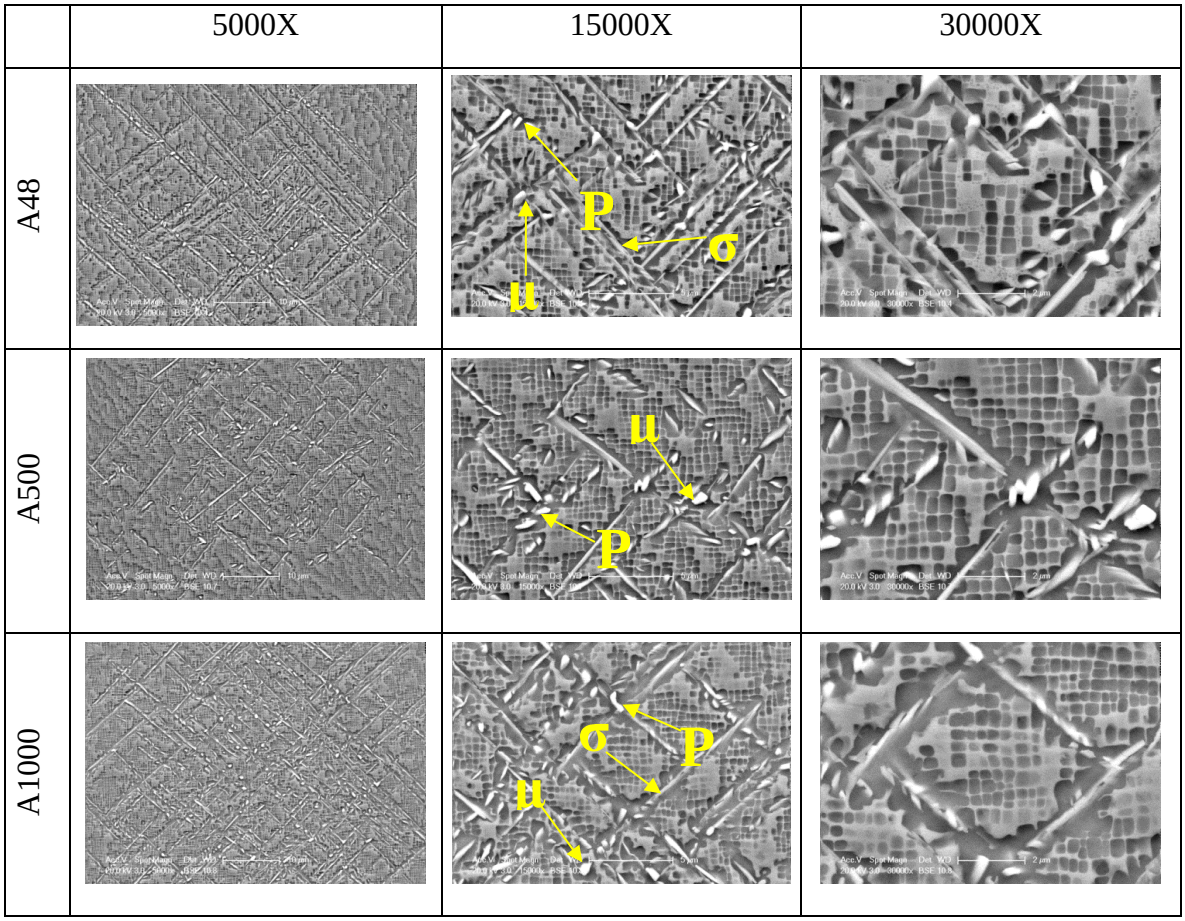

Figure 3.55.Morphology of the representative TCP phase formed at the dendrite core for different aging times. A0, A2, A4, A16, A46, A500, and A1000 samples are aged first at 1140 °C for 6 hours. Then they are aged at 870°C for 0, 2,4,16, 500 and 1000 hours respectively. (cont.)

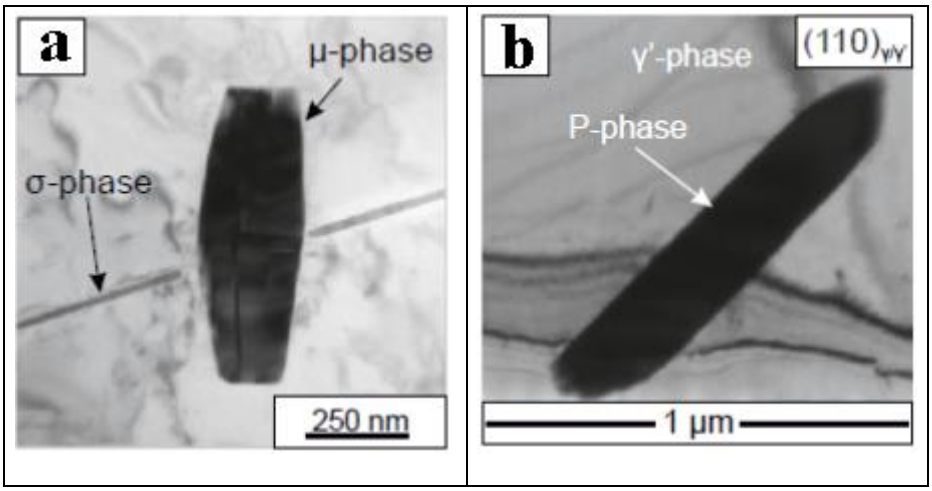

Figure 3.55. Morphology of the Sigma, and Mu phase (a) and P phase (b) [217].

The aging temperature is the main parameter determining the type of the TCP phase. It has been reported [that the Sigma phase could form at temperatures below 950°C while the other TCP phases (Sigma, Mu and P phases) are formed at higher temperatures. During long time aging of the CMSX-4 at 1050 and 1100°C, the presence of the Sigma and P phase has been reported with no sign of the Sigma phase. Moreover, it has been reported [214] that the P phase is more stable than the Sigma and Mu phases at temperature above 1100°C. The free energies for formation of these phases is close to each other and the chemical composition of the alloy and temperature are the main parameters determine the dominant phase. The chemical composition of the TCP phases is determined according to the chemical composition of the parent alloy. Moreover it has been shown [219] that the exposure time increases the amount of the Re and W in the composition of the TCP phases.

The first raw of Figure 3.54 shows the morphology of the TCP phase for the sample A0. This sample shows mainly TCP phase with needle morphology which is representative of the Sigma phase [217]. The Sigma phases evolve at plate-like morphology parallel to the family of pleas {111}. When they are sectioned normal to the <001>direction, appear as needle[209]. The arrangement of the needle or plate shape TCP forms a Widmenstetein structure. Due to the much larger unit cell size of the complex structure of the TCP phases than the matrix, the TCP phases nucleate preferentially on the closed packed planes of the matrix and thereby the interface could be semi-coherent interface with distinct structural relationship with the matrix. Therefore, there will be large activation energy for nucleation of the TCP phases [219]. The Sigma phases were reported to be polycrystalline and when they cut on the $(001)_\sigma/(111)_\gamma$, they show special orientation relationship with the matrix. The σ tetragonal axis [001] σ, is parallel to the $[111]_\gamma$, and the $[110]_\sigma$ axis is parallel $[011]_\gamma$, or $[10\bar{1}]_\gamma$ axes. The precipitation of the Sigma phase has been reported to be with a very low interface energy at σ/γ interface on the (111) planes and lower corresponding activation energy. Therefore Sigma phase nucleation preceded the other types of the TCP phases. A very small amount of Mu phase also observed, which are distinguished by their blocky shapes [217].

Sample A2 shows a very similar morphology with mainly needle shape Sigma phase and a small amount of blocky Mu phases embedded in the dendrite core. The existence of an interface between the Mu and Sigma phase (See yellow ovals in Figure 3.54)proposes

the fact that the Mu phase has nucleated and grown in the expense of the already existing Sigma phase [220]. Due to a lower misfit between the Sigma phase and the matrix, this phase is the first to form at low aging temperatures; however, thermodynamic calculations have shown that this phase is metastable and later the equilibrium phases Mu and P nucleate at the Sigma phase interface rather than the bulk due to lower surface energy. In other words, the Mu and P phases require large activation energy for nucleation and therefore tend to form at the interface of the Sigma phase. The reduction in interface energy may be related to local change in the chemistry at the interface due to Sigma phase [153]. Moreover, the orientation relationship between the Sigma and Mu and the Mu and the matrix has been reported in the CMSX-4 which indicates that Mu phases nucleate on the Sigma phase and consume the Sigma phase to grow [221]. In the sample A4, similar to the samples A0 and A2, the Sigma and Mu morphologies are observed. Moreover, there are signs for evolution of the P phase, too. The sample A16 shows a considerable increase for the Mu phase. To a rather less amount, the amount of the P phase also increases. TEM studies on growth of the P phase have shown that P phase grows as large rectangular parallel to the $[001]_P$. Like what explained for the Mu phase, the P phase grows on the expense of existing Sigma phase, however random nucleation and growth of the P phase is also observed inside the matrix. The sample A48 is similar to the A16 but rather higher amount of the Mu phase is observed in the microstructure. In the sample A500 the major change is the coalescence of the P and Mu phases with their own kind, which leads to enlarged shapes of these phases. Finally, the Sample A1000 shows a higher amount of the Mu and especially the P phase.

The overall result is that the Sigma phase is the dominant phase that forms during isothermal aging at 870°C. A very small percentage of the Mu phase is also formed which grows continuously by aging time. Moreover, the P phase starts to evolve after only 4 hours. Similar to the Mu phase, the area fraction and size of the P phase then increases continuously with aging time.

The occurrence of the TCP phases is studied by the isothermal equilibrium module of the Thermo-Calc at two different temperatures of 1140°C and 870°C. Thermo-Calc predicts that under isothermal thermodynamic equilibrium at 1140°C, only γ and γ' phases are stable. However, the Thermo-Calc results for 870°C predict that the Sigma phase will

be a stable TCP phase. Moreover, the composition of the TCP phases is calculated by Thermo-Calc under isothermal equilibrium at 870°C which is shown in Table 3.9. It is seen that the Sigma phase is mainly composed of the Re and W elements.

Table 3.9. The chemical composition of the Sigma phase during aging at 870°C.

Element	Ni	Co	Cr	W	Re	Al	Mo	Ta	Ti
Sigma phase in ERBALLOY	10.68	18.07	18.05	22.33	29.65	0.012	1.19	0.02	0
Sigma phase in alloy PR2071 at 800°C	34.6	15.6	23.5	-	5.9	4.2	13.5	1.3	0.6

3.5. Rupture Behavior of the Grown Single Crystal Superalloys

The temperature capability of the single crystal Ni base superalloys has increased from the first to third generations due to addition of the refractory elements. The amount of refractory elements in CMSX-2 (first generation), CMSX-4 (second generation) and CMSX-10 (third generation) is 14.6wt%, 15.4wt% and 20.7wt%, respectively [222]. Especially, the Re content has increases from zero in the first generation to 3wt% in the second generation and more than 5wt% in the third generation. The change in the chemical composition of the alloys has increased the temperature capability of the third generation alloys about 30°C and 60°C over the second and first generation alloys, respectively. The superalloys with various compositions even in the same generation have different creep behavior. On the other hand, addition of the refractory elements increases the precipitation of the TCP phases. TCP phases are rich in the refractory elements and reduce the effect of the strengthening mechanisms induced by these elements. The utilization temperature influences the amount and type of the TCP phases as described in section 3.3.3. The other parameters that affect the creep behavior are the temperature and stress. An alloy with known chemical composition may show different creep behavior at various temperature-stress regimes. In this study, the creep behavior of ERBALLOY (a third generation single crystal alloy designed and manufactured in this study) is investigated at an intermediate

temperature (982°C/248MPa) and a high temperature regime (1100°C/137MPa). Moreover, the creep properties of the CMSX-4 (a commercial second generation superalloy manufactured in this study) is tested at 1100°C/137 MPa for comparison with ERBALLOY.

The results of the creep testing at these two different conditions are summarized in Figure 3.56. The first column of the figure provides alloy names and test conditions, the second column shows the strain versus time plots, and the third column shows the strain rate versus the strain plots. The strain rate plots are generated by differentiation of the creep curves in the second column by using Matlab curve fitting tool to better show the different creep stages (primary, secondary, and tertiary) which may not be distinguishable from the strain versus time plots. Moreover, the results of this study are compared to the literature [222]. The literature results are shown in Figure 3.57.

Figure 3.56a shows the creep curve of the CMSX-4 (grown in this study) at 1100°C/137 MPa. The rupture time is 99 hours for this sample. The graph shows some negative creep in the beginning which is probably due to sliding of the extensimeter on the specimen or microstructural changes [223].

The curve shows an instantaneous elastic strain as the load is applied. When the test starts, the strain increases rapidly to almost 1.7%. Strain then reduces to 1.2% in two hours. Then, there is a region where the strain increases with time which is called primary creep region. This region is short and is distinguished by the fall in the strain rate (Figure 3.56b). After that, a long period of the tertiary creep starts where the strain increases with time and the tertiary creep regime governs the rest of the creep deformation up to 99 hours (Figure 3.56a and b). Comparing with the results of CMSX-4 at 1100°C/100MPa available in the literature [222], a similar trend is observed for the strain versus time and strain rate versus strain plots (Figure 3.57 a and b).

The results of the high temperature creep for the ERBALLOY at 1100 °C/137 MPa is shown in Figures 3.56c and d. There is a sudden increase in the creep strain as load is applied. The creep curve for this sample shows a region of primary creep (seen as reduction in the strain rate in Figure 3.56c) followed by a secondary creep (shown as

constant strain rate in Figure 3.56d). Compared to the CMSX-4 (Figure 3.55a and b), longer primary creep is observed for the ERBALLOY. Moreover, ERBALLOY shows a long steady state region (~ 90 hours) which is not observed in the CMSX-4. The improvement in the rupture of about 40 hours is provided by ERBALLOY compared to the CMSX-4.

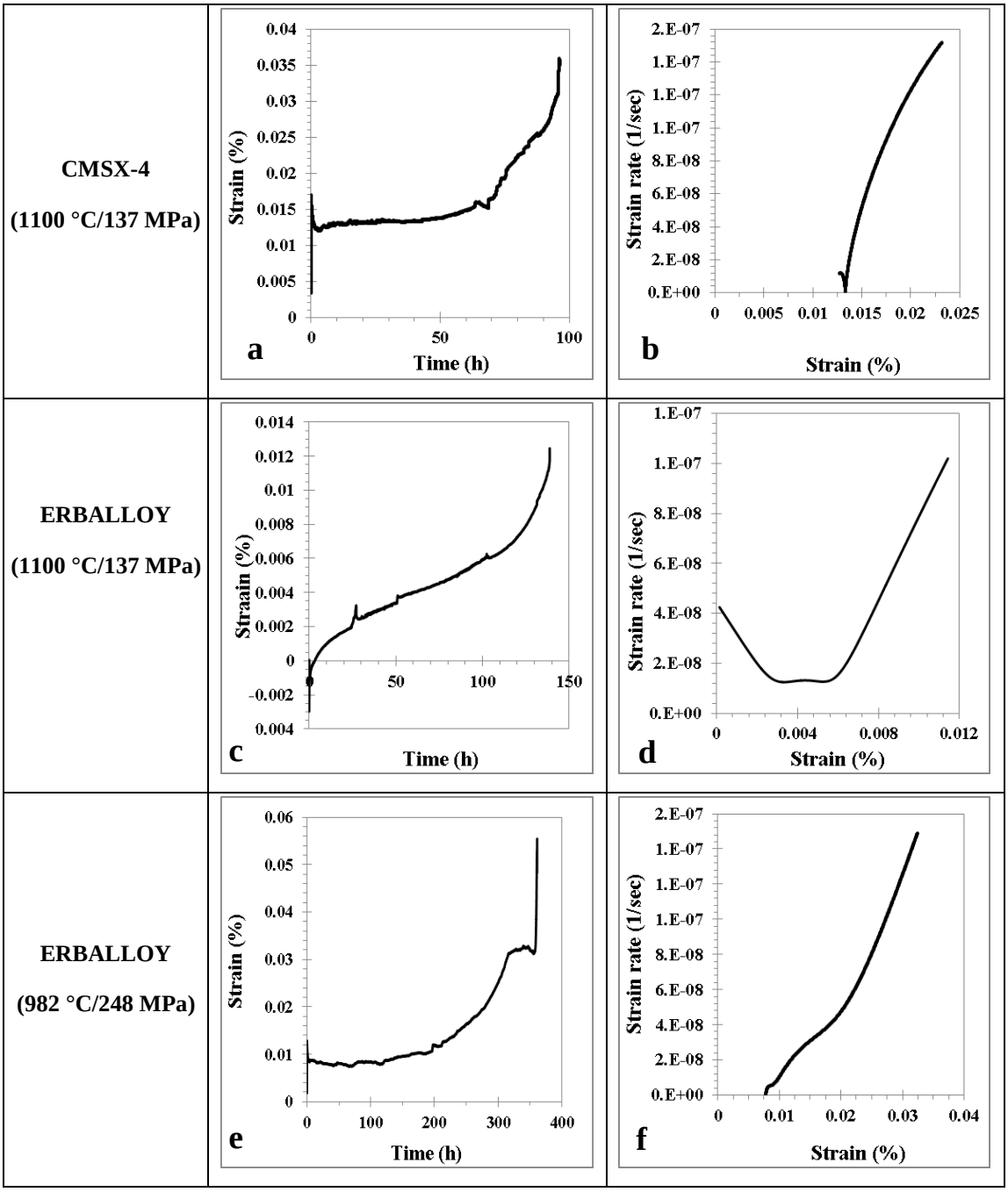

Figure 3.56. The strain vs time curves (a, c, and e), and strain rate vs strain (b, d, and f) for the alloys grown in this study.

Results of the creep testing at intermediate temperature regime (982°C/248 MPa) is shown in Figure 3.56e and f. After an elastic jump of the strain in the beginning of the test, there is a long period of the steady state creep where the strain is almost constant. No primary creep was observed for this sample. The steady state creep continues about 120 hours, after which where the tertiary creep starts and continues up to 361 hours where the rupture occurs. Again, the results are comparable with the creep testing of the commercial CMSX-4 alloy at a similar test condition (Figure 3.57c and d), which shows a monotonic increase of the strain rate with increasing the strain. Another striking similarity between the plots is the absence of the primary creep.

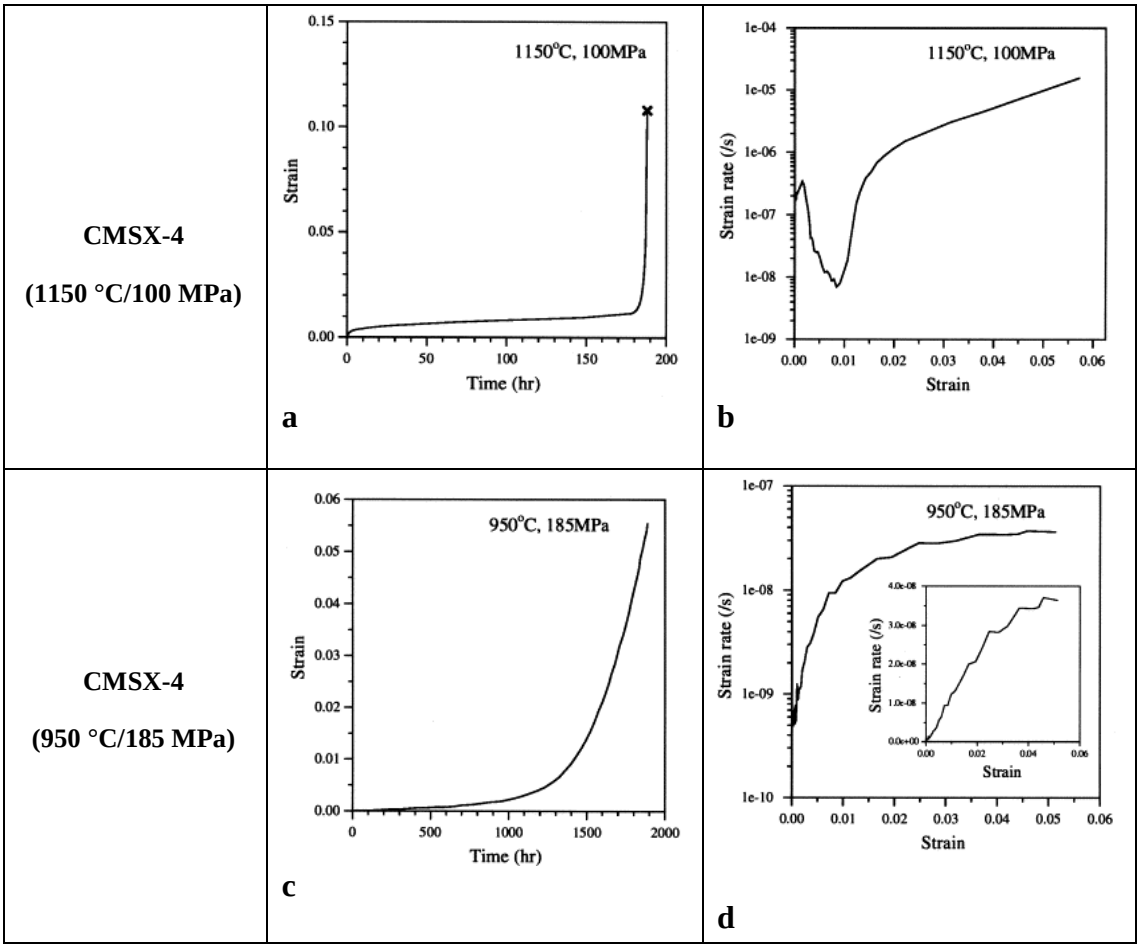

Figure 3.57. Creep test under intermediate and high temperature regime for the alloy CMSX-4 [222].

The different creep behavior in the CMSX-4 and ERBALLOY in Figure 3.56 is due to chemical composition difference between the two alloys, and the different temperature regimes. Transmission electron microscopy microstructural analysis is required to understand the underlying mechanism for the effect of chemical composition and combined effect of the stress and temperature on the creep life. Since such an analysis is out of the scope of this study, the obtained results are analyzed based on the similarity of the results with known commercial Re containing single crystal superalloys [222,224,225]. Emphasis is made on differentiating between the high temperature regime and intermediate temperature regimes which are subject of this study, too. It is also worthwhile to note that in spite of the increasing trend for the turbine entry temperature, the high temperature creep data for the single crystal superalloys is limited [226].

The study of the microstructure of the crept single crystal superalloys at intermediate and high temperatures have shown that a rafted microstructure. The solutionized and aged microstructures contain regular arrays of cuboidal γ' precipitates inside a γ matrix, which raft during creep leading to different morphologies depending on the temperature/stress applied. Figure 3.58a shows the solutionized and aged microstructure for a single crystal superalloy with the nominal Re content between 3 and 5wt% [222]. Figure 3.58 b and c, shows the microstructure of the same alloy after creep under 980°C-250 MPa and 1100°C-120MPa respectively. The rafting of the γ' precipitates normal to the applied load is seen in the Figure 3.58b. Under high temperature creep condition at 1100°C (Figure 3.58c), the thickness of the γ phase has increased significantly forming wavy platelets around the precipitates.

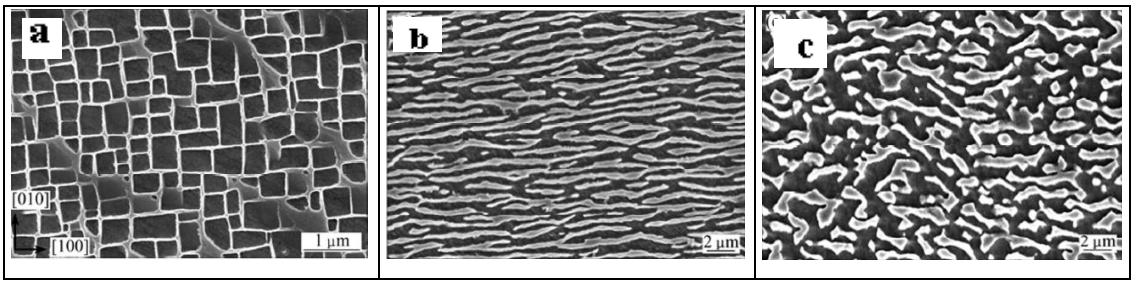

Figure 3.58. Change in the morphology of the γ-γ' microstructure for a Re containing (3 to 5wt%) crystal superalloy. Solutionized and aged sample (a), microstructure after creep under 980°C-248 MPa (b), and microstructure after creep under 1100°C-120Mpa (c) [222].

The interrupted creep tests at high temperature regimes (>1000°C) have shown that a well-developed raft microstructure form at the primary creep stage in times less than 10 hours which will stays undeformed as deformation proceeds [224]. Rafting is gradual changes in the microstructure causing the directional coarsening of the precipitates under loading at high temperatures. The sign and direction of the load and the lattice misfit between the matrix and precipitate are the two parameters that determine the type and extent of the rafting. In superalloys with the negative misfit, under applied tensile stress, the rafting takes place normal to the direction of the applied which is known as the N type rafting. The compressive stress on the other hand leads to the rafting parallel to the load direction, which is known as the P type rafting. The reverse is true for the superalloys with a positive misfit [58,59]. Since most of the important alloys with practical point of view (including CMSX-2, CMSX-4 and CMSX-10), have negative misfit, studying the N type rafting is of greater importance. The driving force for the rafting is diffusion of the solutes from the matrix to precipitate or visa-versa. In alloys with N type rafting, γ forming elements (Cr, Co Re, W, and Mo) diffuse to the horizontal channels and increases the width of the matrix. On the other hand, γ' forming elements (Al, Ta, and Ti) diffuse to the vertical channels and cause the coarsening of the precipitates normal to the applied load [167]. Concurrent to rafting, a network of dislocations with high density has been reported for high temperature/low stress creep regimes. Well-developed irregular network of dislocations could form during the primary creep which becomes more regular as deformation proceeds [224]. The high density of these dislocation network fill entire microstructure at the strain levels below 0.1% and the density increases as the deformation proceeds in the primary creep region [225]. These dislocations form as a result of the misfit in the microstructure. In fact, the stress due to misfit is released at high temperatures by forming a network of the edge dislocations at the interface of the matrix and precipitate. To reduce the effect of the mismatch, the extra half plane of edge dislocations is located in the phase with lower lattice parameter (γ'). The increase in the lattice misfit therefore will increase the density of these dislocations. The dislocation networks then form due to interaction of dislocations with different burgers vectors and different slip planes. When these dislocations move to the same slip plane, the dislocation networks form in three dimensional. The irregular dislocation network is trapped at γ/γ' interface then transforms to arrays of hexagonal or square at the later stages of deformation [225]. The formation of

the rafting above 1000 °C is hard to prevent. A dense dislocation network prevents penetration of the mobile dislocations into the γ' precipitates [227].

These dislocation networks are shown in Figure 3.59a and b for a third generation alloy with the rafted microstructure shown in Figure 3.58 at the intermediate and high temperature regimes, respectively. It is observed that a more regular dislocation network has formed for the alloy tested at higher temperatures. Therefore, the reduction in creep rate during the primary creep is due to formation of the rafted microstructure with dislocation networks [224]. In fact, rafting prevents the gliding and climbing {111}<110> creep dislocations around the γ' particles. Deformation requires shearing of the rafted γ' which is limited due to the resistance of the precipitates to the shearing.

After the decreasing creep rate region (primary) for the CMSX-4 tested at the high temperature (Figures 3.56 a and b), the material deforms continuously and the dislocation climbing and gliding is the deformation mechanism for the increasing creep rate region (tertiary). In the later stages of the tertiary deformation, the localized deformation in the regions close to the final fracture point and the cavitation associated with the casting porosity and TCP phases are the main reasons for the rupture [224].

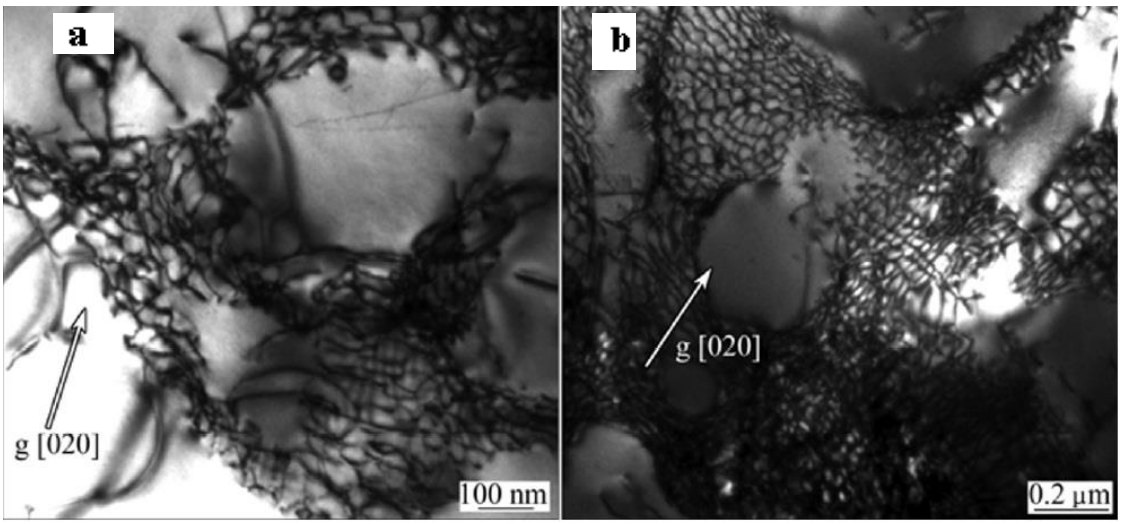

Figure 3.569. a) The interfacial dislocation network for alloy with rafted microstructure shown in Figure 3.58 (b), and b) the denser dislocation network for the microstructure of Figure 3.58 (c) [224].

The higher rupture strength of the ERBALLOY at test condition of 1100°C/137 MPa, compared to the CMSX-4 is mainly related to the effect of the Re element, which has a larger atomic size than the matrix elements. This increases the strain in the matrix and at the matrix and precipitate interface. Due to the mentioned effect, addition of the Re element is effective to hinder dislocation movement into the matrix and the rafted γ' precipitate. The effect of chemical composition on the lattice misfit is important. The increase in temperature capability of superalloys has been reported towards the alloys with more negative lattice misfit. The creep deformation is due to passing of the dislocations through the γ channels. For the movement of the dislocations to happen, the resolved shear stress should be overcome. The external loading and the stress induced by the lattice misfit provide the force for dislocation movement. The compressive stress in the matrix channels is due to negative misfit is superimposed with the tensile loading stress to reduce the net stress is in the γ channels. Since the creep deformation is dependent on the dislocation activity in the γ matrix channels, this reduces the deformation rate. The second effect of the misfit is formation of edge dislocation networks in the microstructure at high temperatures [228].

The ERBALLOY tested at intermediate temperature regime (982°C/248MPa) revealed different creep behavior than high temperature one (1100°C/137MPa). First of all, no primary creep is observed. Compared to the ERBALLOY tested at the high temperature, the strain does not vary much during steady state creep. The minimum strain rate is lower than that of ERBALLOY tested at the higher temperature. The rest of the deformation is accompanied by increase of the strain rate with the strain which is called the tertiary creep. Compared to the alloys tested at high temperatures, it is estimated that the rafts be more regular and form slower. (Figure 3.58b andc). The rafting occurs more rapid at higher temperatures. The deformation in the secondary and tertiary stage is via octahedral slip with {111}<110> creep dislocations gliding and climbing around the γ' particles [224].

The alloys CMSX-4 is developed by Cannon Muskegon corporation [229,230], and several creep rupture tests have been done by this company to investigate the temperature capability of the alloy. Table 3.10 shows the rupture time at several combinations of the stress and temperature [229,230]. An experiment on the CMSX-4 alloy by Cannon

Muskegon (CM) at 982°C/248MPa has yielded the rupture time of 275 h. This shows that the ERBALLOY is 1.3 times stronger in this creep regime.

Table 3.10. The experimental rupture time and Larson Miller parameter for the CMSX-4 by Cannon Muskegon and this study. The last two raws is for the ERBALLOY.

Alloy	**T (°C)**	**Stress (Mpa)**	**Rupture time (h)**	**Larson Miller parameter (T+273)(20+log(t))/1000**
CMSX-4 (Cannon Muskegon) [229,230].	913	517	52	25.76
	982	248	275	28.16
	982	296	88	27.54
	1010	248	82	28.12
	1050	190	90	29.05
	1121	103	640	31.79
CMSX-4 (This study)	1100	137	100	30.21
ERBALLOY (This study)	1100	137	140	30.41
ERBALLOY (This study)	982	248	361	28.31

These data are plotted in the Larson-Miller parameter to see how the results of this study will follow the experimental results by Cannon Muskegon.

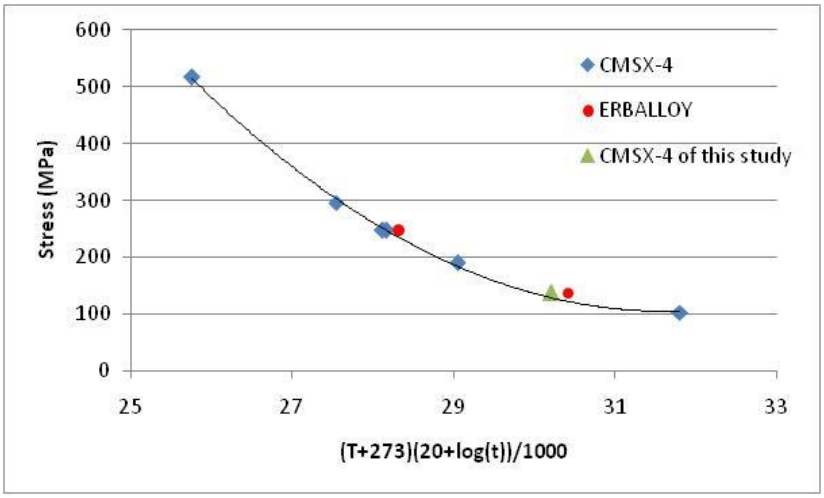

Figure 3.60. The Larson Miller parameter for the CMSX-4 by Cannon Muskegon, CMSX-4 produced in this study and ERBALLOY.

Figure 3.60 shows that the rupture results of the CMSX-4 produced and tested in this study match the Larson-Miller parameter of the CMSX-4 by CM. Moreover, the ERBALLOY locates above the Larson-Miller plot of the CMSX-4 in Figure 3.60. It is seen that ERBALLOY shows better rupture strength than CMSX-4 for the two creep-rupture regimes. This could be better represented by the increase in service temperature measured from the Larson-Miller plots.

The temperature rise with the ERBALLOY is estimated to from 5 to 7°C in the temperature range from 982 to 1100°C. This value has been reported to be 30°C between the CMSX-10 (third generation) and CMSX-4 (second generation) superalloys [230]. Although the temperature superiority of the ERBALLOY is less than CMSX-10, this study allows for selection of any alloy like the Alloy X mentioned in section 3.3.1 with superior creep resistivity to be designed and manufactured. A lower than expected value for ERBALLOY should be due to alloy preparation difficulties due to inadequacy of the available equipment.

4. CONCLUSION

Single crystal superalloys are especially designed to withstand at high temperatures close to the melting temperature of the alloys. Alloying elements are the main alloy design parameters that determine the physical, microstructure, and room temperature and high temperature mechanical properties of the single crystal superalloys. The results of this study has provided an alloy design space which allows for determining the role of every alloying elements and distinguishing the space for every generation of the single crystal superalloys from first to third generation. Based on the results of this study, a good approximation was made for the density, rupture time, volume fraction of the γ' precipitates and propensity to formation of the TCP phases. TCP phase are phases rich in refractory elements (Re, W, Ta, and Mo) which reduce the solid solution strengthening effect of these elements. Several suggestions was made for design of the low density-creep resistant alloys with low propensity to formation of the TCP phases which can be a subject of the future studies on this subject. It was determined that Re is very important in increasing the creep resistivity of the single crystal superalloys. Al is important alloy in providing enough volume fraction of the γ' precipitates which is the main strengthening mechanism. The result of this study clearly showed that the optimum volume fraction of the precipitates is in the range between 55-70%. The alloys with Ta/W ratio of 1 are the ones which withstand for longer times at high temperatures. On the other hand Cr is shown to reduce the creep resistance and this established the correctness of the current trend for reducing the Cr content in third generation alloys.

An alloy was selected and manufactured via directional solidification with the thermal gradient of 24°C/cm with two methods of vertical Bridgman (VB) and vertical Bridgman with submerged baffle (VBSB). The solidification and its relation with the withdrawal velocity during withdrawal process is determined by measuring the interface displacement and temperature variation inside the melt by inserting a thermocouple inside an alumina tube in the melt. The microstructural characteristics of the alloy provided insightful information about solidification characteristics like the melt-back transition, mushy and initial competitive growth regions. These information was used to clarify their substantial role on the primary dendrite arm spacing (PDAS), dendrite core size and

microporosity content along the solidified bars are shown. The microporosity content was shown to be related to the estimated interdendritic width which is calculated by the considering the dendrite core size and PDAS. It has been shown that the microporosity increases along the solidified sample, moreover, the VBSB samples showed lower microporosity which is due to the different solidification characteristics (lower melt-back transition and mushy zone length and larger PDAS) and reduction in the convection provided by lower melt height in VBSB method. The liquidus, solidus, and γ' solvus temperature and the solidification microsegergation were determined by simulation via Thermo-Calc equilibrium and Scheil modules. The solidified samples were then heat treated by first solutionizing the residual γ' inherited from the solidification. This process also reduced the microsegregation considerably. This process was simulated by Dictra. The experimental results are compared with the simulation and showed that a ramped solution treatment is required to prevent the incipient melting and also to remove the undissolved γ' islands from the microstructure. However, a very long solution treatment is required to completely remove the microsegregation which is not economically practical. The aging treatment of the sample revealed a bimodal size distribution of the precipitates which coarsened by aging time. The simulation of the coarsening process during the primary aging process by TC-Prisma revealed a size distribution of similar to the experimental results, however since the TC-Prisma does not consider the pre-existing volume fraction of the precipitates before the aging treatment; the simulation results do not match the experimental results.

Three creep-rupture tests were performed on the deigned alloy (ERBALLOY) at high and intermediate temperature and the results were compared with the results of the NN modeling. NN modeling provided reasonable agreement with the experimental results. The designed alloy showed advancement in the rupture strength by increasing the Re content. The mechanisms for the creep of the alloys were determined by the strain and strain rate plots.

This study provides opportunity for the future projects on designing and manufacturing low density and high creep resistant single crystal superalloys which could be candidates for the future turbine blade materials.

5. FUTURE WORKS

This work was a pioneering work in the field of alloy design and single crystal growth of the Ni base superalloys in Turkey. The results of this work could be studied further in detail especially in the following fields:

- Modification of the single crystal growth system to achieve a higher thermal gradient will provide better microstructural control. Therefore, the effect of thermal gradient on the microstructure and mechanical properties of the superalloys could be studied more in detail. Especially, the temperature distribution, melt-back transition and mushy regions, fluid flow, and freckling can be studied and compared with the results of the lower thermal gradient growth study.

- The optimum alloy compositions forecasted as results of this study can be produced and the results can be compared with the commercial first, second, third and even fourth generation superalloys.

- The solidification of the superalloys could be studied especially for evaluation of the phase dendritic structure by quenching a solidifying alloy. Dendrite tip radius can be determined to aid developing an analytical dendritic solidification model.

- The other parameters like M_d, corrosion and oxidation resistance related parameters, castability, and cost can be included in the neural network (NN) model.

- The effect of solution treatment time and temperature on mechanical properties could be studied, with respect to the amount of the remnant eutectic in the solution treatment the interdendritic region, and the TCP phase evolution.

- Effect of different aging temperatures can be studied on evolution of the coarse and fine precipitates, and the TCP phases.

- The nucleation and growth of the TCP phases could be modeled with Dictra. TEM observation could help characterization of the nucleation and growth of the different TCP morphologies.

- Formation mechanisms of the fine precipitates could be detailed.

- Effect of the fine precipitates on the rupture strength and deformation mechanism of the superalloys can be studied via transmission electron microscopy (TEM).

REFERENCES

1. R.C. Reed, *Superalloys, Fundamentals And Applications*, Cambridge Univ. Press, 2006.

2. T.M. Pollock, S. Tin, "Nickel-Based Superalloys for Advanced Turbine Engines: Chemistry, Microstructure and Properties", *J. Propuls. Power*, *22* ,pp.361-374, 2006.

3. C.T. Sims, "A History Of Superalloy Metallurgy For Superalloy Metallurgists", *Superalloys 1984*, pp. 399-419, 1984.

4. F.D.J. and W.J.R. Harris K, Erickson G L, Schwer R E, "Process and alloy optimization for CMSX-4 superalloy single crystal airfoils High Temperature Materials for Power Engineering", *Proc. Cost Conf. Liege 24-26 Sept. Ed Bachelet E. Al* , Kluwe, Dordrecht, Holland, 1990.

5. T. Yamagata, H. Harada, S. Nakazawa, M. Yamazaki, Y.G. Nakagawa, "Alloy Design For High Strength Nickel-Base Single Crystal Alloys", *TMS 1984*, pp. 157-166, 1984.

6. A. Nowotnik, K. Kubiak, J. Sieniawski, P. Rokicki, P. Pędrak, G. Mrówka-Nowotnik, "Development of Nickel Based Superalloys for Advanced Turbine Engines", *Mater. Sci. Forum*. 783–786, pp. 2491-2496, 2014.

7. A. Kracke, "Superalloys, the Most Successful Alloy System of Modern Times-Past, Present, and Future", *Superalloy 718 Deriv*., John Wiley & Sons, Inc., Hoboken, NJ, USA, pp. 13-50, 2012

8. H.J. Murphy, A.M. Reltran, "PHACOMP Revisited", *Superalloys 1988*, pp. 47-66, 1968.

9. K. Matsugi, Y. Murata, M. Morinaga, N. Yukawa, "Realistic advancement for nickel-based single crystal superalloys by the d-electrons concept", Superalloys 1992, pp. 307-316, 1992.

10. R.C. Reed, T. Tao, N. Warnken, "Alloys-By-Design: Application to nickel-based single crystal superalloys", *Acta Mater*, 57, pp. 5898-5913, 2009.

11. D.J. Crudden, B. Raeisinia, N. Warnken, R.C. Reed, "Analysis of the Chemistry of Ni-Base Turbine Disk Superalloys Using an Alloys-By-Design Modeling Approach", *Metall. Mater. Trans. A*, 44, pp. 2418-2430, 2013

12. Thermo-Calc, Http.*www.thermocalc.com/products-services/software/thermo-calc*, accessed at May 2017.

13. JMatPro, Http.*www.sentesoftware.co.uk/jmatpro.aspx*, accessed at May 2017

14. PANDANT: Calculation of phase equilibria and thermodynamic properties Software, Http.*www.computherm.com/index.php?route=product/category&path=71* , (accessed May 1, 2017).

15. R.C. Reed, T. Tao, N. Warnken, N. Rene, N. Rene, "Alloys-By-Design : Application to nickel-based single crystal superalloys", *Acta. Mater*, 57, pp. 5898-5913, 2009.

16. T. Yamagata, H. Harada, S. Nakazawa, M. Yamazaki, "Effect of Ta/W Ratio in γ' Phase on Creep Strength of Nickel-base Single Crystal Superalloys", *Transactions ISIJ*, 26, pp. 638-641, 1986.

17. T. Yokokawa, H. Harada, K. Kawagishi, Y. Koizumi, T. Kobayashi, "Quantitative Analysis Of Creep Strengthening Factors In Ni-Base Single Crystal Super Alloys", Superalloys 2012, pp. 285-292, 2012.

18. J. Jones, D.J.C. Mackay, "Neural network modelling of the mechanical properties of nickel base superalloys", *Superalloys 1996*, pp. 417-424, 1996.

19. Y.S. Yoo, I.S. Kim, D.H. Kim, C.Y. Jo, H.M. Kim, C.N. Jones, "The Application Of Neural Network To The Development Of Single Crystal Superalloys", *Superalloys 2004*, pp. 941-950, 2004.

20. K. Hornik, M. Stinchcombe, H. White, "Universal approximation of an unknown mapping and its derivatives using multilayer feedforward networks", *Neural Networks*, 3, pp. 551-560, 1990

21. M. Leshno, V.Y. Lin, A. Pinkus, S. Schocken, "Multilayer feedforward networks with a nonpolynomial activation function can approximate any function", *Neural Networks*, 6, pp. 861–867, 1993

22. K. Hornik, M. Stinchcombe, H. White, "Multilayer feedforward networks are universal approximators", *Neural Network*s, 2, pp. 359-366, 1989.

23. A. Milosavljević, "Heat Treatment Effect on Multicomponent Nickel Alloys Structure", *FME Trans*, 35, pp.189-193, 2007.

24. M.J. Donachie, S.J. Donachie, *Superalloys, A Technical Guide Second Edition*, 2001, www.asminternational.org , accessed at august 2017.

25. K. Kawagishi, A.-C. Yeh, T. Yokokawa, T. Kobayashi, Y. Koizumi, H. Harada, "Development Of An Oxidation-Resistant High-Strength Sixth- Generation Single-Crystal Superalloy", *TMS-238*, pp. 189-195, 2012.

26. E. Balikci, A. Deal, R. Abbaschian, S. V. Bykova, V.D. Golyshev, M.A. Gonik, V.B. Tsvetovsky, M.P. Marchenko, I. V. Frjazinov, "A study on the morphological stability of faceted interfaces in antimony-doped germanium single crystals grown by the axial heat processing method", *Cryst. Growth Des*, 4, pp. 377-381, 2004.

27. A. Deal, E. Balikci, R. Abbaschian, "Enhanced Morphological Stability in Sb-Doped Ge", *Metall. Mater. Trans. A*, 38, pp. 100-115, 2007.

28. A. Dario, H. Sicim, E. Balikci, "A new approach for dopant distribution and morphological stability in crystals grown by the axial heat processing (AHP) technique", *J. Cryst. Growth*, 337, pp.65–71, 2011.

29. M. Montakhab, M. Bacak, E. Balikci, "Low Melt Height Solidification of Superalloys", *Metall. Mater. Trans*. A, 47, pp. 3031-3039, 2016.

30. R.C. Reed, *Superalloys, Fundamentals and Applications*, Cambridge Univ. Press, 2006.

31. M.J. Donachie, S.J. Donachie, Superalloys : a technical guide, ASM International, 2002, accessed at September 2017.

32. E. Akca, A. Gürsel, "A Review on Superalloys and IN718 Nickel-Based Superalloy", Period. Eng. Nat. Sci, 3, pp. 15-27, 2015.

33. M.-Y. Li, S.-M. Kuo, Y.-T. Pan, "Microstructure Observation and High-temperature Property of Iron-Nickel-Base Superalloy", *China Steel Technical Report*, 27, pp. 64-69, 2014.

34. D. Coutsouradis, A. Davin, M. Lamberigts, "Cobalt-based superalloys for applications in gas turbines", *Mater. Sci. Eng*, 88, pp. 11-19, 1987.

35. A. Suzuki, H. Inui, T.M. Pollock, "$L1_2$ Strengthened Cobalt-Base Superalloys", *Annu. Rev. Mater. Res*. 45, pp. 345-368, 2015.

36. T.M. Pollock, J. Dibbern, M. Tsunekane, J. Zhu, A. Suzuki, "New Co-based γ-γ′ high-temperature alloys", *JOM*, 62, pp. 58-63, 2010.

37. B. Nithin, A. Samanta, S.K. Makineni, T. Alam, P. Pandey, A.K. Singh, R. Banerjee, K. Chattopadhyay, "Effect of Cr addition on γ–γ′ cobalt-based Co–Mo–Al–Ta class of superalloys: a combined experimental and computational study", *J. Mater. Sci*, 52, pp. 11036-11047, 2017.

38. N. Das, "Advances in nickel-based cast superalloys", *Trans. Indian Inst. Met*. 63, pp. 265-274, 2010.

39. A.G. Evans, B.J. Dalgleish, *Metallurgy of Investment Cast Superalloy Components, in: Superalloys Supercompos. Superceram*, pp. 697-720, 1989.

40. A. Stoloff, N.S. ; Duquette, D.J. ; Giamei, "Critical issues in the development of high temperature structural materials", *Warrendale, PA (United States); Minerals, Metals and Materials Society*, pp. 87-99, 1993

41. F.I. Versnyder, M.E. Shank, "The development of columnar grain and single crystal high temperature materials through directional solidification", *Mater. Sci. Eng*, 6, pp. 213-247, 1970

42. M. Gell, D.N. Duhl, D.K. Gupta, K.D. Sheffler, "Advanced Superalloy Airfoils", *JOM*, 39, pp. 11-15, 1987.

43. J. Lacaze, A. Hazotte, "Directionally Solidified Materials: Nickel-base Superalloys for Gas Turbines", *Textures Microstruct*, 13, pp. 1-14, 1990.

44. David N. Duhl, " Second generatıon Ni-base single crystal superalloys", *Superalloys 1988*, pp. 235-244, 1988.

45. G.L. Erickson, "A new, third-generation, single-crystal, casting superalloy", *JOM*, 47, pp. 36-39, 1995.

46. J.R. Li, Z.G. Zhong, D.Z. Tang, S.Z. Liu, P. Wei, P.Y. Wei, Z.T. Wu, D. Huang, M. Han, "A Low-Cost Second Generation Single Crystal Superalloy DD6", *Superalloys 2000*, pp. 777-783, 2000.

47. Z.-X. Shi, J.-R. Li, S.-Z. Liu, X.-G. Wang, "Creep properties and microstructure evolution of nickel-based single crystal superalloy at different conditions", *Trans. Nonferrous Met. Soc. China*, 24, pp. 2536-2543, 2014.

48. T. Jin, W.Z. Wang, X.F. Sun, Z.Q. Hu, "Role of Rhenium in Single Crystal Ni-Based Superalloys", *Mater. Sci. Forum*, pp. 2257-2262, 2010.

49. A. Mottura, R.C. Reed, "What is the role of rhenium in single crystal superalloys?", *Matec Web Conf.* 14, 2014.

50. E.N. Kablov, N. V Petrushin, Designing Of High-Rhenium Single Crystal Ni-Base Superalloy For Gas Turbine Blades, *Superalloys 2000*, pp. 901-909, 2000.

51. W. Schneider, J. Hamme, H. Mughrabi, "Creep Deformation and Rupture Behaviour of the Monocrystalline Superalloys CMSX-4 - A Comparison with the Alloy SRR 99", *Superalloys 1992*, pp. 589-598, 1992.

52. M.Gell, D.N.Duhl and A.F.Giamei, *Superalloys 1980*, pp. 205-214, 1980.

53. N.E. Prasad, R.J.H. Wanhill, eds., *Aerospace Materials and Material Technologies*, Springer Singapore, Singapore, 2017.

54. A. Sato, H. Harada, A.-C. Yeh, K. Kawagishi, T. Kobayashi, Y. Koizumi, T. Yokokawa, J.-X. Zhang, "A 5th Generation Sc Superalloy With Balanced High Temperature Properties and Processability", *Superalloys 2008*, pp. 131-138, 2008.

55. A. Sato, H. Harada, A.-C. Yeh, K. Kawagishi, T. Kobayashi, Y. Koizumi, T. Yokokawa, J.-X. Zhang, "A 5th Generation Sc Superalloy With Balanced High Temperature Properties and Processability", *Superalloys 2008*, pp.131-138, 2008.

56. K. Kawagishi, A.-C. Yeh, T. Yokokawa, T. Kobayashi, Y. Koizumi, H. Harada, "Development Of An Oxidation-Resistant High-Strength Sixth- Generation Single-Crystal Superalloy TMS-238", *Superalloys 2012*, pp. 189-195, 2012.

57. H. Kitaguchi, Microstructure-Property Relationship in Advanced Ni-Based Superalloys, in: *Metall. Adv. Mater. Process*, pp.19-42, 2012.

58. M. Kamaraj, "Rafting in single crystal nickel-base superalloys - An overview", *Sadhana*, 28 , pp. 115-128, 2003.

59. F.R.N. Nabarro, "Rafting in Superalloys", *Metall. Mater. Trans. A*, 27 , pp. 513-530, 1996.

60. H. Kitaguchi, "Microstructure-Property Relationship in Advanced Ni-Based Superalloys", *Metall. Adv. Mater. Process*, pp. 19-42, 2012.

61. R.A. Mackay, R.A. Mackay, M. V Nathal Nation, "Microstructure-Property Relationships in Directionally Sdidified Single Crystal Nickel-Base Superalloys Microstructure-Property Relationships in Directionally Solidified Single Crystal Nickel-Base Superalloys", *NASA technical memorandum, MiCon 1986, Pennsylvania, 1986.*

62. C. Rae, M. Karunaratne, C. Small, R. Broomfield, C. Jones, R. Reed, "Topologically Close Packed Phases in an Experimental Rhenium-Containing Single Crystal Superalloy", Superalloys 2000, pp. 767-776, 2000.

63. K. Matuszewski, *Precipitation of topologically close packed phases in Ni-base superalloys - the effect of Re and Ru*, Ph.D. Thesis, FAU University Press ein Imprint der Universität Erlangen-Nürnberg. Universitätsbibliothek, 2016.

64. K. Matuszewski, R. Rettig, H. Matysiak, Z. Peng, I. Povstugar, P. Choi, J. Müller, D. Raabe, E. Spiecker, K.J. Kurzydłowski, R.F. Singer, "Effect of ruthenium on the precipitation of topologically close packed phases in Ni-based superalloys of 3rd and 4th generation", *Acta Mater*, 95 , pp. 274-283, 2015.

65. R. Darolia, D. Lahrman, R. Field, R. Sisson, "Formation of Topologically Closed Packed Phases in Nickle Base Single Crystal Superalloys", *Superalloys 1998*, pp. 255-264, 1998.

66. K. Zhao, Y.H. Ma, L.H. Lou, Z.Q. Hu, "Mu Phase in a Nickel Base Directionally Solidified Alloy", *Materials Transactions*, 4, pp. 54-58, 2005.

67. F. Long, Y.S. Yoo, C.Y. Jo, S.M. Seo, H.W. Jeong, Y.S. Song, T. Jin, Z.Q. Hu, "Phase transformation of η and σ phases in an experimental nickel-based superalloy", *J. Alloys Compd*, 478, pp.181-187, 2009.

68. K. Zhao, Y.H. Ma, L.H. Lou, Z.Q. Hu, "μ Phase in a Nickel Base Directionally Solidified Alloy", Mat. Trans, 46, pp. 54-58, 2005

69. J. Huo, Q. Shi, Y. Zheng, Q. Feng, "Microstructural characteristics of σ phase and P phase in Ru-containing single crystal superalloys", *Mater. Charact*, 124, pp. 73-82, 2017.

70. J.-H. Liao, H.-Y. Bor, C.-G. Chao, T.-F. Liu, "Effects of Rhenium on Microstructure and Phase Stability of MAR-M247 Ni-Base Fine-Grain Superalloy", *Mater. Trans*, 51, pp. 810-817, 2010.

71. C. Rae, M. Karunaratne, C. Small, R. Broomfield, C. Jones, R. Reed, "Topologically Close Packed Phases in an Experimental Rhenium-Containing Single Crystal Superalloy, *Superalloys 2000*, pp.767-776, 2000.

72. Q. Feng, T.K. Nandy, L.J. Rowland, B. Tryon, D. Banerjee, T.M. Pollock, "New Phases In Ruthenium-Containing Single-Crystal Superalloys", *Superalloys 2004*, pp. 769-778, 2004.

73. L. Pauling, "The Nature of the Interatomic Forces in Metals", *Phys. Rev*, 54, pp. 899-904, 1936.

74. S. Rideout, W.D. Manly, E.L. Kamen, B.S. Lement, P.A. Beck, "Intermediate Phases in Ternary Alloy Systems Of Transition Elements", *JOM*, 3 , pp. 872-876, 1951.

75. M. Morinaga, N. Yukawa, H. Adachi, H. Ezaki, "New Phacomp And its Applications to Alloy Design", *Superalloys 1984*, pp. 523-532, 1984.

76. K. Matsugi, Y. Murata, M. Morinaga, N. Yukawa, "Realistic Advancement for Nickel-Based Single Crystal Superalloys by the D-Electrons Concept", *Superalloys 1992*, pp. 307-316, 1992.

77. J. Liu, J. Yu, T. Jin, X. Sun, H. Guan, Z. Hu, "Influence of temperature on tensile behavior and deformation mechanism of Re-containing single crystal superalloy", *Trans. Nonferrous Met. Soc. China*, 21, pp. 518-1523, 2011.

78. T.M. Pollock, S. Tin, "Nickel-Based Superalloys for Advanced Turbine Engines: Chemistry, Microstructure, and Properties", *J. Propuls. Power*, 22, pp. 361-372, 2006.

79. N.E. Dowling, Mechanical behavior of materials : engineering methods for deformation, fracture, and fatigue, Pearson, 2013.

80. A.J. Torroba, O. Koeser, L. Calba, L. Maestro, E. Carreño-Morelli, M. Rahimian, S. Milenkovic, I. Sabirov, J. Llorca, J.L. Org, "Investment casting of nozzle guide vanes from nickel-based superalloys: part 1 - thermal calibration and porosity prediction", *Journal of Integrating Materials and Manufacturing Innovation*, pp.1-25, 2014.

81. G. Sjöberg, "Casting Superalloys For Structural Applications", *Superalloys 2010*, pp. 117-130, 2010.

82. R. Prasad, "Progress in Investment Castings", *Sci. Technol. Cast. Process*, 2012, pp. 25-72, 2012.

83. S. Tin, T.M. Pollock, "Nickel-Based Superalloys for Blade Application: Production, Performance and Application", *Encycl. Aerosp. Eng., John Wiley & Sons, Ltd*, Chichester, UK, 2010, pp. 361-374, 2010.

84. S.W. Bogner, D. Ma, M. Müller, E. Ivanova, F. Wang, A. Bührig-Polaczek, "Investigation of the Undercoolability of Ni-Based Alloys Using High Temperature Thermal Analysis", *Met. Open Access J*, 5, pp. 1971–1983, 2015.

85. D.A. Porter, K.E. Easterling, M.Y. Sherif, *Phase transformations in metals and alloys*, CRC Press, 2009.

86. L. Wei, Z. Zhang, H. Zhang, S. Li, S. Gong, "Influence of aging heat treatment on microstructure and hardness of single crystal Ni3Al-base superalloy IC21", *Procedia Eng*, 27, pp. 1081-1088, 2012.

87. B.C. Wilson, J.A. Hickman, G.E. Fuchs, "The effect of solution heat treatment on a single-crystal Ni-based superalloy", J*OM*, 55, pp. 35-40, 2003.

88. S.R. Hegde, R.M. Kearsey, J. Beddoes, "Design Of Solutionizing Heat Treatments For An Experimental Single Crystal Superalloy", *Superalloys 2008*, pp. 301-310, 2008.

89. S. Wang, S. Fang, Z. Shi, J. Jiang, X. Zhou, J. Lin, "Direct powder forging of PM nickel-based superalloy: densification and recrystallisation", I*nt J Adv Manuf Technol*, 88, pp. 2661-2670, 2017.

90. D.R. Chang, D.D. Krueger, R.A. Sprague, "Superalloy Powdier Processing, Properties And Turbine Disk Applications", *Superalloys 1984*, pp. 245-273, 1984.

91. C.P. Blankenship, M.F. Henry, J.M. Hyzak ", R.B. Rohling, E.L. Hall, Hot-Die Forging of P/M Ni-Base Superalloys, *Superlaloys 1996*, pp. 653-662, 1996.

92. R. Udroiu, A. Nedelcu, O*ptimization of Additive Manufacturing Processes Focused on 3D Printing, Rapid Prototyping Technology - Principles and Functional Requirements*, Transylvania University of Brasov, Romania, Intech, 2011.

93. R. Acharya, "Experimental and Theoretical Analysis of Scanning Laser Epitaxy Applied to Nickel-Based Superalloys", *Solid Free. Fabr. Symp*. Univ. Texas Austin, TX, accessed at April 2018.

94. L.N. Carter, M.M. Attallah, R.C. Reed, Laser Powder Bed Fabrication of Nickel-Base Superalloys: Influence of Parameters; Characterisation, Quantification and Mitigation of Cracking, in: Superalloys 2012, John Wiley & Sons, Inc., Hoboken, NJ, USA, pp. 577-586, 2012.

95. W.E. Frazier, "Metal Additive Manufacturing: A Review", *J. Mater. Eng. Perform.* 23 ,pp. 1917-1928, 2014

96. M. Leino, J. Pekkarinen, R. Soukka, The Role of Laser Additive Manufacturing Methods of Metals in Repair, Refurbishment and Remanufacturing – Enabling Circular Economy, Phys. Procedia, 83, 752-760, 2016.

97. Y. TAO, J. JIA, J. LIU, Microstructure Characterization and Mechanical Properties of FGH 95 Turbine Blade Retainers, J. Iron Steel Res. Int, 17, pp.73-78, 2010.

98. T. Murakumo, Y. Koizumi, K. Kobayashi, H. Harada, Creep Strength of Ni-Base Single-Crystal Superalloys on the Gamma/Gamm-Prime Tie-Line, *Superalloys 2004*, pp. 155-162, 2004.

99. R.E. Schafrik, S. Walston, "Challenges for High Temperature Materials in the New Millennium", *Superalloys 2008, 11th Int. Symp. Superalloys*, pp. 3–9, 2008.

100. S. Ahmed, "The Design and Fabrication of Nickel-Base Superalloys", *JOM*, 42, pp. 24-26, 1990.

101. Y. Murata, S. Miyazaki, M. Morinaga, R. Hashizume3 ’, "Hot Corrosion Resistant And High Strength Nickel-Based Single Crystal And Directionally-Solidified Superalloys Developed By The D-Electrons Concept, *Superalloys 1996*, pp. 61-70, 1996.

102. R.A. Hobbs, S. Tin, C.M.F. Rae, R.W. Broomfield, C.J. Humphreys, "Solidification Characteristics Of Advanced Nickel-Base Single Crystal Superalloys", *Superalloys 2004*, pp. 819-825, 2004.

103. R.C. Reed, T. Tao, N. Warnken, N. Rene, N. Rene, "Alloys-By-Design : Application to nickel-based single crystal superalloys", *Acta Mater*, 57, 2009, pp. 5898-5913, 2009.

104. D.J. Crudden, B. Raeisinia, N. Warnken, R.C. Reed, "Analysis of the Chemistry of Ni-Base Turbine Disk Superalloys Using An Alloys-By-Design Modeling Approach", *Metall. Trans. A*, 44, pp. 2418-2430, 2013.

105. M.F. Mark, F. Horstemeyer, *Integrated computational materials engineering (ICME) for metals : using multiscale modeling to invigorate engineering design with science*, TMS-Wiley, 2012.

106. N. Chopra, "Integrated Computational Materials Engineering (ICME) for Metals: Using Multiscale Modeling to Invigorate Engineering Design with Science", *JOM*, 67, pp.118–119, 2015.

107. J.H. Panchal, S.R. Kalidindi, D.L. McDowell, "Key computational modeling issues in Integrated Computational Materials Engineering", *Comput. Des*, 45 ,pp. 4-25, 2013.

108. P. Caron, O. Lavigne, Issue 3 -November 2011 , "Recent Studies at Onera on Superalloys for Single Crystal Turbine Blades High Temperature Materials Recent Studies at Onera on Superalloys for Single Crystal Turbine Blades", *J. Aerospace. Lab*, pp. 1-14, 2011.

109. P. Caron, "High γ' Solvus New Generation Nickel-Based Superalloys For Single Crystal Turbine Blade Applications", *Superalloys 2000*, pp. 737-746, 2000.

110. M. Pessah, P. Caron, T. Khan, "Effect Of Jo Phase On The Mechanical Properties of a Nickel-Base Single Crystal Superalloy", *Superalloys 1992*, pp. 567-576, 1992.

111. B.A. Cowles, C. Consulting, A*dvancement And Implementation of Integrated Computational Materials Engineering (ICME) for Aerospace Applications (Preprint) Materials And Manufacturing Directorate*, AFRL-RX-TP-2010-4151, 2010.

112. P. Caron, "High γ' Solvus New Generation Nickel-Based Superalloys for Single Crystal Turbine Blade Applications", *Superalloys 2000*, pp. 737-746, 2000.

113. K. Matsugi, Y. Murata, M. Morinaga, N. Yukawa, "Realistic advancement for nickel-based single crystal superalloys by the d-electrons concept", *Superalloys 1992*, pp.307-316, 1992.

114. Y. Murata, S. Miyazaki, M. Morinaga, R. Hashizume, "Hot Corrosion Resistant And High Strength Nickel-Based Single Crystal and Directionally-Solidified Superalloys Developed by the D-Electrons Concept, *Superalloys 1996*, pp. 61-70, 1996.

115. M. Mostafaei, S.M. Abbasi, "Designing and characterization of Al-and Ta-bearing Ni-base superalloys based on d-electrons theory", *Mater. Des*, 127, pp. 67-75, 2017.

116. U.R. Kattner, "The Calphad Method And Its Role in Material And Process Development", *Tecnol. Em Metal. Mater. E Min*, 13, pp. 3-15, 2016.

117. P.M. Series, *CALPHAD (Calculation of Phase Diagrams): A Comprehensive Guide*, Elsevier, 1998.

118. J.-O. Andersson, T. Helander, L. Hdghmd, P. Shi, B. Sundman, "THERMO-CALC & DICTRA, Computational Tools For Materials Science", *Pergamon Calphad*. 26, pp. 273-312, 2002.

119. B. Jönsson, B. Sundman, Thermochemical Applications of Thermo-Calc, *Mater. Chem. High Temp*., Humana Press, Totowa, NJ, pp. 263-273, 1990.

120. S.-H. Kang, Y. Deguchi, K. Yamamoto, K. Ogi, M. Shirai, "Solidification Process and Behavior of Alloying Elements in Ni-Based Superalloy Inconel718", *Mat Transactions*, 45, pp. 2728-273, 2004.

121. *History of the Thermo-Calc*, http://www.thermocalc.com/our-company/history/, accessed at September 2017.

122. L. Liu, T. Jin, J. Liang, X. Sun, Z. Hu, "Calculation and Experiments on the Solidification Behavior Of Single Crystal Superalloy Containing Ru", *Rev. Adv. Mater. Sci*, 33, pp. 305-310, 2013.

123. M.C. Flemings, Flemings, M. C., *Solidification Processing*, Mater. Sci. Technol., Wiley-VCH Verlag GmbH & Co. KGaA, Weinheim, Germany, 2006.

124. A. Borgenstam, L. Höglund, J. Ågren, A. Engström, "DICTRA, a tool for simulation of diffusional transformations in alloys", *J. Phase Equilibria*. 21, pp. 269-280, 2000.

125. G. Zhang, B.E. Patuwo, M.Y. Hu, "Forecasting with artificial neural networks: The state of the art", *Int. J. Forecast*, 14 , pp. 35-62, 1998.

126. K. Hornik, M. Stinchcombe, H. White, " sUniversal approximation of an unknown mapping and its derivatives using multilayer feedforward network", Neural Networks, 3,rpp.551–560, 1990.

127. D.M. Titterington, "Bayesian Methods for Neural Networks and Related Models", *Stat. Sci*. 19, pp. 128-139, 2004.

128. K. Hornik, "Approximation Capabilities of Muitilayer Feedforward Networks", Neural Networks, 4 , pp. 251-257, 1991.

129. P. Baron, J. Mendrok, Y. Kasai, "Implementation of a neural network for retrieving atmospheric parameters from remote sensing", J. Natl. Inst. Inf. Commun. Technol. 54, 2007.

130. M.T. Hagan, H.B. Demuth, M.H. Beale, O. De Jesús, Neural network design, Campus publishing sevice, University of Colorado, 2014.

131. P.C. Bhat, H.B. Prosper, Bayesian Neural Networks, "Bayesian neural networks", *Conf.Proc. C050912*, pp. 151-154, 2005, accessed at September 2017.

132. J.S. Lee, J.H. Gu, H.M. Jung, E.H. Kim, Y.G. Jung, J.H. Lee, "Directional Solidification Microstructure Control in CM247LC Superalloy", *Mater. Today Proc*. 1, pp. 3-10, 2014.

133. W. Shyy, *Computational modeling for fluid flow and interfacial transport*, Dover Publications, 2006.

134. N. Stanford, a Djakovic, B. Shollock, M. McLean, N. D'Souza, P. Jennings, "Defect grains in the melt-back region of CMSX-4 single crystal seeds, Superalloys", *Superalloys 2004*, pp. 719-726, 2004.

135. N. Stanford, A. Djakovic, B.A. Shollock, M. McLean, N. D'Souza, P.A. Jennings, "Seeding of single crystal superalloys - Role of seed melt-back on casting defects", *Scr. Mater*, 50 , pp. 159-163, 2004.

136. N. D'Souza, P.A. Jennings, X.L. Yang, P.D. Lee, M. McLean, H.B. Dong, "Seeding of single-crystal superalloys - Role of constitutional undercooling and primary dendrite orientation on stray-grain nucleation and growth", *Metall. Mater. Trans. B.* 36, pp. 657-666, 2005.

137. F.P. Incropera, F.P. Incropera, *Fundamentals of heat and mass transfer*., John Wiley, 2007.

138. L. Li, R.A. Overfelt, "Influence of directional solidification variables on the cellular and primary dendrite arm spacings of PWA1484", *J. Mater. Sci*, 37 , pp. 3521-3532, 2007.

139. A. D. Cetel and D. N. Duhl, "Second-Generation Nickel-Base Single Crystal Supealloy", *Superalloys 2000*, pp. 235-244, 2000.

140. D.M.S. P. A. Curreri, J. E. Lee, "Dendritic solidification of alloys in low gravity", *Metall. Trans. A* ,19, pp. 2671-2676, 1998.

141. J.D. Hunt, "Pattern formation in solidification Pattern formation in solidification", *Sci. Technol. Adv. Mater*, 2, pp. 147-155, 2001.

142. K.Somboonsuk, R.Trivedi, "Dynamical studies of dendritic growth", *Acta Metall*, 33 ,pp. 1051-1060, 1985.

143. H.SWhitesell, R.AOverfelt, "Influence of solidification variables on the microstructure, macrosegregation, and porosity of directionally solidified Mar-M247", *Mater. Sci. Eng. A*, 318 , pp. 264-276, 2001.

144. A.J. Elliott, T.M. Pollock, "Thermal analysis of the bridgman and liquid-metal-cooled directional solidification investment casting processes", *Metall. Mater. Trans. A*, 38 , pp. 871-882, 2007.

145. D. Ma, "Novel casting processes for single-crystal turbine blades of superalloys", Fron. Mech. Eng, 13, pp. 3-16, 2018.

146. A.F. Giamei, J.G. Tschinkel, Liquid metal cooling: A new solidification technique, *Metall. Trans. A.* 7 , pp. 1427-1434, 1976.

147. M. Konter, E. Kats, N. Holynann, N. Hofmann, "Novel Casting For Single Crystal Gas Turbine Components", *Superalloys 2000*, pp. 189-200, 2000.

148. A. Ostrogorsky, "Growth of Ga-doped Ge0.98Si0.02 by vertical Bridgman with a baffle", *J. Cryst. Growth* , pp. 378-383, 2011.

149. J.R. Kim, R. Abbaschian, "Influence of solidification variables on the microporosity formation on Al–Cu (4.5 wt%) alloy with axial heat processing", *J. Mater. Sci*, 46 pp. 6213-6223, 2011.

150. J.C. Ramirez, C. Beckermann, "Evaluation of a rayleigh-number-based freckle criterion for Pb-Sn alloys and Ni-base superalloys", *Metall. Mater. Trans. A*, 34, pp. 1525-1536, 2003.

151. J.B. Wahl, and K. Harris, "New Single Crystal Superalloys, CMSX-7 and CMSX-8,", *Superalloys 2012*, pp. 179-188, 2012.

152. H. Aaronson, J. K. Lee, M. Enomoto, *Mechanisms of Diffusional Phase Transformations in Metals and Alloys*, CRE Press, Taylor & Francis Group, Boca Raton, FL, USA, 2010.

153. J.W. Christian, *Transformations in* Metals and alloys, Part 1, Pergamon Press, 1975,

154. Q. Chen, J. Jeppsson, J. Ågren, "Analytical treatment of diffusion during precipitate growth in multicomponent systems", *Acta Mater*. 56 ,pp. 1890-1896, 2008.

155. A.J. Ardellt, R.B. Nicholsons, "The Coarsening Of γ' In Ni - Al Alloys", *J . Phys . Chem . Solids*. 27 , pp. 1793-1804, 1996.

156. W. Voorhees, "The theory of Ostwald ripening", *J. Stat Phys* , 38, pp. 231-252, 1985.

157. A. Baldan, "Review Progress in Ostwald ripening theories and their applications to nickel-base superalloys Part I: Ostwald ripening theories", *J. Mater. Sci* , 37 , pp. 2171–2202, 2012.

158. D. Hadjiapostolidou, B.A. Shollock, Long Term Coarsening In René 80 Ni-Base Superalloy, Superalloys 2008, pp.733-739, 2008.

159. J. Lapin, M. Gebura, T. Pelachová, M. Nazmy, "Coarsening kinetics of cyboidal γ precipitates in single crystal nickel base superalloy CMSX-4", *Kov. Mater*, 46, pp. 313-322, 2008.

160. *TC-PRISMA*, http://www.thermocalc.com/products-services/software/precipitation-module-(tc-prisma)/ , accessed at March 2018.

161. O. Prat, J. Garcia, D. Rojas, C. Carrasco, G. Inden, "Investigations on the growth kinetics of Laves phase precipitates in 12% Cr creep-resistant steels: Experimental and DICTRA calculations", *Acta Mater*, 58 ,pp. 6142-6153, 2010.

162. M. Perez, A. Deschamps, "Microscopic modelling of simultaneous two-phase precipitation: Application to carbide precipitation in low-carbon steels", *Mater. Sci. Eng. A*, 360, pp. 214-219, 2003.

163. Z.-X. Shi, J.-R. Li, S.-Z. Liu, X.-G. Wang, "Creep properties and microstructure evolution of nickel-based single crystal superalloy at different conditions", *Trans. Nonferrous Met. Soc. China* , 24 , pp. 2536-2543, 2014.

164. Y. Ro, Y. Koizumi, H. Harada, "High temperature tensile properties of a series of nickel-base superalloys on a γ/γ′ tie line", *Mater. Sci. Eng. A.* 223 , pp. 59-63, 1997.

165. D. Mukherji, J. Rösier, "Effect of the γ′ volume fraction on the creep strength of Ni-base superalloys", *Zeitschrift Für Met*, 94 , pp. 478-484, 2003.

166. T. Murakumo, T. Kobayashi, Y. Koizumi, H. Harada, "Creep behaviour of Ni-base single-crystal superalloys with various γ′ volume fraction", *Acta Mater*, 52 , pp. 3737-3744, 2004.

167. S. Tian, B. Zhang, D. Shu, J. Wu, Q. Li, C. Jiang, "Creep properties and deformation mechanism of the containing 4.5Re/3.0Ru single crystal nickel-based superalloy at high temperatures", *Mater. Sci. Eng. A* , 643, pp. 119-126, 2015.

168. A. Fotovati, J. Kadkhodapour, S. Schmauder, "Artificial Neural Networks Investigation of Indentation Force Effects on Nano- and Microhardness of Dual Phase Steels", *J. Metall*, 2014, pp. 1-11, 2014.

169. U.R. Kattner, "The Calphad Method And Its Role In Material And Process Development", *Tecnol. Metal. Mater. Min*, 13, pp. 3-15, 2016.

170. *DICTRA, A software for simulation of Diffusiomal phase transformations*, http://www.thermocalc.com/products-services/software/diffusion-module-(dictra)/ , accessed at March 2018.

171. J.S. Langer, A.J. Schwartz, "Kinetics of nucleation in near-critical fluids", *Phys. Rev. A*, 21, pp. 948-958, 1980.

172. W.S. Rasband, *Imagej, U.S. Natl. Institutes Heal. Bethesda, MD,* 2007. http://rsb.info.nih.gov/ij/.

173. A. Szczotok, B. Chmiela, "Effect of Heat Treatment on Chemical Segregation in CMSX-4 Nickel-Base Superalloy", *J. Mater. Eng. Perfor* , 23, pp. 2739-2747, 2014.

174. R. Hashizume, A. Yoshinari, T. Kiyono, Y. Murata, M. Morinaga, "Development of Ni-Based Single Crystal Superalloys for Power-Generation Gas Turbines", *Superalloys 2004*, pp. 53-62, 2014.

175. M. Huang, J. Zhu, "An overview of rhenium effect in single-crystal superalloys", *Rare Met*, 35, pp. 127-139, 2016.

176. L. Liu, T.W. Huang, J. Zhang, H.Z. Fu, "Microstructure and stress rupture properties of single crystal superalloy CMSX-2 under high thermal gradient directional solidification", *Mater. Lett* , 61, pp. 227-230, 2007.

177. K. Harris, G.L. Erickson, S.L. Sikkenga, "Development of the rhenium containing superalloy CMSX-4 and CM186LC for single crystal blade and directionally solidified vane application in advanced turbine engine", *Superalloys 1992*, pp. 297-306, 1992.

178. G.L. Erickson, "The Development and Application of CMSX@-10", *Superalloys 1996*, pp. 35-44, 1996.

179. E. Fleischmann, M.K. Miller, U. Glatzel, "Quantitative experimental determination of the solid solution hardening potential of rhenium, tungsten and molybdenum in single-crystal nickel-based superalloys", *Acta Mater*. 87, pp. 350-356, 2015.

180. R. Darolia, D.F. Lahrman, R.D. Field, R. Sisson, "Formation of Topologically Closed Packed Phases in Nickle Base Single Crystal Superalloys", *Superalloys 1998*, pp. 255-264, 1998.

181. Z. SHI, S. LIU, X. WANG, J. LI, "Effects of Cr content on microstructure and mechanical properties of single crystal superalloy", *Trans. Nonferrous Met. Soc. China* , 25, pp. 776-782, 2015.

182. M. Moniruzzaman, Y. Murata, M. Morinaga, N. Aoki, T. Hayashida, R. Hashizume, "Prospect of Nickel-based Superalloys with Low Cr and High Re Contents", *ISIJ Int*, 42, pp. 1018-1025, 2002.

183. P. Caron, T. Khan, "Evolution of Ni-based superalloys for single crystal gas turbine blade applications", *Aerosp. Sci. Technol* , 3, PP. 513-523, 1999.

184. C. Beckermann, J.P. Gu, W.J. Boettinger, "Development of a freckle predictor via rayleigh number method for single-crystal nickel-base superalloy castings", *Metall. Mater. Trans. A*, 31, pp. 2545-2557, 2000.

185. E. Fleischmann, M.K. Miller, E. Affeldt, U. Glatzel, "Quantitative experimental determination of the solid solution hardening potential of rhenium, tungsten and molybdenum in single-crystal nickel-based superalloys", *ACTA Mater*, 87, pp. 350-356, 2015.

186. Q. Wu, S.-S. Li, Y. Ma, S.-K. Gong, "First principles calculations of alloying element diffusion coefficients in Ni using the five-frequency model", *Chinese Phys. B*, 21, pp.102-109, 2012.

187. C.L. Fu, R. Reed, A. Janotti, M. Krcmar, "On the Diffusion of Alloying Elements in the Nickel-Base Superalloys, *Superalloys 2004*, pp. 867-876, 2004.

188. Y. Koizumi, Toshiharu Kobayashi, Tadaharu Yokokawa, Zhang Jianxin, Makoto Osawa, H. Harada, Yasuhiro Aoki, M. Arai, "Development Of Next-Generation Ni-Base Single Crystal Superalloys", *Superalloys 2004*, pp. 35-43, 2004.

189. N. Warnken, Studies on the Solidification Path of Single Crystal Superalloys, *J. Ph. Equil. Diff*, 37, pp. 100-107, 2016

190. M. Terner, H.Y. Yoon, H. U. Hong, S. M . Seo, J. H. Gu, J. H. Lee, "Clear path to the directional solidification of Ni-based superalloy CMSX-10: A peritectic reaction", *Mater. Charact*. 105 , pp. 56–63, 2015.

191. N. D'Souza, H.B. Dong, "Solidification path in third-generation Ni-based superalloys, with an emphasis on last stage solidification", *Scr. Mater*, 56, pp. 41-44, 2007.

192. N.D'Souzaa, H.B.Dong, M.G.Ardakani, B.A.Shollock, "Solidification path in the Ni-base superalloy, IN713LC - quantitative correlation of last stage solidification" , *Scr. Mater*, 53, pp. 729-733, 2005.

193. S.M. Seo, H.-W. Jeong, Y.-K. Ahn, D.W. Yun, J.-H. Lee, Y.-S. Yoo, "A comparative study of quantitative microsegregation analyses performed during the solidification of the Ni-base superalloy CMSX-10", *Mater. Charact*, 89, pp. 43-55, 2014.

194. F. Wang, D. Ma, A. Bührig-Polaczek, "Eutectic Formation During Solidification of Ni-Based Single-Crystal Superalloys with Additional Carbon", *Metall. Mater. Trans. A* , 48 , pp. 5442-5448, 2017.

195. Shyy. W, *Computational modeling for fluid flow and interfacial transport*, B.V, Amsterdam, 1994, accessed at May 2018.

196. P.A. Curreri, J.E. Lee, D.M. Stefanescu, "Dendritic solidification of alloys in low gravity", *Metall. Trans. A*, 19, pp. 2671-2676, 1988.

197. B. Mert, *Single Crystal Growth of Ni-Bse Superalloys by The Conventional Bridgman and Novelsubmerged Baffle Methods*, M.Sc thesis, Bogazici University, 2016

198. H. Dai, *A Study of Solidification Structure Evolution during Investment Casting of Ni-based Superalloy for Aero-Engine Turbine Blades*, Ph.D. Thesis, University of Leicester, 2008.

199. W. Wang, P.D. Lee, M. McLean, "A model of solidification microstructures in nickel-based superalloys: predicting primary dendrite spacing selection", *Acta Mater* , 51, pp. 2971-2987, 2003.

200. M.E. Kassner, Taylor hardening in five-power-law creep of metals and Class M alloys, *Acta Mater* ,52 , pp. 1-9, 2004.

201. N. Warnken, R.C. Reed, On the Characterization of Directionally Solidified Dendritic Microstructures, Metall. Mater. Trans. A. 42, pp. 1675-1683, 2011.

202. L. Liu, T. Hang, M. Zou, W. Zhang, J. Zhang, H. Fu, "The Effects Of Withdrawal And Melt Overheating Histories On The Microstructure Of A Nicked-Based Single Crystal Superalloy", *Superalloys 2008*, pp. 287-293, 2008.

203. F. Sadeghi, A. Kermanpur, D. Heydari, M. Bahmani, "Effect of withdrawal rate transition on microstructural features of a single crystal Ni-based superalloy", *Cryst. Res. Technol* , 52, 1700012, 2017.

204. H.. Whitesell, R.. Overfelt, "Influence of solidification variables on the microstructure, macrosegregation, and porosity of directionally solidified Mar-M247", *Mater. Sci. Eng. A*, 318, pp. 264-276, 2001.

205. J. Zhang, J. Li, T. Jin, X. Sun, Z. Hu, "Effect of Solidification Parameters on the Microstructure and Creep Property of a Single Crystal Ni-base Superalloy", *J. Mater. Sci. Technol*, 26, pp. 889-894, 2010

206. J. zhang, J.Li, T. Jin, X. Sun, Z. Hu, " Effect of withdrawal rate on the microstructures of a single crystal Ni-base superalloy", *Ad. Mat. Res.* 97-101, pp. 1016-1019, 2010.

207. Q. Yue, L. Liu, W. Yang, T. Huang, J. Zhang, H. Fu, X. Zhao, "Influence of withdrawal rate on the porosity in a third-generation Ni-based single crystal superalloy", *Prog. Nat. Sci. Mater. Int*, 27, pp. 236-243. 2017.

208. H.. Whitesell, R.. Overfelt, "Influence of solidification variables on the microstructure, macrosegregation, and porosity of directionally solidified Mar-M247", *Mater. Sci. Eng. A* , 318, pp. 264-276, 2001.

209. J.R. Kim, R. Abbaschian, "Influence of solidification variables on the microporosity formation on Al–Cu (4.5 wt%) alloy with axial heat processing", *J. Mater. Sci*. 46 , pp. 6213-6223, 2011.

210. I. Roy, E. Balikci, S. Ibekwe, A. Raman, "Precipitate growth activation energy requirements in the duplex size γ′ distribution in the superalloy IN738LC", *J. Mater. Sci.* 40, pp. 6207-6215, 2005.

211. E. Balikci, D. Erdeniz, "Multimodal Precipitation in the Superalloy IN738LC", *Metall. Mater. Trans. A*, 41, pp. 1391-1398, 2010.

212. K. Kakehi, "Effect of primary and secondary precipitates on creep strength of Ni-base superalloy single crystals", *Mater. Sci. Eng. A* , 278, pp. 135-141, 2000.

213. J.B. Le Graverend, J. Cormier, F. Gallerneau, P. Paulmier, "Dissolution of Fine γ' Precipitates of MC2 Ni-Based Single-Crystal Superalloy in Creep-Fatigue Regime", *Adv. Mater. Res.* 278, pp. 31-36, 2011.

214. *Imagej*, https://imagej.nih.gov/ij/download.html , accessed at april 2018.

215. I. Roy, E. Balikci, S. Ibekwe, A. Raman, "Precipitate growth activation energy requirements in the duplex size γ′ distribution in the superalloy IN738LC", *J. Mater. Sci*, 40, pp. 6207-6215, 2005.

217. K. Matuszewski, R. Rettig, H. Matysiak, Z. Peng, I. Povstugar, P. Choi, J. Müller, D. Raabe, E. Spiecker, K.J. Kurzydłowski, R.F. Singer, "Effect of ruthenium on the precipitation of topologically close packed phases in Ni-based superalloys of 3rd and 4th generation", *Acta Mater*, 95, pp. 274-283, 2015.

218. M. Simonetti, P. Caron, "Role and behaviour of μ phase during deformation of a nickel-based single crystal superalloy", *Mater. Sci. Eng. A.* 254, pp. 1-12, 1998.

219. B. Dubiel, P. Indyka, T. Moskalewicz, A. Kruk, M. Zubko, I. Kalemba-Rec, K. Berent, "Characterization of the μ and P phase precipitates in the CMSX-4 single crystal superalloy", *J. Microsc*, 266, pp. 239-248, 2017.

220. Z. Shi, J. Li, S. Liu, "Effects of Ru on the microstructure and phase stability of a single crystal superalloy, Int. J. Minerals. Metallurgy. Mat, 19, pp. 1004-1009, 2012.

221. C. Rae, M. Karunaratne, C. Small, R. Broomfield, C. Jones, R. Reed, " GCP and TCP Phases Presented in Nickel-base Superalloys", *Maerials today proc*, 3, pp. 936-941, 2006.

222. Z. Shi, J. Li, S. Liu, X. Wang, "Creep properties and microstructure evolution of nickel-based single crystal superalloy at different conditions", *Trans. Nonferrous Met. Soc. China*, 24, pp. 2536-2543, 2014.

223. F. Louchet, "A model of negative creep in nickel-based superalloys", *Scr. Metall. Mater*, 33, pp. 913-918, 1995.

224. R.. Reed, N. Matan, D.. Cox, M.. Rist, C.M.. Rae, Creep of CMSX-4 superalloy single crystals: effects of rafting at high temperature, *Acta Mater*, 47, pp. 3367-3381, 1999.

225. S. Tian, Y. Su, B. Qian, X. Yu, F. Liang, A. Li, "Creep behavior of a single crystal nickel-based superalloy containing 4.2% Re", *Mater. Des*, 37, pp. 236-242, 2012.

226. R.. Reed, N. Matan, D.. Cox, M.. Rist, C.M.. Rae, "Creep of CMSX-4 superalloy single crystals: effects of rafting at high temperature", *Acta Mater*, 47, pp. 3367-3381, 1999.

227. J. Zhang, T. Murakumo, H. Harada, Y. Koizumi, T. Kobayashi, "Creep Deformation Mechanisms in Some Modern Single-Crystal Superalloys", *Superalloys 2004*, pp. 189-195, 2004.

228. J.Y. Chen, Q. Feng, L.M. Cao, Z.Q. Sun, "Improvement of stress–rupture property by Cr addition in Ni-based single crystal superalloys", *Mater. Sci. Eng. A*, 528, pp. 3791-3798, 2011.

229. G.L. Erickson, "The Development of the CMSX-1lb and CMSX-1lc Alloys for Industrial Gas Turbine Applications", Superalloys 1996, pp. 45-52, 1996.

230. J. Wahl, K. Harris, "New single crystal superalloys – overview and update", *MATEC Web Conf*. EDP Sciences, 14, 2014.